https://doi.org/10.15388/vu.thesis.85
https://orcid.org/0000-0002-8826-7847

VILNIUS UNIVERSITY
CENTER FOR PHYSICAL SCIENCES AND TECHNOLOGY

Titas
TIČKŪNAS

Formation of high-resolution functional microdevices and their applications

DOCTORAL DISSERTATION

Technological sciences
Materials engineering T 008

VILNIUS 2020

This dissertation was written between 2015 and 2019 at Vilnius University.

Academic supervisor:
prof. dr. Roaldas Gadonas (Vilnius University, Technological Sciences, Materials Engineering, T 008). From 2015-10-01 to 2019-07-02.
doc. dr. Domas Paipulas (Vilnius University, Technological Sciences, Materials Engineering, T 008). From 2019-07-03 to 2019-09-30.

Dissertation Defense Panel:

Chairman – doc. dr. Andrius Melninkaitis (Vilnius University, Technological Sciences, Materials Engineering, T 008).

Members:
doc. dr. Renata Butkutė (Center for Physical Sciences and Technology, Technological Sciences, Materials Engineering, T 008);
doc. dr. Vytautas Jukna (Vilnius University, Natural Sciences, Physics, N 002);
dr. Evaldas Stankevičius (Center for Physical Sciences and Technology, Technological Sciences, Materials Engineering, T 008);
prof. dr. Tomas Tamulevičius (Kaunas University of Technology, Technological sciences, Materials Engineering, T 008).

The dissertation shall be defended at a public meeting of the Dissertation Defence Panel at 14 p.m. on the 28th of September, 2020 at Vilnius University Laser Research Center, room 306. Address: Saulėtekio al., Room 306, Vilnius, Lithuania, tel. +370 5 236 6005.

The text of this dissertation can be accessed at the Vilnius University, Center for Physical Sciences and Technology libraries, as well as on the website of Vilnius University: www.vu.lt/naujienos/ivykiu-kalendorius

https://doi.org/10.15388/vu.thesis.85
https://orcid.org/0000-0002-8826-7847

VILNIAUS UNIVERSITETAS
FIZINIŲ IR TECHNOLOGIJOS MOKSLŲ CENTRAS

Titas
TIČKŪNAS

Aukštos skyros funkcinių mikrodarinių formavimas ir taikymai

DAKTARO DISERTACIJA

Technologijos mokslai
Medžiagų inžinerija T 008

VILNIUS 2020

Disertacija rengta 2015 – 2019 metais Vilniaus universitete.

Mokslinis vadovas:
prof. dr. Roaldas Gadonas (Vilniaus universitetas, technologijos mokslai, medžiagų inžinerija, T 008). Nuo 2015-10-01 iki 2019-07-02.
doc. dr. Domas Paipulas (Vilniaus universitetas, technologijos mokslai, medžiagų inžinerija, T 008). Nuo 2019-07-03 iki 2019-09-30.

Gynimo taryba:

Pirmininkas – doc. dr. Andrius Melninkaitis (Vilniaus universitetas, technologijos mokslai, medžiagų inžinerija, T 008).

Nariai:
doc. dr. Renata Butkutė (Fizinių ir technologijos mokslų centras, technologijos mokslai, medžiagų inžinerija, T 008);
doc. dr. Vytautas Jukna (Vilniaus universitetas, fiziniai mokslai, fizika, N 002);
dr. Evaldas Stankevičius (Fizinių ir technologijos mokslų centras, technologijos mokslai, medžiagų inžinerija, T 008);
prof. dr. Tomas Tamulevičius (Kauno technologijos universitetas, technologijos mokslai, medžiagų inžinerija, T 008).

Disertacija bus ginama viešame Gynimo tarybos posėdyje 2020 m. rugsėjo 28 d. 14 val. Vilniaus universiteto Fizikos fakulteto Lazerinių tyrimų centro 306 auditorijoje. Adresas: Saulėtekio al. 10, 306 aud., Vilnius, Lietuva, tel. +370 5 236 6005.

Disertaciją galima peržiūrėti Vilniaus universiteto, Fizinių ir technologijos mokslų centro bibliotekose ir VU interneto svetainėje adresu: https://www.vu.lt/naujienos/ivykiu-kalendorius

Contents

LIST OF ABBREVIATIONS

3D	Three-dimensional
4π-MPP	4π multiphoton polymerization
CAD	Computer-aided design
CPD	Critical point dryer
CCD	Charged-coupled device
DOE	Diffractive optical elements
DLW	Direct laser writing
DMD	Digital micromirror device
ETH	Ethanol
FIB	Focused-ion beam
HF	Hydrofluoric acid
IR	Infrared light
IRG	2-benzyl-2-(dimethylamino)-4'-morpholinobutyrophenone
KOH	Potassium hydroxide
LIPSS	Laser-induced periodical surface structures
MAPTMS	Methacryloxypropyl trimethoxysilane
MPP	Multiphoton polymerization
NA	Numerical aperture
PEN	4-methyl-2-pentanone
PSF	Point spread function
SEM	Scanning electron microscope
SLE	Selective laser etching
SLM	Spatial light modulator
STED	Stimulated emission depletion
STED-MPP	Stimulated emission depletion inspired direct laser writing
UV	Ultraviolet light
VIS	Light in the visible spectrum range

INTRODUCTION

Since the invention of the first transistor a miniaturization process becomes apparent, yet there is a need for smaller mechanical, optical, and electrical microfunctional devices in the industry. This trend is supported Moore's law that has been valid for more than fifty years, which states that in the semiconductor industry the transistor number in processors doubles in two years. Miniaturization covers not only electronics industry, but the same principles could be seen in photonics, microoptics, micromechanics, microfluidics, and many other applications. Therefore, new advancements and novel laser technologies are emerging in the market, which lets to process materials and to obtain three-dimensional (3D) functional microdevices in other, non-planar lithography ways.

The appearance of the ultrashort laser pulses opens up new possibilities in the materials processing, especially in the formation of the 3D microstructures. Contrary to longer nanosecond, the femtosecond laser pulses provide extremely high peak intensities, which lead to non-linear absorption effects in transparent material. Thanks to the multiphoton absorption, even the ultrashort laser wavelength is transparent to processable material, the intensities reached at the focus point allow to modify material only at the focal spot. This phenomenon has allowed to use the same laser source for different processes: such as 3D printing (multiphoton polymerization) of polymeric microstructures in an additive way, or creating three-dimensional devices out of a single-piece of glass substrate by subtractive method (selective laser etching).

From a technology development perspective, even though these methods were presented for the first time around two decades ago, these technologies still are in the process of being developed. Continuously increasing number of scientific articles in this field and the potential applications in different fields show these technologies to be very promising, and simultaneously indicate that there is still a lot of room for improvements and developments. The demand of industry for novel sophisticated functional devices is continuously pushing the methods further to technological limits of the process in terms of achievable resolution and higher throughput.

In this thesis, several topics related to 3D laser technologies are explored and discussed. We demonstrate a technological combination of subtractive and additive technologies into a novel type micromechanical sensor for the investigation of polymer mechanical properties. Moreover, the proposed method gives insight into polymeric structures' behavior in different environmental mediums. Furthermore, we introduce a novel method for axial feature resolution improvement for multiphoton polymerization by using a pair of two opposing objectives. For enhancement of technology throughput, we propose a straightforward method to dynamically tune the voxel size during the fabrication in the traditional direct laser writing technique.

The aim of the dissertation

The main aim of this work microfabrication of novel type functional structures by using techniques enabled by the femtosecond lasers and development of these fabrication methods.

The main tasks of the thesis

In order to reach the aim of this scientific work, the following objectives were set:

1. Development and optimization of a functional micromechanical sensor for investigation of mechanical properties of polymeric microstructures fabricated *via* multiphoton polymerization technique. A study of polymeric elastic properties' change in different ambient mediums.
2. Assembly, development, and integration of 4π excitation in the traditional multiphoton polymerization setup. Study of the feature size resolution and its properties related to this technique.
3. Investigation of feature size dependence on the filling of the input entrance of the focusing objective by the laser diameter.

Novelty and importance of the thesis

1. A novel 3D polymer/glass micromechanical sensor concept has been demonstrated by combining two femtosecond laser direct writing processes: selective laser etching of glass combined with two-photon polymerization. It was shown experimentally that this concept can work for investigating mechanical properties of the polymerized microstructures.
2. For the first time, a 4π excitation was implemented in the multiphoton polymerization technique, which allows an enhancement of the axial feature resolution.
3. It was demonstrated that multiphoton polymerization with 4π excitation in polymers could produce a sub-micrometer periodic interference pattern, which produces structural colors in a visible spectrum range.
4. In the multiphoton polymerization, the lateral and axial feature size resolution was tuned by changing the incident laser beam diameter with a motorized beam expander. This method was implemented for the voxel in real-time control during the fabrication of 3D microstructures.

Statements for defence

1. Glass microcantilever system fabricated using selective laser etching technique is suitable for measuring elastic properties (Young's modulus) of polymeric microstructures fabricated by multiphoton polymerization technique, if these structures can be integrated into micromechanical systems. This technique provides the means to measure the changes in elasticity and deformation magnitude when polymeric structures undergo swelling and shrinkage in different mediums.
2. A 4π excitation in the multiphoton polymerization technique allows enhancement of axial feature resolution up to three times in the SZ2080 photopolymer compared to conventional technique using high numerical aperture objectives. Lower numerical aperture objectives are capable of forming periodic structures with sub-micron feature size oriented along the optical axis.
3. Real-time control of the effective numerical aperture of the objective can be realized by dynamical manipulation of the incident laser beam diameter, allowing the tuning of the voxel size in direct laser writing technique. The smallest feature is limited by the nominal numerical aperture of the objective, while the largest feature dimension is defined by the least laser beam diameter that the system achieves.

Layout of the dissertation

The doctoral dissertation consists of four main chapters:

- The **first chapter** explains the physical processes that are relevant in a ultrashort laser pulses interaction with different materials and also presents the capability of formation of the 3D structures using femtosecond lasers.
- In the **second chapter**, a glass microdevice is presented for investigation of the mechanical properties of the structures fabricated by multiphoton polymerization. The working principle of the cantilever, numerical calculations of its deflections are described. The experimental results of cantilever deflection in different mediums are presented.
- The **third chapter** is devoted to the findings on multiphoton polymerization scheme in a combination of 4π excitation. The numerical modeling and experimental results are presented.
- In the **fourth chapter**, the ways for the enhancement of throughput in multiphoton polymerization are discussed. As alternative, the results of

dynamic feature size tuning are presented by changing the input beam diameter in multiphoton polymerization technique. The numerical calculation were done by scalar and vectorial theories, which are compared with experimental results.

Approbation of the research results

This section presents the lists of papers and conferences related to the dissertation.

Scientific articles in periodical journals with an impact factor which are included in the Web of Science database

P1. **T. Tičkūnas**, M. Perrenoud, S. Butkus, R. Gadonas, S. Rekštytė, M. Malinauskas, D. Paipulas, Y. Bellouard, and V. Sirutkaitis, "Combination of additive and subtractive laser 3D microprocessing in hybrid glass/polymer microsystems for chemical sensing applications", Opt. Express. **25**(21), 26280–26288 (2017).

P2. **T. Tičkūnas**, D. Paipulas, and V. Purlys, "4Pi multiphoton polymerization", Appl. Phys. Lett. **116**(3), 031101 (2020).

P3. **T. Tičkūnas**, D. Paipulas, and V. Purlys, "Dynamic voxel size tuning for direct laser writing", Opt. Mat. Express **10**(6), 1432-1439 (2020).

Conference proceedings

PR1. **T. Tičkūnas**, M. Malinauskas, R. Gadonas, Y. Bellouard, and D. Paipulas, "Hybrid laser 3D microprocessing in glass/polymer micromechanical sensor: towards chemical sensing applications", Proc. SPIE. **10675**, 106750C (2018).

PR2. L. Jonušauskas, **T. Tičkūnas**, A. Narmontas, G. Nemickas, V. Purlys, G. Grigalevičiūtė, and R. Gadonas, "Femtosecond laser-assisted etching: making arbitrary shaped 3D glass micro-structures", Proc. SPIE. **10520**, 105201G (2018).

PR3. **T. Tičkūnas**, V. Purlys, and R. Gadonas, "Axial resolution improvement in multiphoton polymerization by 4Pi excitation", Proc. SPIE. **10909**, 1090903 (2019).

Conference presentations, presented by the author of the thesis

1. **T. Tičkūnas**, M. Perrenoud, S. Butkus, R. Gadonas, S. Rekštytė, M. Malinauskas, D. Paipulas, Y. Bellouard, and V. Sirutkaitis, "Combination of additive and subtractive laser 3D microprocessing in hybrid

glass/polymer microsystems for chemical sensing applications", CLEO Europe/EQEC, Munich, Germany (June 2017).

2. **T. Tičkūnas**, M. Perrenoud, S. Butkus, R. Gadonas, S. Rekštytė, M. Malinauskas, D. Paipulas, Y. Bellouard, and V. Sirutkaitis, "Combination of additive and subtractive laser 3D microprocessing in hybrid glass/polymer microsystems for chemical sensing applications", 42nd Lithuanian National Conference of Physics, Vilnius, Lithuania (October 2017).
3. **T. Tičkūnas**, M. Malinauskas, R. Gadonas, Y. Bellouard, and D. Paipulas, "Hybrid additive and subtractive laser 3D microprocessing in glass/polymer microsystems for chemical sensing applications", SPIE Europe, Strasbourg, France (April 2018).
4. **T. Tičkūnas**, M. Malinauskas, R. Gadonas, Y. Bellouard, and D. Paipulas, "Hybrid additive and subtractive laser 3D microprocessing in glass/ polymer microsystems", Laser Precision Microfabrication, Edinburgh, UK (June 2018).
5. **T. Tičkūnas**, M. Malinauskas, R. Gadonas, D. Paipulas, and Y. Bellouard, "Investigation of mechanical properties of polymeric microstructures using glass microcantilevers", ICPEPA 11, Vilnius, Lithuania (September 2018).
6. **T. Tičkūnas**, D. Paipulas, and V. Purlys, "4Pi multiphoton polymerization", SPIE Photonics West, San Francisco USA (February 2019).
7. **T. Tičkūnas**, D. Paipulas, and V. Purlys, "4Pi multiphoton polymerization for improving axial resolution", The 20th International Symposium on Laser Precision Microfabrication, Hiroshima, Japan (May 2019).
8. **T. Tičkūnas**, D. Paipulas, and V. Purlys, "Direct Laser Writing by 4Pi Multiphoton Polymerization", CLEO Europe/EQEC, Munich, Germany (June 2019).
9. **T. Tičkūnas**, D. Paipulas, and V. Purlys, "Towards the improvement of axial resolution: 4Pi multiphoton polymerization", SPIE Photonics West, San Francisco, USA (February 2020).
10. **T. Tičkūnas**, D. Paipulas, and V. Purlys, "Dynamic voxel size tuning for direct laser writing", SPIE Photonics West, San Francisco, USA (February 2020).

Conference presentations, presented by the co-author

11. D. Paipulas, S. Rekštytė, **T. Tičkūnas**, M. Malinauskas, V. Mizeikis. "Reversible deformations in laser-written polymeric microstructures: New platform for sensing and micro-actuation applications", SPIE Photonics West, San Francisco, USA (February 2020).

12. L. Jonušauskas, D. Andrijec, T. Baravykas, A. Butkutė, **T. Tičkūnas**, T. Gadišauskas, V. Purlys. "Hybrid additive-subtractive femtosecond laser 3D fabrication of medical microdevices", SPIE Photonics West, San Francisco, USA (February 2020).

Author contributions in the corresponding papers

The main co-authors of the research results presented in the thesis are dr. D. Paipulas, dr. V. Purlys, and prof. dr. Y. Bellouard. Contribution of the thesis author is further noted in accordance to the list of Thesis articles.

P1: The idea of the article was conceptualized by a Swiss group led by prof. dr. Y. Bellouard. Their substantial knowledge in glass microfabrication and micromechanics was important for obtaining successful results. Initial testing's were done by co-authors, which gave fruitful insights and direction to the project. The author of this dissertation improved the design of the single-micromechanical sensor, fabricated a multi-cantilever system, performed the experiments related to multiphoton polymerization, measurements of shrinkage/swelling in different mediums, was involved in data analysis, contributed to the preparation of the manuscript.

P2: The author of this dissertation assembled the experimental setup, performed the experiments, numerical calculations and wrote the manuscript. Dr. Vytautas Purlys was the conceptual author of the idea, he designed, and supervised the research. Dr. Domas Paipulas was consulted during this research. All authors contributed to the revision and improvements of the article.

P3: The author of the dissertation performed the experiments and numerical calculations, and wrote the manuscript. Dr. Vytautas Purlys was the conceptual author of the idea, he together with dr. Domas Paipulas contributed to experimental planning and preparation of the article. All authors contributed to the revision and improvements of the article.

PR1: This article is continuation of the work, which is presented in P1. The author of the dissertation fabricated the next generation samples, performed the fabrication, characterization, performed the numerical calculations, drafted the figures and prepared the manuscript. Dr. Domas Paipulas conducted the research, contributed in interpretation and analysis of the data. All authors contributed in revision and improvements of the article.

PR2: The author of the dissertation designed and fabricated the structures, provided the information related to this technology to the writer, edited the article. The manuscript was written by Linas Jonušauskas.

PR3: This article presents initial results, which gave a basis for subsequent article P2. The author of the dissertation assembled the experimental setup, performed the experiments, wrote the manuscript. Dr. Vytautas Purlys was the conceptual author of the idea, he designed the system, supervised the research, contributed to the preparation of the article. Dr. Roaldas Gadonas supported the research, provided the necessary equipment.

1. THEORETICAL BACKGROUND

This chapter is dedicated to explain the physical processes that are relevant in ultrashort laser pulse interaction with transparent materials. As the nano and micro 3D structuring was enabled by the appearance of ultrashort pulses this chapter also covers multiphoton polymerization process explanation and following wide range of applications.

1.1. Overview of laser driven applications development

In 1960, after the first demonstration of the laser, it was called "a solution looking for a problem" [1]. It took only one year for lasers to start appearing on the commercial market. In the following decades, the lasers found multiple applications, from material processing to medicine. A huge boost of laser application came after the development of advanced optics fabrication techniques that allowed to produce stable, high quality and power sub-picosecond laser pulses. The high peak pulse power made it possible to trigger the non-linear light-matter interactions and process even transparent materials to the laser wavelength.

The interest in transparent material laser induced modification quickly grew from 1996, when K. Hirao group showed the first demonstration of the fs-laser induced waveguide modification into the bulk of different glasses (silica, borate, soda lime, fluorozirconate) [2]. By using tightly focused Ti:sapphire laser beam, they were able to locally increase the refractive index of the glass by 0.01-0.035 depending on the laser energy and the glass. Using their setup, the authors showed the ability to write optical circuit beneath the glass surface. The waveguide writing process was accomplished by longitudinal and transversal translation of the sample. These results had a great impact on the applicability of ultrashort laser pulses, and many novel applications appeared.

In 1997, the S. Kawata group reported on additive multiphoton polymerization (MPP) technique, which allowed fabrication of truly 3D microstructures out of polymer material resin [3]. It is based on non-linear absorption of a tightly focused femtosecond laser beam, which induces well confined photopolymerization reactions. The polymer chemical properties are locally changed only at the laser beam focus. The whole structure fabrication writing process could be understood as the femtosecond laser “pen”, which is moved spatially within the volume of the polymer in all three dimensions. This process gives ability to form almost any 3D shape structure at the microscale. In case of negative tone photopolymer, all the unexposed areas are simply washed out, leaving only solidified structure.

In 1999, a birefringent modification in the bulk of fused silica was observed by focusing the fs-laser pulses at higher pulse energy than needed for the refractive index change [4]. This effect was investigated by Y. Shimotsuma et al. in detail [5]. The birefringence was attributed to the formation of sub-wavelength periodic nanostructures. This formation of volume periodic structures was interpreted as interference between the incident laser light and the electric field of the bulk electron plasma wave. In 2001, the possibility of 3D microfluidic channel formation with the femtosecond laser writing in fused silica and subsequent etching step for removing the modified zones of the material was shown by A. Marcinkevičius et al. [6]. The exposed areas were etched at much higher etching speed than unmodified fused silica. This discovery has enabled the fabrication of true 3D microstructures from a single piece of glass.

In the following years the femtosecond laser induced-phenomena and their applications were reported in numerous articles. Ultrashort laser pulses were applied to a number of various processing techniques, such as laser-induced periodic surface structures (LIPSS) [7], micromachining of different materials [8], two-photon polymerization [9], and selective laser etching (SLE) [10]. Moreover, these methods push the industry forward, allowing to create new type of data storage [11], provided fabrication of transparent glass photonic devices, microfluidic and biomicrochips [12, 13] for commercial applications.

In the following section, we will discuss the fundamental mechanisms, which are involved in ultrashort laser pulse and matter interactions.

1.2. Interaction of ultrashort laser pulses with transparent mediums

When a low intensity laser beam propagates through a transparent material, the light faces classical linear optical effects, like reflection, refraction, diffraction, or scattering. Transparent materials, in this case dielectrics, are not transparent to all the wavelengths of the light and are defined by the material absorption. In the proximity of the optical range, the blue part of the spectrum absorption is governed by the bandgap of the material, i.e., if the photon energy is larger than the bandgap of the material, the photon is absorbed by the atom. While the red part of the spectrum absorption is due to the material vibrations. For instance, fused silica, depending on its type, could have a 7.5 eV bandgap [14], which would correspond to absorption edge for 165 nm wavelength light. Due to wide bandgap, most of the dielectrics are transparent to visible (VIS) and near infrared (IR) spectrum light. Nonetheless, when the laser peak intensity is sufficiently high, like in the case of ultrashort laser pulses, the absorption of photons can still take place, however, couple of photons needs to be absorbed at once to overcome the material bandgap.

The term "ultrashort laser pulses" is commonly accepted for the pulses with the duration lower than a few tens of picoseconds [15]. A focused laser beam of such duration could have extremely high peak intensity and reach values exceeding 10^{15} W/cm^2. Even in dielectric materials, such high intensity is sufficient to induce non-linear absorption processes. In general, interaction of high intensity laser light and dielectric material could be divided into three main stages: (1) free (or quasi-free) electrons generation, (2) thermal energy generation from relaxation of electrons, and (3) creation of permanent modification in the material if the sufficient energy is absorbed [8].

In dielectrics, the valance band is the energy range where non-excited electrons rest. The top of the valance band is the highest energy level, which non-excited electron can have. Meanwhile, the conduction band is the energy range, where excited electrons can rest, and the bottom of the band is the lowest energy what excited electron can have. These bands are separated by the energy gap called bandgap. At absolute zero temperature, there are no free electrons in the conduction band, while the valence band is filled. Usually, the single photon of VIS&IR light has energy, which is not high enough for the excitation of the electron, however, the transfer of the electron from valence to conduction band could be induced through non-linear excitation mechanisms, such as photoionization and avalanche ionization [16], which will be explained in the following section.

1.2.1. Non-linear photoionization mechanisms

Photoionization refers to a direct electron excitation of the material by electromagnetic wave [17]. Low intensity electromagnetic wave can photoionize only when the frequency is higher (photon energy is higher) than the bandgap. However, when electromagnetic wave intensity is high, the nonlinear photoionization can take place and electron can be excited by the lower frequency electromagnetic wave (lower energy photon) than the material bandgap. The nonlinear photoionization can be separated into two regimes: tunneling and multiphoton ionization, as shown in Fig. 1.1 (a, b). The dominant process will highly depend on the laser parameters, such as laser intensity, frequency, and the bandgap of the material. At lower laser intensities and higher frequencies (but lower than needed for single excitation), the generation of free-electrons is considered to occur through multiphoton ionization. During this process, the electron absorbs multiple photons simultaneously so that the excitation of the electron could take place, this is illustrated in Fig. 1.1 (a). The condition for multiphoton ionization could be described in the following relation:

$$N\hbar\omega \geq E_g, \tag{1.1}$$

where N - the minimum number of photons needed for photoionization, $\hbar$ - the Planck constant, E_g - the bandgap of the material, ω - the frequency of the laser wavelength. For instance, the femtosecond laser wavelength of 1030 nm

(1.2 eV) would need at least 7-photon absorption to induce an excitation in fused silica ($E_g = 7.5$ eV).

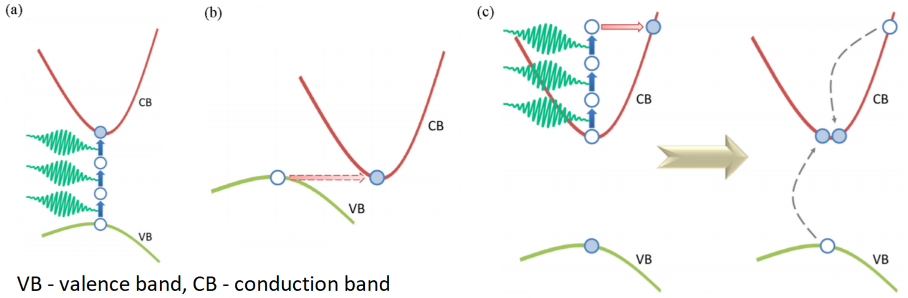

Figure 1.1: Schematic diagrams of non-linear absorption processes found: (a) multiphoton ionization, (b) tunneling ionization, and (c) avalanche ionization: free-carrier absorption followed by impact ionization [16].

Multiphoton absorption probability or photoionization rate $P(I)$ strongly depends on the laser intensity I and the bandgap of the material. $P(I)$ could be expressed [17] as:

$$P(I) = \sigma_N I^N, \tag{1.2}$$

where σ_N - multiphoton absorption coefficient for absorption N photons, N - the number of photons which satisfies Eq. 1.1.

At relatively high laser intensities, the ionization of the material can occur *via* tunneling ionization. The strong electric field of the laser light distorts the electronic band structure of dielectric so that the electron could tunnel through a reduced barrier and become free carrier, as illustrated in Fig. 1.1 (b). In order to know which type of non-linear ionization mechanism, tunneling or multiphoton, is dominant for a certain electromagnetic wave intensity, an adiabatic parameter γ is calculated, which is known as the Keldysh parameter [18]:

$$\gamma = \frac{\omega}{e}\sqrt{\frac{mcn\epsilon_0 E_g}{I}}, \tag{1.3}$$

where ω - laser radiation frequency, e - charge of the electron, m - reduced mass of the electron, c - the velocity of the light, n - refractive index of the material, ϵ_0 - permittivity of the free space. When γ parameter is much lower than 1.5, tunneling ionization plays a major role, and, converse, if γ exceeds much more than 1.5, then multiphoton absorption becomes dominating. There is an intermediate regime at around 1.5 value, where a combination of both tunneling and multiphoton absorptions plays a role.

Apart from discussed photoionization phenomena, there is also another non-linear electron excitation mechanism – avalanche ionization (see Fig. 1.1 (c)).

For this process, initial free-carriers need to be in the conduction band for this regime to start. Under femtosecond laser irradiation of material, it is considered that the initial electrons are generated *via* photoionization. Thereafter, a free-electron present in the conduction band can absorb sequentially several photons. If its energy exceeds the bandgap of the material, then this electron could ionize another electron from the valence band, resulting in two electrons near the conduction band minimum. Then, again, each electron can absorb the energy through free-carrier absorption and excite new carriers. This described process will repeat as long as the laser electric field is present and strong enough, or till all the material is ionized. The density of the electrons generated by an avalanche ionization could be expressed as [19]:

$$p_e = p_0 2^{w_{\mathrm{imp}} t} = p_0 e^{\ln 2 \cdot w_{\mathrm{imp}} \cdot t}, \tag{1.4}$$

where p_0 is initial electron density, w_{imp} – the probability of impact ionization, which depends on laser frequency, intensity, and the bandgap of the material.

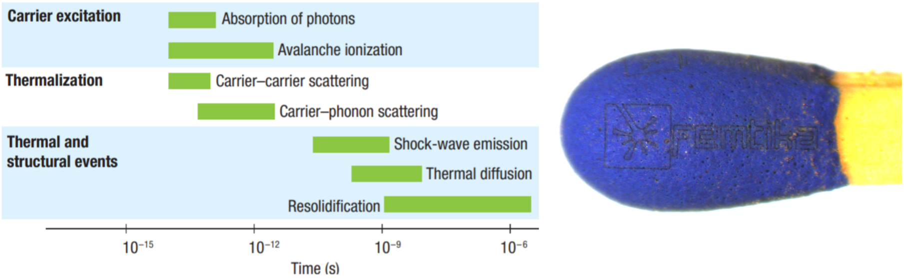

Figure 1.2: (*left*) Timescale of the physical mechanism associated with the interaction of ultrashort laser pulses in transparent materials [20]. (*right*) Ultrashort laser pulses allow "cold" microprocessing even for a match without its ignition.

Once the ultrashort laser pulse is absorbed by nonlinear excitation mechanisms and the deposited energy is sufficiently high, then a modification in the dielectric material could be induced. For sub-picosecond laser pulses, the light-matter interaction is substantially different from that for pulses with longer duration, where thermal phenomena play an important role. Depending on the material, the electron could transfer its energy to the material lattice in picosecond timescale range [19]. This means that, in most cases, the femtosecond (e.g., 100 fs) laser pulses could induce non-linear absorption processes faster the energy can be transferred to the lattice of the processed material. Timescales of the physical mechanisms associated with interaction of ultrashort laser pulses in the transparent material are listed in the Fig. 1.2. For the laser pulses with a few hundred of femtoseconds, the carrier excitation (such as the aforementioned tunneling, multiphoton and avalanche ionization) would start instantly within the pulse duration, meanwhile the material will undergo other physical mechanisms, like thermal and structural phenomena [20], only later in microsecond timescale. Due to this physical mechanism, ultrashort laser pulses allow to minimize thermal effects and process even match without its ignition, as shown Fig. 1.2.

For longer laser pulses, the physical mechanisms will be different – carrier excitation and energy transfer to the lattice processes are happening at the same time, thus it leads to a substantial amount of energy being transferred by thermal diffusion to the vicinity of the processing zone. Therefore, ultrashort laser pulses have an advantage, as only a part of energy is converted to the heat, resulting in suppression of heat affected zone, as well as high-precision and efficient microfabrication.

1.3. Interaction of ultrashort laser pulses with fused silica

The appearance of the femtosecond laser pulses has brought the opportunity to microprocess glass and obtain complicated shape 3D microstructures, which could expand the capabilities and applications over the currently used 2D microfluidics, lab-on-a-chip devices, which are produced mainly by planar surface technologies.

1.3.1. Fused silica

Fused silica is a superb material for many of traditional applications in science and industry. It is particularly noteworthy, as it is the purest form of glass, which has ideal optical properties, such as high transmittance over a broad range of spectrum from 170 nm to 2300 nm (e.g., Lithosil [21]), as well as low self-fluorescence. It also has great thermal durability and excellent chemical resistance [22]. Fused silica is a non-crystalline form of silica, which contains more than 99% of silicon dioxide (SiO_2). It has been accepted that the amorphous phase of quartz contains SiO_4 tetrahedra (a silicon surrounded by four oxygen atoms in the shape of tetrahedron), which are randomly linked in between forming variation of ring members, as shown in Fig. 1.3 [23]. The theoretical modeling shows that 5 and 6-member rings are the most common [24].

There are several different types of commercially available silica, which are defined by the manner of their production [25, 26]. As the manufacturing process varies, the fused silica will have slightly different composition (as OH content or other element impurities), which could have a limitation (reactivity or absorption) on the specific application [27]. The physical, thermal, chemical properties of glass could be significantly different by adding other chemical elements.

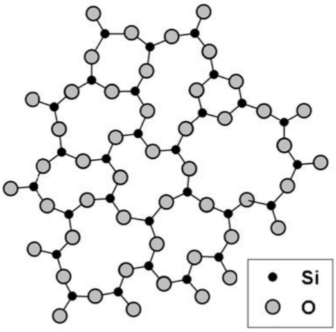

Figure 1.3: Schematic representation of fused silica molecular composition. It is an amorphous material, which consists of multi-membered rings [23].

1.3.2. Types of modifications in fused silica

Due to high-peak intensities, tightly focused femtosecond laser beams can trigger non-linear absorption phenomena. The result of this unique characteristic is that material transparent to the laser wavelength starts to absorb the light, resulting in modification only within the focal point of the focused laser beam if the achieved peak intensity is high enough.

Depending on the femtosecond laser parameters (pulse duration, peak intensity, pulse density), several modifications could be induced in the volume of fused silica. If the applied laser fluence is relatively low, unstable modifications could be produced. In this case, the deposited light energy is not enough to make any mechanical changes in the material but is sufficient to break weaker molecular bonds. This phenomenon is known as a generation of color centers, which results in defects starting to absorb the light. For most glasses (borosilicate, soda-lime, etc.), formation of color centers produce the change of optical properties in the ultraviolet (UV) and VIS spectrum range, meanwhile in fused silica it is seen only absorption peaks in the UV range. It is observed that the part of generated defects will decrease slightly after a certain time or by annealing the sample. It could be explained that excited defects just simply recombine forming stable chemical bonds.

The subsequent increase of applied fs-laser power will lead to irreversible mechanical changes. Three main types of permanent modifications were distinguished in fused silica by C. Hnatovsky et al. [28], as shown in Fig. 1.4. For this experiment, there was used a Ti:sapphire laser with central wavelength λ of 800 nm, operating at 100 kHz repetition rate, meanwhile the light was focused with a microscope objective of 0.65 numerical aperture (NA). Fig. 1.4 shows the working regime of each modification's dependence on laser pulse energy and duration. The first regime is known as isotropic refractive index change [2] and is typically produced at relatively narrow fabrication window at lower pulse energies (from <200 nJ to <400 nJ) and shorter pulse duration values (<200 fs). Under these conditions, the focused femtosecond laser irradiation leads to abrupt melting of the material only at the focus point. Subsequently, when irradiation is over, the fused silica cools down very rapidly due to high thermal gradient, resulting in higher density zone at the core, and, hence, an increase of refractive index [16]. Still, the mechanism for this process has not been fully understood, the current consensus is that it could be a result of the combination of glass densification and color centers' formation [10]. In fused silica, refractive index change leads to a positive modulation, which typically has Δn around 0.001 [8]. This type of modification has a practical application for optical waveguide writing or integrated photonic circuits.

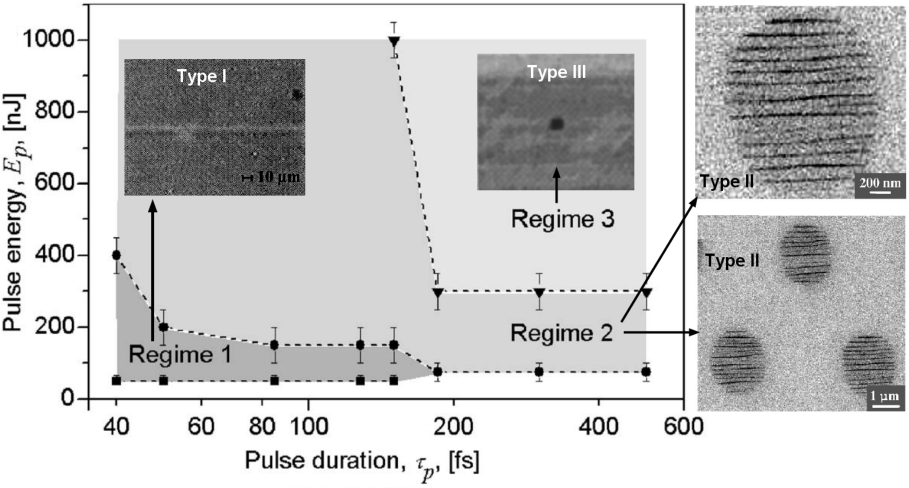

Figure 1.4: Modifications induced by focused fs-laser irradiation in fused silica as a function of laser parameters (pulse energy and pulse duration) [28]. There could be distinguished three types of regimes: (a) homogeneous refractive-index change (type I modification) [2], (b) self-organizing nanogratings (type II modification) [5], (c) microexplosions (type III modification) [29].

There is a second regime known for the generation of periodic self-organizing nanogratings (type II modification) [5], as can be seen in Fig. 1.4. It starts at moderate pulse energies and longer pulse duration. It is necessary to note that there is no abrupt change from one regime to another, it is a more transitional process, when a combination of refractive index change and nanograting formation could be produced at the same time between different regimes [30]. Type II modifications have several interesting properties for practical application. Firstly, nanogratings exhibit birefringence phenomenon, which could be applied for passive photonics devices, such as polarization converters for changing the laser light from linear to radially, azimuthally or almost any shape polarized light [11]. Additionally, these modifications could be applied to 5D optical data storage devices, which could contain huge capacity of data and has a virtually unlimited lifetime at room temperature [31]. Apart from the change of optical properties, the laser modified zones (nanogratings) also exhibit much greater etching rate in hydrofluoric acid (HF) or potassium hydroxide (KOH), than unaffected fused silica. This etching ratio is highly dependent on many exposure (laser wavelength, pulse energy and duration, repetition rate, polarization, focusing, scanning, etching, and others) parameters, which will be discussed in more detail in the following sections.

For longer pulses at even higher pulse energies (>300 nJ), the focused femtosecond laser pulses could produce microexplosions and microvoids [29, 32], which is known as type III modification. The intense light-matter interaction results in abrupt non-thermal bond breaking, leaving positively charged ions behind [10]. If the generated pressure at the focus (Coulomb force) exceeds the material pressure (i.e., Young modulus), then the Coulomb explosion takes place [33]. It was demonstrated that these microvoids are formed as a result of shock and rarefaction waves [34]. This type of modification could be used for laser ablation and optical data storage applications.

In 2020, P. Kazansky et al. reported on an observation of a novel type of modifications (type X) [35], which they attributed to an intermediate regime between already known type I and type II modifications. The discovered regime has a low refractive index, ultra-low loss and birefringence properties. The findings show formation of anisotropic nanoporous silica, which are different than traditional nanograting structures and conventional nanoporous silica. It was shown that type X modification has ultra-low losses with a transmittance as high as 99% in VIS&IR and >90% is UV spectral range. The novel regime has a very narrow fabrication window; at this regime, the laser pulse density and pulse duration are the most critical factors. Fig. 1.5 (a) shows scanning electron microscope (SEM) images, which reveal the evolution of the nanoporous formation by changing the laser pulse density. It can be seen the change from nanoporous material at lower number of pulses to nanogratings at higher density of pulses. These results will be applied for the enhancement of transmission of birefringent optics, as shown in Fig. 1.5 (b). These new findings show that, even after intense research in this field since 2003, still some effects in the fused silica are currently being discovered and revealed.

1.3.3. Self-organized nanogratings

Formation of periodic nanostructures on the surfaces by exposure of laser light was observed several years after the laser invention and its first investigations on laser ablation [36]. The periodicity on semiconductor surface was generated at lower power levels than needed for the ablation threshold. Later, formation of LIPSS was observed on surfaces of various other type materials, such as

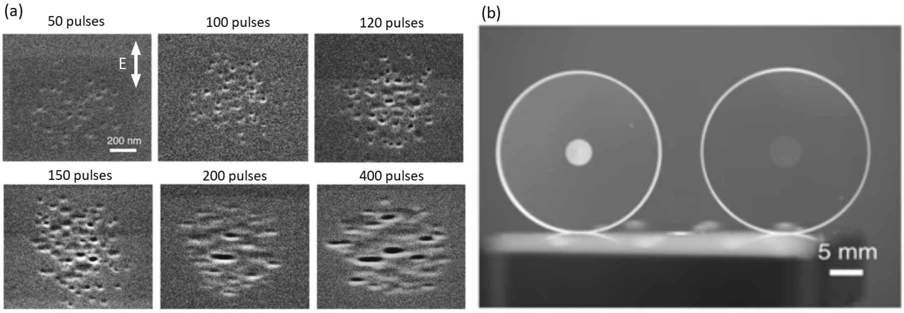

Figure 1.5: (a) SEM images of the polished surface of type X modifications written with a different number of laser pulses. Arrow indicates the direction of the laser light polarization. (b) Photograph of birefringent optics written with high-loss type II (*left*), and low-loss type X (*right*) modifications in fused silica substrate [35].

metals [7, 37], dielectrics [7], ceramics [38], polymers [39], etc. The parameters for LIPSS generation turned out to be universal and could be generated with different laser sources (from pulsed to continuous wave lasers; from UV to IR wavelength) [7]. The spatial resolution and amplitude of LIPSS depend on laser parameters, such as laser wavelength, polarization, the angle of incident light, laser fluence, and others parameters [39].

The appearance of the femtosecond amplified lasers systems allowed to reach high intensities. At the beginning of 2000s, a similar phenomenon of sub-wavelength periodical structure generation in the bulk of fused silica was discovered [5]; since then, this phenomenon has been intensively investigated. It was observed that the produced so-called nanogratings have a periodicity of approximately $\lambda/2n$ [40], which are oriented perpendicularly to the laser polarization. The first findings showed that these periodic structures consist of oxygen-rich and oxygen-depleted zones [5], which have lower refractive index than unmodified regions of fused silica. Later, investigations revealed that oxygen deficient zones are in fact nanopores in glass with Δn of -0.2 [30]. Periodical modulation of the refractive index in the material introduce a different phase shift for incident light with electric field oscillating in perpendicular and parallel directions [41]. Moreover, it was demonstrated that the nanogratings' structure could be erased and overwritten with a new grating at a different orientation [42]. Furthermore, the oxygen deficient zones of nanogratings exhibit higher susceptibility to chemical etching.

The unique properties of nanogratings have already been used for various types of applications: data storage, birefringent optics, micromechanical sensors, microelectromechanical devices, etc. Nonetheless, up till now, the physical processes of nanogratings formation are still a question of debate. It is generally accepted that nanograting formation involves transition of defects, such as color center generation, inhomogeneities and excitons [41]. Several different models and hypotheses have been proposed: interference of incident photons with generated plasma wave [5], asymmetric transient nanoplasmonics growth [42, 43], self-trapped excitons assisted evolution [31, 44].

1.4. SLE technology

The femtosecond laser pulses have enabled high precision fabrication of the 3D structures in glass by SLE technology. Due to their high-peak intensities, tightly focused femtosecond laser beams can trigger non-linear two-photon or multi-photon absorption phenomena. This unique characteristic leads to a modification of transparent material only within the focal point of laser beam. By spatially moving the laser focus, well-defined 3D patterns can be written. In the SLE technique, the glass is structurally modified so that the laser affected zones are etched significantly faster than unaffected ones. This is observed in both HF and KOH etchants.

Fig. 1.6 shows schematics of the main SLE fabrication steps: (1) irradiation of focused fs-laser beam in layer-by-layer fashion and (2) subsequent etching process in HF acid. It is necessary to note that, in most cases, there is no need to scan all the undesired volume of the material. A more cost-effective method is to slice unnecessary volumes into smaller pieces by the contour scanning so that these parts are separated during the etching process. SLE technique allows for processing millimeter-cubes volumes or more with micron resolution. Furthermore, the manufactured 3D parts could be applied in combination with other direct laser writing techniques for lab-on-a-chip devices with an integration of optical waveguide, structures produced by multiphoton polymerization.

The first demonstration of etched 3D microchannels in fused silica of ultrafast laser irradiated zones was done by A. Marcinkevičius et al. in 2001 [6] a few years before the discovery of nanogratings phenomenon [5]. Later, in 2004, this phenomenon was investigated in more detail by Y. Bellouard et al., high aspect ratio channel formation was demonstrated, as well as the relatively high selectivity of 1:100 [24]. One year later, it was reported that nanogratings orientation and etching selectivity highly depend on the polarization state of the laser beam in respect to the scanning direction during the writing process.

If the polarization of the laser beam is parallel to the scanning direction, then nanogratings consists of alternating regions perpendicular to the microchannel, as shown in Fig. 1.7 (c). In this case, the etching rate is relatively low. Much higher etching rates for the grating structures oriented along the writing direction were observed, i.e., the polarization of laser beam is perpendicular to the scanning direction (see Fig. 1.7 (a)) [45]. Meanwhile, the etching selectivity for a polarization state of 45° resulted in etch rate value

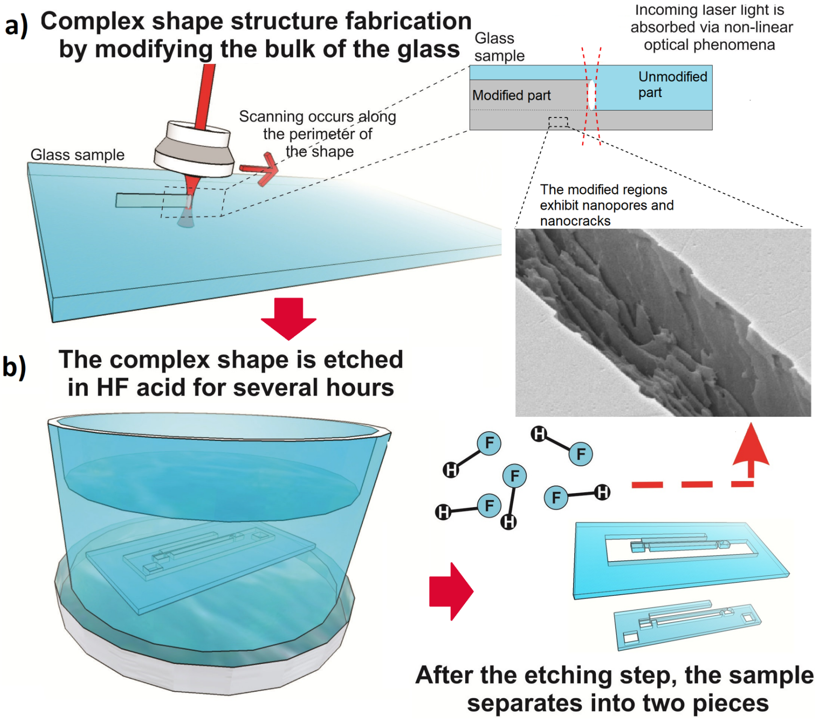

Figure 1.6: Schematic illustration of the main fabrication steps for SLE technique: (a) irradiation of focused fs-laser beam in layer-by-layer fashion all trough the glass substrate, (b) subsequent etching process in HF acid, which etches out the modified laser tracks [45] and microstructure simply falls out from the single piece of substrate.

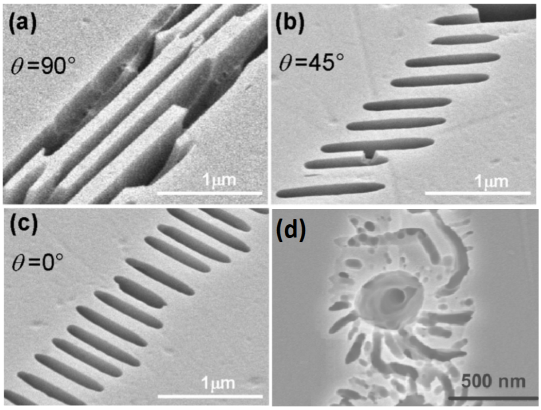

Figure 1.7: SEM images of nanogratings formed along the writing direction for different polarization states: (a) perpendicular $\theta = 90°$, (b) rotated by 45° and (c) parallel $\theta = 0°$ [45]. The induced periodic structures are always being oriented perpendicularly to the polarization of the laser beam. (d) When a circular polarization is used, a chiral structures will be formed [46].

in the middle range between perpendicular and parallel states. The proposed explanation for this phenomenon is that the etchant could simultaneously penetrate faster and easier in the longitudinally oriented nanocracks [42,47]. When the fabrication of 3D microstructures is considered, it could be highly important to control polarization state during the fabrication process, as the etching rate of the wrong polarization could reduce selectivity several times. This issue could be overcome by changing the polarization state dynamically *via* rotation of a $\lambda/2$ waveplate mounted in a motorized stage [48]. However, this method might be a limiting factor for some of microstructures or writing at higher speeds, as complex shape contour would require very quick altering between polarization states. In this case, for specific application, using a circular polarization (see Fig. 1.7 (d)) could be a much better choice, as the etching rate will be independent and equal in all scanning directions [49] due to chiral structure formation [46]. The etching selectivity is defined as the ratio [50]:

$$S = \frac{r_s + r_0}{r_0}, \tag{1.5}$$

where r_0 denotes the etching rate for unmodified pristine material, while r_s is the etching rate of the modified single-line channel.

Certainly, the polarization of the laser beam to the scanning direction is very important factor, but not the only factor, which highly influences the etching selectivity. There are a number of studies, where these parameters have been investigated and summarized [41, 48, 51]. The period of nanogratings corresponds to the laser wavelength with a relation of $\lambda/2n$, therefore, in principle, each of the laser sources could have different optimal etching parameters. A systematic study by S. Richter et al. [52] showed that the nanogratings could be induced in a very wide range of laser repetition rates (from 0.1 to 9.4 MHz), as shown in Fig. 1.8. The experiments were carried out using 515 nm laser wavelength, pulse duration of 450 fs, and 0.55 NA focusing optics. On one hand, at lower repetition rate the nanogratings are generated by exceeding minimal pulse energy. It is necessary to note that multiple laser pulses are required for the formation of a regular formation of nanogratings. On the other hand, at higher repetition rate and pulse energies (above 100 nJ and several MHz repetition rate) there is no subsequent generation of nanogratings due to heat accumulation and melting of the material [52]. In addition, Fig. 1.8 shows that the fabrication window becomes narrower for higher laser frequencies. NA of the objective defines the modification feature size, usually for SLE process an "intermediate sharpness" objective with NA of 0.4-0.5 is used. For most applications, there is no reason to use a high NA objective, as after the etching even smallest modification will be widened by the etchant. However, conversely, an objective with lower NA values could find an application for more rapid laser writing process, as the size of modification could be larger.

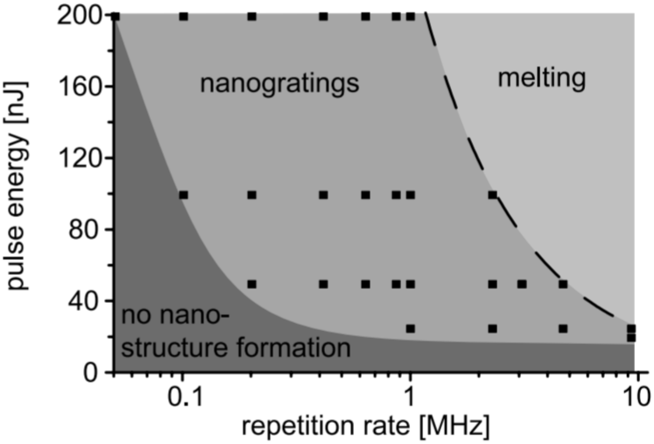

Figure 1.8: Type of material modification within fused silica as determined by laser parameters: pulse energy and laser frequency [52].

Laser pulse duration plays an important role in SLE process too. In the early investigations [28] it was already known that the shortest laser pulse duration is not best suited for this process of inducing type II modifications, the experiments with etching rate confirmed this theory as well [53]. Actually, authors reported that the maximum etching selectivity was obtained for the pulse duration in the range of 500-1000 fs. The formation of nanogratings was observed to start with the pulse energies of 100 nJ [28], while the efficient etching initiates from 200 nJ and could be observed even for 1000 nJ under specific conditions [50, 53]. Nonetheless, the highest selectivity is observed for the low energy pulse regime in the range of 200-400 nJ. The etch rate is influenced by the writing speed. It is considered that the higher pulse density is an essential factor for formation of nanogratings [52], which are necessary for the susceptibility to appropriate etchants. However, J. Gottmann et al. reported a surprising result that a much better selectivity (1:1400) was achieved at higher writing speed (several hundred mm/s) regime. However, in order to reach such a speed, the femtosecond laser system has to operate in combination of galvanoscanners and stages simultaneously.

Last but not least, the separation of the adjacent lines and layers has to be chosen carefully for SLE process. Tight overlapping could increase the etching rate, at the same time it could cause internal stresses, which could be released by induced cracks to the final structure [54]. Conversely, less dense scanning could shorten the fabrication time, but, of course, worsen the selectivity rate [48, 54]. An optimized laser and writing parameters should be set each time separately considering and taking into the account the complexity of the structure, precision, fabrication duration or physical properties, such as surface roughness. Fig. 1.9 shows several representative structures fabricated out of single piece of fused silica.

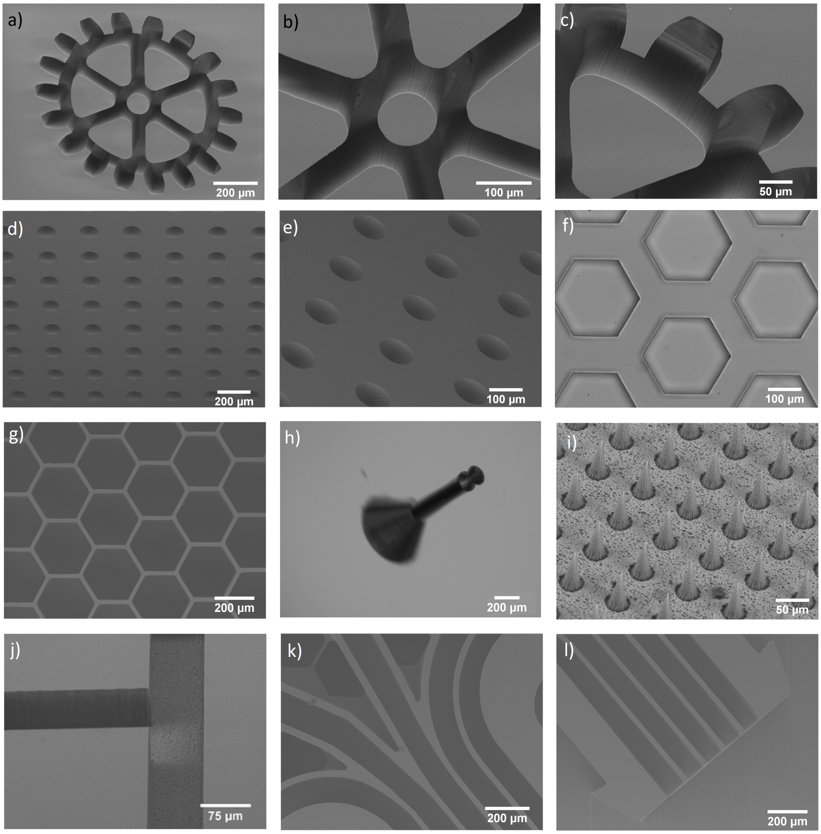

Figure 1.9: Representative images of structures fabricated out of single piece of fused silica by selective laser etching technology: (a-c) a mold for microgear, (d-e) array of blind-holes, (f-g) array of honeycomb-shaped hole, (h) micronozzle, (i) array of high-aspect ratio microneedles, (j-l) various microfluidic channels.

Apart from laser and scanning parameters, the selectivity is strongly dependent on the etching process, i.e., the etching rate for untreated material. As can be seen from Eq. 1.5, the lower the value of denominator, the higher the selectivity. For SLE experiments, mainly two etchants are used: HF or KOH. The former has a great etching rate and provides fast processing; however, it also reacts with unaffected silica at a quite high rate (e.g., ca. 1.5 µm/h for 5% HF (v/v) solution), therefore, it provides a undesirable tapering (conical shape) effect for long microchannels. Meanwhile, KOH solution provides a more effective process, thus it gives lower tapering effect (e.g., 0.2 µm/h for KOH 10 M solution at 85° C) [50], but requires much longer overall etching time. It was recently shown that by changing KOH temperature the etching rate could be improved [55].

Chemical reaction for the fused silica etching process in HF (1) and KOH (2) could be described as follows [56, 57]:

1. $SiO_2 + 4HF \rightarrow SiF_4 + 2H_2O$;
2. $SiO_2 + 2KOH \rightarrow K_2SiO3 + H_2O$.

The complexity or required precision of the microstructure defines the selection of the etchant. Although, it was shown that even an combination of consecutive etching in both of etchants could be advantageous for specific geometry and application [58, 59].

Modifications written by the femtosecond laser irradiation have shown higher susceptibility for appropriate etchant not only for SiO2, but similar processes observed in borosilicate and other type glasses [53, 60] and even in some crystalline materials like sapphire [61].

1.4.1. SLE fabrication method and its limitations

The SLE fabrication method is done in a layer-by-layer fashion from bottom to top surface. A contrariwise scanning is inappropriate as the incident laser light would be partly scattered by already written nanogratings. In order for the etchant to enter into the glass volume, the modified volume needs to have a contact with the surface. The length of dead-end channel cannot be infinitely long, as the etchant dissolves and the etching rate decreases. The etching from both surfaces could significantly prolong the achievable length, and the usage of ultrasonic bath could significantly increase the flow convection and continuously refresh the etchant. The SLE technology is limited not only by the channel length, but also by the glass thickness as well. Due to spherical aberrations the laser focus at higher depths at some point will be highly distorted, the voxel size will inevitably be elongated, and the intensity might be insufficient for the creation of proper modification. To overcome this issue, several aberration compensation techniques could be used, such as spatial light modulator, or objectives with a motorized correction collar for dynamic control of the focused depth in the glass [62].

1.5. MPP technology

Multiphoton polymerization is an additive laser lithography technique, which is based on the structuring of a photosensitive polymer, allowing manufacturing of complex geometrical shape two- and three-dimensional structures. Ultrashort laser pulses provided unique characteristics of gaining high peak intensities, which give rise to a non-linear absorption and induce a polymerization reaction in transparent photopolymer for the laser wavelength. The cross-linking reactions happen only at a tiny focal spot, which is known as a volumetric pixel - voxel. By spatially moving the laser focus in a layer-by-layer fashion, well-defined complex shape 3D structures could be fabricated. Subsequently, in the negative-tone photopolymer case, the areas not exposed to the laser are simply washed out with a developer, leaving only solidified structures behind. This technique could be widely applied in a vast range of the applications, for instance, fabrication of the microoptics [63], metamaterial elements [64], scaffolds for tissue engineering [65], microfluidic devices [66], etc.

Due to the non-linear absorption and threshold phenomenon, the achievable resolution of technology could be smaller than the diffraction limit at the applied laser wavelength. The principle of multiphoton absorption was predicted in 1930 by Maria Goeppert-Mayer [9], but experimentally it was proved only later by the invention of the laser. In 1997, S. Kawata et al. presented 3D polymeric structures made by MPP method for the first time [3]. The uniqueness of the technology is that the polymerization reaction could happen at tiny fraction of the focal point. By exceeding the polymerization threshold the pre-polymer is solidified and could undergo the developing process, while the rest of the pre-polymer is simply washed out.

The sub-diffraction spatial resolution could be obtained by non-linear absorption. In a case of two-photon absorption, two photons need to be absorbed simultaneously to excite the molecule (e.g., photoinitiator) to a higher energy state. Two-photon absorption depends on the square of the light intensity. The initial voxel size corresponds to a shape of focal spot, where polymerization threshold is exceeded over a certain intensity. It is needed to emphasize that the polymerized feature size is dependent on overall exposure dose, thus long laser exposition time (slow writing process) would cause larger voxel dimensions. The voxel grows uniformly to all directions along the intensity distribution due to radical diffusion process [67].

Under very precise exposure dose control, there is no limit for the voxel size in an ideal case. Under optimized writing speed and certain intensities, it was shown that single fibers could be fabricated with transversal voxel resolution of $\sim$15 nm [68]. However, near the polymerization threshold, small local polymer inhomogeneities cause uneven polymerized feature size, also lower degree of monomer conversion will lead to poor mechanical strength of the polymer. Last but not least, the laser power instability/fluctuations also will have an effect on the feature size [12, 69]. Therefore, in practice, for precise repeatable 3D structuring a voxel of several hundred of nanometers is usually used.

In MPP, not only the feature size defines the achievable technology resolution. Another very essential parameter is the minimum distance between two adjacent exposed lines. As MPP is a threshold process, the polymerized features will appear, where exposure dose will exceed critical value. It is necessary to emphasize that, in the vicinity of focused laser spot, the cross-linking reaction still exists, and the exposure dose is "memorized". Successive laser scanning could cause that accumulated exposure dose to exceed the polymerization threshold and two adjacent lines will be merged and unresolved.

Typically, there are three types of femtosecond lasers sources commonly used for MPP technique [70]: (1) Er doped fiber (second harmonic – 780 nm) oscillator, (2) an amplified Yb:KGW source (fundamental wavelength of 1030 nm, and second harmonic at 515 nm could be efficiently used), and (3) Ti:sapphire oscillator or amplifier (fundamental wavelength ~780 nm). As the lasers and their characteristics vary, the parameters for MPP process could be very different. Certainly, the amplified laser source has more average power than needed for MPP technique. The amplified system is more universal, as the same setup could be easily applied for SLE, welding and fs ablation processes.

Several representative examples were fabricated and are provided in Fig. 1.10, showing the capabilities of the MPP technique.

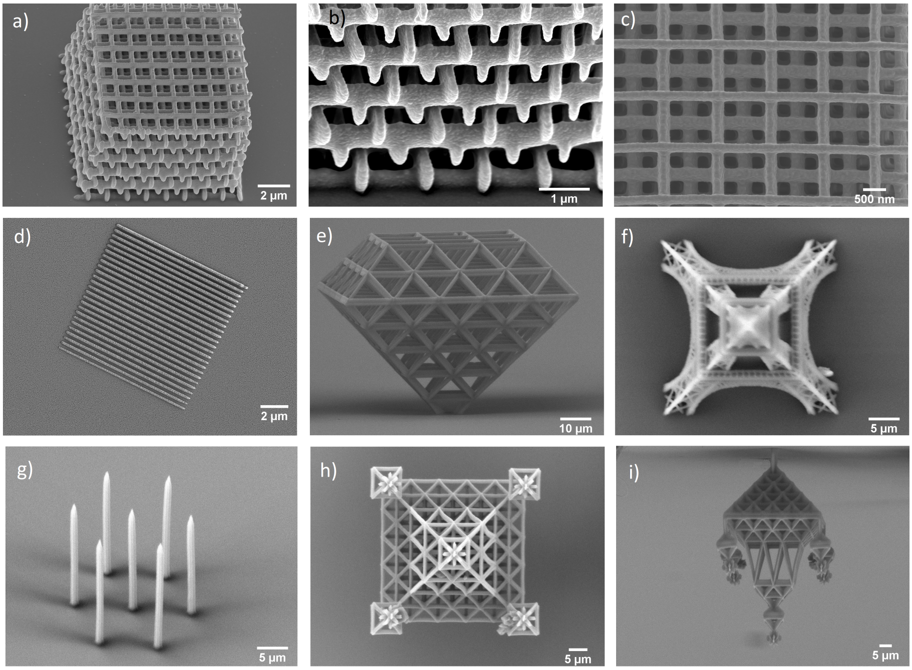

Figure 1.10: Representative images of structures fabricated with MPP technology: (a-c)) photonic crystal with ca. 200 nm lateral and 600 nm axial features sizes. (d) Line array with features width from 170 nm to 210 nm, (e) diamond-shaped microlattice structure, (f) top-view of Eiffel tower, (g) array of high aspect ratio microneedles, (h) top- and (i) side-view of Lithuanian micro straw gardens standing on a thin support.

1.5.1. Photopolymerization reaction

MPP technology has four main fabrication steps, which are depicted in Fig. 1.11. (1) Firstly, the polymer is prepared from the light-sensitive material. Most of the MPP photoresists are liquids, which are simply drop-casted on a glass coverslip (Fig. 1.11 (a)). For some of the photopolymers, an additional prebake process is needed – to heat up and keep at a certain temperature. (2) Then, the polymer is selectively exposed by point-to-point writing approach of predefined trajectory by tightly focused fs laser irradiation (Fig. 1.11 (b)). The polymerization reaction happens only locally at a tiny voxel. (3) Thereafter, when the writing is completed, the process is followed by the development step, when the dissoluble areas of the polymers are simply washed out by immersing the specimen into the solvent bath (Fig. 1.11 (c)). (4) Subsequently, the fabricated structures are dried out in ambient air or through special treatment techniques (Fig. 1.11 (d)). Then, the specimen is usually inspected under the SEM or optical microscope.

By definition, polymers are huge macromolecules bonded together of long repeated chains – monomers, while polymerization means the chemical reaction, which leads to network formation (conversion from smaller molecules to larger ones). If this process is triggered by the light (UV, VIS or IR), then it is called photopolymerization. The cross-linking reaction of photopolymers could be based on cationic or free-radical mechanism [9].

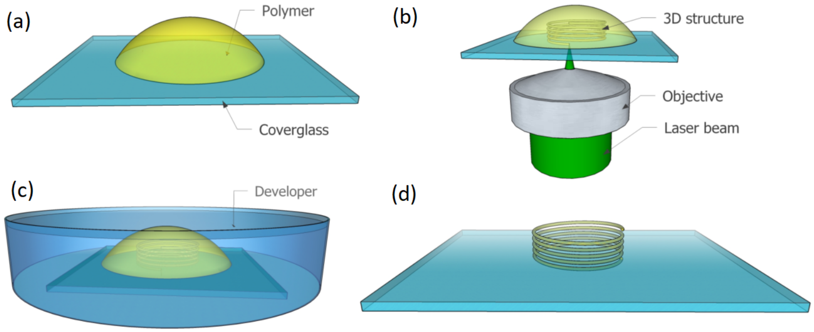

Figure 1.11: Schematic illustration of the main fabrication steps for MPP technique: (a) sample preparation, (b) irradiation of focused fs-laser beam, (c) development in a solvent bath, (d) the sample drying process and inspection.

The pre-polymer for MPP consists of the main substance of monomers or oligomers. In addition, it could contain additional components, such as solvents, quenchers, stabilizers, etc. However, this pre-polymer itself has a very low (<1) quantum yield, which is simply the ratio of polymerized monomer units to the absorbed number of photons. For this reason, the pre-polymer is also mixed with a small amount of photoactive material, which is known as photoacid generators in cationic and photoinitiators in radical polymerization case. Most polymers used for MPP belong to a class of radical type. Incorporation of a photoinitiator to the photopolymer significantly increases the quantum yield, which could reach several thousands of cross-linking reactions by absorbing only one photon [71]. The photoinitiator is selected to have high two-photon cross-section for the used laser wavelength. For MPP application, the polymer have to satisfy the requirements of high thermal stability, solubility in the pre-polymer, stability in the darkness [72].

There are at least three different kinds of reactions for the photopolymerization process, which could be simply described in the following equations [72,73]:

$$\begin{aligned}
\textit{Photoinitiation}: &\quad PI \xrightarrow{h\nu} 2R^{\bullet} && (1.6)\\
\textit{Propagation}: &\quad R^{\bullet} + M \rightarrow RM^{\bullet} && (1.7)\\
&\quad RM^{\bullet} + M \rightarrow RM^{\bullet} && (1.8)\\
&\quad RM_n^{\bullet} + M \rightarrow RM_{n+1}^{\bullet} && (1.9)\\
\textit{Termination}: &\quad RM_n^{\bullet} + RM_m^{\bullet} \rightarrow RM_{n+m}R && (1.10)\\
&\quad RM_n^{\bullet} + RM_m^{\bullet} \rightarrow RM_n + RM_m && (1.11)
\end{aligned}$$

The first step is a photoinitiation reaction (Eq. 1.6), when, by absorbing the incident light, the photoinitiator PI is decomposed and cleaved into highly reactive molecules – radicals $R^{\bullet}$, which have an unpaired electron. For MPP technique, these light-matter interactions happen *via* nonlinear – multiphoton absorption. In the following step, the activated molecules react with stable monomers M, making them radicals as well. Subsequently, these radicalized monomers continue to add other monomers constituting even longer molecular chains. This process is known as propagation (Eq. 1.7–1.9). These cross-linking reactions could be terminated in two ways: (1) by a recombination reaction, when two propagating radicals encounter each other (Eq. 1.10), or (2) by disproportion (Eq. 1.11), when an atom like hydrogen is relocated from one radical chain to another, resulting in two non-radical products. After the cross-linking reaction, if the molecular weight of the particular chain exceeds a certain threshold value, the polymer becomes insoluble to the developer. The term – monomer conversion – determines the fraction of functional monomer groups (e.g., acrylate groups) that are polymerized [9].

1.5.2. Photopolymer materials

There are plenty of materials (acrylates, organic-inorganic hybrid materials, epoxy-based photopolymer, etc.) suitable for the MPP method, which makes this technique very attractive for multiple applications [74]. Historically, the early materials used for two-photon polymerization technology were borrowed from UV lithography, because their excitation energy corresponds to approximately double the photon energy needed for excitation by near infrared light [9]. In the early stage, the commonly used fs-laser was Ti:Sapphire with a wavelength of 790 nm [3], which made it a perfect candidate for two-photon absorption, because a number of UV photo-curable resins start to absorb the light linearly in the near UV range. Later, the gamut of suitable materials was gradually filled with newly developed photoresists. Photopolymers could be divided into positive- and negative-tone ones. In the former case, the light induces dissociation between the chemical bonds of molecules, therefore these exposed polymer sections become soluble in the developer solution. Conversely, the light exposure of the negative-tone resists starts cross-linking reaction of the monomer chains. The exposed areas become solidified and undergo the subsequent developing process. For 3D microfabrication, the positive-tone resists are rarely used, but these photopolymers could have an advantage for simplicity and efficiency for specific structures, where lower volume needs to be removed. Moreover, the positive resists have negligible distortions and shrinkage effects [75].

Nonetheless, for 3D microfabrication mainly negative-tone photopolymers are used, such as commercially available hybrid organic-inorganic SZ2080 or OrmoComp, acrylate-based SCR500, epoxy-based SU-8. As the chemical composition varies strongly, each of the resists is distinguished by different optical, mechanical, chemical, thermal, bio-compatibility and other properties. Usually, the application defines the requirements and the suitability for the photoresist. For instance, firstly used MPP photopolymer – SCR-500 [3] – has low shrinkage, is chemically and mechanically stable, which could be applied in the semiconductor field [76]. SU-8 was inherited from UV lithography for microelectronics and micromachining applications. In contrast to most of MPP used polymers, in this case the cross-linking reaction is based on cationic polymerization, which requires specific pre- and post-treatment processes. SU-8 has high thermal stability, is chemically stable, optically transparent in VIS light range, provides ability of fabrication of high aspect ratio structures. SU-8 has been already employed for microelectromechanics systems, photonics, and microfluidic applications [77]. Later, hybrid glass/polymers materials were developed (like SZ2080 and OrmoComp), which consist of inorganic (–Si–O–Si–) backbone and organic functional groups. These materials are easily processable, have excellent optical properties, high temperature stability, good chemical resistance. The main applications for these photopolymers are microoptics, micromechanics, scaffolds for tissue engineering [78].

Besides aforementioned polymers, there are plenty of other materials, which were explored [77] for MPP application, including sugar, protein, polyethylene glycol based materials, which are compatible and suitable for fabrication of tissue engineering scaffolds. Moreover, the polymer properties could be easily tuned by changing the ratio of compounds or doping photoresist with special substances. Incorporation of different nanoparticles materials could provide additional functionalities, such as conductivity, magnetizability, electrical, mechanical, fluorescent and many others [79]. The properties of commonly used MPP photopolymers are listed in Table 1.1. It is important to emphasize that the listed values are only indicative, as they were measured mainly for polymers photocured by UV source.

Table 1.1: Comparison of properties of commonly used photopolymers for MPP technology [9, 78, 80–85].

Photopolymer	OrmoComp	SZ2080	SU-8	SCR500
Refractive index	~1.52	1.49-1.53	~1.57	1.52-1.53
Young modulus, GPa	~1.27	1.74	4.0	1.6
Shrinkage, %	5-7	~1	~7.5	
Highest resolution	<100 nm	<100 nm	<100 nm	<100 nm

SZ2080 photopolymer

SZ2080 photoresist [85] is widely used among scientific groups across the world, therefore we will discuss it in more detail. SZ2080 belongs to ORMOSIL (ORganically MOdified SILica) class material. ORMOSIL is a hybrid material consisting of an inorganic (–Si–O–Si–) part with a component of partially replacing Si atom by Zr, Ta, Al, Ge or other metallic element, and organic part of methacrylate groups. In the case of SZ2080, zirconium is a key element and the photopolymer consists of (–Si–O–Zr–O–Si–) backbone chains. The digits in the name indicate that 80% of molar mass consist of organic (Methacryloxypropyl trimethoxysilane (MAPTMS) and methacrylic acid) and 20% of inorganic (zirconium propoxide and the alkoxysilane groups of MAPTMS) parts. A combination of both groups provides glass properties like high optical transmittance in VIS range, it has low shrinkage behavior, thermal and chemical inertness, mechanical hardness; and polymer characteristic of elasticity, functionality. Also, the polymerization reaction happens through organic acrylate groups. By simply changing the molar ratio between the components, photopolymer properties could be tuned, for instance, the refractive index n could be changed in the range of $1.495 - 1.53$ [85]. Additionally, the index of refraction change Δn for SZ2080 depends on the degree of polymer cross-linking and could be tuned up to 1.54×10^{-2} [86]. It is necessary to note that the higher molar mass of inorganic content in hybrid photopolymer, the more glass properties are observed, such as brittleness, hardness, thermal stability and vice versa. The higher concentration of organic part will make the elasticity increase and alters the coefficient of thermal expansion [87].

The photopolymer is synthesized through sol-gel process [88]. The manufacturing consists of several main steps [72, 85]. Firstly, the precursors or monomers are needed to mix with water. This procedure requires an additional catalyst (hydrochloric acid or ammonia) to start chemical reaction. Then, the mixed solution undergoes condensation process, resulting in formation of porous interconnected network of strong covalent bonds of Si-O-Si, Zr-O-Zr, and Si-O-Zr [85]. After the first preparation step of the photopolymer, the resist has different solvents (water, alcohol and others) present in its composition. Therefore, before the laser exposure, the SZ2080 requires a supplementary prebake process at a low temperature to evaporate the remaining solvent. During this process, the photopolymer shrinks and changes its aggregate phase from liquid to gel, the result of which is that afterwards Z2080 exhibits negligible low shrinkage in subsequent post-laser exposure step [89]. Subsequently, the photopolymerization reaction follows, then the light triggers radical excitation and propagation reaction, resulting in formation of long chains between the organic functional group. It is necessary to emphasize that there is no volume reduction during this process. Eventually, the polymer is rinsed in an appropriate solvent, which washes out unpolymerized pre-polymer network. Solubility is determined by solvent characteristics, such as polarity, which describes the ability of solvating polar or non-polar species, and the availability of labile protons [90]. The former property describes the solvent ability to occur, for instance, in hydrolysis reactions between Si-O-Si bonds.

In general, SZ2080 is very convenient for laser microprocessing, as the gel phase has the advantage over the liquid form of MPP photoresists. During the direct laser writing process, the liquid medium of photoresist could flow and produce distortions to the projected structure. In this case, the writing algorithm should be chosen appropriately, firstly attaching the initial layer to the glass coverslip. In addition, for the subsequent layers, the light will have to be focused through already exposed cured material, which could cause distortions as well. In contrast, solid or gel type photoresists do not face such limits and complexity.

1.5.3. Special treatment techniques

When the laser structuring process is completed, the sample is immersed into a developer bath to gently wash out the light unexposed areas (in the negative-tone resist case). Thereafter, the developing step is followed by the drying process. However, at this stage, most photopolymers suffer from shrinkage phenomenon. This effect is more observed for the structures polymerized near the polymerization threshold. For some applications, shrinkage could be an indirect way to obtain smaller dimensions of the structures and reduce the size up to 35% of the original values [89]. For instance, it could be applied for uniform reduction of photonic crystal structure, where feature resolution could be required very close to the technology capabilities. However, in most of the cases the shrinkage phenomenon is undesired, which could cause deformations and distortions from the designed model. During the drying process in air, ambient solvent evaporation induces a rise of capillarity forces, which might generate significant strengths to compress and deform the MPP parts. It is especially an issue for fragile parts with features of high resolution and high-aspect ratio structures. Fig. 1.12 shows the impact of surface tension (capillarity forces) for an array of straight micropillars. Each pillar was fabricated by a single laser scan. It can be seen that at lower laser average power the micropillars are completely collapsed, while at higher power range the structures become more robust and the deformations produced by surface tension are less observed.

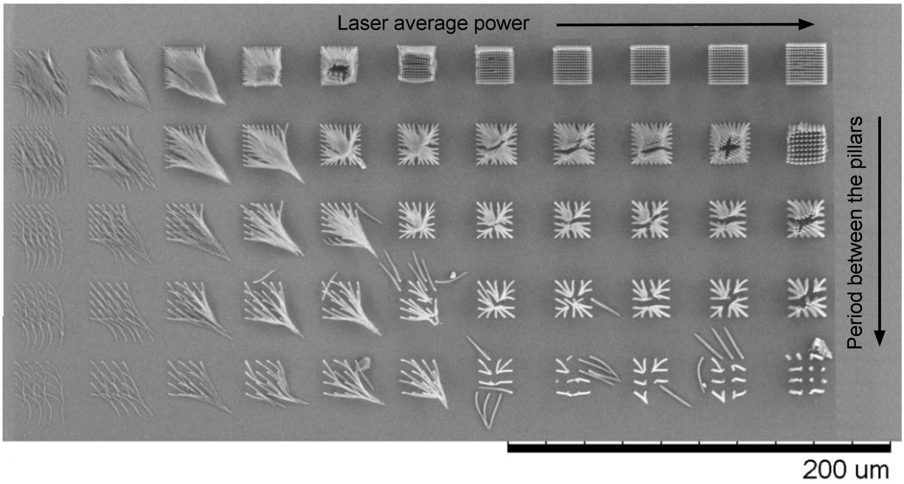

Figure 1.12: Top-view SEM image of micropillars fabricated by MPP under different laser average power and spacing between the pillars. The drying process was done in ambient air.

The impact of capillarity forces could be neglected by using additional special treatment techniques, such as critical point dryer (CPD) [91]. This supplementary method is usually used for biological samples before the inspection of SEM. CPD eliminates the surface tensions, as there is an indirect transition from liquid to gas phases [92]. There are several different gases used for this process, but the carbon dioxide (CO_2) substance is the most popular due to a low critical point of 31.1°C at 7.39 MPa pressure. This temperature is still convenient, as it does not have any heat impact, neither for biological samples nor for MPP structures.

Basically, the procedure of CPD is firstly followed by taking out the sample from ethanol (or other solvent) bath and inserting the sample into a sealed hermetic chamber chilled in the range of 0-5°C. Then, the chamber is closed and filled with the liquid CO_2 medium, which is later vented. The procedure is repeated a few cycles that the ethanol (or other solvent) would be fully removed. Thereafter, the chamber gradually starts to heat. As the temperature is getting higher in the sealed chamber, the pressure is rising as well. By exceeding the critical point for the CO_2 condition, the substance changes its aggregate form from liquid and becomes supercritical fluid. The phase diagram

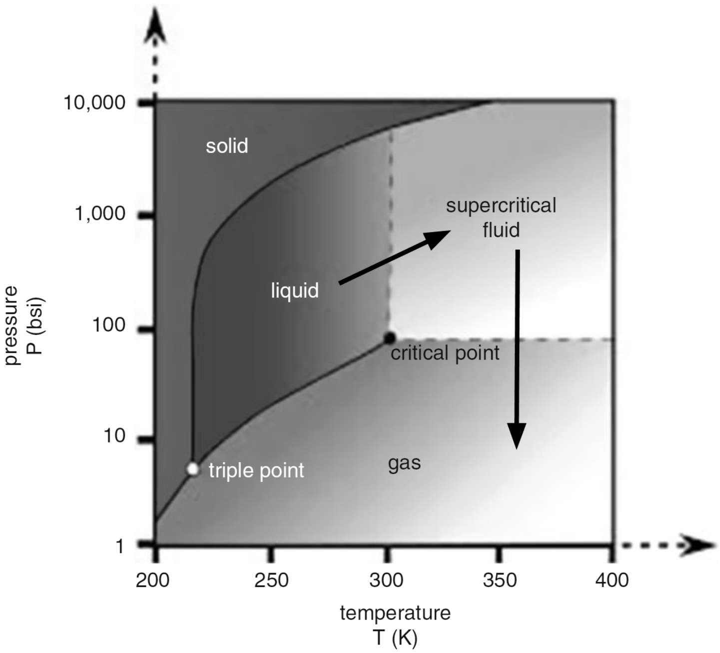

Figure 1.13: The phase diagram of carbon dioxide (CO_2) adapted from [91]. Solid arrows show the sequence of transition between phases.

of carbon dioxide is shown in Fig. 1.13. Supercritical fluid is an intermediate phase, which has properties of both high-density gas and diffusible liquid [92]. The key point is that there is no surface tension anymore for supercritical fluid. By keeping the temperature above the critical point values, the pressure in the chamber is slowly lowering by venting supercritical fluid outside. Then, the CO_2 changes its phases from supercritical fluid to gas. Eventually, the chamber is fully depressurized and the sample is ready for inspection. In general, this procedure of critical point drying minimizes the effect of deformation and makes it possible to obtain very delicate microstructures. In this work, we used commercial CPD device (K850, Quorum Technologies). Later, the majority of the structures were coated with a conductive layer *via* sputter-coater (Q150R, Quarum Technologies) in order to prevent the charging of the specimen during SEM inspection.

Fig. 1.14 shows a comparison of identical arrays of micropillars, which were dried naturally and using CPD. In former case, almost all arrays of micropillars were collapsed or compressed due to surface tension. Meanwhile, a much lower number of deformed micropillars were observed using CPD drying.

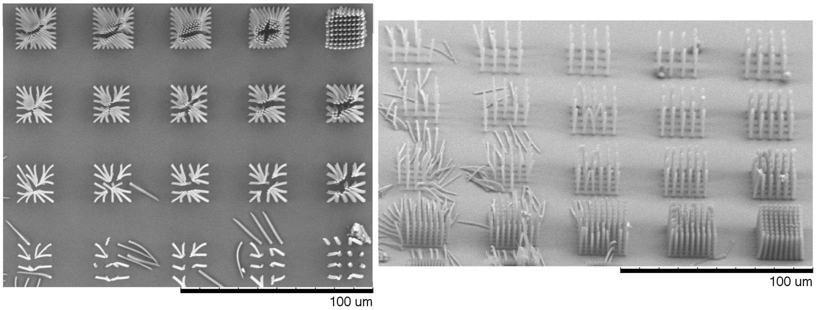

Figure 1.14: SEM images of micropillar structures produced by air-drying (*left*) and supercritical CO_2 drying (*right*).

1.6. Super-resolution techniques in optical microscopy

In classical optical microscopy, the resolving power of the device has been restricted by the diffraction limit, which was found by Ernst Abbe almost 150 years ago. E. Abbe derived and formulated that, in optics, the closest distance which could be resolved, between the two adjacent objects could be express by:

$$d = \frac{\lambda}{2n \sin \alpha} = \frac{\lambda}{2\mathrm{NA}}, \tag{1.12}$$

where λ - wavelength of the light, n - refractive index in the material, angle α of the cone of focused light, NA - numerical aperture. In optics, in order to increase the achievable resolution, shorter light wavelengths should be selected, meanwhile NA should be as high as possible. For instance, the wavelength of λ=400 nm and 0.95 NA microscope objective would result in resolution of 210 nm. This result could be still too small for some applications (e.g., biological field), where lower than 200 nm features have to be observed without using electron microscopy methods.

In the last 30 years, there has been proposed a number of techniques that could achieve resolution beyond the diffraction limit barrier. These techniques are known super-resolution microscopy methods. Several of them were invented by Stefan Hell, such as: (1) stimulated emission depletion (STED) microscopy [93], which allowed to achieve 35 nm lateral, (2) 4π confocal fluorescence microscopy improved the axial resolution down to 100 nm [94], (3) a subsequent combination of STED and 4π microscopies gave rise to 33 nm axial resolution [95]. In super-resolution techniques, the light still obeys the diffraction law, but STED microscopy is based on selective deactivation of fluorescence in the diffraction limited focal spot, minimizing the area of illumination. In this case, the Eq. 1.12 could be modified as [96]:

$$d = \frac{\lambda}{2n \sin \alpha \sqrt{1+\zeta}} = \frac{\lambda}{2\mathrm{NA}\sqrt{1+\zeta}}, \tag{1.13}$$

where ζ - the saturation factor, which mainly depends on the laser intensities. Meanwhile, 4π microscopy allows the improvement of axial resolution. In that case, the system arrangement consists of only one laser source, but the laser beam is divided and focused with two opposed microscope objectives into the same focal spot.

The principles of microscopy and lithography are related, as they share the same concepts. The developments and improvements suited for microscopy could be neatly integrated into lithography systems as well.

1.7. Direct laser writing inspired by STED microscopy

Stefan Hell was awarded the Nobel prize in 2014 for the invention of STED microscopy. Identical STED principles could be implemented into traditional MPP (STED-MPP) systems, as it was demonstrated by several groups [97,98], resulting in the improved achievable resolution. As in STED-microscopy, the idea behind STED-MPP is depletion of excited molecules in the outer ring of the focused diffraction-limited spot. The STED-MPP arrangement consists of combination of two different lasers simultaneously. Ultrashort infrared laser pulses are used for two-photon excitation, meanwhile for depletion process the second laser (continuous wave or pulsed, with longer pulse duration) works at different wavelength (e.g., green) in order to avoid excitation. Tightly focused femtosecond laser pulses are used to excite the photoinitiator and start radical polymerization in a confined focal lateral spot. At the same time, the continuous wave laser is focused to the same focal spot with a doughnut-shaped light distribution, which hinders the cross-linking reaction in the periphery zone around the center point. In this way, the effective point spread function in lateral axis is substantially improved, thus the polymerized transversal features sizes are far smaller than the limits of traditional MPP technology alone.

There are several STED-based and STED-inspired lithography techniques [69, 97, 99], nonetheless, the concepts are quite similar. We will discuss the mechanism of "true" STED lithography in more detail [97, 100]. As in the standard MPP, the excitation of photoinitiator happens through multiphoton absorption of femtosecond laser pulses, the molecules are excited from ground into an electronically excited state (see Fig. 1.15 (a)). This process is also followed by subsequent non-radiative relaxation to singlet state S_1, where excited molecules stay for a short time. They could either fluoresce or undergo intersystem crossing to lower triplet T_1 state. Nonetheless, the quantum yield is high only for the latter process, therefore, the majority of excited molecules are relaxed to a reactive T_1 state. In the case of radical polymerization, radical generation is initiated leading to cross-linking reactions. In negative tone polymer, if the polymerized molecule is sufficiently long, it becomes insoluble to the developer. In STED-MPP, the key point is that stimulated emission takes place just before the molecules' relaxation to triplet state T_1. This depletion process is done through the second laser irradiation with different wavelength. In this way, the excited molecules are brought back to the ground state. Moreover, alternatively the molecules in the triplet state or formed radicals could absorb the depletion laser irradiation, leading to de-excitation and stopping of cross-linking reaction.

In STED-MPP, the sufficient cross-linking reaction has to take place at the center of the focus point, meanwhile the depletion mechanism should be stronger at the outer ring of the focus point in order to hinder the polymerization reaction and improve the voxel size. This is implemented by shaping the depletion laser Gaussian beam intensity with a vortex phase mask element, which present a helical phase increase from 0 to 2π in one turn along the azimuth axis, and thus produces a toroid-shaped intensity around the voxel in XY plane. However, this arrangement only improves the lateral feature size, meanwhile the axial distribution is unaffected. For the longitudinal feature improvement, a second phase mask is used with cylindrical central disk of π phase shift, which produce a bottle-shaped distribution along the optical axis, while the intensity at the center of the focus is equal to zero. Due to the π–phase shift between the central and outer part of the incident beam, at the focus point the phase difference produce a destructive interference. Meanwhile, the waves are in phase in the vicinity of the focus, resulting in constructive interference. A combination of two differently shaped beams are used, which could improve the feature resolution transversely and longitudinally (see Fig. 1.15 (b)) at the same time.

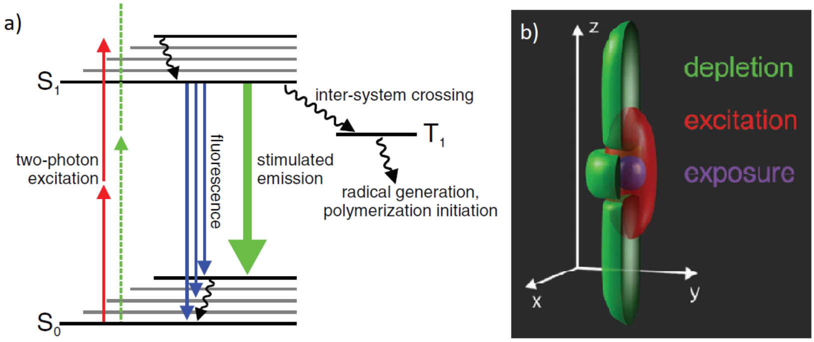

Figure 1.15: (a) Energy level diagram of the photoinitiator showing transition processes relevant to STED-MPP [100], (b) schematic illustration of typical intensity profiles for the depletion, excitation laser and resulted voxel [69].

STED-MPP requires special photoinitiators, which should satisfy several conditions, such as efficiently deplete molecules excitation *via* stimulated emission, have a sufficiently large lifetime of the excited states, also must not absorb the wavelength used for excitation and have to be stable on the irradiation of depletion laser [9]. So far, there have been only two radical photoinitiators (ITX, DETC), which have been proposed for STED-MPP [97,101]. Nevertheless, this technology shows to be promising. Theoretically, these STED-based and inspired techniques allow to achieve much smaller than diffraction-limited feature size, currently, 65 nm ($\lambda/12.5$) [100] or 55 nm ($\lambda/14$) [98] were demonstrated. It is necessary to note that in 3D lithography not only feature size is important, but also the writing resolution, which is defined as the smallest distance between two polymerized lines. For STED-MPP, center-to-center distance of 120 nm was demonstrated [98].

STED-MPP showed significant improvement in resolution achievement under the laboratory conditions; however, this arrangement has not been yet transferred to industrial applications due its complexity, stability, and repeatability issues [102].

2. 3D POLYMER/GLASS MICROMECHANICAL SENSOR

In this chapter, we consider different femtosecond laser technologies for processing transparent materials. We address advantages and disadvantages of each technology for 3D microfabrication. Alternatively, we propose a new method in a combination of SLE and MPP technologies for microtester to investigate mechanical properties of the MPP polymeric structures. By using this functional microdevice, we present the results on the mechanical properties of the polymeric structures fabricated by MPP.

*The results provided in this chapter are based on Papers [**P1, PR1, PR2**] and presented at [**1 – 5**] conferences.*

2.1. Overview of 3D microstructures fabricated out of glasses/polymers and their properties

Glass is one of the most common used materials in science. It is a superb material providing robustness, transparency and bio-compatibility, which are essential properties for many applications, especially for microfluidics, lab-on-a-chip devices, micro total analysis systems. However, the glass microprocessing requires multiple steps and large amount of time to build up complex shape microstructures using conventional planar lithography. Alternatively, femtosecond laser pulses have enabled high precision maskless fabrication of 3D structures in glass by several main techniques: (1) laser drilling from the back side of the glass [13, 103], (2) structuring out of photosensitive glass [104, 105], and (3) selective laser etching [53].

In the first technique, the ultrashort laser pulse irradiation, is focused through the glass to rear surface of the substrate. The sample is immersed into distilled water, which eases the removal of the ablated debris. The channels could theoretically have an unlimited length and complex geometry [13]. Moreover, other advantages of this method are that the process does not require additional process (e.g., etching process) and the fabrication could be done almost in any material transparent to laser wavelength. However, in practice, when the depth of channels reaches several hundred micrometers, the ablated debris blocks effective processing.

There are photosensitive glasses (Foturan [104] or Apex [105] glasses), which could be used for 3D micro fabrication. These materials were originally designed to be structured without the need of photoresist, as an alternative for classical photolithography. The Foturan and Apex glasses have very similar composition and the working principle is the same. For simplicity, we consider the properties of Foturan only. Photosensitive glass consisting of lithium aluminosilicate glass is doped with silver and cerium impurities. The latter, Ce^{3+} atoms make the material sensitive to UV light with absorption edge around 315 nm [106]. Therefore, if Foturan glass is irradiated with shorter light wavelength, the photon is linearly absorbed by cerium ion, which releases an electron and becomes Ce^{4+}. Then, the silver ion captures the free electrons and results in formation of a silver atom. In near-IR wavelength femtosecond laser irradiation, the described photochemical process happens only at the focus point due to non-linear multiphoton absorption, which creates the possibility of 3D structuring. Thereafter, the Foturan glass needs to be annealed at ca. 500°C, leading to the formation of silver clusters. During this thermal treatment at around 600°C, a silver cluster works as a nucleus for the formation of crystalline phase of lithium metasilicate, which is more susceptible for etching in HF acid. It is reported a 1:50 ratio of etching rate (selectivity) of modified in respect to pristine material [10]. A major advantage of Foturan is relatively low melting temperature of ca. 550°C, the fabricated structures could be significantly smoothened by the additional post-annealing process. However, the Foturan glass is relatively expensive, and has additional high absorption in near UV range.

Alternatively, the glass 3D structuring could be done by SLE, however, not all transparent materials work for this technique. This is defined by the nanograting formation in the volume of material, which is observed just in several materials. Fused silica works very well for this technology under appropriate laser and writing settings; the selectivity could be as high as 1:1400 [50]. The unmodified regions of the glass are also etched simultaneously, just at a much slower rate than modified material. Therefore, long hollow channels will have a conical shape, as during the etching process successive channel sections will be revealed a at different timescale, which certainly is an undesired phenomenon. Fortunately, the taper angle could be easily pre-compensated up to a certain extent by taking this angle into account of the computer-aided design (CAD) model design or pre-programmed algorithm trajectory [107].

SLE technique allow processing of cubic millimeter volumes with micron resolution. The technology provides structures with surface roughness of tens to hundreds of nanometers, which is enough for microfluidics, micromechanical sensors, but it is not sufficient for optical quality required applications. Nonetheless, the mean surface roughness could be improved to several nanometers by post-processing in several ways: by thermal annealing [108], flame polishing [109] or CO_2 laser morphing process [110, 111].

As glass (fused silica) is non-crystalline material, its mechanical properties are identical in all directions. As usual quartz fiber, thin cantilever out of fused silica could be very flexible (see Fig. 2.1) and distinguish reversible

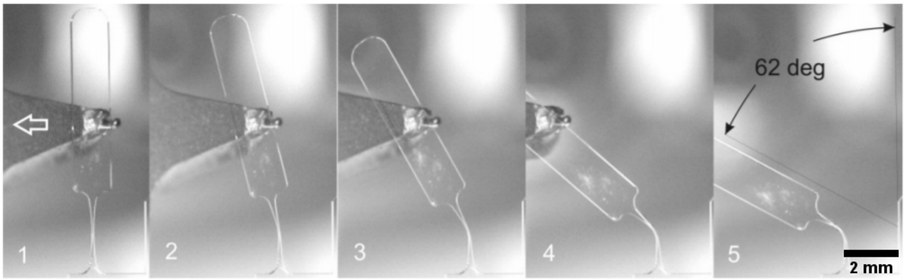

Figure 2.1: Illustration of reversible elastic bending capabilities of flexure-based glass microstructure [112]. The thickness of thinnest part is 40 µm.

deformations. In general, differently than most materials, it is plausible that glasses have elastic characteristics without plastic domain. Once the point load on the glass structure exceeds a certain extent, the breakage appears [113]. Therefore, the elasticity of the glass mechanics could be described in linear regime – reversible deformations obey the classical mechanics (as Hooke's law). Moreover, as the glass is uniform, it is not difficult to evaluate the acting forces for deformations by knowing precisely the physical dimensions of the glass part. It is known that fused silica structures processed by SLE could exhibit high stresses, well above 1 GPa [114, 115], which makes this material excellent for micromechanics application. SLE technology provides the ability to make 3D arbitrary-shape microstructures, while fused silica gives great mechanical properties, which are researched and well-known. This combination of aspects opens a new way for monolithic glass micromechanics for functional flexible devices. It could serve as microtensile tester for investigation of glass properties [114], microactuator [116, 117], optical microdisplacement sensor [118], flexure-based pivots elements [112, 119], onetime adjustable micromirror elements [120], advanced and complex medical devices for surgical puncturing [121].

Meanwhile, the additive MPP technology provides stretchable, but at the same time soft, biocompatible, complex-shape polymeric structures with a typical feature size resolution of a few hundred nanometers. These characteristics allow to employ this technique for extensive applications: microoptics, photonic crystals, optofluidics, and tissue bioengineering [122]. Moreover, by changing the processing parameters, optical and mechanical polymer properties could be tailored, such as refractive index [86], Young's modulus [12], or structural properties like creating metamaterials with different behavior [123]. Furthermore, the polymeric structure could be sensitive to the response of outer stimulus, such as heat [124], electric field [125], shrinkage and swelling in solvents [126, 127]. These properties could be applied for the 3D functional microdevices fabricated by MPP technique.

Certainly, in order to apply 3D structures fabricated by MPP in science and industry, the mechanical properties of the structure have to be known and sufficiently robust for specific application. However, measuring the mechanical properties of the structures with tens of micrometers in dimensions is not a trivial task, which requires complicated measurement procedures, as well as extremely precise methods for controlling the applied force. Different methods have been used to quantify and characterize the mechanical behavior of the structure at the microscale [114]. Usually, micro- and nano-indentations are widely-used, when the tip of a probe loads the specimen, which results in plastic deformation. By knowing precisely the tip displacement and applied force, the Young's modulus could be estimated. However, thin film, conventionally cured by UV light source, or bulk photopolymer will have different properties (Young's modulus) than 3D structures at the microscale provided by MPP technique [128]. In literature, there have been proposed other different methodologies for measurements of these mechanical properties for polymeric structures [129, 130], however, there is no unanimously accepted method, also the results are not consistent. In order to develop the applicability of the MPP technology, it is necessary to fully understand and know mechanical properties of microstructures, which could be applied for opening up new applications for integral microsystems.

An important feature of MPP-made structures is that, during the development and drying processes, there is always a change in material state, as the cross-linking degree of polymer chains is dependent on the laser voxel overlapping conditions. The change comes from the fact that point-by-point laser scanning will provide not entirely uniform polymerization. This could be explained by the example of focused Gaussian beam, which provides a non-uniform spatial intensity distribution. The center of the voxel will undergo higher light intensity than the outer section around it. Therefore, the mechanical properties of polymerized material will be defined not only by the used photopolymer, but mainly by – the degree of monomer conversion *via* polymerization reaction. For instance, tighter overlapping of the voxels will typically lead to a denser material with better mechanical properties. On one hand, as the polymerized material becomes denser, consequently geometrical structure dimensions turn out inevitably smaller than expected. This irreversible volume reduction is an effect of the dissolution of the non-polymerized internal nanometer size pores of the structure. On the other hand, it is observed that polymeric structures can also swell after rinsing them in solvents after (or during) the developing process. Strongly wetting solvents tend to penetrate the nanometric pores washed out by the developer so that the polymeric structure expands. Nevertheless, after the drying process, the solvent evaporates and nanopores collapse, leading to a reduction of geometrical dimensions. However, for some of applications even a slight deviation of dimensions is critical, therefore, the overall shrinkage could be taken into account by pre-compensation of the CAD model or programmed algorithm [97]. In addition, the shrinkage phenomenon could also be used to indirectly improve the achievable resolution. However, it might be difficult to fully eliminate this effect, especially, if the change of dimensions is non-linear, e.g., layers attached to the coverslip glass will undergo less distortions than successive layers of the structure [89]. Although these shrinkage/swelling phenomena have been investigated in a few articles [126, 131], most of the studies have been done only qualitatively and within a range of one to several tens of micrometers. Furthermore, shrinkage and swelling phenomena have a potential to be applied in chemical sensing applications.

MPP-formed microstructures are also used in applications in the fields of microelectromechanics [132, 133] and bioengineering [134], where knowledge of the mechanical and elastic properties of a structure are essential. Several studies have investigated the elastic behavior of microstructures made with the MPP technique: H.B. Sun et al. used optical tweezers to deflect polymeric microsprings [129, 135], while others applied distance-force probing with a commercial atomic force microscope [136] or MEMS based force sensing probes [12]. These studies indicate that laser fabricated microstructures have lower stiffness if compared to the bulk polymer, due to inhomogeneous (voxel-to-voxel) polymerization [136], while in some cases giant elasticity (extreme low stiffness/shear module values) was reported in Ref. [129]. Permeation of organic liquids in the polymer or scaling effects were considered as plausible causes for such unexpected behavior [129]. The wide range of factors that can contribute to microstructure elasticity makes this topic particularly challenging to investigate, but the emerging attractive applications that rely on elastic properties require detailed investigation.

2.2. The concept of micromechanical glass/polymer sensor and its working principle

In collaboration with École Polytechnique Fédérale de Lausanne (EPFL) university, it was designed a proof-of-concept device – 3D polymer/glass micromechanical sensor for investigation of mechanical properties of polymeric structure. The idea behind it was to combine the SLE technique with MPP method and provide a new functionality. As SLE and MPP techniques exhibit different advantages and drawbacks, the combined use of subtractive and additive techniques opens new possibilities for the fabrication of microstructures whose manufacturing was difficult or inaccessible using only one of the two techniques individually. New applications and functionalities could be achieved with such hybrid fabrication method for creating microfluidic devices for cell sorting, counting, liquid mixing and filtering applications [66, 137–140].

The design and working principle of the glass microsensor done by SLE

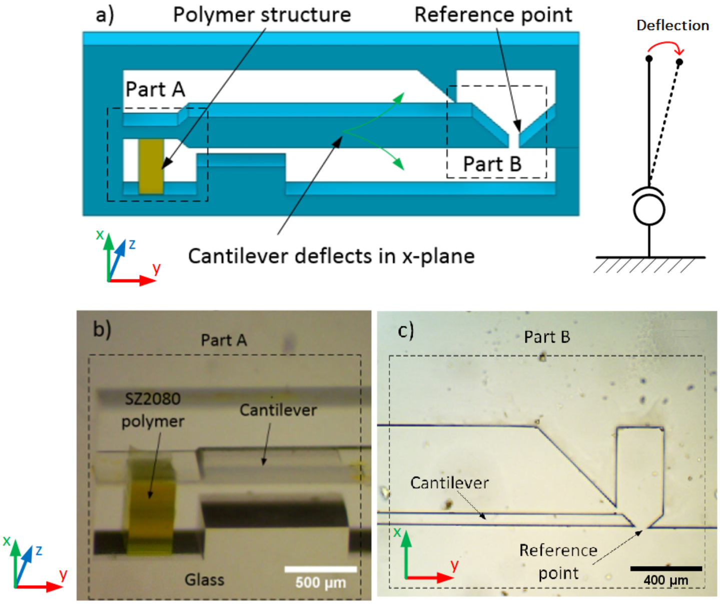

Figure 2.2: (a) CAD model of the primary design of the cantilever concept to be fabricated out of a fused silica substrate with an integrated polymerized structure attached to it, as well as the schematic of sensor kinematics. (b) Close-up view of the real structure showing the polymer attached to the cantilever. (c) Example of cantilever deflection measurement with respect to a fixed reference point.

is outlined in Fig. 2.2 (a). The passive flexure-based sensor is a long (∼10 mm) cantilever, which is statically fixed to one end. The opposite end of the cantilever is freely movable. This glass cantilever element has a low stiffness in-the-plane (XY) while remaining stiff for out-of-the-plane (YZ) movement. A fixed reference point (see Fig. 2.2 (a, c)) on the other side of the cantilever's tip works as a ruler to determine the displacement of the glass sensor end.

By MPP method integrated polymeric rectangular-shape column links the fixed glass base to the cantilever sidewall. Upon shrinkage or swelling, the column shrinks or expands, causing the cantilever to bend upwards or downwards in the XY plane. In a first approximation, this system can be analyzed as a cantilever with a point-load. The well-defined geometry of the fused silica cantilever acts as an amplification system. In principle, even a slight change in the dimensions of the polymeric column would result in an amplified displacement of the end of the cantilever. As the elastic properties of fused silica are well known, and considering the fact that silica is inert in most chemicals, the cantilever deflection allows to evaluate the reaction force applied to the polymer and, in turn, to estimate its elastic properties in different media. It is necessary to note, that the deflection magnitude of the glass cantilever's end largely depends on point-load position along the cantilever and the applied force.

In order to optimize the coupled glass/polymer system for the highest sensitivity (largest displacement), the polymeric column position along the glass cantilever has to be chosen carefully. In general, integration near the fixed glass end would induce the highest deflection; however, at this position making a change requires higher force, which could be insufficient. In that case, if the generated force of shrinkage/swelling effect is not enough to push the glass sensor, the polymeric column could be deformed itself. In contrast, if the polymeric column is integrated far from the base point, then the needed force is lower to deflect the glass cantilever, but the overall amplification will give a lower deflection magnitude too. There should be found an optimized position at which the polymeric column is not deformed yet and gives the highest amplification of the system. Usually, the photopolymers used for MPP technology are designed to have a relatively low shrinkage effect, for instance, Ormocomp exhibit 5-7% [141], while SZ2080 is expected to have an even lower value. However, as it was stated earlier, it is highly dependent on monomer degree of conversion, e.g., tightly laser-scanned structure most likely will have a lower shrinkage value.

In order to calculate the force-deflection relationship for such a glass/coupled system, we need to derive an analytical formula. In general, the displacement of the glass sensor could be calculated using beam bending theory [113], also known as Euler-Bernoulli beam theory. Cantilever deflection at any point could be described by the following equation:

$$M(x) = -EI\frac{d^2\delta}{dx^2}, \tag{2.1}$$

where $M(x)$ is the bending moment, E is the elastic (or Young's) modulus of the material, I is denoted as the second moment of inertia of the cantilever, x is the cantilever's length coordinate, and $d\delta/dx$ is the slope of deflection. For a point load scenario, the bending moment is $M(x) = F\Delta x$, there F - the loading force and Δx - displacement at the loading point. Under marginal condition, one cantilever's end is statically fixed, and another is freely movable. Based on the assumptions formulated above, by solving equation and making rearrangements of the expression, the magnitude of the cantilever's tip deflection could be expressed as follow:

$$\delta = \frac{E_p S_p (L_p - d_g)(3L_g - a)a^2}{2(E_p S_p a^3 + 3E_g I_g L_p)}, \tag{2.2}$$

where E_g is Young's modulus of fused silica, L_g – the total cantilever length, d_g – the distance between the cantilever and the glass base, a – the distance between the fixed cantilever end and the polymer, I_g is the silica's second moment of inertia (which for a rectangular cross-section is $I_g{=}t_g w_g^3/12$, with w_g

denoting the cantilever width, and t_g – its thickness). The polymeric structure cross-section is denoted by $S_p = W \times H$, where W - width and H - height, as marked in Fig. 2.3.

A set of initial parameters needed for modeling the primary column displacement approximation could be known, by choosing the primary design dimensions, which are specified below. The thickness of the cantilever was chosen to be 480 µm, L_g – 10 mm, w_g – 35 µm, d_g – 35 µm, S_p – 50 µm × 50 µm, E_c is known to be 72 GPa [113]. However, still two parameters remain unknown in Eq. 2.2: E_p – the Young's modulus of the polymer, and L_p – the final length of the polymer after swelling or shrinkage in the absence of a reaction force. If the first parameter is set to be a constant, the dynamics of cantilever deflection could be evaluated by changing the second parameter values and the polymer's integration position a, and vice versa. Fig. 2.3 (*right*) shows typical plots of cantilever deflection with different polymer elasticity and shrinkage values, when either of parameter is a constant. One can see that the shrinkage of the polymer (change in L_p value) influences only the overall magnitude of deflection, while a change in E_p shifts the maximum deflection position along the cantilever.

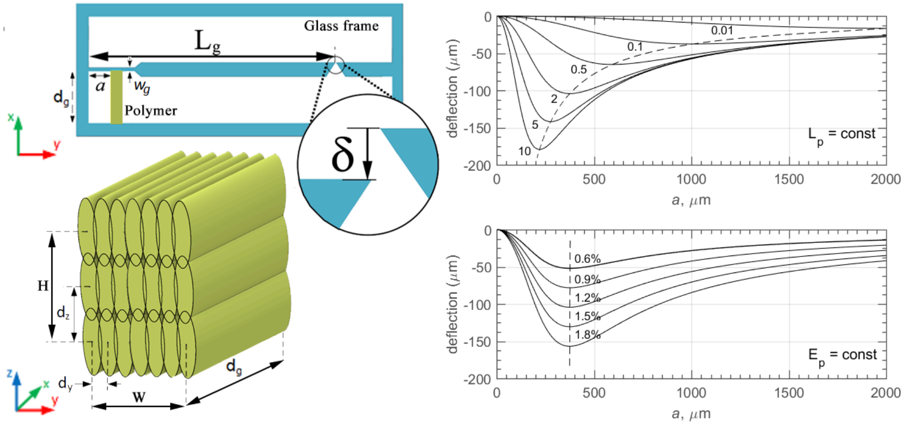

Figure 2.3: A sketch of the glass cantilever with integrated polymeric rectangular column that may induce cantilever deflection due to the shrinkage/swelling effects. (*bottom-left*) A schematic construction of a polymer square column fabricated by MPP methods. (*right*) Modeled cantilever tip deflection values versus distance along the cantilever where the polymer is integrated. Top graphs are modeled with a constant polymer shrinkage value (in this case 1.2% from the original design value (d_g)) and a different Young's modulus, while the bottom graph depicts a situation where the Young's modulus is constant (2 GPa) and shrinkage value is varied. Dashed curves depict maximum deflection trends in both graphs.

It is necessary to note, the modulus of elasticity is a material property, while the stiffness (k) describes elasticity of a structure made from the material in question. In our case the polymeric structure is a rectangular column made by DLW with a dense patterning algorithm. Although the structure is made by combining discrete patterns, we assume it is dense enough, so that it is reasonable to consider it as a plain and homogeneous column of Young' modulus E_p. If necessary, E_p could be interchanged with stiffness k in Eq. 2.2 using Young's modulus expression as $E_p = kL_p/S_p$.

A slightly different cantilever sensor can be designed by linking several identical cantilevers into one combined system, as shown in Fig. 2.4. Here, each cantilever's reaction force applies to all polymeric segments that are below the cantilever, therefore in each segment different force scaling is achieved, allowing for probing the polymer elasticity. To compute each cantilever deflection, one needs to solve the linear system equation depicted in Fig. 2.4. As in Eq. 2.2, there are two unknown parameters: E_p and L_p. The benefit of such a system lies in its simpler polymeric column integration procedure, as the polymeric column can be recorded in one single step (simultaneously through all cantilevers), automatically making all segments identical in terms of geometry and exposure parameters, an increase in repeatability can be expected. The main drawback is the reduced lack of accuracy, because polymeric segments close to the glass base experience a higher glass stiffness, resulting in greater reaction forces that considerably reduce the cantilever deflections, making it hard to measure (optimizing the sensor design by making each cantilever of different thickness can overcome this problem). This design was created as a substitute for the simple cantilever model if sufficient polymeric integration repeatability could not be achieved in the former case. Later, it turned out that repeatability was not a problem; therefore we used the coupled cantilever design as an alternative method to estimate polymeric elastic properties.

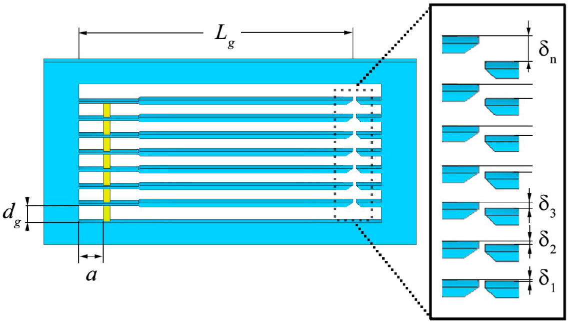

$$\begin{bmatrix} k+f & f & f & f & \dots & f \\ -k & k+f & f & f & \dots & f \\ 0 & -k & k+f & f & \dots & f \\ 0 & 0 & -k & k+f & \dots & f \\ \vdots & \vdots & \vdots & \vdots & \ddots & \vdots \\ 0 & 0 & 0 & \dots & -k & k+f \end{bmatrix} \begin{bmatrix} \delta_1 \\ \delta_2 \\ \delta_3 \\ \delta_4 \\ \vdots \\ \delta_n \end{bmatrix} = \frac{(3L_g - a)(L_p - d_g)k}{2a}$$

$$f = \frac{3E_g I}{a^3} \qquad k = \frac{E_p S_p}{L_p}$$

Figure 2.4: A sketch of a coupled cantilever system consisting of several cantilevers interlinked with the polymer column (each polymer segment is identical). A linear system equation that can be used to compute the deflection of each cantilever is also included.

Several SLE experiments were conducted on the system to have optimized parameters for the fabrication of the designed cantilever concept. For this process it was used a 1030 nm laser wavelength, repetition rate was set to be 610 kHz, and circular polarization was selected. The laser irradiation was delivered to 20×/0.4 NA objective lens. The experiments showed that 600-700 fs had the highest etching rate for written modifications, while pulse energy should be set in the range of 200-500 nJ. However, at higher energies the channels have much rougher surface. Moreover, it was observed that at higher energies the volumetric modified areas are prone to crack, therefore, the laser average power and overlapping conditions should be chosen carefully. In a *single* sensor case (see Fig. 2.3), the actual glass chip consisted of a set of 17 identical, separated cantilevers for more rapid testing of MPP process parameters. This allowed to eliminate any differences between the cantilevers of the same batch, resulting from different experimental conditions (e.g., etching process time). The designed structure was sufficiently large of 17×20 mm, which required fast microprocessing. The writing velocity was set to be 15 mm/s, which showed sufficiently good precision and a relatively fast etching process at the same time. The etching rate and selectivity highly depend on the etchant. For indicative purpose, a comparison of etching rates in different etchants for unmodified fused silica are listed in Table 2.1. The fused silica substrates were etched at different timescales (from one hour to fifteen hours) depending on the etchant concentration, but the duration was sufficiently long enough that significant thickness would be etched. Then, the etch rates were estimated by measuring the remained thickness. It is necessary to note, that the etching rate of superficial layer might depend on surface quality of the glass substrate.

Table 2.1: Comparison of etching rate for laser unmodified, pristine fused silica (JGS1) in different etchants.

Acid	Concentration, %	µm/h
HF	1	0.286
	2.5	0.764
	5	1.455
	10	3.415
	20	10.56
	48	79.29
KOH	10 mol/L @ 90°C	0.774

The glass processing and polymer integration experiments were conducted using a DLW method employing a single Yb:KGW femtosecond laser system (Pharos, Light Conversion), the scheme is outlined in Fig. 2.5. The sample was translated using dual XY linear stages (ANT130-XY, Aerotech Inc.), while the laser focus spot was changed using a vertical Z stage (ANT160L-Z, Aerotech Inc.).

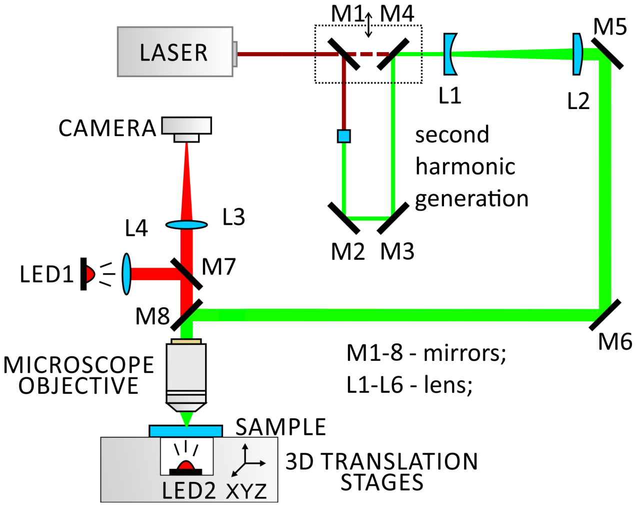

Figure 2.5: Simplified schematic diagram of DLW setup for subtractive and additive techniques. For SLE process fundamental laser wavelength of 1030 nm was used, meanwhile, for MPP the second harmonic – 515 nm.

The monolithic glass cantilevers were produced from a single piece of 500 µm-thick fused silica substrate by combining femtosecond laser radiation and subsequent chemical etching. Glass modifications were written using 1030 nm laser wavelength, 270 mW laser power (rep. rate 610 kHz), while focusing with 0.4 NA objective. The polarization was set to be circular that the etching rate would be independent on the scanning direction. Laser pulse duration was increased to 600 fs in order to achieve better etching selectivity [53]. The multiple laser-modified tracks along the predefined cantilever perimeter were recorded at 15 mm/s velocity in layer-by-layer fashion with 4.5 µm spacing. In addition to scanning the contour of the cantilever, additional slicing was done in order to divide unnecessary separated glass blocks into smaller pieces for easier removal during the etching process.

Then, after laser exposure, the fused silica substrate was immersed in a 5% (v/v) concentration HF solution for 6 hours. It is necessary to note that the acid etched out the modified areas all through the thickness of the substrate in much faster time, but, as the sensor has very fragile sections, it was left in the etchant longer so that the separated parts completely fall out by themselves. Thereafter, the cantilevers were later rinsed in distilled water, taken out and left to dry. Fig. 2.6 (a, b) show the fabricated glass microsensors.

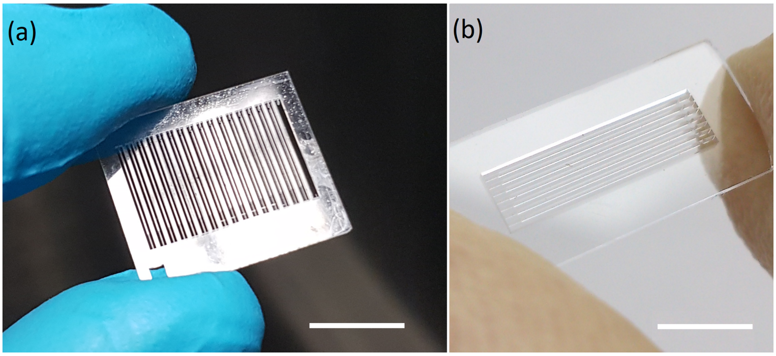

Figure 2.6: Images of fabricated glass microsensors: (a) a set of *single* cantilevers and (b) structure of 7-coupled cantilevers. Scale bar, 10 mm.

2.5. Preparation and microfabrication of polymeric structures by MPP

Afterwards, the fabricated cantilever structure was put on a standard microscope cover glass and fully covered with photosensitive polymer using the drop-casting method. For this experiment we used a hybrid inorganic/organic photosensitive polymer SZ2080, which was additionally photo-sensitized with 1% wt of 2-benzyl-2-(dimethylamino)-4'-morpholinobutyrophenone photoinitiator. SZ2080 polymer was immersed in glass cantilevers and prebaked for 1.5 h on a hot-plate with a temperature ramp of 40°C – 90°C; alternatively, a series of samples were heated at 50°C for 15-18 hours. The same laser and setup were used for MPP experiments as for SLE technology (see Fig. 2.5), just different laser, focusing and scanning parameters were set. The MPP experiments were carried out using a frequency-doubled wavelength (515 nm) at 200 fs-width pulses operated at a 610 kHz repetition rate. The specimen was loaded on the same XY linear stage system; the focusing was done using an objective lens with 0.8 of NA.

2.6. Experimental results

During these experiments, several initial technical challenges arose. It is important to note that naturally there is no deflection at the end of the sensor if there is no force that pushes the cantilever. It was observed that when the glass cantilever is dipped with high viscosity photopolymer by drop-casting, the gaps in glass are filled at different timescales. Initially, as soon as the first polymer droplet gets into the gap between the cantilever and the glass base, the fluid starts to flow along the channel because of high wettability between polymer and glass. Apparently, this effect creates such huge forces that the cantilever at the end is largely deflected. As SZ2080 polymer is high viscosity material, the glass sensor cannot easily get back to former equilibrium position. Moreover, during the relatively quick prebake process, the solvent, which is a compound of SZ2080 pre-polymer, evaporates, resulting in a liquid of even higher viscosity. Eventually, liquid photopolymer becomes a gel. If the cantilever end position was "frozen" at some deflection angle, the measurements would be inappropriate and would produce an error. To overcome this issue, it was observed that, in most cases, even if there is a deflection, the cantilever slowly gets back to its initial position after a certain time if the prebake process is slow and long enough. Both heating procedures are specified in Section 2.5.

The glass cantilever dimensions were chosen correspondingly to initial modeling predicting shrinkage and modulus of elasticity, which largely affects the deflection of the glass cantilever. It is necessary to emphasize that the design of the cantilever was improved several times depending on obtained results. A set of different glass cantilevers were fabricated by varying the width w_g in the ranges between 20-40 µm and the distance between the cantilever and the glass base d_g between 70-340 µm. Experimental findings showed that the best results were obtained with w_g=30 µm and d_g=340 µm.

After the integration of MPP structures, the samples were developed and dried in ambient air. However, the first cantilever tests indicated no or very low deflection. For instance, the suspended polymeric column underwent several different defects, such as cracks generation or detachment (see Fig. 2.7). The latter defect is simply polymer dis-attachment at one end due to poor adhesion to the glass sidewall. It could be related to the fact that the focused laser beam would be scattered and undergo distortions near the glass/polymer interface due to the mismatch of refractive indices between both materials. This effect was even more pronounced at higher fabrication depths. Also, the adhesion is weaker between two dissimilar materials, e.g., polymer/glass interface. Several methods were applied in an attempt to overcome dis-attachment due to poor adhesion: (1) optimization of suitable parameter set (not only the laser average power, but also by changing the dimensions of polymeric column), (2) usage of adhesion promoter, (3) the glass cantilever geometry improvement (adding a chamfer to the sidewall of the glass in order to avoid the refractive indices mismatch effect, (4) usage of a CPD for drying process. Defects formation of the polymeric structure mainly occurred during the development step in the transition from liquid medium to ambient air. During this drying process the glass cantilever is deflected at maximum angle due to capillarity forces, which results in either the polymeric column dis-attachment from the glass surface, or an occurrence of cracking in the polymeric column.

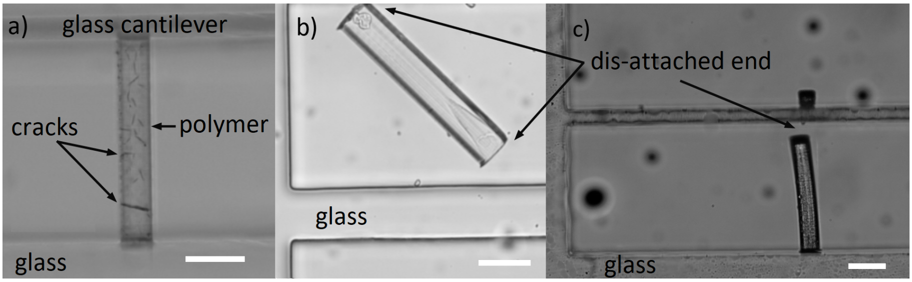

Figure 2.7: Defects obtained in SZ2080 polymer after the developing process: (a) formation of cracks, (b) detachment at both ends, or (c) at one end. Scale bar, 100 µm.

Several solutions helped to improve the adhesion. Firstly, before the drop-casting process, the glass samples were immersed in a mixture of 20 ml dichlormethane and 250 µl MAPTMS and kept for roughly 24 hours. Afterwards, the structures were rinsed in ethanol for a few minutes and allowed to dry naturally. This step creates a durable monolayer and bonds organic (polymer) and inorganic (glass) material. The hydroxyl (Si-OH) groups in the surface of the glass substrate are eliminated and replaced with oxane bonds (Si-O-Si), while organofunctional groups later form the bonds with polymer matrix.

Secondly, the experimental findings showed that a narrow polymeric column tends to deform itself even at intermediate laser power range and relatively tight scanning conditions. This result supposed that the cross-sectional should be increased, however, there were a few limitations. On one hand, the column height should be preferably as low as possible in order to minimize the effect of light scattering. On the other hand, the width of the polymeric column should be as small as possible so that the structure could be kept as a point load. We found that the cross-section of 50 × 50 μm^2 meets both requirements quite well. In a case where the micromechanical sensor needs to be dried, the critical point dryer must be used to avoid strong capillarity forces.

In general, the unknown two polymer parameters (Young's modulus and shrinkage) can be estimated using a set of cantilevers in which the polymer columns are attached at different positions a (see Fig. 2.3). Shifting the polymer beam attachment position scales the reaction force and allows for probing the polymer elasticity under fixed conditions. Therefore, it is possible to unambiguously fit the data to both unknown parameters using Eq. 2.2. As we will see later, both parameters are environmentally dependent and can be utilized for chemical sensing applications.

A polymeric rectangular-shape column was integrated in a single cantilever structure (top surface of the polymer was 10 µm below the glass surface level).

The total size of the polymeric column ($H \times W \times d_g$, as shown in Fig. 2.3) was 50×50×342 µm^3, while two different pattern densities were used: one (I) with distance between parallel lines $d_y = 0.25$ µm and adjacent layers $d_z = 1.5$ µm, while the other (II) with $d_y = 0.5$ µm and $d_z = 4.5$ µm (see Fig. 2.3). The voxel transversal and longitudinal dimensions were larger than parameters d_y and d_z, respectively. In both pattern scanning cases the voxels overlap in all three dimensions, forming a continuously polymerized structure. However, in the higher density (I) pattern case, the total exposure dose is higher, allowing for a higher degree of conversion of monomers, which impacts the polymer swelling properties [126]. In both pattern scanning cases, an average power of 0.8 mW was used, and the writing velocity was set to be 3 mm/s. To scale the cantilever reaction force, polymeric rectangular-shaped columns were integrated at different positions a from the cantilever base and, in each configuration, three equal polymer-cantilever systems were fabricated in order to test the experiment's repeatability. After MPP processing, the samples were immersed in a developer bath (4-methyl-2-pentanone (PEN)) for 20 – 30 min to wash out unexposed material. The composite micromechanical cantilever system was immersed in different liquids (PEN, ethanol (ETH) and water), which resulted in different cantilever deflection angles, demonstrating the sensing mechanism.

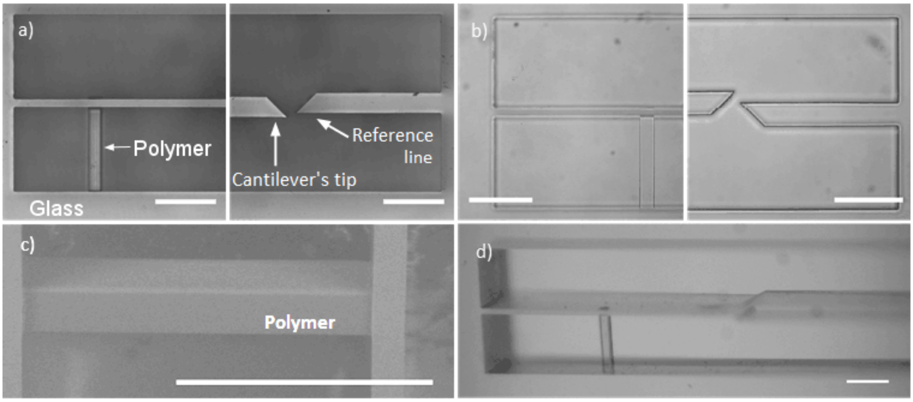

Figure 2.8: Fused silica cantilever with integrated SZ2080 polymeric column fabricated by the hybrid femtosecond laser processing technique. The optical microscope images indicate the deflection of the cantilever after (a) polymer shrinking in air and (b) swelling in solvent medium. (c) SEM image shows a closure image of integrated polymeric column. (d) Stereoscopic microscope image of a hybrid sensor. Scale bar, 250 µm.

The fabricated cantilever with an integrated polymer column is shown in Fig. 2.8 (a-d). The deflection direction of the cantilever indicates shrinkage or swelling phenomenon of the polymeric column, as can be seen from Fig. 2.8 (a, b). The magnitude of the cantilever's tip deflection was evaluated from the images, which were taken through optical microscope. Then, a projected line was drawn along the cantilever end towards the reference direction. The displacement between the reference line and the projected line was measured. It is important to emphasize that the cantilever length is sufficiently long ($\sim$ 10 mm) compared with the maximum deflection of the cantilever's end tip ($<$200 µm), therefore, the overall deflection angle is negligible. If measurements are done at the same point, the influence of the radial deflection trajectory on the distance of the projected and reference lines could be neglected.

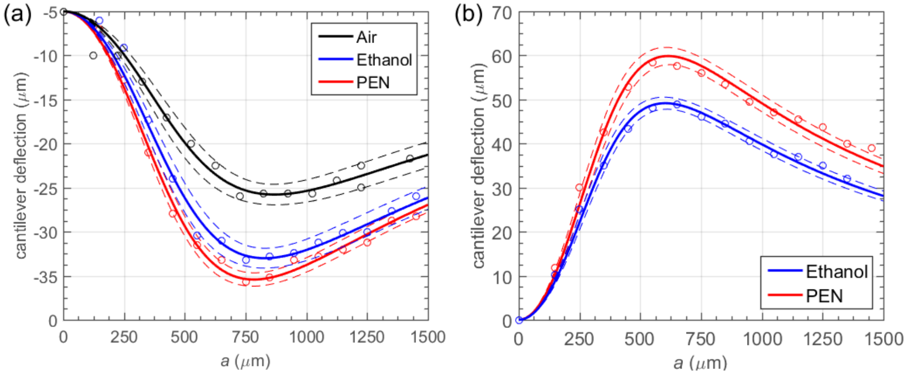

Figure 2.9: Glass cantilever deflection induced by polymer (a) shrinkage and (b) swelling in various mediums. A polymeric column was fabricated with the lateral (a) $\mathrm{d}_y x = 0.25$ µm and axial $\mathrm{d}_z x = 1.5$ µm hatching steps, meanwhile (b) was done with $\mathrm{d}_y x = 0.5$ µm and $\mathrm{d}_z x = 4.5$ nµm, respectively. Points represent experimental results, solid lines – the least square fit of measured data, while dashed lines show fitting errors, which are within the 95% confidence interval.

The polymeric column fabricated at high density pattern condition (I), as discussed in the previous paragraphs, undergoes shrinkage right after development. Measured cantilever's tip deflection values versus the distance a of polymeric column position along the cantilever in different media are depicted in Fig. 2.9 (a). Initially, the deflection is measured when the sensor is still in the developer (PEN), which later is interchanged with ethanol. In contrast, by interchanging the medium, it was observed a lower magnitude of cantilever deflection, which could be attributed to different properties of polymer-solvent affinity [126]. Afterwards, the liquids are evaporated and the deflection is measured in air. The evaporation has to be carried out in a critical point drying condition to prevent capillary forces from acting on the glass cantilever, resulting in polymer breakage or detachment of the polymeric column from the glass substrate. In all cases the measured data points were fitted using the least square method applied to the Eq. 2.2. As evident, there is a good fit of the experimental data with the theoretical model. The fitting parameters (E_p, L_p) are as follows: immersed in PEN: (0.188 ± 0.005 GPa; 339.5 ± 0.1 µm); in ethanol: (0.158 ± 0.007 GPa; 339.6 ± 0.1 µm); and in air: (0.138 ± 0.008 GPa;

340.1 ± 0.1 µm). Fitting errors are within the 95% confidence interval, as shown by dashed curves in Fig. 2.9 (a). It is important to emphasize that the possible cantilever geometry estimation errors are not present in the fitted data (all cantilevers are identical), and are not important if comparative analysis between three different environments is carried out. If one includes geometrical measurement errors (i.e., assuming 5% precision in measuring all cantilever dimensions), the absolute values for Young's modulus and shrinkage/swelling can be estimated with ∼25% precision (evaluated by Monte Carlo simulation) by this method. Nonetheless, as a chip with identical single sensors were used and tested in different media, the impact of geometrical measurement errors could be neglected for these comparative results.

The results show that the average polymer shrinkage is about 0.6%. This value is expected, as SZ2080 is considered to be an ultra-low shrinkage photosensitive polymer [85]. However, there is an evident increase in the Young's modulus when the polymeric column is immersed in the organic liquid. The cantilever reaction force builds up due to the increased polymer stiffness and not to the polymer shrinkage.

A similar tendency is present in samples made with the lower density (II) scheme. In this case, the samples swell as high affinity (strongly wetting) solvents, such as PEN or ethanol, penetrate the internal nanoscale pores, causing the polymer to expand. In contrast, water or other low affinity solvents empty the pores causing the polymers to shrink [126]. The magnitude of cantilever's end displacement was measured through optical microscope. The cantilever deflection curves are shown in Fig. 2.9 (b), and fitted values are as follows: PEN (0.467 ± 0.018 GPa; 345.8 ± 0.1 µm) and ethanol (0.493 ± 0.015 GPa; 345.1 ± 0.1 µm). Samples were also tested in water, but the cantilever did not show any deflection, suggesting that shrinkage/swelling is too low to induce sufficient forces (for the same reason sample drying was not attempted in this case). Remarkably, these results indicate an increase of up to 3 times in the Young's modulus if compared to the higher density patterning scheme. Internal presence of organic liquid molecules in the polymer network considerably increases its stiffness and makes cantilever actuation stronger.

Alternatively, in order to compare the results, it was replicated the same experimental conditions with lower density (II) scanning pattern into a coupled cantilever system, as shown in Fig. 2.10. Contrary to the previous experiment, the polymer column was positioned at a fixed distance $a = 600$ µm. Similar swelling values for polymer elastic properties were acquired with the coupled cantilever system. The least square fit of the model gives slightly lower Young's modulus values than in the previous case, but, taking into the account the absolute 25% precision, the values match in both experiments. The fitted values indicate the modulus of elasticity E_g and the final length of the polymer after deformation L_p to be as follows: PEN (0.40 GPa, 346.4 µm) and ethanol

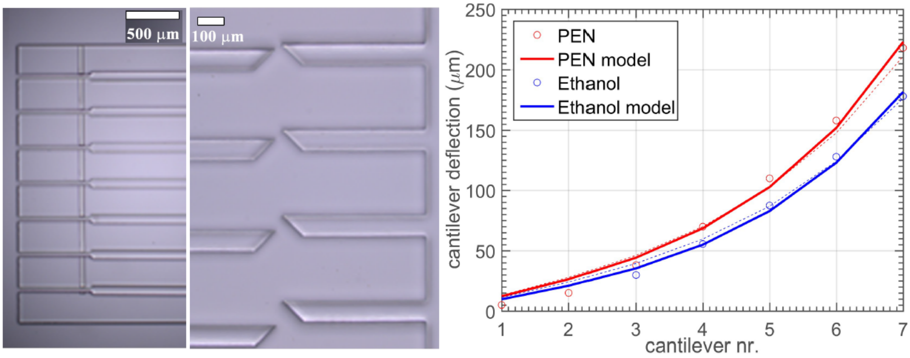

Figure 2.10: The manufactured cantilever system, consisting of seven interlinked cantilevers. Microscope images are shown on the left and center (cantilevers are immersed in PEN). (*right*) Deflection of the coupled system in different solvents: solid curves show the least square fit of the data computed from the coupled cantilever model, while dashed curves show the model fit with parameters evaluated from the single cantilever experiment (Fig. 2.9 (b)).

(0.389 GPa, 345.6 µm).

The scanning density (i.e., laser exposure dose) of column structure affects the polymer behavior (shrinkage/swelling) in solvents, as it was shown in Fig. 2.9. This phenomenon was researched in more detail. It was investigated the polymer mechanical properties' dependence by incrementally changing the laser exposure dose under the same scanning parameters. It was fabricated a set of the polymer columns, which are attached at different positions a for successive of cantilever. The experiment was replicated with four different laser average powers (0.5 mW, 0.7 mW, 0.9 mW and 1.2 mW). The obtained results are depicted in Fig. 2.11. Up to 0.9 mW, the polymeric columns were swollen in PEN, while shrinkage was observed at 1.2 mW. For all the plots, the peak of the slope of the deflection was observed at a different position. This indicates that by changing the fabrication parameters we can impact elasticity modulus E_p. In Table 2.2, the obtained modeling and experimental results of polymeric column properties are listed. The calculated modulus of elasticity reveals that it is possible to achieve a change of up to ∼2 GPa for SZ2080 by changing the laser writing power.

Alternatively, the polymeric structure behavior dependence on the exposure dose was investigated in slightly different manner. In order to systematically investigate the polymer behavior, we conducted a qualitative study. It was chosen to integrate the polymeric column at an optimum position to obtain high deflection of the glass cantilever, which corresponded to approx. 600 µm, as can be seen as dashed line in Fig. 2.11. A series of polymeric columns were fabricated at a fixed position a (600 µm) with an increased laser average power for successive column in the range of 0.4 – 2.8 mW. The rest of laser and fab-

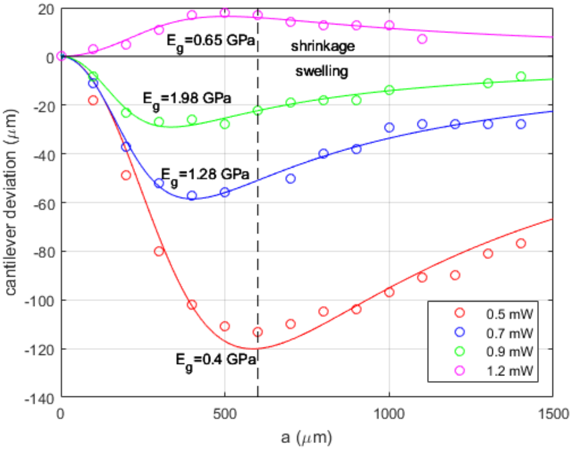

Figure 2.11: The dependence of cantilever deflection (induced by polymer swelling and shrinkage) in PEN solvent versus the distance a along the cantilever, where the polymer is integrated, for several different laser average power used for MPP process. Points represent experimental results, solid lines – the least square fit of measured data.

Table 2.2: Calculated polymer properties (Young's modulus E_p, the final length of the polymer after deformation L_p and strain ϵ) from glass cantilever deflections by changing the laser average power P.

P, mW	Effect	L_p, µm	ϵ, %	E_p, GPa
0.5	Swelling	348.23 ± 0.37	2	0.4 ± 0.02
0.7	Swelling	343.39 ± 0.13	0.7	1.28 ± 0.07
0.9	Swelling	342.00 ± 0.08	0.3	1.98 ± 0.18
1.2	Shrinkage	340.15 ± 0.11	0.25	0.65 ± 0.06

rication parameters were kept constant. Each polymeric column ($H \times W \times d_g$) was 50×50×342 µm^3, fabricated with laser scanning parameters of d$_y$ = 0.5 µm and d$_z$ = 4.5 µm. Then, these samples were rinsed in PEN solvent and the cantilever's tip deflection was measured. The experimental results are plotted as a function of the writing laser power in Fig. 2.12 (a). There could be observed three distinguishable regimes (I, II, III), which are marked in the graph. A visible polymerization reaction starts from 0.4 mW, however, at this lowest power the polymeric column has bent itself after the development process. At a slight higher laser power of 0.5-0.6 mW (I regime), the polymeric column becomes more robust that it could pull the glass cantilever. Then, it could be seen a huge deflection of the cantilever's end tip, which is induced by polymer swelling. This could be attributed to the fact that at low laser power range there is a lower degree of conversion of monomers (larger nanopores), and, subsequently, a strongly wetting solvent (such as PEN and ethanol (ETH)) could easily penetrate and wash out the internal nanoscale pores, causing the polymer largely to expand. A different tendency is present at a moderate exposure dose, by continuously increasing the laser average power (II regime) in the range of 0.7-1 mW the cantilever deflection is becoming smaller as more of material becomes polymerized, leaving fewer and smaller nanopores behind. Eventually, at around 1.2 mW, there is a reverse behavior from swelling to shrinkage phenomenon. At this point the solvent cannot penetrate into the polymeric column anymore. The polymeric structure shrinks even more for the higher exposure doses. By exceeding a critical exposure dose (III regime) for the polymeric column, there is no enhancement of shrinkage; instead, above 1.75 mW it was observed a saturation point, as all the volume of the polymeric column is already polymerized.

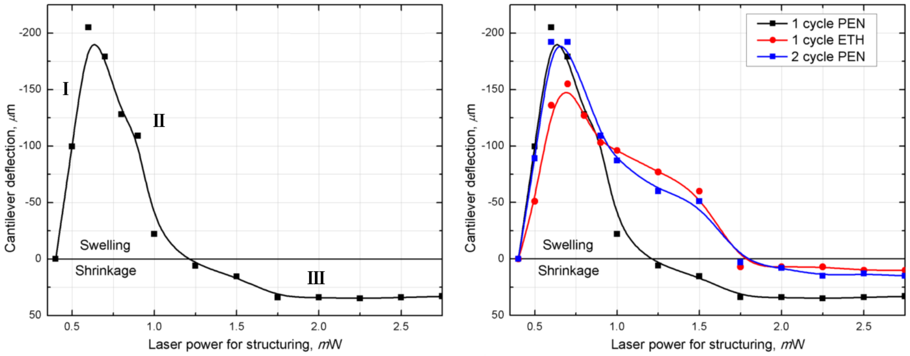

Figure 2.12: The dependence of cantilever deflection induced by SZ2080 polymer swelling and shrinkage in PEN solvent on the laser average power used for polymerization. (b) Cantilever deflection influence on the solvent cycle number between interchanged PEN and ETH solvents. Points represent experimental data, while solid lines are the results of fitted data.

Afterwards, similar observations were seen by rinsing the same sample in ethanol (Fig. 2.12 (b)). However, there are also a few distinctions from PEN. As expected, the overall deflection magnitude is a bit lower than that for PEN [126], but, more surprisingly, at the moderate laser average power (III), where the shrinkage was expected to be the same as in PEN, the glass cantilever indicates a swelling effect instead. This change could be attributed to ETH (C_2H_6O) molecules, which are smaller than PEN ($C_6H_{12}O$) and could penetrate the nanometric pores more effectively. The nanopores of pre-polymer are washed out and replaced with ethanol, forming a sponge-shape polymeric structure at a microscale. This change is irreversible and, in result, the polymeric structures start to swell. Afterwards, the same sample was immersed into PEN solvent again. This interchange back to the previous examined solvent will be called as a cycle. It is noteworthy that the change of dimensions is not instantaneous. In our structure case, it took a few minutes to get a constant value. Therefore, after each interchange of solvents it was kept at least 10 minutes before next measurement procedure. At the second cycle in PEN, it is observed a similar dynamic of cantilever's end deflection, as it was observed in ETH. When more of nanopores with pre-polymer are washed out, then the ETH could be interchanged by PEN molecules. Thus, at the second cycle in PEN the dynamics of cantilever's end deflection is similar as seen in ETH solvent.

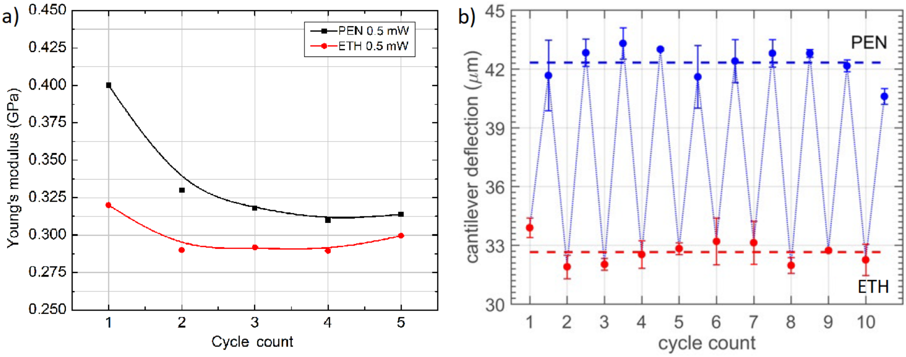

Figure 2.13: (a) Dependence of Young's modulus of SZ2080 polymeric structure in various solvents on the solvent change cycle number. Points represent calculated results, the solid lines are fits to the obtained data. (b) Dependence of cantilever deflection on the cycle number of the interchange solvent. The points represent the mean value, the error bars show maximum and minimum deviation. Blue and red dashed lines indicate the average cantilever deflection in PEN and ETH solvent, respectively.

As it was observed a change of different cantilever's end deflection in the solvent at the second cycle, the repeatability was researched in more detail. It was used the same sample with the maximum magnitude of cantilever deflection, which was fabricated with 0.5 mW laser average power (see Fig. 2.11 (a)). Overall, the sample was interchanged with PEN and ETH 5 cycles, measuring the cantilever's deflection each time. The dependence of calculated the Young's modulus on cycle count is shown in Fig. 2.13 (a). We observed that the Young's modulus decreases with the first cycles of solvent change and then becomes a constant value. One of plausible explanations for this observation could be again the smaller ethanol molecules, which permeate more effectively, removing remnant unwashed nanopores with pre-polymer.

Subsequently, once the saturation point is reached, the experimental findings showed that the swelling behavior is reversible and repeatable. Fig. 2.13 (b) depicts the cantilever deflection change when the sample is periodically immersed in different liquids. Three identical samples were tested after saturation. The finding show that even after 10 cycles of ETH–PEN changes, the deflection magnitude remained the same. This also applies to water–organic solvent cycles, when deflection changes are maximized. This fact makes such hybrid micromechanical systems attractive for chemical sensing applications.

Moreover, it was investigated the mechanical properties' dependence on scanning geometry of the polymeric column, as well as the influence of the temperature stimulus. The former experiments were done in PEN solvent with already developed and swollen structure by observing the glass cantilever deflection. The PEN solvent was cooled down to -20°C, then heated incrementally with 10°C temperature ramps to 50°C. However, there was observed almost no influence on the glass cantilever deflection variation, i.e., the polymeric column almost did not change its dimensions.

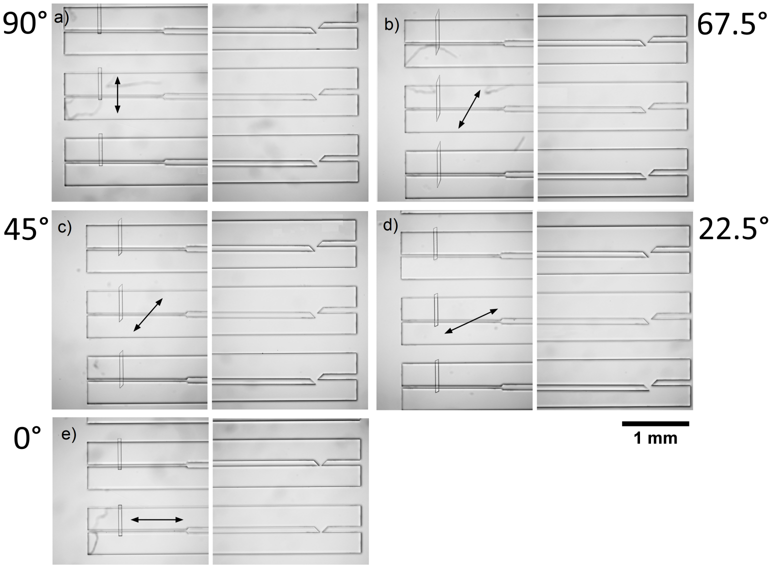

Figure 2.14: The cantilever deflection induced by SZ2080 polymer in PEN solvent with different laser scanning orientation: (a) 90°, (b) 67.5°, (c) 45°, (d) 22.5°, (e) 0°. Black arrows indicate the scanning direction.

All the previous experiments were done in the same laser scanning manner. The polymeric column was fabricated by writing the multiple lines across the distance between the cantilever and the glass base in a layer-by-layer fashion. It was raised a hypothesis that scanning direction might influence the mechanical properties of the polymeric structure. For testing, it was fabricated a set of polymeric columns which were structured with incrementally rotated laser scanning orientation for each cantilever with 0°, 22.5°, 45°, 67.5°, 90° angles. When the scanned lines direction is perpendicular to the sidewall of the cantilever, it is considered this orientation to be 90°, while the individual line scanning direction conforms with the sidewall of cantilever, we denote it to be 0° orientation. Each of the polymeric columns was $50\times50\times342$ µm^3 in dimensions. In the 0° orientation case, the polymeric column would consist of multiple short lines of 50 µm along the cantilever. In order to have the uniform exposure dose at different polymeric column positions for different orientations, the effect of acceleration and deceleration of the linear stages have to be taken into account. Moreover, the polymer cross-section S_p ($W \times H$, as shown in Fig. 2.3) should remain the same irrespective of orientation. Therefore, for better precision, in this experiment it was reduced the laser writing velocity to 0.5 mm/s, also, we programmed to move the linear stages additionally before and after the polymerized section with closed laser shutter. It was done to eliminate acceleration and deceleration and keep a constant velocity for assuring identical experimental conditions. The distance between parallel lines was d = 0.5 µm, while spacing between adjacent layers was d_z = 4.5 µm. A set of 3 identical polymeric columns were fabricated at a fixed position a (600 µm for each orientation to average the results and keep track of repeatability (see Fig. 2.14)).

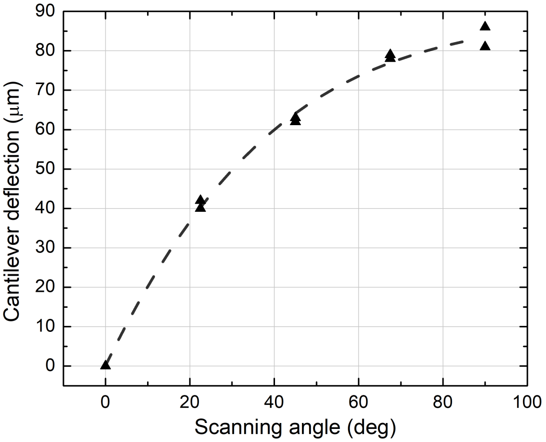

Figure 2.15: The dependence of cantilever's end deflection induced by SZ2080 polymer swelling in PEN solvent on laser scanning orientation in the range of 0-90°. Points represent experimental results, while the dashed line show a fit of this data.

Fig. 2.15 below depicts a graphical representation of experimental data. It is observed an incremental increase as the scanning angle approaches 90°. Although, the distance between parallel and spacing between adjacent layers parameters were kept the same for the whole set of cantilevers, but the result indicates that the scanning direction matters, as PEN solvent can easier permeate in longitudinally scanned polymeric columns. In this case, once the solvent molecules manage to permeate easier into zones polymerized at a lower degree of monomer conversion, it could easily propagate along the polymeric column length. Meanwhile, in the case of transversely scanned geometry, the multiple parallel planes polymerized at higher degree work as insulators from one region to another. In fact, the scanning at 0° resulted in no deflection at all.

A rectangular-shaped polymeric columns were chosen for simplicity of calculation and fabrication. Nonetheless, more complicated polymeric structures could be integrated by MPP and their mechanical properties could be tested with the same glass micromechanical sensor. For demonstration purpose it was carried out formation of 3D structure in Fig. 2.16: (a) 8- and (b) 4-turn springs out of SZ2080 polymer.

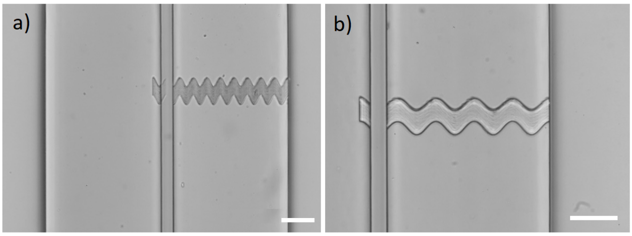

Figure 2.16: Different shape SZ2080 microstructures could be integrated into the glass microsensor for testing the mechanical properties (e.g., (a) 8- and (b) 4-turn springs). Scale bar, 100 µm.

2.6.1. Microfabrication of other polymeric materials by MPP

It was considered microfabrication of other photopolymer materials in order to measure their mechanical properties and compare the results with SZ2080. Firstly, it was used SZ-based photopolymer with different moieties between organic/inorganic compounds. The experiments were run with SZ5050, SZ4060, SZ3070, SZ1090, which were prepared slightly differently than the previous photopolymer – mixed by weight (w/w) concentration. For preparation, it was used a drop-casting method for covering the whole glass cantilever sensor, and subsequent heating step. However, there was observed a generation of multiple cracks (see Fig. 2.17 (*center*) and (*right*)) in the volume of those polymers, where the inorganic part was relatively large. This change of compound ratio results in the material becoming less elastic and more prone to crack under tension. Alternatively, the formation of cracks was observed even in these samples which were unheated and left for the solvent to evaporate naturally in ambient air. Surprisingly, if the same SZ5050 and SZ4060 materials were drop-casted on coverglass, there the polymer underwent the heating step without any cracking at all. This outcome suggests that formation of cracks happens only under tension conditions, when the polymer with higher inorganic part content cannot shrink equally from all directions. When polymer is embedded in glass cantilever sensor, the polymer is restricted in the gap. It results in shattering process, if tension level exceeds critical value. Better results were obtained with SZ3070; still, several cracks were obtained in the volume of polymer in random places.

Figure 2.17: Glass cantilevers before immersing the structure with polymer (*left*). The same structure after the polymer heating step: generated cracks into the volume of SZ5050 (*center*) and SZ4060 (*right*) photopolymers. Scale bar, 500 µm.

Table 2.3: Calculated polymer properties (Young's modulus E_p, the final length of the polymer after deformation L_p and strain ϵ) from glass cantilever deflections by changing the laser average power P.

Solvent	P_{ave}, mW	Effect	L_p, µm	ϵ, %	E_p, GPa
PEN	0.5	Swelling	352.81 ± 0.40	2	0.42 ± 0.04
	0.7	Swelling	348.64 ± 0.24	0.8	1.08 ± 0.10
	0.9	Swelling	346.89 ± 0.10	0.3	1.56 ± 0.22

Meanwhile, no crack generation was obtained in SZ1090, as the ratio of the organic part, and therefore elasticity, increases. Thus, the experiments were done with this material only, the calculated mechanical properties of polymeric column are listed in Table 2.3: final length after deformation L_p, strain ϵ, Young's modulus E_p. In comparison to SZ2080, the SZ1090 polymer swelling values were similar in all cases. However, the Young's modulus was lower for higher (0.7 and 0.9 mW) laser writing power range. In fact, at 1.2 mW it was not obtained reverse behavior to shrinkage as it was observed for SZ2080, actually, the cantilever's end deflection remained in the equilibrium position. The results prove that mechanical properties are weaker for SZ1090, which is more elastic in comparison to SZ2080.

2.7. Conclusions

In this chapter, it was presented a novel hybrid coupled-device concept consisted of SLE fabricated cantilever out of fused silica substrate with the direct integration of a polymeric column *via* the MPP technique. Through this combination of techniques, it was demonstrated how a glass/polymer micromechanical sensor could be used for investigating the elastic properties of polymeric microstructure and its behavior in different environmental mediums. It was shown that deformations of the polymer structures in solvents could exhibit bidirectional movement (due to shrinkage and swelling), depending on the laser exposure conditions. In higher density laser scanning case, after the development process the polymeric column showed shrinkage behavior in solvents. If the physical dimensions of the structure are known, the mechanical polymer properties could be calculated from the magnitude of glass cantilever's end deflection. Evaluated Young's modulus for the polymeric structure in different mediums gave a result of 0.188 GPa – in PEN, 0.158 GPa in ethanol, and 0.138 GPa in air. Meanwhile, less dense laser scanning algorithm provided a swelling effect for the same size structure, for which cantilever deflection dynamics showed Young's modulus to be 0.467 GPa in PEN and 0.493 GPa in ethanol. These findings indicate that the polymer is sensitive to the outer stimulus of the ambient environment. Moreover, it was experimentally shown that polymeric structures undergo reversible deformations (shrinkage or swelling) when immersed in different solvents. Moreover, the Young's modulus of polymeric structures made out of SZ2080 photopolymer could be varied depending on laser exposure from 0.4 GPa to ∼2 GPa in PEN solvent. Furthermore, the results indicate that stiffness of SZ2080 polymeric structure increases when immersed in organic liquids.

Experimental results show that the Young's modulus in MPP fabricated structures differs by an order of magnitude from typical values (∼1.74 GPa) for bulk SZ2080 polymer hardened by continuous UV radiation [82]. The result in not surprising, as a similar trend was observed in other laser-polymerized photosensitive resin, such as SR499/368 (0.4 GPa vs 2 GPa) [101, 136]. In contrast, H.B. Sun et al. reported much lower stiffness values when a sample is immersed in organic liquid [129,135]. Solvent permeation into the polymer was speculated as one of the possible causes for a drop in the polymer elasticity. In our research, we show that organic solvent increases the polymer stiffness, especially in those cases where the degree of monomer conversion was lower. These contradicting results can be attributed to different polymer type and/or scaling effects.

The polymeric structures made by MPP have reversible deformations, which after a few cycles of interchanged solvents have constant shrinkage/swelling and stiffness (Young's modulus) values. These stable, repeatable results show that it could be successfully embedded in microfluidics channels for chemical sensing applications.

3. 4π EXCITATION IN MPP

In this chapter, we will consider and discuss the limitations of achievable feature size resolution in MPP technology. Alternatively, we propose an integration of 4π excitation in MPP fabrication scheme in order to enhance axial resolution for MPP. We will discuss experimental challenges and benefits against traditional excitation methods. Moreover, we will present a theoretical simulation analysis of the light intensity distribution based on vectorial Debye theory. We have systematically studied axial field distribution influence on many parameters. The measured experimental results of the voxel feature sizes were compared with theoretical ones.

Material related to this chapter is published in [P2, PR3] articles and presented in [6 – 9] conferences.

3.1. Overview of achievable resolution by MPP

MPP polymerization is a powerful tool allowing the fabrication of arbitrary shape three-dimensional microstructures with feature sizes beyond diffraction limited resolution [3, 74]. Typically, this technology allows to achieve the lateral feature resolution of a few hundred of nanometers, however, the axial dimension is at least ~ 3 times larger than the transversal dimension even when using high NA state-of-the-art microscope objectives [9, 142]. As in optical microscopy, the attainable resolution (or resolving power) is limited by diffraction law formulated by Ernst Abbe [143]. The lateral optical resolution is directly proportional to the used wavelength of the light, and inversely dependent on NA of the objective: $d_{xy} = \lambda/2\mathrm{NA}$, while axial resolution is around $d_z = 2\lambda/(\mathrm{NA})^2$. These equations show that the axial dimension will mostly be larger than the lateral one. These principles of optical microscopy are similar, and proportional to the ones valid in direct laser writing.

This focus point anisotropy might be a limiting factor for some applications, e.g., for fabrication of woodpile photonic crystals, where not only the transversal, but also the axial feature size is important. Therefore, a focal spot with 1:1 aspect ratio could significantly enhance the final resolution and functionality of the fabricated structures. In general, to fundamentally overcome this aspect ratio problem, more advanced focusing techniques need to be implemented, such as stimulated emission depletion [142, 144], spatial light modulator [145], or spatiotemporal beam shaping technique [146].

In microscopy, which shares the same focusing principles as MPP, 4π focusing technique can be used for improving the resolution in the axial direction. The 4π excitation principles were firstly pioneered by S. Hell et al. [147–149].

The idea behind the 4π microscopy is to provide the uniform excitation over the complete solid angle of 4π steradians, hence the name. Under such conditions the excitation region is completely spherical. However, even using high NA oil immersion objectives of 1.4, which is very commonly used for direct laser writing, can cover only an aperture angle of 136 deg (1.25π) [147, 150]. Higher possible angle is technically limited by the total internal reflection. In comparison, different NA microscope objectives and their characteristics are listed in Table 3.1. To date, there are commercial objectives with even higher NA [151], which could provide 1.57 of NA, and a full angle of 142 deg. Unfortunately, it has several crucial drawbacks: relatively high cost, the requirement for a non-standard immersion oil ($n = 1.661$), as well as requires refractive index matching coverslips of special glass. However, even focusing objective with 1.57 of NA, the full angle is still far from an ideal illumination of the half-sphere. This leads to the fact that the voxel is elongated along the optical axis.

The ellipsoid-shape focus point could be overcome by using two opposing high NA objectives in such a way that the foci spatially coincide. By using this optical configuration, the effective solid angle could be increased by twofold, which becomes much closer to the ideal 4π excitation. In such a way, the constructive interference at the common focus takes place, leading to the axial resolution being improved several times. In practice, the entire 4π solid angle is not covered, therefore the central peak is also followed by the so-called sidelobes above and below the focal spot for high NA objectives. The lower the NA, the more pronounced this effect becomes, leading to a periodic intensity pattern along the optical axis. Additional optical techniques could be used to suppress the sidelobes, such as non-linear excitation [148, 152]. Similarly, the integration of 4π illumination into the traditional MPP setup could be used to sharpen the spatial light distribution in the focal region, and hence, reduce the axial feature sizes for 3D microstructures made by MPP technology.

Table 3.1: Different microscope objectives and their corresponding semi-angle (α), full-angle values (2α) of the numerical aperture. Higher NA microscope objectives require immersion in a medium of appreciable refractive index (n).

NA	0.1	0.25	0.4	0.8	0.95	1.4	1.49	1.57
n	1	1	1	1	1	1.518	1.518	1.661
α,°	5.7	14.5	23.6	53.1	71.8	67.3	79.0	71.0
2α,°	11.5	29.0	47.2	106.3	143.6	134.5	158.0	142.0

This sidelobe generation of multiple sub-micron layers in MPP was already reported in several articles, it is the so-called interference assisted MPP [153–156]. In this way, the incident laser beam interacts with the reflected beam from the material interface with different refractive index, e.g., glass or silicon. The physical mechanism is identical to 4π excitation, however such multi-layer structures could be generated only in the boundary of different mediums interface.

3.1.1. Theoretical modeling of point spread function

We have modeled a theoretical simulation for the focal intensity distribution of a standard focusing with high NA objective and later, for illumination of 4π excitation. It is important to note that for higher NA objectives paraxial approximation is not valid. In order to calculate the point spread function (PSF) at high NA focusing conditions several effects of the light need to be considered, as apodization function of the objective, depolarization of the light and introduced optical aberrations. Therefore, the vectorial Debye theory [157] has to be applied. Török and Varga derived the mathematical model including stratified mediums [158], which was designed for calculation of PSF in optical microscopy. It takes into account contributions of spherical aberrations due to several interfaces between the objective lens and the focus. The model involves the aforementioned apodization function, which is a property of the used objective. It includes the depolarization effect of the light at the focus point as well. It is important to emphasize that Török and Varga model could also be extended with corrections for different than designed objective parameters: as non-standard coverslip thickness, different refractive-indices of materials. In our theoretical simulation we followed the model with these corrections, which was demonstrated by M.J. Nasse et al. [159].

In our theoretical simulation, it was considered that linearly polarized monochromatic light with a Gaussian distribution is incident into the input entrance of the high NA objective, which converts a planar wavefront into spherical. Thereafter, the convergent light propagates through a stratified material on its path to the sample, as shown in Fig. 3.1(a), which is a very common situation in MPP technique or optical microscopy. In MPP, the incident light typically propagates through air (or immersion oil) ((1) material) n_1, glass coverslip (2) n_2, and is focused in the volume of the polymer (3) n_3. The interfaces between materials are denoted as h_1 and h_2 (see Fig. 3.1(a)). Usually, the microscope objectives are designed to correct the focus point for a certain refractive index and thickness of glass coverslip. In essence, if non-standard glass coverslips are used, the quality of the PSF, in turn, will be affected. Therefore, in order to precisely evaluate the PSF all these conditions should be taken into account.

In general, for single objective illumination, the solution for the electric field vector E at the focus point P in third (3) material could be expressed in a different coordinate system as [147,158,160]:

$$E_p = E_3(u, v, \phi) = (E_{3x}, E_{3y}, E_{3z}), \tag{3.1}$$

while the PSF for a single objective could at the same point be given as follows:

$$\mathrm{PSF}_{single} = |E_p|^2 = |E_{3x} + E_{3y} + E_{3z}|^2. \tag{3.2}$$

The components are defined as:

$$E_{3x} = -iK(I_0^{(3)} + I_2^{(3)} \cos 2\phi), \tag{3.3}$$

$$E_{3y} = -iKI_2^{(3)} \sin 2\phi, \tag{3.4}$$

$$E_{3z} = -2KI_1^{(3)} \cos \phi. \tag{3.5}$$

Here, ϕ denotes the angle between the polarization direction of the incident field and the observation direction. K is a constant, which could be calculated by $K = \pi f l_0/\lambda$, where the objective focal length f, light wavelength λ and amplitude factor l_0. The integrals $I_0^{(3)}$, $I_1^{(3)}$, $I_2^{(3)}$ are defined by:

$$\begin{aligned} I_0^{(3)} = \int_0^\alpha & A(\theta_1) \sin\theta_1 \exp[ik_0\psi](T_s^{(2)} + T_p^{(2)} \cos\theta_3) \\ & \times J_0(k_1 r \sin\theta_1) \exp(ik_3 z \cos\theta_3) \mathrm{d}\theta_1, \end{aligned} \tag{3.6}$$

$$\begin{aligned} I_1^{(3)} = \int_0^\alpha & A(\theta_1) \sin\theta_1 \exp[ik_0\psi] T_p^{(2)} \sin\theta_3 \\ & \times J_1(k_1 r \sin\theta_1) \exp(ik_3 z \cos\theta_3) \mathrm{d}\theta_1, \end{aligned} \tag{3.7}$$

$$\begin{aligned} I_2^{(3)} = \int_0^\alpha & A(\theta_1) \sin\theta_1 \exp[ik_0\psi](T_s^{(2)} - T_p^{(2)} \cos\theta_3) \\ & \times J_2(k_1 r \sin\theta_1) \exp(ik_3 z \cos\theta_3) \mathrm{d}\theta_1, \end{aligned} \tag{3.8}$$

where α is the aperture angle ($\mathrm{NA} = n_1 \sin\alpha$), r - the radial distance, wave vector in the different media is given as $k_3 = k_0 n_3 = 2\pi n_3/\lambda_0$, λ_0 - the wavelength in vacuum and n - the refractive index of the medium. J_0, J_1, J_2 are the Bessel functions of the first kind, and ψ stands for the aberration function. $A(\theta_1)$ - describes apodization function, which satisfies the sine condition. The terms T_s and T_p are transmission coefficients through stratified media for s- and p-polarized light, respectively. The angles $\theta_1, \theta_2, \theta_3$ are linked by Snell's law as shown in Fig. 3.1(a). ψ and $A(\theta_1)$ terms could be given as follows:

$$\psi = h_2 n_3 \cos\theta_3 - h_1 n_1 \cos\theta_1 + (h_1 - h_2) n_2 \cos\theta_2; \tag{3.9}$$

$$A(\theta_1) = \exp\left[-{\beta_G}^2 \frac{\sin^2\theta_1}{\sin^2\alpha}\right] \sqrt{\cos\theta_1}. \tag{3.10}$$

Here, the term β_G refers to the filling ratio of the objective aperture radius to the beam waist radius. α corresponds to marginal ray angle of microscope objective. In this theoretical model, we kept that the input aperture of the objective is completely covered ($\beta_G = 1$). The transmission coefficient $T_{s,p}$ for a three-layer mediums could be obtained as follows:

$$T_{s,p} = \frac{t_{12s,p} t_{23s,p} \exp(i\beta)}{1 + r_{12s,p} r_{23s,p} \exp(2i\beta)}, \tag{3.11}$$

where $\beta = k_2|h_2 - h_1| \cos\theta_1$. The Fresnel coefficients for reflection r and transmission t from i to j medium could be expressed as:

$$t_{ij,s} = \frac{2n_i \cos\theta_i}{n_i \cos\theta_i + n_j \cos\theta_j}, \tag{3.12}$$

$$t_{ij,p} = \frac{2n_i \cos\theta_i}{n_j \cos\theta_i + n_i \cos\theta_j}, \tag{3.13}$$

$$r_{ij,s} = \frac{n_i \cos\theta_i - n_j \cos\theta_j}{n_i \cos\theta_i + n_j \cos\theta_j}, \tag{3.14}$$

$$r_{ij,p} = \frac{n_j \cos\theta_i - n_i \cos\theta_j}{n_j \cos\theta_i + n_i \cos\theta_j}. \tag{3.15}$$

In a 4π focusing case, the final PSF could be expressed as a superposition of electric field components of both objectives [94]:

$$\mathrm{PSF}_{4Pi} = |E_{4Pi}(u, v, \phi)|^2 = |E_1(u, v, \phi) + E_2(-u, v, \phi)|^2, \tag{3.16}$$

where E_1 and E_2 are the electric fields generated by the illumination from the first and second objectives, respectively.

The theoretical modeling of PSF's were done using the aforementioned equations under different parameters. To keep the model simple, it was considered that the laser light propagates through three different media under the same conditions for both objectives. Firstly, each laser beam travels through air ($n = 1$ for 0.4 or 0.8 NA objectives; alternatively, immersion oil with $n = 1.518$ for 1.4 NA), then through 165 µm thick glass coverslip ($n = 1.5071$), and is focused 5 µm below the glass interface into SZ2080 pre-polymer ($n = 1.504$). The results of the theoretical analysis of the light intensity distribution at the focal region under different illumination conditions are shown in Fig. 3.1 (b-i). Fig. 3.1 (b) show the results of intensity distribution calculations when laser ($\lambda = 1030$ nm) irradiation is focused by 0.8 NA single objective, while Fig. 3.1 (c) illustrates 4π excitation under the same conditions. In the latter case, the voxel shows a similar ellipsoid-shaped distribution, but additionally

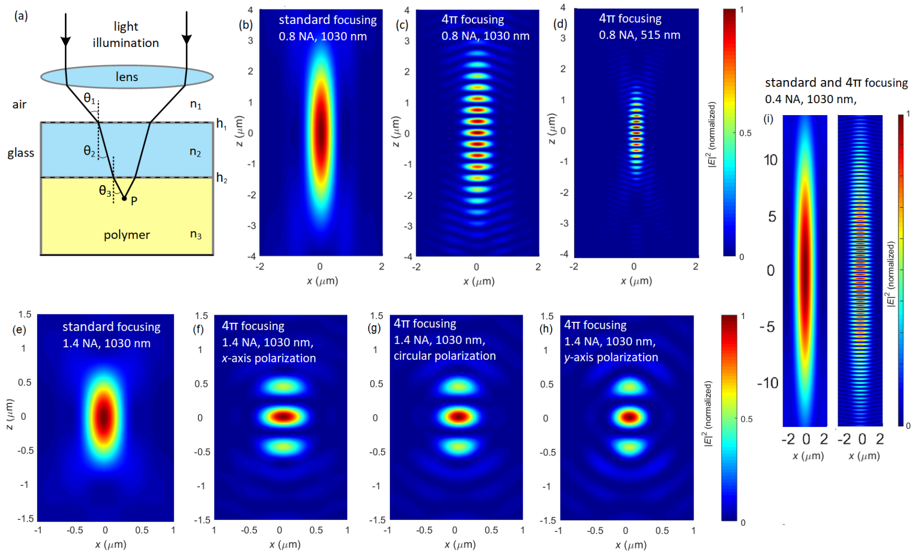

Figure 3.1: (a) A schematic illustration of laser beam propagation through stratified media. Comparison of calculated longitudinal PSF of (b) single 0.8 NA objective, (c) an interfered PSF of 4π excitation with a pair of 0.8 NA with laser wavelength $\lambda = 1030$ nm and (d) 515 nm. The PSF simulations in XZ plane for 1.4 NA objective with (e) standard illumination and 4π illumination for (f) linearly x-axis, (g) circularly and (h) y-axis polarized light. (i) Comparison of calculated PSF for standard and 4π focusing conditions with 0.4 NA.

having an interference pattern of periodic evanescent sidelobes. The distance between the sidelobes is dependent on laser wavelength, refractive index of the material, and slightly on NA of the objectives. For 0.8 NA and $n_3 = 1.504$ the distance of the interference pattern resulted in ~360 nm for the 1030 nm laser wavelength. While 4π excitation using the same conditions and 515 nm laser beam would produce approximately two times smaller voxel, the distance between the sidelobes would be shrunk by twofold to ~180 nm as well (see Fig. 3.1 (d)). For comparison, the modeling was also done for a pair of 0.4 NA objectives and 1030 nm laser wavelength, which would produce an even higher number of sidelobes, as can be seen in Fig. 3.1 (i).

The number of generated sidelobes could be reduced by increasing the NA of the objectives, but even by using 4π excitation with 1.4 NA objectives, the modeling shows a rise of a pair of primary sidelobes with 0.64 intensity of the central peak. The resulted PSF's of standard and 4π illumination are depicted in Fig. 3.1 (e, f). It is needed to emphasize that the polarization of both laser beams has to coincide to obtain an interference pattern in the axial dimension. In contrast, spatial overlapping of two differently polarized beams (i.e., x- and y-axis linearly polarized beams) does not give advantage at all, such a focusing would result in a standard elongated voxel, which could be obtained by a single objective. When linear polarization of two opposed laser beams coincides, then asymmetric distribution is obtained in the lateral voxel dimension, as can be seen in Fig. 3.1 (f, h), while the axial size remains unchanged. In contrast, a circular polarization of both laser beams would give an intermediate voxel size (see Fig. 3.1 (g)) and rotationally symmetric voxel in lateral dimension.

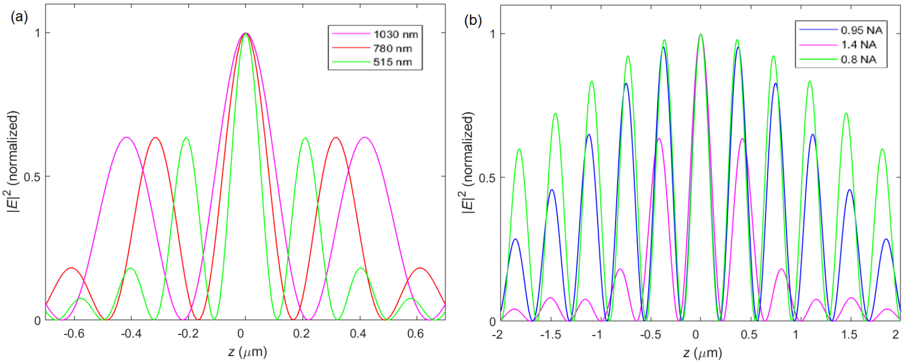

Figure 3.2: (a) Comparison of intensity distribution along the z-axis of focused beam with 4π excitation with a pair of 1.4 NA objectives for different laser wavelengths. Graph (b) depicts periodicity between sidelobes dependence on NA of the used objectives, when the laser wavelength is 1030 nm.

In order to investigate the behavior of the interference pattern regarding the periodicity and intensity of sidelobes in greater detail, it was calculated the theoretical simulations of 4π excitation under different parameters, such as the laser wavelength λ, NA of the objective lens, and N-photon absorption. Firstly, the influence of laser wavelength λ was investigated; the numerical calculations results are shown in Fig. 3.2 (a). Here, the simulation parameters are: NA = 1.4, while the composition of stratified media and focusing depth remained unchanged, as in previous calculations. Three different laser wavelengths λ, corresponding to nowadays commonly used femtosecond laser sources for MPP technique, were chosen: Er doped fiber 2^{nd} harmonic – 780 nm, Yb:KGW fundamental and 2^{nd} harmonic wavelengths – 1030 nm and 515 nm, respectively. The figure shows that the periodicity is linearly dependent on the laser wavelength λ, and corresponded to approximately 420 nm, 320 nm and 210 nm for λ = 1030 nm, 780 nm and 515 nm, accordingly. Noteworthy, the intensity profiles of the generated sidelobes are narrower for shorter wavelengths, accordingly.

It is needed to emphasize that the intensity of the sidelobes is not affected by the laser wavelength, but it strongly depends on the NA of the used objective, as can be seen in Fig. 3.2 (b). In this case, the laser wavelength λ was kept to be 1030 nm, while NA was modeled for several higher values. It can be clearly seen that the number of the sidelobes are higher for lower NA objectives, the comparisons of intensities of sidelobes compared to the central peak are listed in Table 3.3. It was also found that the peak positions of the sidelobes also are slightly dependent on the NA as well, the period in the interference pattern increases with higher NA values. For a fixed 1030 nm laser wavelength, the center-to-center periodicity was approximately 420 nm for 1.4 NA, 370 nm – 0.95 NA, 360 nm – 0.8 NA, respectively.

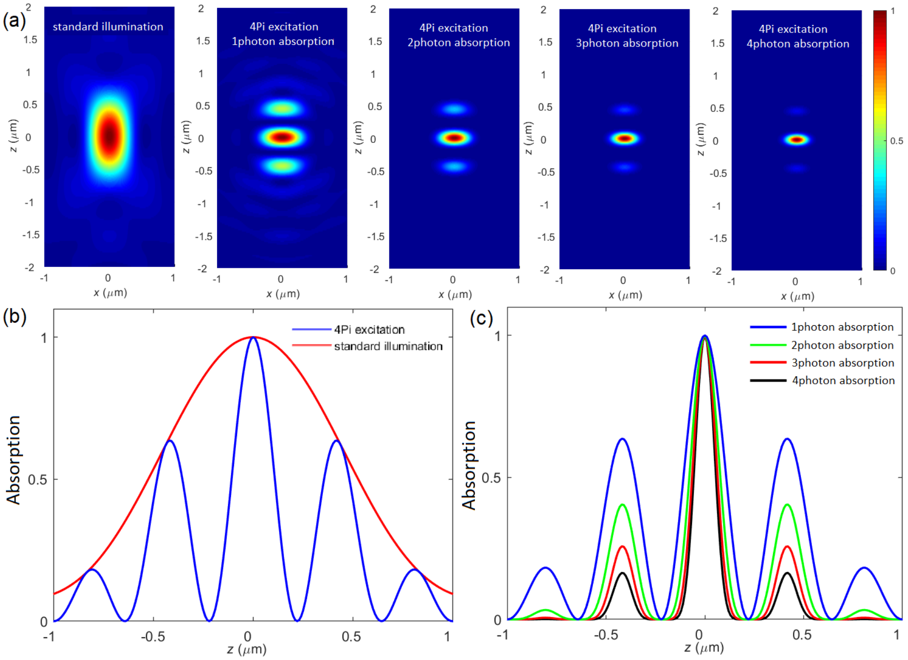

Figure 3.3: (a) Calculated axial PSF's with 1.4 NA and 1030 nm laser wavelength for different illumination conditions. (b) A comparison of intensity distribution along the longitudinal axis for standard illumination with single objective and 4π excitation *via* single-photon absorption. (c) Axial profiles of absorption for one-, two-, three-, and fourth-photon cases, the relative height of lobes' would be 0.64, 0.4, 0.26, 0.16 of the main peak, respectively.

If multiphoton absorption is used for 4π excitation, the intensity of the sidelobes could be effectively suppressed, as can be seen in Fig. 3.3 (a, c). As there is a quadratic dependence on the intensity, two-photon (N=2) absorption would result in narrower and lower intensity profiles of sidelobes peaks. For 1030 nm laser wavelength and NA = 1.4, for two-photon absorption the axial primary sidelobes would have a relative height of 0.4 of the central peak, whereas three- and fourth-photon absorption would produce even lower relative height levels of 0.26 and 0.16, respectively. Thus, in 4π multiphoton absorption case, the axial voxel resolution could be reduced several times. The used parameters for modeling and obtained results are given in the Table 3.2.

However, even by using sharp focusing in 4π excitation for 4-photon absorption will produce relatively high primary sidelobes. In MPP method, it is possible to reduce the laser intensity in such a way, that the polymerization threshold is exceeded only at the central peak, while the intensity of the sidelobes remain below the threshold. As demonstrated further, such conditions lead to the nearly spherical voxel shape. It is worth noting that some background cross-linking might appear at the sidelobe regions even if they are below the polymerization threshold. If the same sidelobe regions are exposed multiple times, the background cross-linking might accumulate and prevent the development of these regions. In such cases the scanning trajectories and exposure parameters have to be selected more carefully. On the other hand, the generation of the sidelobes could be a benefit – the highly periodic interference pattern is difficult to produce using the conventional technique, as the feature sizes of individual planes is far below the excitation wavelength.

Table 3.2: Comparison of the axial resolution for 4π excitation under different laser and focusing parameters: NA of objectives, N-photon absorption, incident laser wavelength λ, center-to-center distance between sidelobes Λ, and ratio of intensity of primary I_1 (prominent secondary I_2 and higher order I_n) sidelobes to the central peak I_0.

NA	Absorption	λ, nm	Λ	I_1/I_0, $I_{2,..,n}/I_0$
1.4	1-photon	1030	420	0.64
	1-photon	780	320	0.64
	1-photon	515	210	0.64
	2-photon	1030	420	0.40
	3-photon	1030	420	0.26
	4-photon	1030	420	0.16
0.95	1-photon	1030	370	0.95, 0.82, 0.65, 0.45, 0.28
0.8	1-photon	1030	360	0.98, 0.92, 0.84, 0.72, 0.6

3.2. Experimental investigation

To experimentally verify the theoretical predictions, we implemented the 4π excitation to the traditional MPP setup. The schematics and realized setup is shown in Fig. 3.4 and Fig. 3.5 (a). A femtosecond Yb:KGW laser system (Pharos, Light Conversion) was employed, with a laser wavelength of 1030 nm, 180 fs pulse duration, and 200 kHz pulse repetition rate. The laser power was precisely controlled by an external motorized attenuator, which consisted of $\lambda/2$ waveplate and a pair of polarizers. Then, the laser beam was split into two equal-intensity beams by a 50:50 beamsplitter. The separated beams were directed into two different optical paths: upper and lower optical arms, as shown in Fig. 3.4. Both beams were guided by dielectric mirrors and focused into the volume of SZ2080 pre-polymer by a pair of two identical (dry-type 20×/0.8 NA; or 63×/1.4 NA oil immersion) objectives. Objectives of the same NA were selected to have the identical voxel size. In 4π excitation the laser beams have to be perfectly overlapped in space and the laser pulses need to coincide in time. For aligning the foci spatially, the fluorescent light anticipated from photoinitiator molecules within the sample was used. It is needed to note that the fluorescence is observed at much lower laser power than needed for polymerization threshold. The fluorescent light originated within the sample was collected through the focusing objective and directed to the tube lens into the charged-coupled device (CCD) camera. A dichroic mirror in front of the camera was used to filter the laser beam from the fluorescence signal. By observing the camera view of the fluorescence emission within the sample, the laser beam path of the upper arm was adjusted accordingly using fine adjustment screws. Then, the laser pulses from both optical arms were overlapped temporally by precisely moving a motorized stage with a pair of mirrors in a delay line. During the temporal and spatial adjustment, the laser intensity was kept at much lower than multiphoton polymerization threshold in the photoresist. A proper spatial and temporal alignment of 1.4 NA objectives gave a rise of almost twofold stronger fluorescence signal, detected by the silicon photodiode.

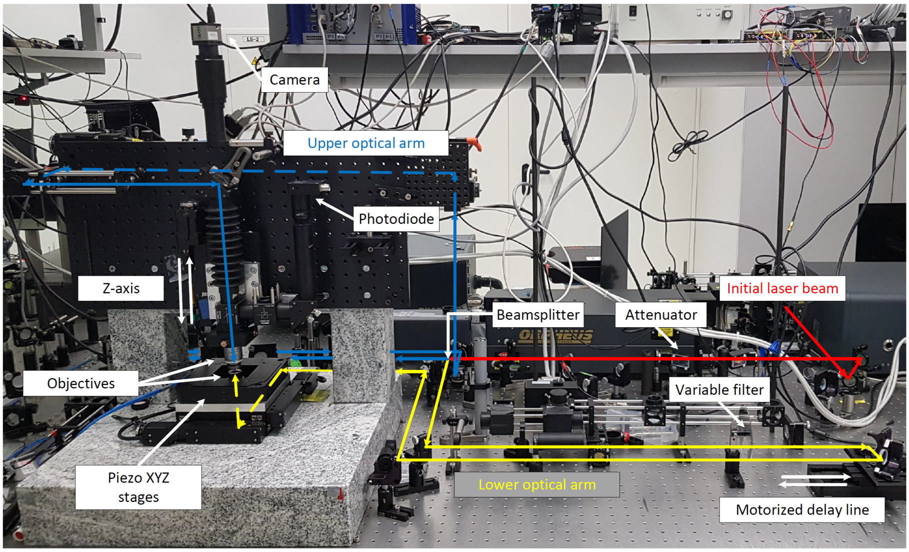

Figure 3.4: The realized experimental setup of multiphoton polymerization with integrated 4π excitation. Initial laser beam (red line) was divided by a 50:50 beamsplitter into equal intensity two beams and directed to the upper (blue line) and lower (yellow line) optical arms.

In MPP technique, typically the laser writing process is done by focusing

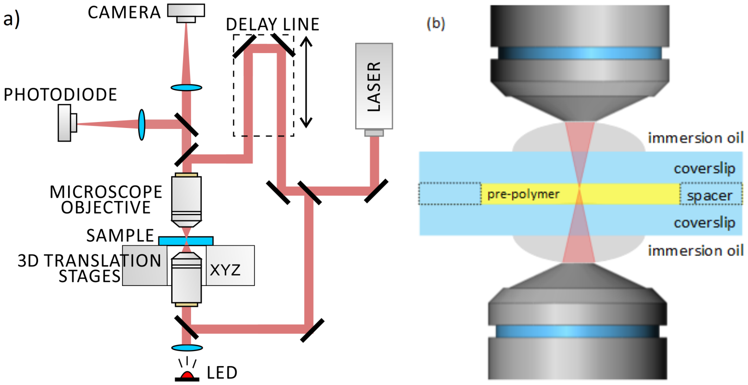

Figure 3.5: (a) Schematic drawing of the experimental setup used for 4π excitation in MPP (4π-MPP) with oil-immersion high NA objectives, (b) more detailed view of the sample with the photopolymer enclosed between two glass coverslips.

the femtosecond laser beam sharply through the glass coverslip into the volume of the polymer. On one had, it is done in order to achieve the desired spatial resolution, the focused laser beam firstly needs to pass through a flat interface of materials in order to avoid wavefront distortions. On the other hand, commonly used microscope objectives are designed to be aberration-free for focusing through a certain (e.g., 170 µm) thickness glass coverslip. Therefore, in 4π-excitation case, the polymer should be enclosed between two glass coverslips, as illustrated in Fig. 3.5 (b). Due to finite working distances of high NA objectives, the polymer thickness has to be limited and preferably be less than one hundred microns. Also, a constant resist thickness needs to be assured over the working field of the intended structure, otherwise the laser foci could be misaligned in space and/or pulses mismatch in time due to the change in the length of optical path. For these aforementioned reasons, it was manufactured a finite spacer from fused silica substrate by selective laser etching technique. A U-shaped structure was fabricated from 250 µm thickness glass substrate by using SLE parameters written in Section 2.4. Subsequently, the glass substrate was completely etched in 5% (v/v) HF. Moreover, the thickness of the part was reduced to 100 µm, leaving the structure for more time in acid, which etches fused silica at a fixed rate, as listed in Table 2.1.

The 4π experiments were performed with a negative tone resin SZ2080 [161] with 0.5% of 4,4'-bis(diethylamino)benzophenone photoinitiator [162]. This polymer has a refractive index of around 1.5 at 632.8 nm [86]. The polymer was drop-casted on a standard glass coverslip with a thickness of 170 µm. Then, the samples were prebaked on a hot-plate with temperature short ramps 40°C, 70°C, and kept at 90°C for 1 hour. During the heating step, a U-shaped 100-µm-thick glass spacer was put on the coverslip to ensure even polymer thickness.

Finally, this structure was enclosed with a second 170-µm-thick glass coverslip on top. After that, the laser irradiation samples were immersed into a PEN developer bath for 1 hour to wash out the laser unexposed material. Later, the samples were submerged into pure ethanol and developed with a critical point dryer. For inspection with SEM the samples were coated with 5-10 nm thick gold layer *via* sputter-coating. For direct laser writing, the sample positioning was achieved by piezo XYZ motion stages (P-563 PIMars, Physic Instrumente). During the structure fabrication, the samples were translated at a 50 µm/s velocity.

For the fabrication process, the "sandwich" type sample was placed and fixed on top of piezo stages surface. The distance between the specimen and the lower objective had to be precisely chosen so that the focal point fit into the volume of enclosed pre-polymer between glass coverslips. While the position of the upper objective, hence the focus point, was adjusted with an additional motorized Z-axis. When both beams were overlapped, the 4π-MPP experiments were done by translating the sample by piezo stages with respect to the laser focus point.

3.2.1. Challenges of 4π-MPP technique

In practice, the 4π excitation arrangement is complicated and the alignment process is technically challenging. For proper experimental conditions a number of parameters need to be adjusted carefully in order to perform successful experiment. The 4π geometry system could be considered as an optical interferometer [163], which requires to ensure the distances fixed with sub-wavelength positioning of the laser beam foci for focusing with high NA objectives. Moreover, the 4π arrangement preferentially requires high NA objectives, thus the maximum height of the fabricated structures is limited by the free working distance of the objectives, which in 1.4 NA objective case is around 150 µm. Last, but not least, 4π excitation of two opposed microscope objectives with sharply-focused laser beams creates a danger of damaging the front surfaces of the lenses, therefore, the alignment require very careful control.

In order to achieve 4π excitation several conditions have to be completely fulfilled. Firstly, the laser power needs to be precisely equalized for upper and lower optical arms so that the intensity at both focal points are identical. It was done by measuring the average laser power just before the input entrance of the objectives and manually rotating the position of variable neutral density filter in the lower optical path. Then, the structures for resolution tests were experimentally fabricated by making suspended fibers between two supporting non-deformable blocks, as shown in the computer-aided design (CAD) model in Fig. 3.6 (a). A set of lines was written by increasing the laser power for each of the lines, starting from below polymerization threshold till moderate intensities, resulting in rigid structures. Afterward, the fabricated structures

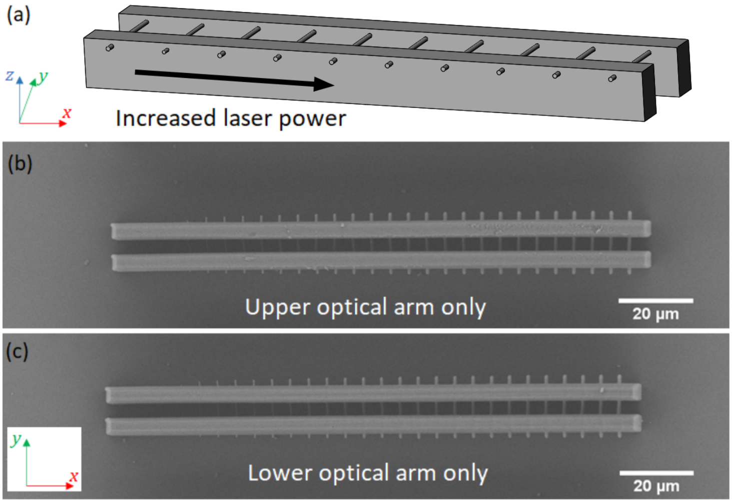

Figure 3.6: (a) CAD model design of the structures for the power calibration tests: two supporting blocks and a series of suspended lines with incrementally increased laser power for each of them. Top-view SEM images of the fabricated structure with objective from the (b) lower, (c) upper optical arm only.

were developed in solvent, dried *via* CPD and inspected under SEM. If the number of suspended lines conforms in both of the optical arms, then the laser power was kept being calibrated (see Fig. 3.6 (b-c)). This step allowed to minimize the differences between the objectives and optical paths possibly resulting from incomplete laser beam filling of input entrance objective, different age or production batch of the microscope objectives.

Then, the laser average power is calibrated in both optical arms, the same 3D structures with multiple suspended lines can be performed simultaneously with 4π excitation. In order to realize this, not only precise spatial overlapping of the two laser foci needs to be done but also the pulses have to coincide perfectly in time. As the length of each optical path was around 3 meters, an overlapping of the pulses at tight focusing (high NA) is not a trivial task. In addition, a set of different transmitted optical elements introduce a significant change in optical length. The temporal alignment was done by using a motorized delay line in a lower optical arm. By detecting fluorescence signal from foci plane, the signal was detected by a sensitive photodetector. A proper temporal alignment of both pulses gave an increase of fluorescence signal, which was tested under several focusing conditions. The 4π excitation with lower NA objectives had lower intensity change, approximately up to 70% and 30% increase for a pair of 0.8 and 0.4 NA objectives, respectively. Noteworthy, due to the photobleaching effect of the polymer the fluorescence signal was consistently weakening in time, therefore during the adjustment the piezo stages were translated in XY plane using a raster scanning technique.

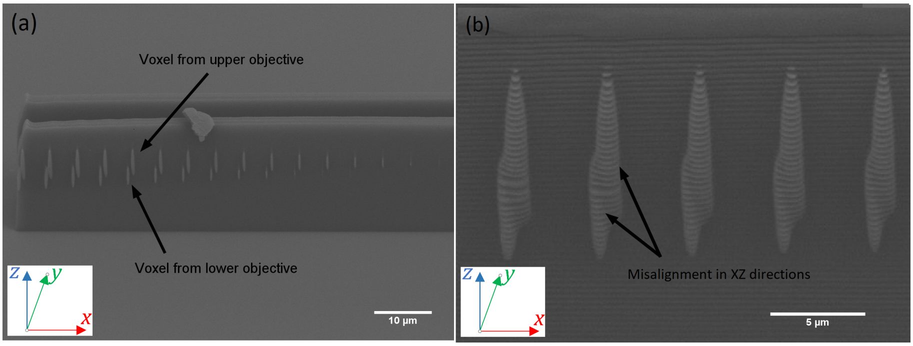

Figure 3.7: SEM images of the structures revealing the examples of misalignment issues for the 4π excitation with two different foci: (a) spatial and temporal misplacement, (b) spatial misalignment in XZ coordinates, as temporal matching of pulses produce a formation of the interference pattern along optical axis.

The first experiments of 4π-MPP showed the complexity of temporal and spatial alignment process. In general, several different types of errors can be obtained: (1) non-equal intensity of laser beams, (2) spatial misplacement in at least one axis, (3) mismatch of the laser pulses in time. Fig. 3.7 (a-b) shows SEM images of a few possible misalignment examples. If one (or more) of aforementioned conditions is not fulfilled completely, the obtained results do not provide the proper intensity distribution at the focus point. At appropriate temporal alignment of the pulses, it was found that the theoretically predicted interference pattern of sidelobes remains in the structures' sidewall, as can be seen in Fig. 3.7 (b).

3.2.2. Experimental results

4π excitation with lower NA objectives

A structure with suspended lines were fabricated with illumination from both objectives (20×/0.8 NA) to the same local focus point, under two different conditions: when (1) the pulses were temporally overlapped and (2) separated in time. In the latter case, in order to separate the pulses in time an optical window of BK7 material with anti-reflection coatings (losses up to 1%) was placed in the path of the lower optical arm. This substrate of 1 mm thick glass introduced a delay of 1.69 ps between the counter-propagating laser pulses. A comparison of the structures fabricated with 4π excitation by temporally separating and matching pulses in time are shown in Fig. 3.8 (a-b), respectively. Each line was fabricated with an incrementally increased laser average power. From the number of polymerized lines it can be seen that the polymerization threshold for MPP process was much lower when pulses from both optical

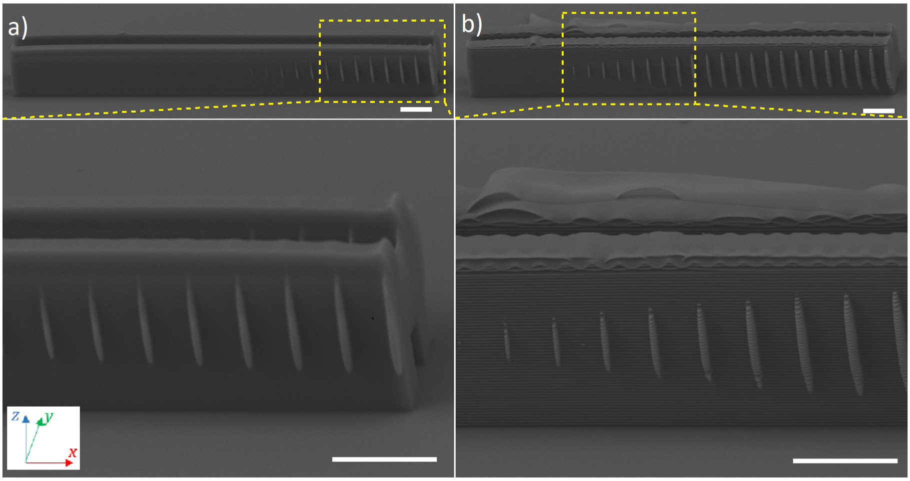

Figure 3.8: Tilted SEM images of the structures fabricated with 4π excitation by temporally (a) separating and (b) matching the pulses in time. A set of suspended lines were written with an incrementally increased laser average power for each line. The polymerization threshold was observed to be much lower for the lines, which were written with temporal overlapping. Scale bar, 10 µm.

arms overlap in time. Moreover, a clear interference pattern along optical axis was observed, as shown in Fig. 3.8 (b). It can be seen that individual voxels are layered from multiple planes with sub-micron scale. Interestingly, the supporting block consisted of a continuous periodic pattern without defects until the top section, where several layers were wavy and even peeled off. The reduced MPP threshold show that the focus intensity is increased through the interference of counter-propagating laser beams.

Afterwards, for an easier axial feature characterization of the structure done by 4π-MPP, a series of individual pillars ($5\times5\times25$ µm^3) were fabricated using 0.8 NA objectives by a raster scanning. The used laser power was set to 0.6 mW for a single objective. Fig. 3.9 (a) shows a schematic construction of a pillar structure by using 4π-MPP technique. The resulting voxels consisted of periodic planes oriented along the optical axis due to the interference of counter-propagating beams. Each pillar was fabricated by overlapping the voxels transversely with a hatching step of 0.5 µm, while axial separation between the adjacent layers was 4.5 µm. Even after the development process, the structures with sub-micron thickness planes remained, as can be seen in Fig. 3.9 (b-c). The distance between these planes was ~340 nm, which is in a close agreement with the numerical modeling. The theoretically predicted value was ~5% (360 nm) higher than experimental, which could be presumably related to the shrinkage of the polymer or a slightly different refractive index than used in calculations.

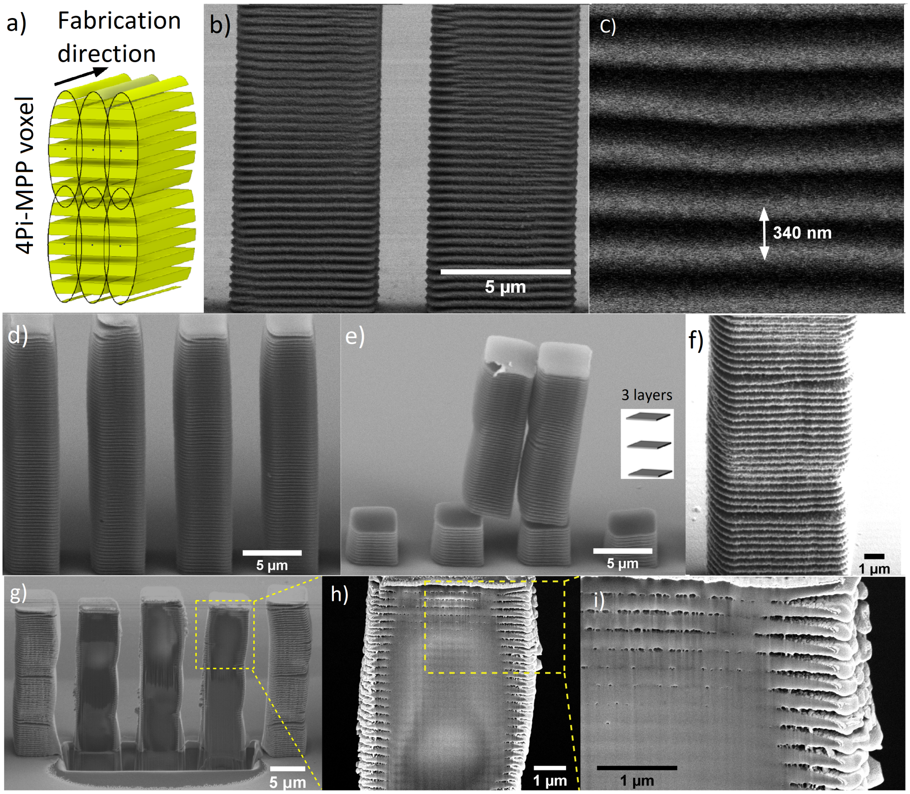

Figure 3.9: (a) Principle sketch of the micropillar structure fabrication using 4π-MPP excitation, and (b-c) side-view SEM images of fabricated by using 4π-MPP excitation. An interference pattern was obtained with a period of around 340 nm. The interference pattern remained (g) even under very tight (1 µm) spacing between the layers, while (e-f) large spacing (7 µm) resulted in sections polymerized at lower degree of conversion, which is prone to detach. (g-i) Cross-section of FIB-milled micropillar structure revealing the interior morphology.

To investigate the interference pattern in more detail, a series of pillars were created in the same raster scanning manner by changing the separation between the adjacent layers S_z (i.e., spacing). Each structure was fabricated with a fixed slicing between 1 and 10 µm. The parameter S_z was incrementally increased by 0.1 µm for the subsequent pillar. Noteworthy, the overall height of structure remained similar by reducing the number of layers. The experiments were done using the same conditions, as in the previous paragraph. The findings showed that a regular interference pattern of periodic polymerized planes remained even with a dense scanning pattern ($S_z = 1$ µm), as shown in Fig. 3.9 (d). In this case, the voxel axial dimension v_z (10 µm) was 10× larger than the slicing step (v_z/S_z=10). In a less dense scanning case ($v_z/S_z \sim 1.4$), the interference pattern was polymerized at lower degree of monomer conversion, eventually resulting in subdivision into several parts (see in Fig. 3.9 (e-f)). This interference pattern was investigated in more detail to understand the interior morphology of the structure.

The obtained structures were partly milled by focused-ion beam (FIB) to reveal the core of the micropillars structure, as depicted in Fig. 3.9 (g-i). The cross-section showed a non-uniform structure. The exterior section consisted of the interference pattern of alternating air/polymer planes, which was seen in a thin superficial layer around the micropillar structure. Towards the core, the air-gap layers turn to lower density zones of the polymer. The center section was polymerized at higher degree of conversion in cross-linking, but still the interference pattern of different density polymer zones is clearly visible. Most likely, the solvent could not effectively penetrate and wash out the zones polymerized at lower degree of monomer conversion. From the practical point of view, it would be preferable to have even alternating planes with higher refractive index change between the adjacent layers (e.g., air/polymer). However, the material and solvent need to be optimized if wider multilayered structures are required.

In addition, it was observed that the gaps between the interference planes of narrow microstructures could be completely washed out. This could be applied to the narrow structures suspended between additional supports, which allow to maintain the order of the inter-layers and avoid collapse between each polymerized plane. This idea has been tested by manufacturing a structure (see Fig. 3.10 (a)) as a demonstration of structural coloration [153]. The overall size of the structure was 150×75 µm^2, composed of 4 µm width and 75 µm length periodic rectangular supports that were spaced with gaps of 4 µm distance. A series of narrow parallel suspended polymerized lines were fabricated by a single laser scan between the supporting blocks using the 4π-MPP method. The support structures were fabricated with a single objective only. The applied concept would result in a stack of thin suspended polymeric planes with well-defined air cavities in between. Multiple alternation of periodic sub-micron features provide a Bragg reflection, which causes the coloration effect. The reflected wavelength of the light could be calculated through Bragg's equation. In the case the incident light is perpendicular to the periodic structure, the relation could be expressed as [153, 164]:

$$m\lambda = 2(n_1 d_1 + n_2 d_2), \tag{3.17}$$

where m is the order of reflection, d_1, d_2 denotes the thickness and refractive index n_1, n_2 for each material layer, respectively.

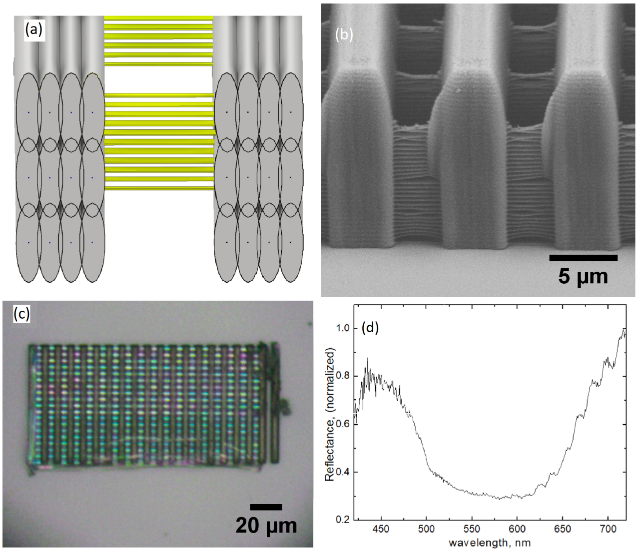

Figure 3.10: (a) A sketch of the structure fabrication scheme, (b) a 60° degree-tilted-view SEM image of the grating structure, (c) structural colors visible by an optical microscope in reflection mode, resulting from the periodic features in the fabricated lines and (d) the measured reflectance spectrum.

After the development, the structure was analyzed under an optical microscope in reflection mode. Coloration was observed in the purple/blue/green light spectrum range, as demonstrated in Fig. 3.10 (c). SEM inspection of the structure showed multiple polymeric layers along the optical axis, each of them was approximately 180 nm, while the air-gap was around 160 nm of thickness. According to Eq. 3.17, such alternation between air and polymer (n=1.504) multi-layers would produce a reflection at 860 nm in near-infrared range, while the second order of reflection would result in the blue spectrum range. The spectrometer measurements of the reflection showed similar results with peaks at 440 nm and in near IR range (see Fig. 3.10 (d)), which was limited by the wavelength range of the detector. The observed broad spectrum of coloration happened due to slightly uneven distance between alternating layers caused by the development process (see Fig. 3.10 (b)). Moreover, the number of planes and the thicknesses of the polymer/air layers depends on the applied laser average power. Since the periodicity of the planes is directly proportional to the wavelength, the 4π-MPP experiments using shorter wavelengths would reduce the distance between the polymerized planes. For instance, in our case a frequency doubled wavelength (515 nm) would reduce it by twofold. In such case we expect the reflectance in the visible spectral range to be even stronger, as it would be caused by the first reflection order. However, we could not test it experimentally, as the current laser system setup was limited for optics in infrared only.

Alternatively, the generation of interference pattern in the structures fabricated by MPP could be obtained by interference assisted MPP [153–156]. In general, this light interaction is similar to 4π excitation, nonetheless, such multi-layer structures could be generated only near the boundary of the polymer and other material with relatively high difference in refractive index.

4π excitation with higher NA objectives

The subsequent experiments were carried out with 1.4 NA objectives in order to improve the feature size in axial dimension and reduce the voxel aspect ratio using 4π excitation. According to the numerical calculations, it was expected that the higher NA objectives significantly reduce the number of generated sidelobes. Then, it was expected that under appropriate conditions only the main peak will exceed the polymerization threshold. The feature resolution tests were done by fabricating a series of pillars and a set of suspended lines between them. Each line was written with an incrementally decreasing the laser average power.

At higher excitation power, the obtained suspended lines consisted of several sidelobes along the optical axis. The measured periodicity between the sidelobes Λ was 410 nm, while the numerical calculations predicted the result of 420 nm for 1030 nm laser wavelength and 1.4 NA objectives (see Table 3.2). An incremental attenuation of the laser average power for each suspended line gradually reduced the number of sidelobes. Eventually, at 40 µW average laser power, it was achieved the condition, when the polymerization threshold was exceeded only at the central peak. SEM images revealed that the axial size of the voxels was 150 nm while the lateral feature size was 200 nm (see Fig. 3.11 (a)). In this way, the longitudinal feature size was improved to be lower than the transversal dimension. The aspect ratio was decreased towards 1:0.75. It is worth noting that we considered only the suspended lines, which had survived the developing process and were still hanging between the supporting pillars. Some torn lines showed even better results, axial feature size was down to even 110 nm. In comparison, focusing with a single objective resulted in 200 nm lateral and 450 nm axial feature sizes of the suspended lines, while using 4π excitation, but separating the pulses in time, gave the best result

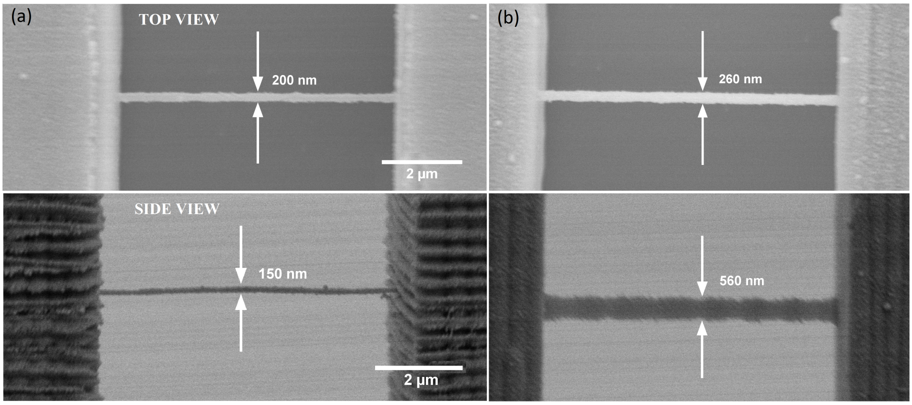

Figure 3.11: Top- and side-view SEM images of the voxel feature sizes fabricated with 4π excitation, then temporally (a) the laser pulses coincide and (b) are separated in time by introducing additional delay to one of the pulses.

of 260 nm and 560 nm feature resolution (see Fig. 3.11 (b)), respectively.

Similarly to 4π, STED inspired MPP also allows the enhancement of resolution [99, 165]. It was shown that the axial feature sizes could be decreased down to $\lambda/20$ [99]. However, in contrast to 4π-MPP, it supports a very limited amount of suitable photoinitiators and requires special spatial beam profiles [142]. Both, STED-MPP and 4π-MPP require precise alignment of two lasers beams, which is not a trivial task in both cases. Moreover, in principle these two techniques can be combined together, resulting in a STED with 4π excitation (as demonstrated in advanced microscopy setups [95]).

Compared to the traditional MPP, the 4π arrangement is a more complex technique, requiring a very precise adjustment of both beams in space and time. In principle, the foci matching can also be slightly deteriorated by the already exposed regions, especially if the refractive index change after the exposition is high or the exposed regions are long (i.e., having large differences in the optical path), however under our experimental conditions we did not observe any strong influence of this effect. In order to solve these issues and broaden the applicability for 3D structure fabrication of 4π-MPP technique, the alignment procedure could be automated by using piezo or similar positioners and a feedback loop from the fluorescence signal.

3.3. Conclusions

In conclusion, we have reported for the first time (to the best of our knowledge) the implementation of 4π excitation in multiphoton polymerization technique. The theoretical modeling was done revealing the generation of interference pattern along the optical axis, which depends on the laser, multiphoton absorption, focusing parameters and the polymer material. Experimental results showed that highly sub-micrometer periodic pattern of polymerized planes remains in the fabricated structures by 4π focusing in even a single scanned line. Moreover, in thin structures, the polymerized regions at lower degree of monomer conversion could be successfully washed out resulting in alternating air/polymer layers, which could produce a coloration effect due to multi-layer interference. The used infrared laser light generally defines the period between the alternating layers, and had an effective reflection in infrared light. These experimental findings might have a practical application for generation of controllable structural color.

Using high numerical aperture objectives in 4π excitation could lead to the improvement of the axial resolution. It was showed that by using a pair of 1.4 NA objectives in 4π-MPP, the number of generated sidelobes could be kept below polymerization threshold, resulting in an improved voxel feature size. In comparison to the standard focusing with a single objective, the axial feature size was enhanced by approximately 3 times down to 150 nm, while the lateral resolution was 200 nm. In this way, the resulting aspect ratio was 1:0.75. In practice, by implementing the automated alignment procedure, we assume that the 4π-MPP could be used to provide an improved diffraction limited voxel for 3D nanofabrication.

4. DYNAMIC VOXEL TUNING IN MPP

In this chapter, we will consider and discuss what are the current ways to enhance the MPP fabrication throughput and how the process speed could be improved. As an alternative to known techniques, we propose a novel method, and present the results on implementing the dynamic voxel control for traditional MPP system by using a motorized beam expander. In this way, the voxel could be expanded in the lateral and the axial directions without changing the objective. In addition, we present the theoretical simulation analysis of the light intensity distribution for different objective's underfilling conditions, as well as the measured experimental results of the voxel feature sizes for high numerical aperture objectives.

Material related to this chapter is published in [P3] article and presented in [10] conference.

4.1. Overview of approaches for enhancement of the MPP throughput

MPP allows the fabrication of complex shape 3D microstructures with the feature sizes beyond sub-diffraction limited resolution. However, apart of versatility of technological capabilities, the major drawback of MPP technology is its relatively low throughput using high numerical aperture objectives. In additive manufacturing, the common principle is to hatch a 3D object into multiple separate lines on each of the planes and stack up into layers. The voxel spacing parameters have to be selected more carefully so that each individual voxel overlaps onto the previous one. Usually, larger voxels are selected for bulky structures that require less precision, while critical microscopic features need to be done with smaller voxels. Under tight focusing conditions, the typical layer-by-layer processing method of the mm-size structure fabrication with high resolution features would require an unreasonable and impractical laser processing time. For instance, in traditional MPP system under tight focusing conditions the fabrication of a 1 mm^3 cube would take more than 100 days [13].

Nonetheless, there are multiple ways to increase the writing speed and shorten the process time. For instance, the processing speed could be improved by using alternation of different numerical aperture objectives [166], shaped laser beams (e.g., Bessel [167] or ring-Airy [168]), multiple laser beam focus by diffractive optical elements [169] or spatial light modulator [169, 170], advanced holographic light shaping [171], interference-lithography [172], voxel control by spatiotemporal focusing [146], scanning with synchronized linear stages and galvanoscanner mirrors [173]. Throughput could also be improved by different scanning approaches, as fabrication of the superficial layer (shell) of the structure and subsequent ultraviolet exposure [174], or applying adaptive stitching algorithms [175]. These methods will be discussed in the following paragraphs in more detail.

Simultaneous spatial and temporal focusing technique has been applied in DLW applications for writing in the glasses [176] and polymers [146]. The technique separates the spectral components of the laser pulse spatially by a pair of parallel chirped gratings (or optical prisms), and then all the components are recombined together at the focus of the objective. This method does not experience non-linear effects as the pulse is broadened, therefore the peak intensity remains low in all the optical path until the objective. As all the spectral components are reassembled only at the geometrical focus of the objective, at this point it leads to the shortest pulse duration and highest peak intensity. Interestingly, this method provides almost spherical voxel using a relatively low NA objective. This technique was successfully implemented for MPP with 0.35 NA objective [146], providing isotropic voxels, which could be linearly tunable from ∼10 to 40 µm depending on the exposure dose. The uniform scaling effect was produced by changing the incident laser power. It was shown that as large as ∼1.3 centimeter-height complex structures with small features could be successfully written by MPP technique. However, simultaneous spatial and temporal focusing method suffers from sophisticated tuning, adds extra complexity and cost to the traditional MPP system.

The traditional MPP technique process could be speeded up multiple times by parallel laser beam microprocessing. This approach could be enabled by diffractive optical elements (DOE), spatial light modulator (SLM), digital micromirror device (DMD). The DOE is a passive optical element with microstructured relief on one of the surfaces, which transforms the incident laser beam into fixed particular intensity distribution by amplitude or phase modulation. In such a manner, the DOE could shape the laser beam and work as a 1D or 2D beamsplitter, beamshaper, multifocal element, axicon, etc. [177] The elements are usually made out of glass (e.g., fused silica), therefore, they are suitable for high laser power application, which could make them a perfect candidate for industrial microprocessing application. Nonetheless, this method also has several drawbacks, as it is a passive, relatively expensive element, the focusing parameters are not tunable and changeable (e.g., periodicity is constant), which limits the flexibility and applicability to only one specific task. Alternatively, the single beam could be transformed into multi-foci pattern by active elements matrix, such as liquid crystal microdisplays (SLM) [170, 178]. In this case, the high density matrix consists of tiny pixels (e.g., <4 µm) [179], which provide smooth light modulation. The beam is expanded to cover all the active pixels. The desired structure is converted into a computer generated hologram and is transferred to SLM, which is set at some specific angle. The beam wavefront is modulated and reflected back. Typically, the first order of diffraction is selected due to high diffraction efficiency, while zeroth and higher orders are filtered off by spatial filters. SLM device provides multi-foci parallel processing. In general, a hundred of foci could be realized, however, the laser power should be sufficient for each focus to induce the modification in the material. Typically, SLM provides a phase modulation over 0-2π interval. Besides, this device could also pre-compensate and take into account spherical aberrations, which might be important due to several materials interface and deep focusing depth. Though the method allows to have multiple parallel foci, however, the refresh rate of most SLM devices is limited to 60 Hz at the maximum, what could make the writing process slow. Certainly, the movements could be used by (or in combination with) linear stages, still the refresh rate might be a limiting factor for some of applications. Moreover, the use of SLM requires an optimization process for new structures, which might be impractical solution if the design consistently changes. Lastly, the SLM is made of liquid crystals, which could be unsuitable for higher laser power application due to low damage threshold.

Alternatively, DMD can be moved at a much higher frequency of 22.7 kHz [180]. In this case, the two-dimensional matrix consists of deformable micro mirrors, which are actuated by electrostatic forces. Each of individual micromirrors have two states, which could be set to off and on. The former state means that the mirrors are deflected at the marginal angle, therefore, the light is reflected to the blocking device, while the "switch on" state deflects the light along to the desired optical path. In comparison to SLM, DMD device has a better contrast, however, due to switching between the states the laser power losses are more higher [9, 178].

Various different engineering methods could be used for DLW process [9, 173]. The first MPP systems had an ability to move the sample by XYZ stages or scan the focused laser beam through galvanoscanner mirrors. MPP technique could provide structures with the feature resolution of a few hundred nanometers, therefore, the stages and galvanoscanner must meet ultra-precision and accuracy requirements. The sample could be moved by precise XYZ piezo stages, which have a typical repeatability in the range of several nm, but these stages lack speed (usually <1 mm/s or lower) and have very limited travel range (typically $<300\times300\times300$ µm^3). Alternatively, there are linear stages, which have 10 centimeters travel range and the typical writing speed could be as fast as several of mm/s. The repeatability is worse (e.g., <50 nm), but still is fully sufficient for MPP process. Also, the linear stages, because of the mass, have huge inertia, which limits their usage for fast microfabrication of complicated microstructures. Another approach is to combine movements of galvanoscanners mirrors and linear stages, which solves precision and speed fabrication problems. The galvanometric scanners are very light and have low-inertia elements, therefore their rotation motion could steer the laser beam in XY directions at a speed of hundreds of mm/s (depending on objective lens). However, the working distance is limited by the field of view of the objective, which could be as small as $\sim 140 \times 140\ \mu m^2$ for 1.4 NA, which is very common for MPP application. Usually, the structure is processed in 2D with galvanoscanner mirrors only within the objective's field of view. If the structure dimensions are larger than the field of view, then the overall structure is divided into several individual fields (tiles). Then, after the fabrication of one field, the XY stages jump consecutively to the following ones till all the structure is done. However, this method has a major drawback – stitches, i.e., error points between the two adjacent fields. These stitches could be a crucial factor and highly undesired for most of the precision requiring applications, i.e., microoptics. As an alternative, there is a much better way to move XYZ linear stages synchronized with galvanometer mirrors, at the same time [173, 181]. This method provides stitchless and fast microfabrication. This method also reduces the acceleration and deceleration effects to the projected trajectory path, assuring relatively smooth speed over the entire working field. At the start of fabrication, the movements are done with fast low-inertia galvanoscanner mirrors, meanwhile the linear stages are being accelerated to reach the projected writing speed. Thereafter, the writing process is continued with the linear stages only.

Another approach for faster MPP fabrication could be using multi-beam interference lithography [172, 182]. This method allows to obtain mainly 2D periodic pattern with micron or even sub-micron feature resolution. The multi-beam interference lithography has several advantages over the usual DLW techniques. It is a one-step process, when the desired periodic patterns are generated with a single static exposure procedure. Additionally, the technique gives ability to precisely form the pattern over a large working area of photoresist. The working principle is based on interference phenomenon of two or more beams. The initial laser beam is divided into several beams by a beamsplitter (or by DOE), then these beams are overlapped in the photoresist sample plane at a certain angle. The interference pattern is generated at the intersections of multiple beams. At the local maxima the light intensity is sufficient for photopolymerization threshold, while at the minima the intensity remains too low. Different shape patterns (pillars, cubes, lenses) could be produced by changing the number of intersected beams or the angle between interfering laser beams. The feature size could be varied by changing the laser exposure dose. However, this approach could suit for a small number of applications (for patterning large area with identical structures, e.g., microlens array) due to limited flexibility.

Apart from various physical techniques, the standard writing throughput could also be improved by simplified writing algorithms. For instance, in 3D printing, in most cases there is no need to completely scan all the volume of the structure. Contrary, a time- and cost-effective method is to print only the external contour of the structure, with internal scaffold to maintain the shape. Similar principles could be applied for multiphoton polymerization by structuring a part of the volume or only the closed superficial layer (shell) of the structure without scanning all the volume (e.g., lens profile). Subsequently, the applied UV exposure could solidify the remained and isolated part of unpolymerized material. Optimization of the writing trajectory is another parameter, which could speed up the fabrication time and improve the quality of the structure. Smooth spherical surfaces made by MPP require small voxels and tight overlapping conditions. However, the structure profiles with sharp/gentle slopes require different slicing steps. If the spacing between the two-adjacent layers is constant, it could cause uneven overlapping or even the condition that voxels are separated at some point. To overcome this issue, a few different scanning strategies [67] were proposed, such as: two-dimensional [183], sub-region slicing method [184], annular [185] or equal-arc [186] scanning modes. Two-dimensional and sub-region slicing methods take into account the slope angle. In principle, the whole structure is divided into at least two or more sections, if there is a steep slope, the slicing step is changed accordingly, and vice versa. The annular and equal-arc are similar scanning modes, the slicing step is continuously varied for each of layers, which is defined by different equation.

In contrast to the aforementioned methods and strategies, the throughput of the technology could be increased by modifying the voxel shape. Recent advances of the shaping of the Gaussian laser beam makes it possible to transform into Bessel, vortex, ring-Airy, top-hat profile beam, etc. For instance, the so-called Bessel beam is well-known for its ability of maintaining diffraction-limited shape over a long propagation. The most common ways that can be used for producing the Bessel beam are: diffractive optics, SLM or axicons. In glasses by femtosecond laser micromachining, it was already demonstrated that the generated aspect ratio of modification can even exceed 100, while the lateral dimension remained less than a micron [187]. This unique behavior makes this technique attractive for application in MPP too [167, 188], especially for potential 2D application, as scaffolds for tissue engineering [189]. However, the generation of the Bessel beam requires special modifications to the traditional MPP systems.

As an alternative method to the already known methods and strategies, we present our results on implementing the dynamic voxel control for traditional MPP system by using a motorized beam expander. In contrast to the feature size change by incrementally increasing the laser exposure, this method extends the fabrication window for a single objective. We demonstrate that by changing the focusing condition, the resolution of feature size could be easily tuned and used in real-time during the fabrication of 3D structures. Furthermore, this feature gives the ability to optimize the fabrication process, and have on-demand feature size control without sacrificing the precision.

4.2. Theoretical modeling

Typically the laser beam is expanded to completely fill the input objective aperture in order to obtain ultimate feature size resolution. In this case, the voxel size is mainly defined by NA of the objective. Certainly, it could be enlarged and tuned by the applied laser power, i.e., laser exposure dose. If the laser beam is not covering the front aperture of the objective completely, then this effect would lead to a numerical aperture drop and, hence, to larger voxel size. We have done numerical calculations in order to calculate the PSF dependence on laser beam size to the entrance of the objective aperture. We will define the amount of laser light covering the input aperture of the objective as a filling factor $T = \omega/a$, i.e., simply the ratio of the Gaussian beam waist radius (ω) (at the $1/e^2$) to the objective's aperture radius (a) [159, 190]. As reported in Ref. [190], the focused Gaussian beam is unclipped for the values $T < 0.5$. The moderate filling ratio increases the achievable resolution. However, it also provides a hybrid beam spot size, as the Gaussian beam starts to be truncated and transforms into an Airy pattern as $T \to \infty$. Moreover, a slight overfilling ($T > 1$) condition provides just a minor change in beam spot size, while the total power loss increases together with intensities of the diffraction rings of the Airy pattern [9, 190].

Contrary, if the filling ratio T is below 1, then underfilling of the objective input aperture leads to a drop of effective numerical aperture ($\mathrm{NA_{eff}}$), which could be recalculated using $\mathrm{NA_{eff}} = n \sin\theta_{\max}$, where n - refractive index of the propagation medium, $\theta_{\max}$ - highest marginal ray angle. By simply changing the incident beam waist, the voxel could be enlarged in the lateral and the axial directions. If the $\mathrm{NA_{eff}}$ of the objective is lower, the voxel aspect ratio increases and becomes even more elongated in respect to the optical axis. Under low-NA focusing condition, the beam propagation could be treated using standard scalar theory [9].

4.2.1. PSF modeling through scalar model

Under low-NA focusing condition, the semi-aperture angle is rather small, therefore a paraxial approximation could be used for calculations of PSF [9]. Firstly, the spatial intensity distribution of Gaussian laser beam could be expressed as:

$$I(r,z) = I_0 \frac{\omega_0^2}{w(z)^2} \mathrm{e}^{\frac{-2r^2}{w(z)^2}}, \tag{4.1}$$

where r is the distance from the center along the cross-section, z – the position along the optical axis, ω_0 - beam waist radius. $\omega(z)$ – the beam waist radius dependence along the optical axis z could be expressed:

$$\omega(z) = \omega_0 \sqrt{1 + \left(\frac{z}{z_0}\right)^2}; \tag{4.2}$$

While the focused laser beam spot dimensions could be calculated through the following equations, the laser beam spot at the new waist position (after the lens/objective) (at $1/e^2$):

$$\omega_0' = \sqrt{\frac{\lambda z_0}{\pi}} = \frac{\lambda f}{\pi D} = \frac{\lambda}{\pi \mathrm{NA}}, \tag{4.3}$$

depth of focus of laser beam spot size (at FWHM) is:

$$2z_0 = 2\frac{n\pi {\omega_0'}^2}{\lambda} = 2\frac{n\lambda}{\pi}\left(\frac{f}{D}\right)^2 = 2\frac{n\lambda}{\pi}\frac{1}{\mathrm{NA}^2}, \tag{4.4}$$

where λ - laser wavelength, f - effective focal length of the objective, D - laser beam diameter at the lens/objective.

4.2.2. PSF modeling through vectorial model

On the other hand, higher NA objectives are typically employed for MPP process to ensure high feature resolution. In that case, the incident light at marginal angle $\theta_{\max}$ make a larger angle with optical axis than the rays at the center, causing the depolarization effect (when the focal field is not linear anymore) [9] and, therefore, the paraxial approximation cannot be used anymore. To calculate the PSF under the tight focusing conditions with a high NA objective, spherical aberrations and the polarization effects have to be considered. For this purpose, the PSF needs to be calculated using vectorial Debye theory [9, 157].

The theoretical simulation of the light intensity distribution for different underfillings of the objective was done using vectorial and scalar models. The equations used for the vectorial Debye model can be found elsewhere [159]. This model takes into account the polarization state (circular in our case), spherical aberrations due to several interfaces (see Fig. 4.1 (a)) between the objective lens and the focal point. However, it is necessary to note that our vectorial model does not include diffraction effects in the beam due to the clipping aperture. Fig. 4.1 (b-g) show the variation of the PSF of intensity distribution calculations for different T (from 0.2 to over 1) filling factors for 0.95 NA objective with 515 nm laser wavelength. For instance, the filling factor T of 0.5 would mean that the diameter of the Gaussian laser beam is twice smaller than the objective's entrance diameter. In general, Eq. 4.3 and 4.4 show underfilling influence on the lateral voxel resolution, which is inversely proportional to NA, while the axial dimension to NA^2. As can be seen in Fig. 4.1 (b-g), by incrementally changing the filling factor, the feature axial size could be tuned from sub-micron to tens of microns regime within the same high NA objective.

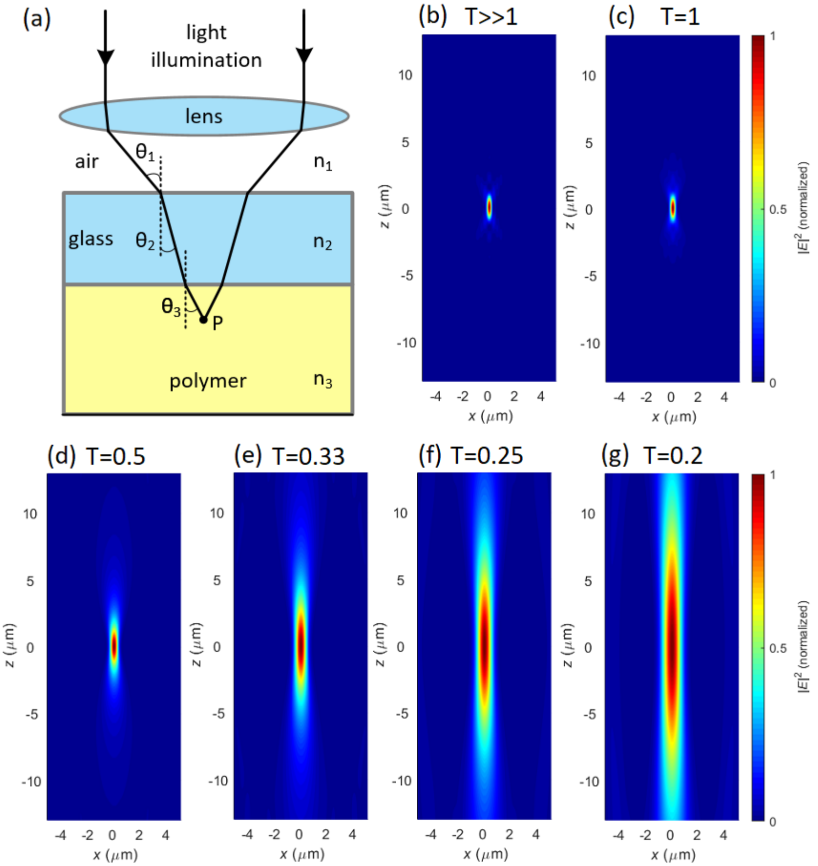

Figure 4.1: (a) Schematic illustration of laser beam propagation through stratified media using a dry-objective. Calculated PSF by vectorial theory for 0.95 NA objective with λ=515 nm laser wavelength with different filling factors T for the input aperture of the objective. Parameters: (b) $T \gg 1$, (c) $T = 1$, (d) $T = 0.5$, (e) $T = 0.33$, (f) $T = 0.25$, (g) $T = 0.2$.

4.3. Experimental method

The experiments were performed using a commercial laser system (Laser Nanofactory, Femtika Ltd.) with an Yb-based femtosecond laser (Carbide, Light Conversion Ltd.), which was operated at a frequency-doubled wavelength of 515 nm, ~250 fs pulse duration and at a 1 MHz repetition rate. The principal experimental setup is displayed in Fig. 4.2 (a). The initial laser beam

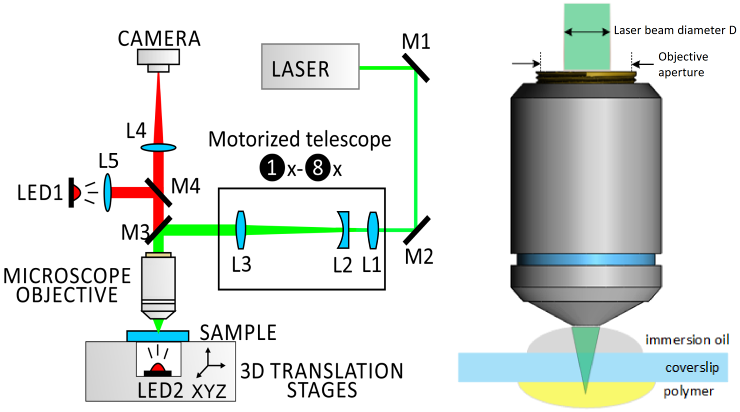

Figure 4.2: (a) Schematics of direct laser writing optical setup with a motorized telescope (1-8× expansion ratio) and high NA objective. M1-M4 – reflective mirrors; L1-L4 – lenses.

radius was 0.55 mm (at $1/e^2$). The laser beam was directed to the entrance aperture of an integrated motorized telescope. Then, the expanded beam was delivered to the high NA microscope objective, which focused the light into the volume of photosensitive resin. The fabrication process was realized by moving XYZ linear motion stages, and the average laser power was varied by an acousto-optical modulator. The fabrication speed was kept at 100 µm/s for all the structures.

To change the beam diameter, we used a motorized beam expander (MEX18, Optogama Ltd.), which had a possibility to enlarge the beam up to eight-fold. It consisted of 3 lenses with the surfaces: (1) convex/convex, (2) plano/concave and (3) convex/convex. The third element was fixed, while the first two lenses were driven by two independent motors along the optical axis. It is needed to emphasize that three lenses are mandatory to maintain collimated beam over the entire beam expansion range. The motorized telescope that was used had a high pointing stability of <0.2 mrad and the response time of <50 ms from sent command to the stage/motor motion. Any beam expansion is achievable within 0.2 s by moving the positions of the lenses, which are later corrected and stabilized. Practically, any operation took less than 1 s, including the movement and stabilization process over the entire dynamic beam expansion range. Moreover, the motorized beam expander had the ability to regulate/compensate laser beam divergence. Therefore, in principle, the same setup could work as a dynamic laser focus along the optical z axis, which could be applied for 3D microprocessing.

For the experiments, we used a hybrid inorganic/organic pre-polymer SZ2080 [85] with 1%wt of IRG photoinitiator, which is added to make the mixture more photosensitive to our used laser wavelength (515 nm). The negative tone SZ2080 liquid polymer was drop-casted on a standard glass coverslip and then prebaked on a hot-plate with short temperature ramps at 40°C, 70°C, and kept at 90°C for 1 h. During the prebake procedure, the solvent was evaporated and the polymer turned into soft gel. Afterwards, the sample was used for the laser fabrication step. The laser irradiated samples were immersed into a PEN developer bath for 30 minutes to wash out the laser non-scanned, not polymerized areas. Later, the samples were submerged into isopropanol and dried in ambient air. For inspection with a SEM, the samples were coated with a thin gold layer *via* sputter-coating.

4.4. Results and discussion

To quantitatively investigate the voxel dimensions dependence on the input filling factor of the objective, we chose to fabricate suspended fibers between supporting pillars. A series of narrow parallel fibers were made while incrementally increasing the laser power for each following fiber from polymerization to damage thresholds. In this experiment, we used tight focusing conditions with a 0.8 NA dry and 1.4 NA oil-immersion objectives, which are commonly used for the MPP application. Several input filling factors of the objective were chosen for each series of fibers. The lateral and axial dimensions of the fabricated structures were measured under the SEM. Fig. 4.3 shows voxel growth dynamics from polymerization to damage threshold for several $\mathrm{NA_{eff}}$ values (1.4 and 0.32), when the same physical objective was used.

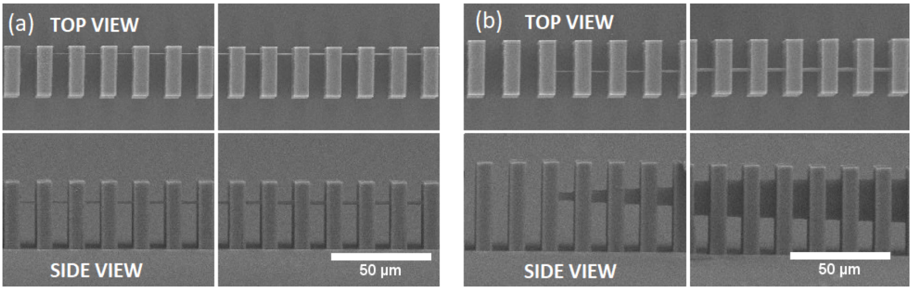

Figure 4.3: Top- and side-views of SEM images of suspended fibers between supporting pillars for $\mathrm{NA_{eff}}$ of (a) 1.4 and (b) 0.32. The set of individual lines shows voxel growth dynamics with increasing laser power for (a) 1.4 $\mathrm{NA_{eff}}$, near the (*left*) polymerization (0.09-0.14 mW) and close to (*right*) damage threshold (0.16-0.21 mW). While for (b) 0.32 $\mathrm{NA_{eff}}$, in the ranges of (*left*) 0.17-0.25 mW and (*right*) 0.43-0.53 mW, respectively.

Fig. 4.4 (a) shows the graphical representation of the experimental data, as well as results of theoretical modeling, which are plotted as a function of filling factor T. Firstly, the modeling and experiment were done with nominal 1.4 NA objective and λ=515 nm wavelength. As can be seen from for different underfilling conditions of the objective, there is a good agreement between vectorial and scalar models as the beam diameter is small, up to ∼0.7 of T. By exceeding this value, the paraxial approximation cannot be applied anymore, only the vectorial model is valid. The numerical calculations fit quite well with experimental data, which represent the polymerization threshold for each set of the experiment with different filling factors T. In a complete filling case ($T = 1$), the theoretical modeling predicts better feature resolution than it was achieved during the experiment. It is worth noting that feature size could be experimentally improved by narrowing the distance between the supporting pillar, as well as applying additional post-processing techniques, as critical point dryer for the development process.

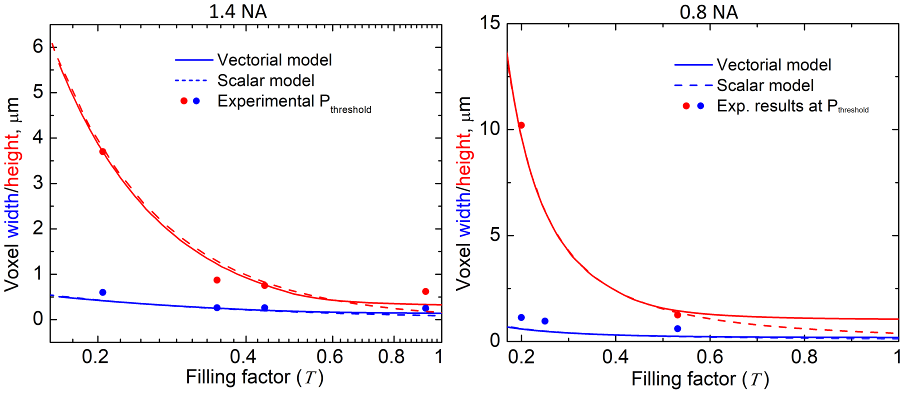

Figure 4.4: Comparison of modeled PSF size by using scalar and vectorial theories for (a) 1.4 NA and (b) 0.8 NA objective. Dots represent experimental measurements of polymerization threshold under different filling factor conditions.

In addition, the modeling and experiment were repeated with nominal 0.8 NA objective, as shown in Fig. 4.4 (b). The tendency was similar to the 1.4 NA objective, showing non-linear dependence on filling factor (T). Nonetheless, there is also a difference, as the obtained results for scalar and vectorial theoretical modeling were in a good agreement up to ∼0.55 of T for 0.8 NA objective.

Fig. 4.5 (a) show the experimental data of transversal and longitudinal voxel dimensions for different light filling conditions for 1.4 NA objective. The measurements were done through SEM analysis, each suspended fiber was measured at the middle of the line. The data is depicted on a double logarithmic scale, which separates the datasets better. Moreover, the depicted graph is indicative, fitted lines show the trend of the feature size growth. Our motorized telescope allowed to change the laser beam expansion up to eightfold, which enabled to have the $\mathrm{NA_{eff}}$ of 1.4 with a complete filling of the aperture while the not expanded beam dropped the $\mathrm{NA_{eff}}$ to 0.32, respectively. The experiments showed that the 1.4 $\mathrm{NA_{eff}}$ allowed to produce fine voxels, but had a short fabrication window of features from 0.25 µm to 0.5 µm in lateral and from 0.62 µm to 1.27 µm in axial dimensions. In contrast, 0.32 $\mathrm{NA_{eff}}$ suffered from limited resolution, but exhibited a large dynamic range from 0.6 µm to ∼2 µm transversely and from 3.7 µm to 22 µm longitudinally. A dynamic variation of $\mathrm{NA_{eff}}$ would give the ability to overlap those high and low NA objective regimes, and largely extend the dynamic range within the same single objective.

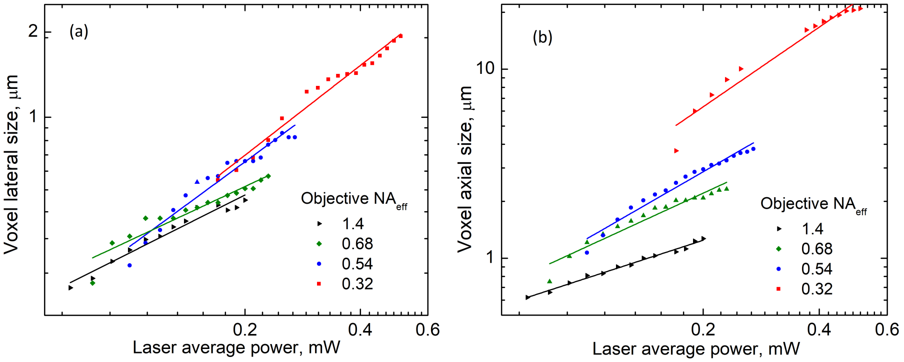

Figure 4.5: Measured (a) lateral and (b) axial voxel dimensions fabricated with a single objective by varying its $\mathrm{NA_{eff}}$ and laser exposure dose over the entire fabrication window for 1.4 NA objective.

Thereafter, the experiments were carried out with 0.8 NA objective, which showed the same qualitative tendencies. In this case, the input aperture of the objective was larger than some physical apertures in the current experimental setup, therefore the achievable maximum $\mathrm{NA_{eff}}$ was limited to 0.43 NA. In addition, two lower magnification values were chosen, which corresponded to the effective NA of 0.2 and 0.15. The obtained lateral and axial feature results are depicted in Fig. 4.6 (b). In this case, the voxel could be enlarged up to ∼3.5 µm and ∼50 µm in transversal and longitudinal dimensions, respectively. It is needed to emphasize that finer features obtained as well, however, for lower magnification values the fabrication regime near the polymerization threshold should be avoided due to worse repeatability. The values of the voxel dimensions in the middle of fabrication window for different experimental conditions are listed in Table 4.1.

In order to demonstrate the potential capability of the dynamics of the voxel size in one structure, we fabricated a woodpile structure, which fully reveals the single voxel size contrast by changing the incident laser beam on-demand. The grating structure consisted of two different optimized pattern sets (see Fig. 4.7). The upper and lower sections of the structure were done with first pattern with horizontal periods d_{xy}=5 µm and vertical spacing d_{z}=6 µm, $\mathrm{NA_{eff}}$=0.54, laser average power P=0.4 mW, while the middle part with second

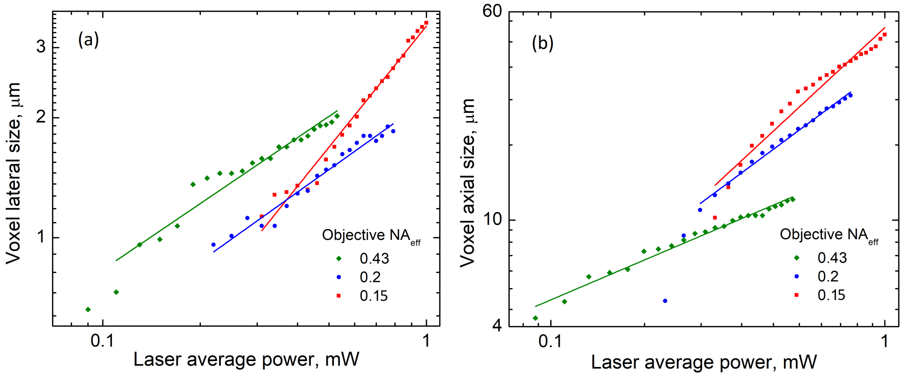

Figure 4.6: Measured (a) lateral and (b) axial voxel dimensions fabricated with a single objective by varying its NA$_{\mathrm{eff}}$ and laser exposure dose over the entire fabrication window for 0.8 NA objective.

Table 4.1: Experimentally measured voxel feature dimensions in the middle of fabrication window for different NA$_{\mathrm{eff}}$, P_{ave} – laser averaged power, which represents median value of fabrication window. Here, AR is voxel aspect ratio.

Objective	NA$_{\mathrm{eff}}$	P_{ave}, mW	d_{xy}, μm	d_z, μm	AR
63×/1.4 NA	1.4	0.14	0.41	0.91	2.2
	0.68	0.15	0.48	1.84	3.83
	0.54	0.19	0.7	2.86	4.09
	0.32	0.37	1.42	16.1	11.3
20×/0.8 NA	0.43	0.33	1.58	9.48	6.0
	0.2	0.64	1.80	25.0	13.9
	0.15	0.67	2.27	34.8	15.3

pattern of d_{xy}=2.5 µm and d_z=1.5 µm, NA$_{\mathrm{eff}}$=1.23, P=0.12 mW. Using fixed scanning speed of 100 µm/s the structure was printed in 8 min.

In microscopy, the principles of the resolving power (or resolution) dependence on the lens aperture was already known by E. Abbe more than a century ago, however, this straightforward method has never been applied for the additive manufacturing. For the MPP technique, a high NA objective is not always considered as the first choice for all applications (e.g., scaffolds in bio-medicine). The lower NA objectives are even more desired for bigger structures, which provide larger voxels and faster structuring [191]. However, the large-size structures with small features require tight focusing conditions, which could prolong the fabrication process to an unreasonable time. In this case, compared to the traditional MPP scheme, the dynamic voxel control gives an extra degree of freedom in the MPP fabrication process for the same objective. For 1.4 NA objective, a large NA$_{\mathrm{eff}}$ tuning range has been achieved from 1.4 to 0.32 NA. It should be noted that we were limited by the least laser beam size,

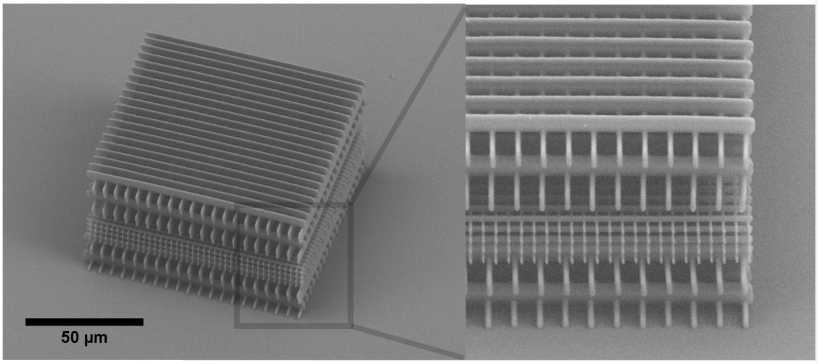

Figure 4.7: SEM image of the woodpile structure having two different voxel segments: upper and lower parts were done with $\mathrm{NA_{eff}}$=0.54, while the middle section with $\mathrm{NA_{eff}}$=1.23.

which was achievable by the experimental system. A reduction of the beam size would result in an even lower achievable $\mathrm{NA_{eff}}$. However, from an engineering point of view, this method requires a precise alignment of the optical system, otherwise variation of beam diameter may introduce laser focus shift in the field of the objective. Preferentially, the motorized telescope should be placed as close as possible to the objective that any imperfections of alignment would be less sensitive. In addition, the focal spot size could be easily scaled by this technique, however, the physical focal length and field of view remain unaffected. As the high NA objectives have a short working distance, the overall height of the achievable structures could be a limiting factor for some of the applications. Nonetheless, this beam expansion/reduction approach could easily be integrated into MPP systems and applied for large-size (mm) prototype structures with tiny features with hundreds of nanometers of feature resolution. It could be used as an alternative to currently used approaches or solve the need to change objectives for up-scaling the voxel size with different objectives.

4.5. Conclusions

In this chapter, we presented the possibility to employ dynamic voxel control by changing the incident laser beam diameter to the input of the objective with a motorized telescope. The smallest feature was fabricated with a complete filling of the input aperture of the objective resulting in 1.4 $\mathrm{NA_{eff}}$, while the largest feature dimension was defined by the least laser beam diameter that the system allowed to achieve resulting in $\mathrm{NA_{eff}}$ being 0.32 for the same objective. An expanded laser beam with a complete filling of the input aperture for 1.4 NA objective allowed to obtain the voxel feature size of 0.25 µm in the lateral and 0.62 µm in the axial direction, while an unexpanded beam ($T = 0.2$)

allowed to enlarge the voxel up to ∼2 µm transversely and 22 µm longitudinally, respectively. Even larger dimensions of the voxels were obtained for 0.8 NA objective resulting in up to ∼3.5 µm and ∼50 µm in transversal and longitudinal dimensions. This ability provides an extension of the fabrication window for high NA objective. We modeled the PSF by vectorial and scalar models, which had a relatively good agreement with our experimental results. It should be noted that straightforward scalar model well describes the PSF variation well up to 0.7 (for 1.4 NA objective) and 0.55 (for 0.8 NA objective) of the filling factor, above these values the vectorial theory should be used only. Finally, we successfully demonstrated the realization of dynamically tunable voxel size. The presented approach extends the technological capabilities and could significantly increase the fabrication speed while maintaining the possibility to obtain high resolution features at the same time.

MAIN RESULTS AND CONCLUSIONS

1. A novel concept of hybrid glass/polymer micromechanical sensor was proposed. The coupled device was made through selective laser etching technique out of fused silica substrate with the direct integration of a polymeric beam *via* the multiphoton polymerization technique. Through this combination of techniques, it was demonstrated that a glass/polymer micromechanical sensor enable the possibility to investigate the elastic properties of polymeric microstructures.

2. It was experimentally shown that polymeric structures undergo deformations (shrinkage or swelling) immersed in different solvents. The results indicate that Young's modulus of polymeric structures done out of SZ2080 photopolymer could be varied depending on laser exposure from 0.4 GPa to $\sim$2 GPa in PEN solvent. Moreover, the findings show that mechanical properties depend on the surrounding medium, which resulted in lower Young's modulus value in air compared to obtained values in solvents.

3. The polymeric structures fabricated by MPP have reversible deformations in different solvents. After a few cycles of interchanged solvents, the sensor shows a constant shrinkage/swelling and stiffness (Young's modulus) values, which potentially could be applied for chemical sensing application in microfluidics.

4. For the first time, the implementation of 4π excitation in MPP traditional setup was demonstrated. By using a pair of 0.8 NA objectives, the fabricated structures consisted of an interference pattern of multiple alternating polymerized zones at lower and higher degree of monomer conversion along the optical axis. For 1030 nm laser wavelength, the periodicity of 340 nm was measured between the center-to-center lines in the structures, which showed a good agreement with theoretical modeling. In thin structures, the zones polymerized at lower degree showed the possibility to be washed out, resulting in air/polymer layers, which resulted in a coloration effect due to defined high refractive index change and appropriate periodically spaced layers.

5. It was demonstrated that using a pair of high NA (1.4) objectives in 4π excitation allowed to effectively suppress the sidelobe generation. Under certain exposure dose the axial feature resolution was improved threefold to 150 nm of feature resolution in comparison to standard focusing conditions.

6. In MPP technique, the motorized control of incident laser beam size

makes it possible to dynamically tune the voxel feature size. Underfilling of the input aperture of the objective leads to effective NA drop. It was shown that using a single 1.4 NA objective, the feature voxel size could be obtained from 0.25 µm to ∼2 µm in lateral and 0.62 µm to ∼22 µm in axial dimensions.

SANTRAUKA

ĮVADAS

Nuo pat pirmojo tranzistoriaus išradimo, industrijoje stebimas miniatiūrizacijos procesas, kai pramonė siekia išgauti vis mažesnius mechaninius, optinius ir elektrinius mikrofunkcinius prietaisus. Šią tendenciją patvirtina jau daugiau nei penkiasdešimt metų puslaidininkių industrijoje galiojantis G. Moore'o dėsnis, kuris teigia, kad komponentų skaičius integriniuose grandynuose padvigubėja kas dvejus metus. Miniatiūrizacija apima ne tik elektronikos pramonę, funkcinių mikrodarinių mažėjimo tendencijas galime pastebėti ir fotonikos, mikrooptikos, mikromechanikos ar mikrofluidikos darinių formavime bei daugelyje kitų sričių. Sparčiai plėtojamos naujos lazerinės technologijos, turinčios privalumų prieš tradicinius litografijos metodus, leidžia suformuoti 3D funkcinius mikrodarinius dviejų žingsnių procesais.

Ultratrumpų lazerio impulsų atsiradimas atvėrė naujas galimybes medžiagų apdirbime, ypatingai 3D mikrodarinių formavime. Priešingai nei mikroapdirbimas ilgesniais – nanosekundiniais impulsais, femtosekundiniai impulsai leidžia pasiekti ypač aukštą ($\sim$TW/cm^2) smailinį intensyvumą, o tai suteikia galimybę indukuoti netiesinius sugerties procesus apdirbamoje medžiagoje. Dėl daugiafotonės sugerties, net ir lazerio bangos ilgiui įprastai skaidrios medžiagos pasiekus itin aukštus intensyvumus pradeda sugerti lazerio spinduliuotę bei leidžia modifikuoti medžiagą lokaliai. Šis efektas leidžia femtosekundinį lazerinį šaltinį panaudoti skirtingoms 3D darinių formavimo technologijoms, kaip daugiafotonė polimerizacija ar selektyvus lazerinis ėsdinimas. Pastaroji technologija leidžia sukurti 3D mikrodarinius iš monolitinio stiklo padėklo subtraktyviu būdu. Tuo tarpu, dvifotonė polimerizacija yra adityvus metodas, leidžiantis suformuoti praktiškai neribotos geometrijos mikrodarinius iš polimero.

Nors šie formavimo metodai buvo pirmą kartą pademonstruoti prieš maždaug du dešimtmečius, šios technologijos vis dar vystomos ir yra aktualios. Vis didėjanti mokslinių straipsnių gausa ir galimi šių technologijų pritaikymai įvairiose srityse rodo, kad šios technologijos yra itin perspektyvios. Naujų kompleksinių mikrodarinių poreikis pramonėje plečia šių technologinių procesų apribojimus pasiekiamai mikrodarinių raiškai bei vis didesniam procesų našumui.

Šioje disertacijoje nagrinėjamos ir aptariamos kelios su 3D mikrodarinių formavimu lazerinėmis technologijomis susijusios temos. Elastinėms polimerinių mikrodarinių savybėms tirti pademonstruotas naujo tipo mikrojutiklis, kuris pagamintas apjungiant kelias (adityvias ir subtraktyvias) lazerines technologijas. Pasiūlytas metodas suteikia naujų įžvalgų apie polimerinių mikrodarinių elgseną skirtingose aplinkose (skysčiuose, ore). Taip pat, daugiafotonėje polimerizacijoje pademonstruotas išilginės darinių raiškos gerinimo metodas panaudojant vienas prieš kitą fokusuojančių objektyvų porą. Be to, tiesioginio lazerio rašymo technologijoje pasiūlytas naujas nesudėtingas spartinimo metodas dinamiškai valdant darinių raišką realiu laiku.

Disertacijos tikslas

Pagrindinis šios disertacijos darbo tikslas buvo naujo tipo funkcinių mikrodarinių formavimas panaudojant femtosekundinių lazerių technologijas bei šių metodų plėtojimas.

Darbo uždaviniai

1. Funkcinio mikromechaninio jutiklio gamyba ir optimizavimas, tinkantis polimerinių mikrodarinių, pagamintų daugiafotoninės polimerizacijos metodu, mechaninėms savybėms ištirti. Polimerinių elastinių savybių kitimo skirtingose aplinkos terpėse tyrimas.
2. 4π fokusavimui reikalingos eksperimentinės schemos surinkimas, tobulinimas ir integravimas į daugiafotonės polimerizacijos sistemą. Tokio metodo formuojamų darinių raiškos bei savybių tyrimas.
3. Daugiafotonės polimerizacijos technologijoje formuojamų darinių raiškos priklausomybė nuo objektyvo įėjimo apertūros užpildymo lazerio pluoštu tyrimas.

Mokslinis tyrimų naujumas

1. Pademonstruotas naujo tipo polimero/stiklo mikromechaninis jutiklis apjungiantis dvi tiesioginio lazerinio rašymo femtosekundiniais šviesos impulsais technologijas: selektyvaus lazerinio ėsdinimo bei daugiafotonės polimerizacijos. Eksperimentiškai pademonstruota, kad jutiklis gali būti panaudotas suformuotų polimerinių darinių mechaninėms savybėms tirti.
2. Pademonstruotas 4π fokusavimas daugiafotonės polimerizacijos technologijoje, kuris leido pasiekti aukštesnę išilginę darinių raišką.
3. Panaudojant 4π fokusavimą daugiafotonėje polimerizacijoje pademonstruotas polimeruose submikrometrinio dydžio periodinių plokštumų formavimasis, kuriantis struktūrines spalvas regimajame spektro ruože.
4. Daugiafotonėje polimerizacijoje pademonstruota, jog keičiant kritusio lazerio pluošto diametrą motorizuotu pluošto plėstuvu galima keisti skersinius ir išilginius darinio matmenis. Šis metodas panaudotas 3D mikrodarinių formavime keičiant erdvinę darinių raišką realiu laiku.

Ginamieji teiginiai

1. Mikromechaninių jutiklių sistemos pagamintos iš stiklo selektyvaus lazerinio ėsdinimo technologija yra tinkamos daugiafotone polimerizacija pagamintų darinių elastinėms savybėms (Jungo moduliui) tirti, jei šie dariniai gali būti integruoti į mikromechanines sistemas. Toks metodas leidžia išmatuoti darinių tamprumą bei deformacijų dydžio pokyčius skirtingose terpėse dėl traukimosi ar plėtimosi reiškinių.

2. 4π fokusavimas daugiafotonės polimerizacijos technologijoje leidžia pasiekti iki 3 kartų aukštesnę išilginę darinių raišką, formuojant darinius SZ2080 polimero pirmtake su aukštos (NA = 1,4) skaitinės apertūros objektyvais. Mažesnės skaitinės apertūros objektyvai leidžia suformuoti submikrometrinio dydžio periodinius darinius orientuotus išilgai optinės ašies.

3. Tiesioginio lazerinio rašymo metode dinamiškai valdant kritusio lazerio pluošto diametrą galima keisti efektyvią skaitinę objektyvo apertūrą, o kartu ir įrašomų darinių erdvinę raišką realiu laiku. Aukščiausia raiška yra ribojama nominalia objektyvo skaitinės apertūros verte, tuo tarpu žemiausia - nulemta siauriausio lazerinio pluošto diametro, kurį naudojama sistema gali pasiekti.

Disertacijos struktūra

Disertacija susideda iš 4 pagrindinių skyrių:

- Pirmasis skyrius supažindina su ultratrumpųjų lazerio impulsų panaudojimu skirtinguose taikymuose. Apžvelgiami ultratrumpųjų šviesos impulsų sąveikos mechanizmai skaidrių medžiagų tūryje. Aprašoma trimačių stiklo bei fotopolimerinių mikrodarinių gamyba paremta femtosekundinių lazerių apdirbimo technologijomis. Aptariami šių metodų fizikiniai mechanizmai ir pagrindiniai formavimo principai.

- Antrajame skyriuje pristatomas stiklo mikrojutiklis, skirtas ištirti daugiafotonės polimerizacijos būdu pagamintų mikrodarinių mechanines savybes. Pateikiamas tokio funkcinio darinio veikimo mechanizmas, pristatomi modeliavimo bei eksperimentiniai polimerinių darinių pokyčiai skirtingose aplinkos terpėse.

- Trečiasis skyrius skirtas aptarti 4π fokusavimą daugiafotonėje polimerizacijoje. Pateikiami skaitmeninio modeliavimo bei eksperimentinio tyrimo rezultatai.

- Ketvirtame skyriuje aptariami daugiafotonės polimerizacijos našumo gerinimo metodai. Kaip alternatyva, pateikiamas naujas būdas daugiafotonėje polimerizacijoje formuojamo darinio erdvinę raišką dinamiškai valdyti keičiant kritusio lazerio pluošto diametrą. Pateikiami skaitmeninio modeliavimo, naudojant vektorinę ir skaliarinę teoriją, bei eksperimentiniai rezultatai.

Disertacinio darbo aprobacija

Publikacijos leidiniuose, turinčiuose cituojamumo rodiklį Web of Science duomenų bazėje:

P1. **T. Tičkūnas**, M. Perrenoud, S. Butkus, R. Gadonas, S. Rekštytė, M. Malinauskas, D. Paipulas, Y. Bellouard, and V. Sirutkaitis, "Combination of additive and subtractive laser 3D microprocessing in hybrid glass/polymer microsystems for chemical sensing applications", Opt. Express. **25**(21), 26280–26288 (2017).

P2. **T. Tičkūnas**, D. Paipulas, and V. Purlys, "4Pi multiphoton polymerization", Appl. Phys. Lett. **116**(3), 031101 (2020).

P3. **T. Tičkūnas**, D. Paipulas, and V. Purlys, "Dynamic voxel size tuning for direct laser writing", Opt. Mat. Express **10**(6), 1432-1439 (2020).

Publikacijos konferencijų leidiniuose:

PR1. **T. Tičkūnas**, M. Malinauskas, R. Gadonas, Y. Bellouard, and D. Paipulas, "Hybrid laser 3D microprocessing in glass/polymer micromechanical sensor: towards chemical sensing applications", Proc. SPIE. **10675**, 106750C (2018).

PR2. L. Jonušauskas, **T. Tičkūnas**, A. Narmontas, G. Nemickas, V. Purlys, G. Grigalevičiūtė, and R. Gadonas, "Femtosecond laser-assisted etching: making arbitrary shaped 3D glass micro-structures", Proc. SPIE. **10520**, 105201G (2018).

PR3. **T. Tičkūnas**, V. Purlys, and R. Gadonas, "Axial resolution improvement in multiphoton polymerization by 4Pi excitation", Proc. SPIE. **10909**, 1090903 (2019).

REZULTATŲ APŽVALGA

3D POLIMERO/STIKLO MECHANINIS JUTIKLIS

Šio skyriaus medžiaga publikuota [P1, PR1, PR2].

Stiklas yra viena dažniausiai moksle ir industrijoje naudojamų medžiagų. Ši medžiaga tvirta, turi puikias optines savybes, pasižymi inertiškumu bei biosutaikomumu. Šios ir kitos medžiagos ypatybės tinka daugelyje taikymo sričių, tokių kaip įvairiausių mikrofluidikos lustų gamyboje. Kai kuriuose stikluose, kaip lydytas kvarcas, nesudėtinga ultratrumpųjų impulsų pagalba suformuoti 3D mikrodarinius panaudojant selektyvaus lazerinio ėsdinimo (SLE) technologiją.

Kadangi stiklas yra amorfinė medžiaga, jo mechaninės savybės visomis kryptimis išlieka tos pačios. Labai ploni stiklo dariniai pasižymi lankstumu, kaip pavyzdžiui, šviesolaidžio gija, o šios deformacijos – elastinės. Panašius lanksčius mikromechaninius darinius ar tik jų tam tikrus elementus galima suformuoti ir SLE technologija. Tokių darinių elastines deformacijas galima aprašyti paprasčiausia klasikine mechanika. Tiksliai žinant darinio geometrinius matmenis, mechanines stiklo savybes bei deformacijos dydį, tampa nesudėtinga apskaičiuoti veikiančias jėgas. SLE technologija atveria galimybes formuoti lanksčias stiklo sistemas įvairiems tiksliems taikymams, kaip: mikrojutikliams (stiklo savybėms tirti) [114], mikroaktiuatoriams [116, 117], optiniams mikroposlinkio jutikliams [118], reguliuojamiems mikroveidrodžių elementams [120] ar medicininiams mikroįrenginiams [121].

Daugiafotone polimerizacija pagaminti mikrodariniai yra elastingi. Šia technologija galima suformuoti sudėtingos formos polimerinius darinius, kurių įprasta skersinė erdvinė darinių skyra gali siekti kelis šimtus nanometrų. Daugiafotonė polimerizacija yra plačiai pritaikoma įvairiems taikymams: mikrooptikos, fotoninių kristalų, optofluidikos, audinių bioinžinerijoje elementams gaminti [173]. Be to, keičiant lazerio ekspozicijos dozę iš esmės galima moduliuoti tokių polimerinių darinių optines [86] ar mechanines savybes [12]. Verta pažymėti, kad polimerai gali turėti atsaką į aplinkos poveikį, kaip formos pakitimą veikiant šiluma [124], elektriniu lauku [125], ar susitraukimu ir brinkimu tirpikliuose [126, 127]. Vis dėlto, daugiafotone polimerizacija suformuotų darinių savybės priklauso nuo formavimo parametrų, o norint platesnio šios technologijos taikymo šių darinių mechaninės savybės turi būti ištirtos ir žinomos.

Daugiafotone polimerizacija suformuotų darinių mechaninėms savybėms tirti, buvo sukurtas naujo tipo jautrus mikromechaninis jutiklis, pasitelkiant SLE technologiją. Tokio funkcinio mikrodarinio dizainas pavaizduotas 4.8 pav., kuris susideda iš ilgo (∼10 mm) mikrojutiklio, kuris yra statiškai fiksuotas viename gale. Priešingas jutiklio galas yra nepritvirtintas ir gali laisvai judėti XY plokštumoje veikiant apkrovai.

Sekančiu žingsniu pasinaudojus daugiafotone polimerizacija integruojama polimerinė sija, sujungianti stiklo jutiklį su stiklo rėmu, kaip pavaizduota 4.8 pav. Formavimo metu medžiaga yra supolimerizuojama, o nesupolimerizuotos sritys yra paprasčiausiai išplaunamos. Skirtingose terpėse gali būti stebimas polimerinių darinių susitraukimas ar išbrinkimas, kuris veiks kaip taškinė apkrova ir lems stiklo jutiklio atsilenkimą XY plokštumoje į vieną ar kitą pusę. Tiksliai parinkus geometriją, stiklo mikromechaninio jutiklio sistema bus itin jautri ir leis užfiksuoti net ir mažą polimerinio darinio matmenų pokytį. Tiksliai žinant tokios hibridinės stiklo/polimero sistemos geometriją, bei stiklo (lydyto kvarco) mechanines savybes, iš išmatuoto stiklo jutiklio atsilenkimo galima apskaičiuoti jį veikiančią jėgą, bei elastines polimerinio darinio savybes.

Stiklo mikromechaninio jutiklio atsilenkimą galima nusakyti tokia formule:

$$\delta = \frac{E_p S_p (L_p - d_g)(3L_g - a)a^2}{2(E_p S_p a^3 + 3E_g I_g L_p)}, \tag{4.5}$$

kur E_g – lydyto kvarco Jungo modulis, L_g – visas stiklo jutiklio ilgis, d_g – atstumas tarp stiklo jutiklio ir stiklo rėmo, a – atstumas nuo jutiklio pradžios taško iki polimerinio darinio integravimo pozicijos. I_g yra stiklo jutiklio antrasis inercijos momentas, kuris jam esant stačiakampio formos gali būti išreikštas, kaip I_g=$t_g w_g^3/12$ (kur w_g – stiklo jutiklio plotis ir t_g – storis). Polimerinio darinio skerspjūvis žymimas $S_p = W \times H$, kur W žymi darinio plotį ir H aukštį, kaip parodyta 4.8 pav.

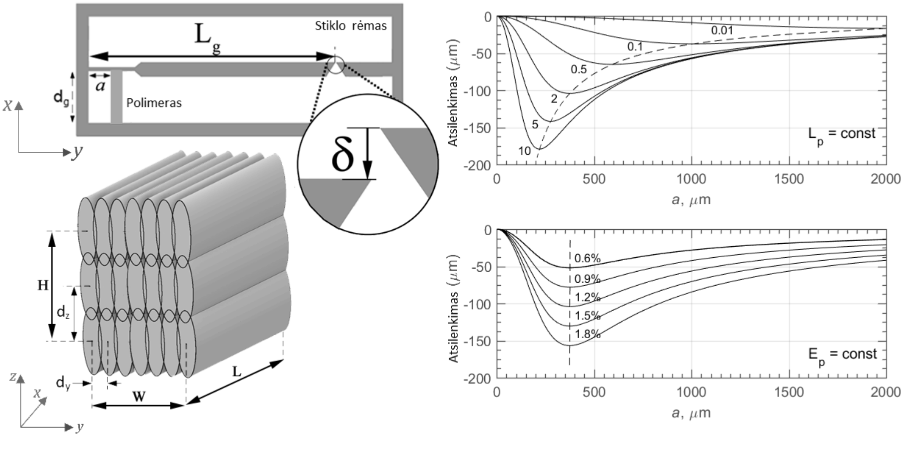

4.8 pav.: Stiklo jutiklio su integruotu polimeriniu mikrodariniu schematinis brėžinys, bei tokio jutiklio atsilenkimo dinamika priklausomai nuo traukimosi/brinkimo reiškinių. (*dešinėje*) Sumodeliuotas stiklo jutiklio galinės padėties atsilenkimo vertės priklausomai nuo polimerinio darinio integravimo pozicijos. Viršutinis grafikas sumodeliuotas prie skirtingų polimero Jungo modulio verčių, kai traukimasis polimeriniam dariniui būtų fiksuotas – 1,2%, tuo tarpu apatiniame grafike – varijuojama polimero traukimosi vertė, kai polimero Jungo modulio fiksuotas (2 GPa).

Pagal 4.5 formulę, žinant mikrojutiklio geometriją bei mechanines stiklo savybes, galima sumodeliuoti apytikslę jutiklio galo atsilenkimo dinamiką priklausomai nuo užduodamų pradinių parametrų. Skaičiavimams pasirinkti parametrai: stiklo jutiklio storis 480 µm, L_g – 10 mm, w_g – 35 µm, d_g – 35 µm, S_p – 50 µm × 50 µm, o E_c – 72 GPa. Tokiu atveju, 4.5 formulėje lieka du nežinomieji: E_p – polimero Jungo modulis, ir L_p – galutinis polimerinio darinio ilgis po deformacijos. Varijuojant šiuos du parametrus, stiklo jutiklio atsilenkimo priklausomybė nuo polimero darinio integravimo pozicijos a pavaizduoti 4.8 pav.

Selektyvaus lazerinio ėsdinimo ir daugiafotone polimerizacija gaminti dariniai suformuoti ta pačia lazerine sistema su Yb:KGW femtosekundiniu lazeriniu šaltiniu. Stiklo mikrosensoriaus gamybai naudotas 1030 nm lazerio bangos ilgis, 610 kHz pasikartojimo dažnis, 600 fs impulsų trukmė, 270 mW vidutinę lazerio galią naudojant 0,4 NA objektyvą. Modifikacijos lydyto kvarco tūryje 15 mm/s greičiu su 4,5 µm atstumu tarp gretimų sluoksnių. Tuomet, norimas darinys gautas ėsdinant 5% (v/v) vandenilio fluorido (HF) rūgštyje. Vėliau, sekančiu žingsniu suformuotas stiklo jutiklis padengiamas SZ2080 polimero pirmtaku (fotojautrintu 1% 2-benzyl-2-(dimethylamino)-4'-morpholinobutyrophenone), atkaitinamas išgarinant tirpiklius. Daugiafotonei polimerizacijai naudotas 515 nm lazerio bangos ilgis, 200 fs impulsų trukmė, 610 kHz pasikartojimo dažnis, fokusavimui naudotas 0,8 NA objektyvas.

Bendrai, nežinomus polimero parametrus (Jungo modulį ir traukimosi/plėtimosi pokytį) galima nesudėtingai įvertinti padarius rinkinį atskirų mikrojutiklių, kurių kiekviename identiškas polimerinis darinys yra integruojamas vis skirtingoje pozicijoje a išilgai stiklo jutiklio (žr. 4.8 pav.). Tokiu būdu, keičiant tik polimerinio darinio tvirtinimo tašką galima stebėti vis skirtingą stiklo jutiklio galo atsilenkimo amplitudę nulemtą traukimosi/plėtimosi reiškinių skirtingose terpėse. Vėliau, aproksimuojant šių atsilenkimų rezultatus pagal 4.5 formulę galima gauti nežinomus narius: polimerinio darinio Jungo modulį E_p bei darinio ilgį po deformacijos L_p.

Daugiafotone polimerizacija suformuotos stačiakampio formos sija buvo (H×W×L=50×50×342) µm^3 dydžio. Parinkti du lazerio skenavimo algoritmai: (1) kai perklojimas – tankus, tarp gretimų linijų atstumas buvo d_y = 0,25 µm ir tarp sluoksnių d_z = 1,5 µm, kitu atveju – (2) retesniu perklojimu, kai d_y = 0,5 µm ir d_z = 4,5 µm (žr. 4.8 pav.). Abiems atvejais lazerio vidutinė galia buvo 0,8 mW, o skenavimo greitis – 3 mm/s. Suformuoti kompozitiniai stiklo/polimerų dariniai buvo merkiami/patalpinami skirtingose terpėse ir fiksuojamas stiklo jutiklio atsilenkimas, sąlygotas polimerinio darinio traukimosi/brinkimo.

Suformuotas stiklo mikromechaninis jutiklis su integruotu SZ2080 polimeriniu dariniu matomas 4.9 pav. (a). Tankaus skenavimo algoritmu suformuotas polimerinis darinys pasižymėjo traukimusi 4-metil-2-pentanone (PEN), etano-

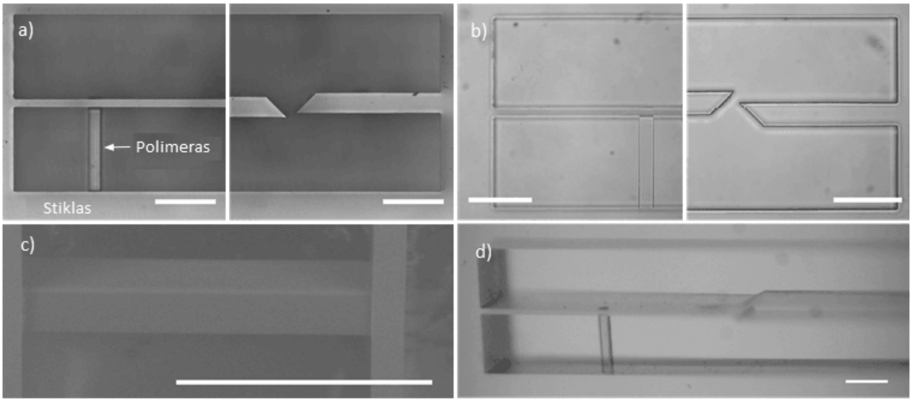

4.9 pav.: Suformuotas stiklo mikromechaninis jutiklis su integruotu SZ2080 polimeriniu dariniu. Optinio mikroskopo nuotraukos, parodančios stiklo jutiklio atsilenkimą, nulemtą (a) polimerinio darinio traukimosi ore ir (b) brinkimo reiškinio tirpiklyje. (c) Rodomas tokio darinio SEM ir (d) stereoskopinio mikroskopo vaizdas. Skalės mastelis: 250 µm.

lyje ir išryškinus ore (žr. 4.10 pav.). Tuo tarpu, retesnio skenavimo atveju, buvo stebimas brinkimas PEN, etanolyje, kaip parodyta 4.10 pav. (b). Traukimosi atveju, aproksimavus pagal 4.5 formulę buvo įvertintas polimerinio darinio Jungo modulis E_p bei darinio ilgis po deformacijos L_p, PEN tirpiklyje: (0,188 ± 0,005 GPa; 339,5 ± 0,1 µm); etanolyje: (0,158 ± 0,007 GPa; 339,6 ± 0,1 µm) bei ore: (0,138 ± 0,008 GPa; 340,1 ± 0,1 µm). Tuo tarpu retesnio skenavimo atveju, E_p ir L_p PEN buvo (0,467 ± 0,018 GPa; 345,8 ± 0,1 µm) ir etanolyje (0,493 ± 0,015 GPa; 345,1 ± 0,1 µm). Šie rezultatai rodo Jungo modulio padidėjimą iki 3 kartų palyginus su tankesniu skenavimu. Retesnio skenavimo atveju tirpiklio molekulės įsiskverbia į polimerinio darinio vidų, taip sustiprina pačio darinio standumą.

Sekančiu žingsniu, ištirta polimero mechaninių savybių priklausomybė nuo lazerio ekspozicijos dozės, kai naudotas reto (d_y = 0,5 µm, d_z = 4,5 µm) skenavimo algoritmas. Nustatėme, kad derinant lazerio ekspozicijos dozę, galima keisti stiklo jutiklio atsilenkimo dinamiką (žr. 4.11 pav.). Stiklo jutiklio atsilenkimo amplitudė indukuoja traukimosi/plėtimosi vertę, o maksimumo taško padėtis – Jungo modulį. Polimeriniai dariniai pagaminti prie keturių skirtingų lazerio vidutinių galių (0,5 mW, 0,7 mW, 0,9 mW ir 1,2 mW). Iš 4.11 pav. matyti, kad prie žemiausios galios vertės plėtimasis yra didžiausias, o Jungo modulis mažiausias. Didinat lazerio ekspozicijos dozę, plėtimasis mažėja, o maksimumo taško padėtis slenka arčiau nulinės padėties. Eksperimentinių taškų aproksimacija leidžia įvertinti mechanines darinio savybes. Gauta, kad keičiant lazerio ekspoziciją tokiu atveju Jungo modulis keičiamas plačiame diapazone nuo 0,4 GPa iki 2 GPa. Verta pažymėti, kad viršijus tam tikrą kritinę lazerio ekspozicijos vertę (1,2 mW šiuo atveju), gaunamas nebe polimerinio

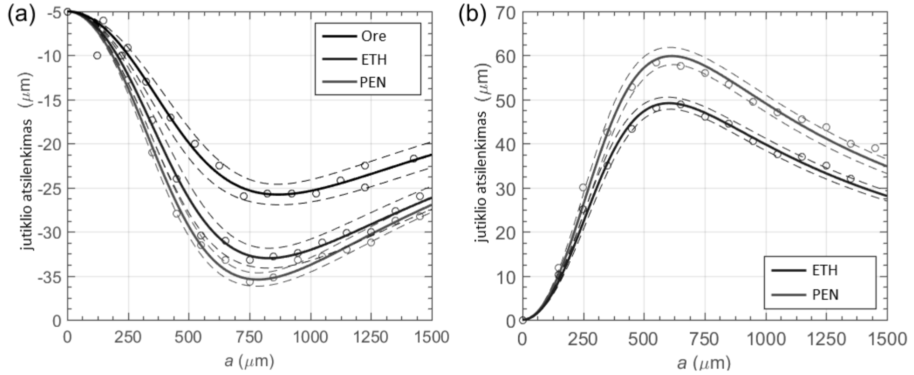

4.10 pav.: Stiklo jutiklio atsilenkimas sąlygotas SZ2080 polimerinio darinio (a) traukimosi ir (b) brinkimo reiškinių skirtingose terpėse (ore, etanolyje (ETH), 4-metil-2-pentanone (PEN)). Polimerinis darinys suformuotas (a) reto (d_y = 0,5 µm, d_z = 4,5 µm), (b) tankaus (d_y = 0,25 µm, d_z = 1,5 µm) skenavimo atveju.

darinio brinkimas, o traukimasis, kadangi visas darinio medžiagos tūris yra supolimerizuotas ir tirpiklio molekulės nebeįsiskverbia į darinį. Eksperimento rezultatai pateikti 4.2 lentelėje.

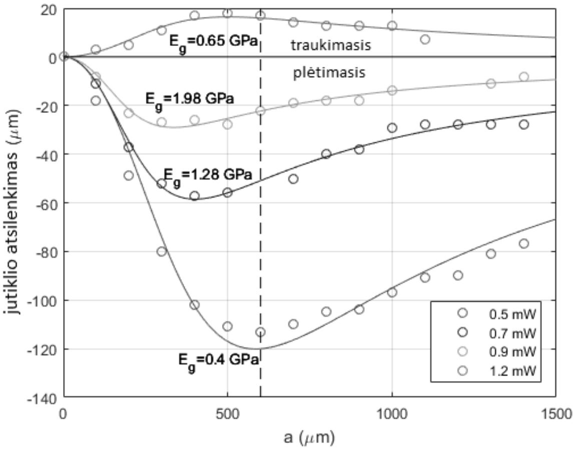

4.11 pav.: Stiklo jutiklio atsilenkimas sąlygotas SZ2080 polimerinio darinio traukimosi/brinkimo reiškinių PEN tirpiklyje, kai polimerinis darinys suformuotas skirtingomis vidutinėmis lazerio galiomis P_{ave}.

Vėliau ištirtas tokių polimerinių darinių deformacijų atsikartojamumas skirtingose terpėse. Pirmiausia, tirtas polimerinio darinio Jungo modulio pokytis skirtinguose skysčiuose priklausomai nuo keitimų ciklų skaičiaus. Pirmo ciklo metu stiklo jutiklis buvo įmerkiamas į PEN tirpiklį, o vėliau į etanolį (ETH), tokią seką pakartojant 5 kartus (ciklus). Rezultatai rodo, jog Jungo modulis

4.2 lentelė: Iš stiklo jutiklio atsilenkimų apskaičiuotos SZ2080 polimerinio darinio savybės (Jungo modulis E_p, matmenų pokytis po deformacijos ΔL), kai polimerinis darinys suformuotas skirtingomis vidutinėmis lazerio galiomis P_ave.

P_{ave}, mW	ΔL, %	Efektas	E_p, GPa
0,5	2	Plėtimasis	0,4 ± 0,02
0,7	0,7	Plėtimasis	1,28 ± 0,07
0,9	0,3	Plėtimasis	1,98 ± 0,18
1,2	0,25	Traukimasis	0,65 ± 0,06

sumažėja po pirmųjų trijų ciklų, o vėliau įgauna pastovią savo vertę. Pasiekus įsisotininimą, eksperimentiniai duomenys parodė, kad tolesnis tokių polimerinių darinių brinkimas yra grįžtamas ir pilnai atsikartojantis 4.12 pav. (b). Net ir po 10 etanolio ir PEN keitimo ciklų, deformacijos dydis išliko toks pats. Šis rezultatas rodo, kad tokias hibridines mikromechanines sistemas galima naudoti cheminiam jutikliams kurti.

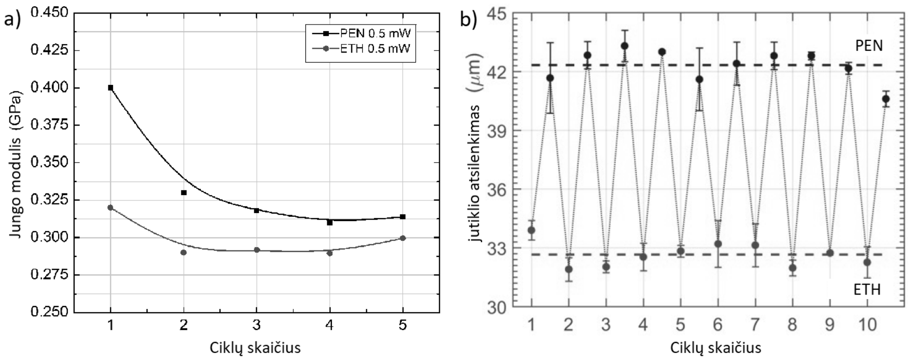

4.12 pav.: (a) SZ2080 polimerinio darinio suskaičiuoto Jungo modulio pokytis nuo (PEN-ETH) skysčio keitimo ciklo. (b) Stiklo jutiklio atsilenkimo priklausomybė nuo (PEN-ETH) skysčio keitimo ciklo.

Pristatytas naujo tipo hibridinis stiklo/polimero mikromechaninis jutiklis, pasitelkiant selektyvaus lazerinio ėsdinimo bei daugiafotonės polimerizacijos technologijas. Šis jutiklis tinkamas tiriant daugiafotone polimerizacija suformuotų polimerinių mikrodarinių elastines savybes bei jų elgseną skirtingose aplinkose (skysčiuose, ore). Buvo pademonstruota, kad priklausomai nuo ekspozicijos dozės galime gauti tiek polimerinio darinio traukimosi, tiek plėtimosi reiškinius skirtinguose skysčiuose. Priklausomai nuo ekspozicijos dozės, polimerinių mikrodarinių Jungo modulis gali būti varijuojamas nuo 0,4 GPa iki 2 GPa intervale 4-metil-2-pentanone skystyje. Taip pat, rezultatai rodo, kad SZ2080 polimerinio darinio standumas padidėja panardinant į organinius skysčius. Be to, skysčiuose polimerinio darinio deformacijos yra grįžtamosios, po kelių skysčių pakeitimo ciklų, jų savybės yra atsikartojančios, tai gali būti panaudota cheminių jutiklių taikymams.

4π FOKUSAVIMAS DAUGIAFOTONĖJE POLIMERIZACIJOJE

Šio skyriaus medžiaga publikuota [P2, PR3].

Daugiafotonė polimerizacija (MPP) yra unikali technologija, leidžianti gaminti praktiškai bet kokios geometrijos trimačius mikrodarinius, kurių erdvinė raiška gali būti mažesnė nei difrakcijos apribotas pluošto diametras [74]. Įprastai, šia technologija formuojamų darinių skersinė raiška gali siekti kelis šimtus nanometrų, tačiau išilginė raiška yra bent ~ 3 kartus didesnė nei skersinė, net ir naudojant aukštos skaitinės apertūros (NA) objektyvus [9, 142]. Optinėje mikroskopijoje pasiekiama skiriamoji raiška yra apribota difrakcijos dėsnio, suformuluoto dar XIX a. pab. E. Abės. Iš esmės, skersinė optinė raiška d_{xy} yra tiesiogiai proporcinga krintančiam šviesos bangos ilgiui ir atvirkščiai proporcinga NA: $d_{xy} = \lambda/2\mathrm{NA}$. Tuo tarpu išilginė skyra lygi $d_z = 2\lambda/(\mathrm{NA})^2$. Šios lygtys parodo, kad optikoje pasiekiama skiriamoji raiška išilgine beveik visada bus didesnė (žemesnė) nei skersine kryptimi. Šie optinės mikroskopijos principai yra panašūs, ir proporcingai galioja tiesioginio lazerinio rašymo technologijoje.

Tokia fokusuojamo taško (vokselio) matmenų anizotropija gali būti ribojantis veiksnys, kai kuriems taikymams, kaip pvz. fotoninių kristalų gamyboje, kur svarbūs ne tik skersiniai, bet ir išilginiai mikrodarinių matmenys. Isotropinė formuojamų darinių erdvinė raiška galėtų ženkliai pagerinti galutinę darinių kokybę bei funkcionalumą. Norint pagerinti raišką išilgine kryptimi, galima naudoti sudėtingesnius fokusavimo metodus, kaip STED (angl. *stimulated emission depletion*) mikroskopiją apjungiant su MPP technologija [142, 144].

Mikroskopijoje, kurioje fokusavimo principai yra panašūs kaip MPP technologijoje, skiriamąją gebą ašine kryptimi taip pat galima pagerinti naudojant 4π fokusavimą [147–149], kuomet šviesa surenkama iš to paties erdvinio taško dviem vienas prieš kitą fokusuojančiais aukštos NA objektyvais. Tokiu atveju, šviesa surenkama iš dvigubai didesnio erdvinio kampo, o tai leidžia pasiekti aukštesnę išilginę raišką. Pažymėtina, kad tokiu fokusavimo principu gaunamas centrinis maksimumas, apsuptas fiksuotu periodu nutolusiais šalutiniais maksimumais (angl. *sidelobes*) išilgai optinės ašies. Šių maksimumų skaičius tuo didesnis, kuo žemesnė objektyvų NA vertė. 4π mikroskopijos principai gali būti realizuoti ir MPP technologijoje.

Pirmiausia buvo atliktas teorinis modeliavimas siekiant apskaičiuoti intensyvumo pasiskirstymą fokusuojant su aukštos NA objektyvais. Prie didesnių NA objektyvo verčių, paraksialinis artinys nebegalioja. Dėl šios priežasties, fokusavimo su didesnės NA objektyvais atveju, norint apskaičiuoti taško sklaidos funkciją (TSF) reikia naudoti vektorinę Debajaus teoriją, kuri įskaičiuoja papildomus efektus (depoliarizaciją, sferines aberacijas, objektyvo apodizacijos funkciją). Teorinis modeliavimas paremtas Török ir Varga [158] teoriniu modeliu su papildomomis korekcijomis [159].

Teoriniame modelyje laikyta, kad krintanti šviesa yra tiesiškai poliarizuota, o lazerio pluoštas atitinka Gauso intensyvumo profilį. Objektyvu fokusuojama šviesa sklinda per sluoksniuotą aplinką, kaip parodyta 4.13 pav. (a). Pirmiausia, lazerio spinduliuotė keliauja oru (ar imersine alyva), tuomet per dengiamąjį stikliuką, kol galiausiai, šviesa sufokusuojama į polimero pirmtaką.

Bendru atveju, sprendinys elektriniam lauko vektoriui E fokusuojamo židinio taške (trečioje medžiagoje) gali būti išreikštas per skirtingas koordinačių sistema [147, 158, 160]:

$$E_p = E_3(u, v, \phi) = (E_{3x}, E_{3y}, E_{3z}). \tag{4.6}$$

Fokusuojant šviesą vienu objektyvu TSF tame pačiame taške gali būti aprašoma:

$$\mathrm{PSF}_{single} = |E_p|^2 = |E_{3x} + E_{3y} + E_{3z}|^2. \tag{4.7}$$

4π geometrijos fokusavimo sistemoje, galutinė TSF gali būti išreikšta taip [94]:

$$\mathrm{PSF}_{4Pi} = |E_{4Pi}(u, v, \phi)|^2 = |E_1(u, v, \phi) + E_2(-u, v, \phi)|^2, \tag{4.8}$$

kur E_1 ir E_2 yra elektrinis laukas generuojamas židinio taške pirmojo ir antrojo objektyvo, atitinkamai.

Skaitmeninis modeliavimas buvo atliktas naudojant skirtingas pradines sąlygas, prie skirtingų lazerio bangos ilgių bei keičiant fokusavimo sąlygas. Paprastumo dėlei 4π fokusavimo atveju, buvo laikoma, kad šviesa sklinda per tris skirtingas terpes tomis pačiomis sąlygomis abiem objektyvams. Pirmiausia, konverguojantys lazerio pluoštai sklinda oru (arba per imersinę alyva, kurios n = 1,518), tuomet per dengiamąjį stikliuką (n = 1,5071, stiklo storis = 165 µm), ir galiausiai SZ2080 polimero pirmtaką (n = 1,504; gylis = 5 µm). Apskaičiuotos TSF prie skirtingų pradinių sąlygų yra pavaizduotos 4.13 pav. (b-i). Pirmiausia, pateikiamas TSF fokusuojant su vienu objektyvu 0,8 NA bei 1030 nm lazerio bangos ilgiu (4.13 pav. (b)). Palyginimui pateikiamas 4π fokusavimas (žr. 4.13 pav. (c)) su analogiškomis pradinėmis sąlygomis. Matyti, kad abiem atvejais intensyvumo pasiskirstymas išilgine kryptimi atitinka panašią – elipsoido formą, tačiau 4π fokusavimo atveju, matomi periodiniai slopstančio intensyvumo kraštiniai maksimumai išilgai optinės ašies. Atstumas tarp kraštinių maksimumų priklauso nuo lazerio bangos ilgio, medžiagos lūžio rodiklio ir šiek tiek nuo objektyvų NA. Naudojant 0,8 NA ir n_3 = 1,504, apskaičiuotas atstumas tarp periodų siekė ∼360 nm, kai lazerio bangos ilgis 1030 nm. Tuo

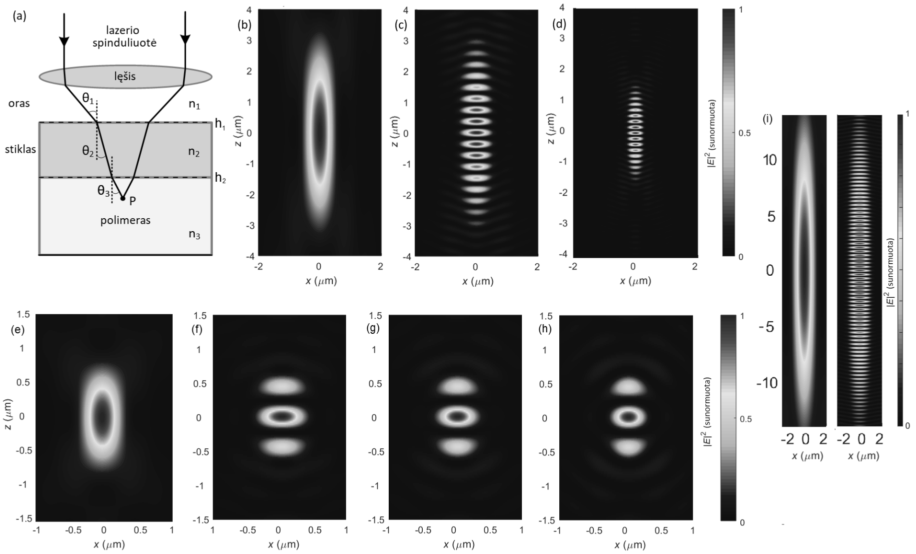

4.13 pav.: a) Schematinis vaizdas lazerio spinduliuotės fokusavimo per tris skirtingas terpes. Apskaičiuotos išilginės TSF palyginimas fokusuojant su (b) vienu 0,8 NA objektyvu, (c) 4π fokusavimu dviem 0,8 NA objektyvai su $\lambda =$ 1030 nm, ir (d) 515 nm lazerio bangos ilgiu. TSF modeliavimas XZ plokštumoje su 1,4 NA, su (e) standartiniu apšvietimu, ir 4π fokusavimu, kai 1030 nm lazerio spinduliuotė poliarizuota f) X-, (g) apskritimine ir (h) Y-kryptimi.

tarpu, tų pačių sąlygų ir 515 nm lazerio spinduliuotės naudojimas leistų išgauti dvigubai mažesnį vokselį, bei atstumą tarp periodų sumažinti du kartus – iki $\sim$180 nm (žr. 4.13 pav. (d)). Palyginimui, skaitmeninis modeliavimas buvo atliktas su 0,4 NA objektyvais bei 1030 nm lazerio bangos ilgiu, kurie 4π fokusavimo atveju duotų didesnį vokselį su dar didesniu kraštinių maksimumų skaičiumi 4.13 pav. (f).

Kraštinių maksimumų skaičių galima efektyviai sumažinti naudojant aukštesnės NA objektyvus. Tačiau net ir labai aštraus fokusavimo atveju naudojant 1,4 NA objektyvus, modeliavimas rodo (žr. 4.13 pav. (f)), kad išlieka kraštinių maksimumų pora su santykinai aukštais intensyvumais, kurie atitinka 64% centrinio maksimumo intensyvumo.

Nagrinėjant detaliau, atliktas skaitmeninis modeliavimas tiriant 4π fokusavimo sąlygomis generuojamų kraštinių maksimumų intensyvumo bei atstumo priklausomybę nuo skirtingų parametrų (objektyvų NA, lazerio bangos ilgio, bei N-fotonų sugerties). Lazerio bangos ilgis tiesiškai lemia atstumą tarp kraštinių maksimumų padėčių, kaip parodyta 4.14 pav. (a). Naudojant skirtingus lazerio bangos ilgius λ iš esmės galime keisti atstumus tarp kraštinių maksimumų padėčių, $\lambda =$ 1030 nm, 780 nm, 515 nm generuotų 420 nm, 320 nm, 210 nm periodą, atitinkamai. Trumpesnis bangos ilgis leistų generuoti siaures-

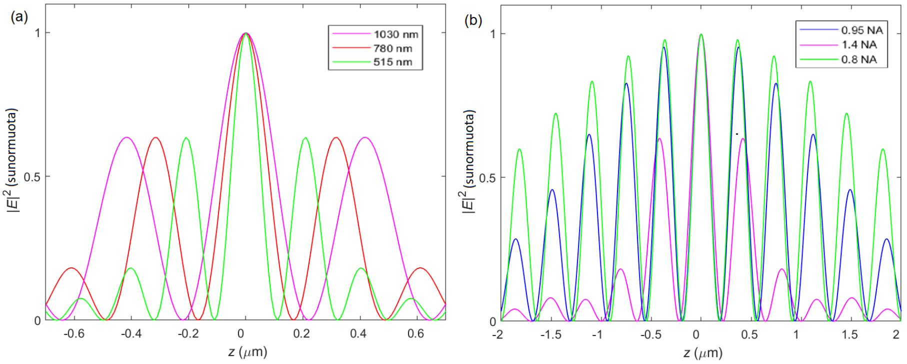

4.14 pav.: Fokusuojant 4π intensyvumo pasiskirstymas išilgai optinės z ašies priklausomai nuo (a) lazerio bangos ilgio (kai NA = 1,4), ir (b) nuo objektyvų NA (kai λ = 1030 nm).

nius centrinio bei kraštinių maksimumų intensyvumo profilius.

Reikia pažymėti, kad kraštinių maksimumų amplitudė nesikeičia nuo bangos ilgio, bet stipriai priklauso nuo fokusavimo sąlygų (t.y. objektyvo NA), kaip galime matyti 4.14 pav. (b). Šiuo atveju, kai lazerio bangos ilgis – 1030 nm, pasirinktos didesnės NA vertės, kurios atitinka MPP aplikacijai dažnai naudojamų objektyvų nominalias vertes (0,8 NA, 0,95 NA, 1,4 NA). Iš teorinio modeliavimo rezultatų galime matyti generuojamų kraštinių maksimumų skaičius bei jų intensyvumo vertė kinta. Reikia atkreipti dėmesį, kad atstumas tarp kraštinių maksimumų padėčių šiek tiek slenkasi nuo NA vertės. Stebimas didesnis atstumas tarp generuojamų pasikartojančių pūpsnių, kai fokusavimas "aštresnis". Naudojant 1030 nm lazerio bangos ilgį, 4π fokusavimas su 1,4 NA objektyvais atitiktų 420 nm atstumą tarp maksimumų, kai 0,95 NA – 370 nm, 0,8 NA – 360 nm, atitinkamai.

Nors kraštinių maksimumų intensyvumas išlieka santykinai nemažas, tačiau 4π fokusavimo atveju daugiafotonėje polimerizacijoje, prie mažesnių ekspozicijos dozės verčių būtų galima pasiekti, kad polimerizacijos slenkstis būtų viršytas tik centrinio maksimumo. Tuo tarpu kraštinių maksimumų intensyvumas neviršytų šios vertės ir jų poveikis galutiniam dariniui nebūtų matomas. Tokiu atveju, daugiafotonėje polimerizacijoje būtų galima pasiekti beveik sferinį fokusuojamą erdvinį tašką ir stipriai pagerinti išilginę darinių raišką.

Norėdami eksperimentiškai patikrinti teorinius modeliavimo rezultatus, į tradicinę MPP sistemą integravome 4π fokusavimą. Principinė eksperimento schema pavaizduota 4.15 pav. (a, b). Buvo naudojama Yb:KGW lazerio sistema, kurios bangos ilgis buvo 1030 nm, impulsų trukmė - 180 fs, o impulsų pasikartojimo dažnis - 200 kHz. Lazerio spindulys buvo padalintas į du vienodo intensyvumo spindulius 50:50 pluošto dalikliu. Atskirti pluoštai buvo nukreipti skirtingais optiniais keliais ir fokusuojami į SZ2080 polimero pirmtaką dviem

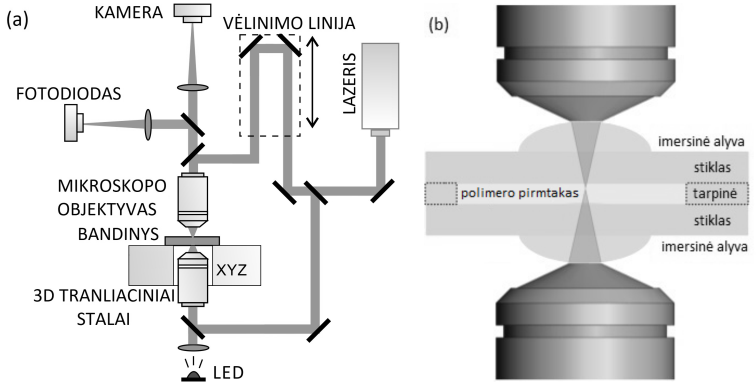

4.15 pav.: (a) Schematinis 4π-MPP eksperimentinės įrangos brėžinys naudojant aukštos NA objektyvus, (b) detalesnis vaizdas lazerio spinduliuotės 4π fokusavimo atveju per tris terpes: imersinę alyva, stiklą, bei polimero pirmtaką.

identiškais objektyviais (20×/0,8 NA; 63×/1,4 NA). 4π fokusavimo atveju, fokusuojami lazerio pluoštai turi sutapti erdvėje, o taip pat skirtingų pluoštų femtosekundiniai lazerio impulsai turi idealiai būti perkloti laike.

4π-MPP eksperimentai buvo atlikti su neigiamo tipo fotopolimeru SZ2080 [161] su 0,5% (4,4’-bis(diethylamino)benzophenone) fotoiniciatoriumi. Šio polimero lūžio rodiklis yra apie 1,5, 632,8 nm šviesos bangos ilgiui [86]. Bandinių paruošimas vyko polimerą užlašinant ant standartinio dengiamojo stiklo, kurio storis buvo apie 170 µm. Tuomet bandiniai buvo pakaitinami. Siekiant užtikrinti fiksuotą polimero storį didesniame plote, ant dengiamojo stikliuko taip pat buvo dedama papildoma U-formos 100 µm storio stiklo tarpinė. Galiausiai, visa struktūra uždengiama antruoju 170 µm storio dengiamuoju stiklu. Po įrašymo proceso mėginiai apie 1 val. buvo įmerkiami į 4-metil-2-pentanono tirpiklį, kad lazerio šviesos nepaveiktos sritys būtų išplautos. Vėliau, bandiniai buvo merkiami į etanolį ir išdžiovinami naudojant kritinio taško džiovintuvą.

Siekiant pasižiūrėti išilginę darinių raišką buvo formuojami mikrobokšteliai, kurių matmenys buvo 5×5×25 µm. Kiekvienas bokštelis buvo daromas sluoksniais rastriniu skenavimu su 0,5 µm perklojimu tarp gretimų linijų bei 4,5 µm atstumais tarp gretimų sluoksnių. Formavimo metu naudoti 0,8 NA objektyvai ir 0,6 mW lazerio vidutinė galia kiekvienam iš objektyvų. Po ryškinimo proceso, analizuojant bandinius su SEM, buvo matyti, kad periodiniai dariniai išilgai optinės ašies išlieka. Išmatuotas atstumas tarp periodinių sluoksnių buvo $\sim$340 nm ir neblogai atitiko teorinio modeliavimo apskaičiuotą vertę (360 nm). Teorinių skaičiavimų vertė buvo 5% mažesnė nei eksperimentiškai gauta, šis nors ir nedidelis nesutapimas galėtų būti aiškinamas dėl fotopolimero traukimosi reiškinio, ar šiek tiek kitokia fotopolimero lūžio rodiklio verte, nei naudota skaičiavimuose.

Tyrinėjant detaliau periodinę darinio sandarą, buvo padarytas analogiškų matmenų bokštelių masyvas, keičiant tik skenavimo atstumą tarp gretimų sluoksnių. Šis dydis S_z buvo keičiamas nuo 1 iki 10 µm, kas 0,1 µm. Reikia pažymėti, kad vokselio išilginis matmuo d_z bet kuriuo atveju buvo didesnis nei atstumas tarp sluoksnių. Buvo gauta, kad periodiniai sluoksniai išilgai optinės ašies išlieka net labai tankaus ($S_z \gg d_z$) skenavimo atveju, kaip matyti 4.16 pav. (d). Tuo tarpu, retesnio (7 µm) skenavimo atveju (žr. 4.16 pav. (e-f)), tarpinės sluoksnių zonos pasižymėjo silpniau sutankintomis vietomis, kurios po ryškinimo proceso buvo linkusios atsiskirti.

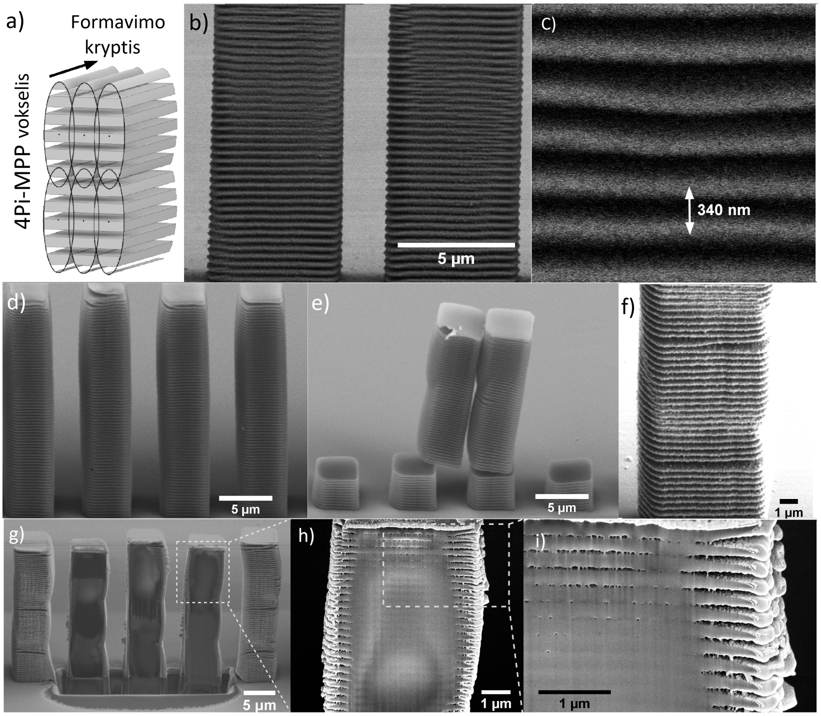

4.16 pav.: (a) Principinis mikrobokštelių formavimo brėžinys, bei (b-c) tokio suformuoto mikrodarinio SEM vaizdas iš šono naudojant 4π-MPP metodą. Išmatuotas atstumas tarp interferencinių maksimumų atitiko 340 nm. Interferenciniai maksimumai mikrodariniuose išliko (g) net ir tankaus skenavimo tarp gretimų sluoksnių atveju (1 µm). Tuo tarpu, (e-f) retesnio (7 µm) skenavimu atveju, bokšteliai tarp sluoksnių pasižymėjo silpniau sutankintomis vietomis, kurios po ryškinimo proceso buvo linkusios atsiskirti. (g-i) Mikrobokštelių skerspjūvis gautas naudojant sufokusuotą jonų pluoštą (FIB).

Vėliau, dalis mikrobokštelio buvo nupjauta, naudojant sufokusuotą jonų pluoštą (FIB), kuris leido pažvelgti į vidinę tokio mikrodarinio sandarą, kaip pavaizduota 4.16 pav. (g-i). Skerspjūvis išilgai darinio Z ašies, atskleidė, kad darinys nėra vientisas. Buvo matyti, kad paviršinį ploną sluoksnį sudaro fiksuoto periodo oro/polimero sluoksniai. Tuo tarpu, tolyn link darinio centrinės dalies, stebėta, kad oro tarpai pereina į supolimerizuotas sritis. Vis dėlto, periodiniai sluoksniai išliko matomi, parodantys, kad šios sritys yra supolimerizuotas skirtingu monomerų konversijos laipsniu. Tikėtina, kad ryškinimo metu tirpiklis negali efektyviai įsiskverbti į darinio tūrį ir išplauti žemesniu monomerų konversijos laipsniu supolimerizuotų sričių.

Buvo pastebėta, kad plonuose dariniuose šios sritys gali būti pilnai išplautos, taip išgaunant periodinę oro/polimero sluoksnių sandarą – gardelę. Tokiu principu formuojant linijas tarp standžių atramų, naudojant 4π fokusavimą vienu skenavimu galėtų būti suformuota daugybė apibrėžto storio ir periodo kabančių linijų išilgai optinės ašies. Tai buvo išbandyta eksperimentiškai: pirmiausia suformuotas darinys iš periodinių (kas 8 µm) atraminių sienų, kurių plotis buvo 4 µm, o ilgis 75 µm. Tuomet, vienu lazeriniu skenavimu naudojant 4π-MPP metodą, buvo suformuotas atskirų linijų masyvas tarp atraminių sienų. Tokiu principu, dėl 4π fokusavimo tik vienu skenavimu įrašyta linija tarp atramų susidėtų iš daugybės polimerinių plokštumų su tiksliai apibrėžtu atstumu tarp jų. Dariniai, sudaryti iš periodiškai kintančio lūžio rodiklio sričių, galėtų lemti Brego atspindį krintančiai šviesai. Atspindėtą šviesos bangos ilgį galima apskaičiuoti pagal Brego lygtį. Tuo atveju, jei krintanti šviesa yra statmena iš periodinių sluoksnių sudarytam dariniui, sąryšis būtų toks [153]:

$$m\lambda = 2(n_1 d_1 + n_2 d_2), \tag{4.9}$$

kur m – difrakcijos eilė, d_1, d_2 žymi storį ir lūžio rodiklį n_1, n_2 skirtingiems medžiagų sluoksniams, atitinkamai.

Po ryškinimo procedūros, šis darinys buvo tiriamas optiniu mikroskopu atspindžio režimu. Buvo stebimos tam tikros struktūrinės spalvos mėlynoje/žalioje spektro dalyje generuojamos tokios gardelės (žr. 4.17 pav. (c)). Vėliau, šio darinio SEM analizė parodė, kad vieno skenavimo metu suformuota linija susidėjo iš daugybės pasikartojančių polimerinių plokštumų su oro tarpais tarp jų, kaip parodyta 4.17 pav. (b). Polimerinio sluoksnio storis siekė apytiksliai 180 nm, o oro sluoksnis buvo apie 160 nm. Pagal formulę 4.9, jei polimero lūžio rodiklis $n = 1{,}504$, tokia periodinė gardelė generuotų pirmos eilės Brego atspindį 860 nm, tuo tarpu antros eilės difrakcija atspindėtų 430 nm šviesos bangos ilgį. Išmatuotas tokios gardelės atspindžio spektras regimojoje spektro srityje pateiktas 4.17 pav. (d). Matyti, kad yra dvi gana plačios atspindžio smailės – artimojoje infraraudonojoje bei mėlynoje spektro srityse. Iš esmės, platus atspindžio spektras galėtų būti paaiškintas dėl kintančio atstumo tarp gretimų sluoksnių, kaip matyti iš SEM nuotraukų (4.17 pav. (b)). Submikrometrinio storio ir pločio linijos galėjo būti deformuotos ryškinimo procesu metu.

Vėlesni 4π-MPP eksperimentai buvo atliekami naudojant 1,4 NA objektyvus siekiant išgauti aukštesnę formuojamų darinių išilginę raišką bei kartu sumažinti vokselio pločio/aukščio santykį. Remiantis skaitmeninio modeliavimo

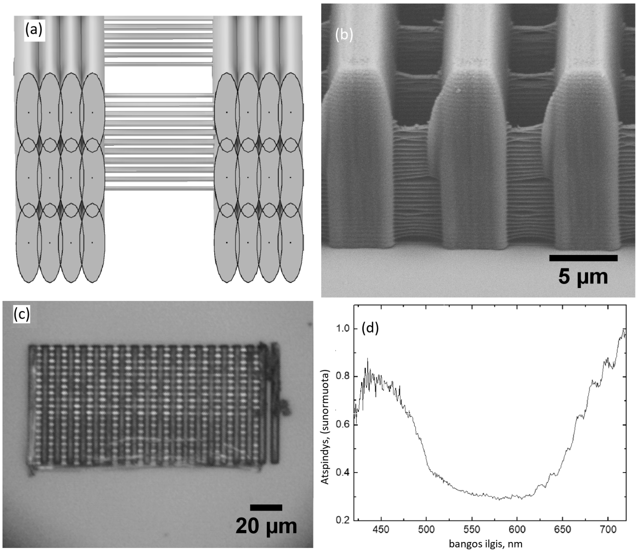

4.17 pav.: (a) Schematinis gardelės formavimo brėžinys, (b) SEM vaizdas kampu suformuoto darinio, (c) atspindžio režimu veikiančio optinio mikroskopo užregistruotas atvaizdas, bei (d) atspindžio spektras regimojoje spektro srityje.

rezultatais, buvo tikimasi, kad aukštesnės NA objektyvai leis ženkliai sumažinti generuojamų šalutinių maksimumų skaičių, kol galiausiai parinkus tinkamą lazerio ekspozicijos vertę, tik centrinio maksimumo pasiektas intensyvumas viršys polimerizacijos slenksčio ribą. Šiems eksperimentams ant dengiamojo stikliuko buvo suformuotas bokštelių masyvas, tarp kurių buvo išskenuojama viena linija su vis laipsniškai mažėjančia lazerio vidutine galia tarp bokštelių.

Prie didesnių lazerio vidutinės galios verčių, buvo gautos kelios kabančios linijos išilgai optinės ašies. Išmatuotas periodas tarp gretimų linijų buvo 410 nm, kai tuo tarpu skaitmeninio modeliavimo rezultatai numatė 420 nm naudojant 1030 nm lazerio bangos ilgį. Mažinant lazerio vidutinę galią, buvo stebimas vis mažėjantis šių periodinių linijų skaičius. Galiausiai prie 40 μW buvo formuojama tik viena linija. SEM analizė parodė, kad tokios suformuotos linijos išilginė skyra siekė 150 nm ir buvo mažesnė nei skersinis matmuo – 200 nm, kaip parodyta 4.18 pav. (a). Tokiu atveju, suformuotos linijos pločio/aukščio santykis sumažėjo iki 1:0,75. Rezultatų palyginimui, buvo padaryta analogiški eksperimentai su vienu objektyvu, kurie leido išgauti taip pat 200 nm skersinę formuojamų darinių raišką, tačiau išilginis matmuo šiuo atveju siekė 450 nm. Taip pat, eksperimentas atliktas su 4π fokusavimu atskyrus lazerio impulsus laike, kuris geriausiu atveju leido pasiekti 260 nm ir 560 nm skersinę ir išilginę formuojamų darinių raišką, atitinkamai.

Pirmą kartą pademonstruotas 4π fokusavimas daugiafotonės polimerizacijos

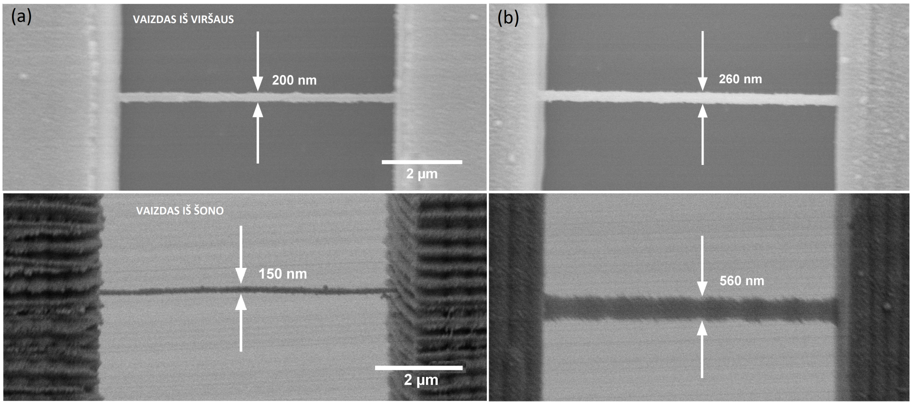

4.18 pav.: SEM vaizdas iš viršaus ir šono suformuotos linijos fokusuojant 4π sąlygomis, kai lazerio impulsai yra (a) perkloti ir (b) atskirti laike.

technologijoje, kuris leido naudojant aukštos (NA = 1,4) skaitinės apertūros objektyvus SZ2080 fotopolimere suformuoti 150 nm išilginę darinių raišką, tuo tarpu skersinė buvo 200 nm. Įprasto fokusavimo su vienu objektyvu atveju, gauta aukščiausia darinių raiška išilgine kryptimi buvo 3 kartus prastesnė (450 nm), o skersine buvo identiška – 200 nm. Naudojant 1030 nm lazerio bangos ilgį ir 4π fokusavimą su žemesnės skaitinės (NA = 0,8) apertūros objektyvais leido suformuoti submikrometrinio dydžio periodinius (340 nm) darinius išilgai optinės ašies.

DINAMINIS VOKSELIO DYDŽIO VALDYMAS

Šio skyriaus medžiaga publikuota [P3].

MPP technologija leidžia gaminti sudėtingos formos 3D mikrodarinius, kurių formuojamų darinių erdviniai matmenys gali siekti kelis šimtus nanometrų. Tačiau MPP technologijos vienas iš pagrindinių trūkumų yra palyginti žemas našumas, ypač naudojant didesnės skaitinės apertūros (NA) objektyvus. Daugiafotonėje polimerizacijoje galioja panašūs principai kaip ir 3D spausdinimo technologijoje: norimas suformuoti 3D darinys yra sudalinamas į daugybę sluoksnių, o kiekvienas sluoksnis sudarytas iš atskirų linijų. Atstumas tarp gretimų linijų ir sluoksnių parenkamas toks, kad vokselis pilnai perklotų prieš tai įrašytą suformuotą liniją. Tokiu atveju, didesni vokseliai gali būti parenkami didesnių matmenų, mažesnės raiškos reikalaujantiems dariniams gaminti. Tačiau, mažesnės kritinės detalės turi būti įrašomos su aukščiausia raiška. Tokiu atveju, norint formuoti aukšta submikrometrine erdvine raiška, didesnių matmenų (mm) mikrodarinių gamyba užtruktų neracionaliai ilgą laiką.

Vis dėlto, šiai problemai spręsti yra pasiūlyti įvairūs šios technologijos spartinimo metodai, kurie leidžia pagreitinti darinių formavimo procesą. Kaip pavyzdžiui, skirtingų NA objektyvų kombinavimas [166], skirtingo profilio pluošto generavimas (e.g., Beselio [167] ar Airy [168]), paraleliai generuojamų židinio taškų matrica [169,170], interferencinė litografija [172], ir kiti metodai [146,171]. Technologijos našumas gali būti padidintas naudojant 5-ašių lazerines sistemas, kai judinamas bandinys ne tik XYZ poslinkio stalais, bet ir lazerio pluoštas tuo pačiu metu skenuojamas visame objektyvo matymo lauke [173]. Taip pat, yra pasiūlyti ir kiti spartinimo metodai, kaip paviršinio sluoksnio formavimas, vėliau likusią darinio tūrį supolimerizuojant UV spinduliuote [174].

Kaip alternatyva esamiems MPP metodams, buvo pasiūlytas naujas nesudėtingas būdas dinamiškai valdyti vokselio dydį keičiant kritusio į objektyvą pluošto diametrą motorizuotu pluošto plėstuvu.

Įprastai MPP technologijoje lazerio pluoštas yra išplečiamas, kad pilnai užpildytų objektyvo įėjimo apertūrą ir būtų pasiekta aukščiausia pasiekiama darinių raiška. Tokiu atveju, vokselio dydis iš esmės yra apibrėžtas objektyvo NA. Žinoma, formuojamo darinio erdvinius matmenis galima valdyti keičiant ekspozicijos dozę formavimo lango ribose. Jei lazerio pluoštas nepilnai užpildo objektyvo įėjimo apertūrą, tai efektyvi objektyvo skaitinė apertūra $\mathrm{NA}_{\mathrm{eff}}$ sumažės ir lems didesnį generuojamą vokselį. Šis $\mathrm{NA}_{\mathrm{eff}}$ dydis iš esmės gali būti apskaičiuojamas pagal sąryšį $\mathrm{NA}_{\mathrm{eff}} = n \sin\theta_{\mathrm{max}}$, kur n – terpės lūžio rodiklis, kuria sklinda fokusuojama šviesa, θ_{max} – yra maksimalus kritusių spindulių kampas. Tokiu principu, keičiant kritusio lazerio pluošto diametrą, galima valdyti vokselio dydį. Prie mažesnių θ_{max} kampo verčių galioja paraksialinis artinys ir vokselio dydį galima apskaičiuoti pagal skaliarinį modelį [9].

Gauso pluošto erdvinį intensyvumo skirstinį galima aprašyti taip:

$$I(r,z) = I_0 \frac{\omega_0^2}{w(z)^2} \mathrm{e}^{\frac{-2r^2}{w(z)^2}}, \tag{4.10}$$

kur r yra radialinė koordinatė, z – pozicija išilgai optinės ašies, ω_0 - pluošto radiusas sąsmaukoje. $\omega(z)$ – pluošto radiuso kitimas išilgai optinės ašies z:

$$\omega(z) = \omega_0 \sqrt{1 + \left(\frac{z}{z_0}\right)^2}; \tag{4.11}$$

Tuo tarpu sufokusuoto lazerio dėmės dydis gali būti apskaičiuojamas pagal sekančią formulę, lazerio pluošto dėmės dydis naujoje pozicijoje ($1/e^2$ intensyvumo lygyje):

$$\omega_0' = \sqrt{\frac{\lambda z_0}{\pi}} = \frac{\lambda f}{\pi D}, \tag{4.12}$$

o Relėjaus ilgis gali būti išreikštas (50% intensyvumo lygyje):

$$2z_0 = 2\frac{n\pi {\omega'_0}^2}{\lambda} = 2\frac{n\lambda}{\pi}\left(\frac{f}{D}\right)^2, \tag{4.13}$$

kur λ - lazerio bangos ilgis, f - objektyvo efektyvus židinio nuotolis, D - lazerio pluošto diametras prieš lęšį/objektyvą.

Kita vertus, MPP technologijoje naudojami daugiausia aukštos NA objektyvai, kad būtų galima išgauti aukštą darinių raišką. Maksimalus kritusių spindulių kampas $\theta_{\max}$ pakankamai didelis ir paraksialinis artinys nebetinkamas naudoti. Norint tiksliai įvertinti intensyvumo pasiskirstymą fokusuojant su aukštos NA objektyvais, tokiu atveju reikia įskaičiuoti sferinių aberacijų ir poliarizacijos reiškinių įtaką. Šiam tikslui naudojama vektorinė Debajaus teorija [9, 157].

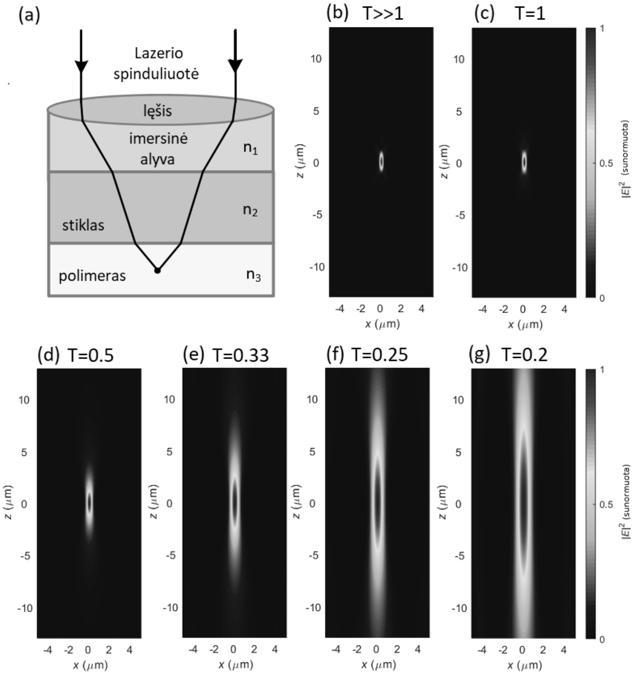

4.19 pav.: (a) Schematinis vaizdas lazerio spinduliuotės fokusavimo per tris skirtingas terpes. Apskaičiuotos TSF vektoriniu modeliu 0,95 NA objektyvui su λ=515 nm lazerio bangos ilgiu bei skirtingais objektyvo apertūros užpildymo T parametru: (b) $T \gg 1$, (c) $T = 1$, (d) $T = 0{,}5$, (e) $T = 0{,}33$, (f) $T = 0{,}25$, (g) $T = 0{,}2$.

Atliktas teorinis modeliavimas intensyvumo skirstiniui suskaičiuoti prie skirtingų objektyvo apertūros užpildymo (T) verčių naudojant tiek vektorinį, tiek skaliarinį modelį. Vektorinis modelis įskaičiuoja poliarizacijos įtaką (mūsų atveju buvo naudota apskritiminė), ir sferines aberacijas dėl sluoksniuotos

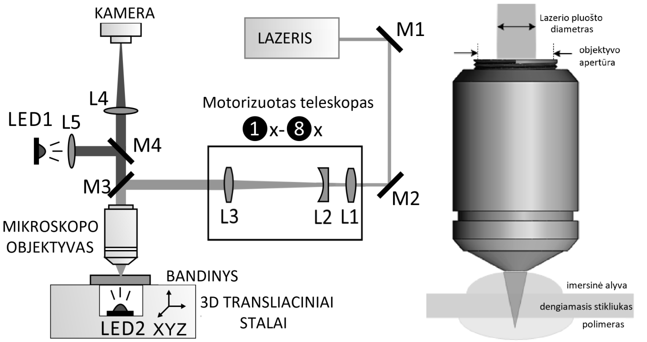

4.20 pav.: (a) Schematinė tiesioginio lazerio rašymo sistema su motorizuotu pluošto plėstuvu (1-8× plėtimo santykis) naudojant aukštos NA objektyvą. M1-M4 – veidrodėliai; L1-L4 – lęšiai.

struktūros, kaip parodyta 4.19 pav. (a). TSF pateiktos esant skirting objektyvo apertūros užpildymo T vertėms (nuo 0,2 ir daugiau nei 1) 4.19 pav. (b-g) (kai parametrai NA = 0,95, λ = 515 nm). Matyti, kad tokiomis sąlygomis naudojant vieną objektyvą vokselio išilginį matmenį galima keisti proporcingai nuo užpildymo vertės nuo kelių iki keliasdešimt mikrometrų.

Eksperimentams naudota komercinė lazerinė sistema (Laser Nanofactory, Femtika Ltd.) su Yb:KGW femtosekundiniu lazeriu (Carbide, Light Conversion Ltd.). Buvo naudojamas 515 nm lazerio bangos ilgis, impulsų trukmė 250 fs, o impulsų pasikartojimo dažnis - 1 MHz. Principinė eksperimento schema pavaizduota 4.20 pav. (a). Pradinis lazerio pluošto radiusas (0,55 mm intensyvumo lygyje $1/e^2$) buvo išplečiamas motorizuoto objektyvo. Tuomet, išplėstas pluoštas nukreipiamas į objektyvo įėjimo apertūrą ir lazerio spinduliuotė nukreipiama į fotojautraus polimero pirmtako tūrį.

Eksperimentams naudotas SZ2080 polimero pirmtakas, kuris buvo fotojautrintas su 1%wt IRG fotoiniciatoriumi. Pirmiausia bandinys atkaitinamas 40°C, 70°C, ir palaikytas 90°C temperatūroje 1 h. Po lazerio eksponavimo, bandinys išryškintas 4-metil-2-pentanone ryškiklyje.

Vokselio matmenims nuo objektyvo apertūros užpildymo tirti naudojome kabančių linijų masyvą tarp gretimų atraminių bokštelių, kaip matyti 4.21 pav. Kiekvienu skirtingu apertūros užpildymo atveju, linijos suformuotos nuo polimerizacijos iki polimero pažeidimo slenksčio. Vėliau, šių linijų skersiniai ir išilginiai matmenys buvo fiksuojami SEM mikroskopu. 4.21 pav. pateikti vokselio kitimo dinamika keičiant objektyvo užpildymą, kai $\mathrm{NA}_{\mathrm{eff}}$ yra (a) 1,4 ir (b) 0,32.

4.22 pav. parodo tiek teorinius rezultatus skaičiuotus su skaliariniu ir vektoriniu modeliu, tiek ir eksperimentinius rezultatus. Modeliavimas atliktas su 0,8 NA ir 1,4 NA objektyvais, kai lazerio bangos ilgis λ=515 nm. Kaip matyti

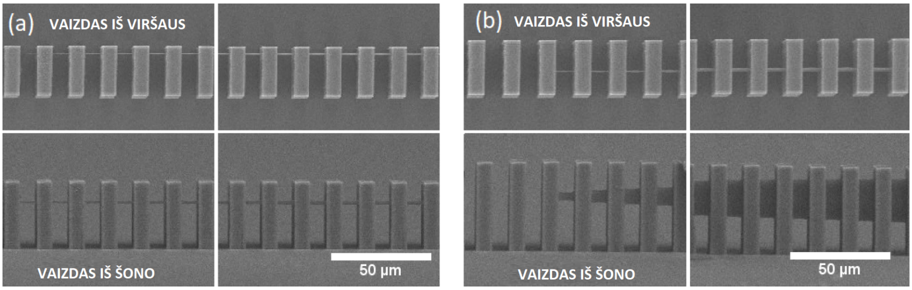

4.21 pav.: SEM vaizdas iš viršaus ir šono kabančių linijų masyvo tarp atraminių bokštelių, kai NA_{eff} = (a) 1,4 ir (b) 0,32. Linijų masyvas rodo vokselio didėjimo dinamiką formuojant arti (*kairėje*) polimerizacijos ir (*dešinėje*) pažeidimo slenksčio.

iš 4.22 pav. (a), prie mažesnių iki 0,7 objektyvo įėjimo apertūros užpildymo vertės T matyti, kad abiejų teorinių modelių vokselio dydžio rezultatai gerai sutampa. Viršijus šią T vertę, paraksialinis artinys nustoja galioti, o skaliarinio modelio rezultatai tolsta nuo vektorinio modelio verčių. Todėl prie didesnių NA_{eff}, tik vektorinis modelis turi būti naudojamas norint tiksliau įvertinti fokusuojamo taško matmenis. Eksperimentinės polimerizacijos slenkstinės vertės, gautos prie skirtingo užpildymo faktoriaus, atitiko teorinių rezultatų dinamiką. Panašios tendencijos buvo matyti ir su 0,8 NA objektyvu, kaip parodyta 4.22 pav. (b), šiuo atveju nesutapimas tarp skaliarinių ir vektorinių modelių buvo pradedamas matyti ties T~0,55 verte.

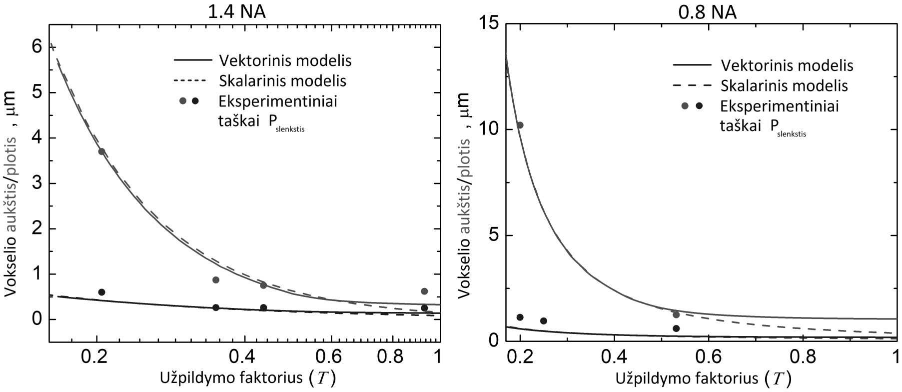

4.22 pav.: Apskaičiuotos vokselio dydžio priklausomybė nuo užpildymo faktoriaus (T) vertės, skaičiuojant su vektoriniu ir skaliariniu modeliais, kai NA = (a) 1,4 ir (b) 0,8. Atskiri taškai atitinka eksperimentinius rezultatus gautus prie skirtingų objektyvo apertūros užpildymo verčių.

Dinaminio diapazono kitimas, nuo polimerizacijos iki pažeidimo slenksčio, esant skirtingoms objektyvo apertūroms užpildymo sąlygoms buvo atliktas su

1,4 NA objektyvu, rezultatai pavaizduoti 4.23 pav. (a, b). Eksperimentinėje schemoje naudotas motorizuotas teleskopas leido varijuoti lazerio spindulio išplėtimą nuo 8× iki 1×, o tai leido turėti 1,4 NA_{eff} pilnai užpildant objektyvo įėjimo apertūrą, tuo tarpu, neišplėstas pluoštas (1× didinimas) sumažino NA_{eff} atitinkamai iki 0.32 vertės. 1.4 NA_{eff} leido pasiekti aukštą darinių raišką, tačiau formavimo langas keičiant lazerio ekspozicijos dozę buvo pakankamai siauras, kuris leido darinių skersinius matmenis keisti nuo 0,25 µm iki 0,5 µm, o išilginius – 0,62 µm iki 1,27 µm. Priešingu atveju, mažiausias lazerio pluošto didinimas (NA_{eff} = 0,32) leido pasiekti didesnius vokselio matmenis: nuo 0,6 µm iki ∼2 µm skersine ir nuo 3,7 µm iki 22 µm išilgine kryptimi. Iš esmės, toks dinaminis objektyvo NA_{eff} keitimas leistų tam pačiam objektyvui turėti galimybę formuoti darinius tiek su aukštos, tiek ir žemos raiškos režimu, bei leistų išplėsti formavimo lango ribas.

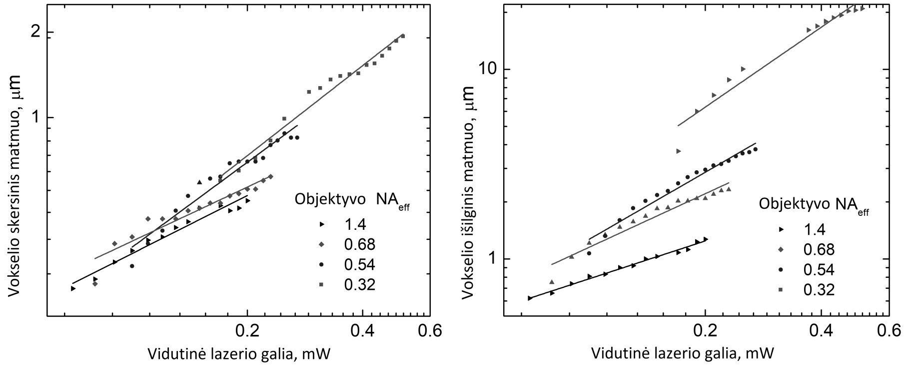

4.23 pav.: Išmatuoti (a) skersiniai ir (b) išilginiai vokselio erdviniai matmenys keičiant to pačio (1,4 NA) objektyvo NA_{eff} visame formavimo lango diapazone.

Norėdami parodyti galimas keičiamo vokselio viename darinyje galimybes, mes pagaminome rąstu rietuvės geometrijos gardelę, kuri suformuota su dviem skirtingo vokselio dydžio segmentais, kaip parodyta 4.24 pav. Apatinė ir viršutinė dalys buvo pagamintos su d_{xy}=5 µm tarpais tarp linijų ir d_z=6 µm tarp gretimų sluoksnių, NA_{eff}=0,54 bei su vidutine lazerio galia P=0,4 mW. Kai tuo tarpu vidurinė dalis su d_{xy}=2,5 µm, d_z=1,5 µm, NA_{eff}=1,23, P=0,12 mW. Įrašymo greitis buvo fiksuotas ir siekė 100 µm/s.

Tiesioginio lazerinio rašymo metode pademonstruota, jog keičiant kritusio lazerio pluošto diametrą motorizuotu teleskopu galima efektyviai keisti skersinius ir išilginius formuojamo darinio matmenis plačiame diapazone. Naudojimas 1,4 NA objektyvo, pilnai padengto objektyvo įėjimo apertūros lazerio pluoštų,

Naudojant 1,4 NA objektyvą su pilnu objektyvo įėjimo apertūros užpildymu lazerio pluoštu, leido pasiekti aukštą darinių raišką: 0,25 µm skersine ir 0,62 µm išilgine kryptimi. Tuo tarpu, siauriausio lazerinio pluošto diametras

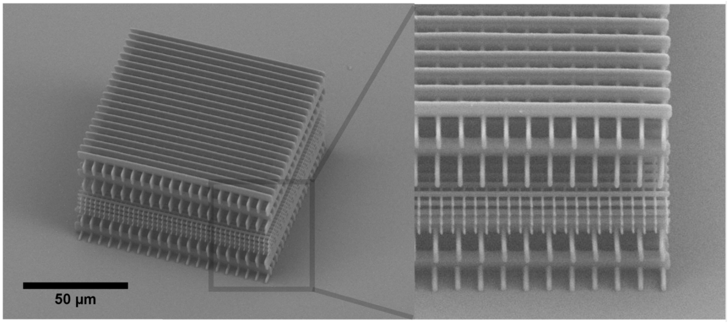

4.24 pav.: Rąstu rietuvės geometrijos gardelės atvaizdas, užregistruotas SEM mikroskopu. Darinys suformuotos su dviem skirtingais vokselio dydžio segmentais: apatinė ir viršutinė dalys pagamintos su $\mathrm{NA}_{\mathrm{eff}}$=0,54, o vidurinė – su $\mathrm{NA}_{\mathrm{eff}}$=1,23.

(kurį sistema leido pasiekti) leido sumažinti $\mathrm{NA}_{\mathrm{eff}}$ vertę iki 0,32 vertės tam pačiam objektyvui. Tokiu atveju, formuojamų žemiausia darinių raiška siekė $\sim$2 µm skersine ir 22 µm išilgine kryptimi.

PAGRINDINIAI REZULTATAI IR IŠVADOS

1. Pademonstruotas naujo tipo stiklo/polimero mikromechaninis jutiklis, pasitelkiant selektyvaus lazerinio ėsdinimo bei daugiafotonės polimerizacijos technologijas. Šis jutiklis tinkamas tiriant daugiafotone polimerizacija suformuotų polimerinių mikrodarinių elastines savybes.

2. Eksperimentiškai pademonstruota, kad daugiafotone polimerizacija suformuoti polimeriniai dariniai gali patirti traukimosi/brinkimo reiškinius skirtingose skystose terpėse. Priklausomai nuo ekspozicijos dozės, polimerinių mikrodarinių Jungo modulis gali būti varijuojamas nuo 0,4 GPa iki 2 GPa intervale 4-metil-2-pentanone. SZ2080 polimerinio darinio mechaninės savybės priklauso nuo jį supančios aplinkos terpės, rezultatai rodo mažesnę Jungo modulio vertę ore, nei organiniuose skysčiuose.

3. Daugiafotone polimerizacija suformuotų polimerinių darinių deformacijos yra grįžtamosios skirtinguose skysčiuose. Po kelių pakeitimo ciklų tarp skirtingų skysčių, polimerinių darinių elastinės savybės yra atsikartojančios, tai galėtų būti panaudota cheminių jutiklių taikymams.

4. Pirmą kartą pademonstruotas 4π fokusavimas daugiafotonės polimerizacijos technologijoje. Mažesnės (NA = 0,8) skaitinės apertūros objektyvai leidžia suformuoti submikrometrinio dydžio periodinius darinius orientuotus išilgai optinės ašies. Naudojant 1030 nm lazerio bangos ilgį, atstumas tarp periodinių darinių siekė 340 nm.

5. Pademonstruota, kad 4π fokusavimas daugiafotonės polimerizacijos technologijoje naudojant aukštos (NA = 1,4) skaitinės apertūros objektyvus SZ2080 polimero pirmtake leidžia pasiekti 150 nm išilginę darinių raišką, kuri buvo iki 3 kartų aukštesnė nei naudojant standartines fokusavimo sąlygas.

6. Tiesioginio lazerinio rašymo metode pademonstruota, jog keičiant kritusio lazerio pluošto diametrą motorizuotu pluošto plėstuvu galima dinamiškai keisti formuojamo darinio matmenis. Nepilnas objektyvo įėjimo apertūros užpildymas lazerio pluoštu lemia efektyvų NA sumažėjimą. Pademonstruota, kad naudojant 1,4 NA objektyvą, vokselio matmenys gali būti keičiami nuo 0,25 µm iki ∼2 µm skersine ir 0,62 µm to ∼22 µm išilgine kryptimi.

Bibliography

[1] J. Hecht, A short history of laser development, Appl. Opt. **49**(25), F99–F122 (2010).

[2] K. M. Davis, K. Miura, N. Sugimoto, K. Hirao, Writing waveguides in glass with a femtosecond laser, Opt. Lett. **21**(21), 1729–1731 (1996).

[3] S. Maruo, O. Nakamura, S. Kawata, Three-dimensional microfabrication with two-photon-absorbed photopolymerization, Opt. Lett. **22**(2), 132–134 (1997).

[4] L. Sudrie, M. Franco, B. Prade, A. Mysyrowicz, Writing of permanent birefringent microlayers in bulk fused silica with femtosecond laser pulses, Opt. Commun. **171**(4-6), 279–284 (1999).

[5] Y. Shimotsuma, P. G. Kazansky, J. Qiu, K. Hirao, Self-organized nanogratings in glass irradiated by ultrashort light pulses, Phys. Rev. Lett. **91**(24), 247405 (2003).

[6] A. Marcinkevičius, S. Juodkazis, M. Watanabe, M. Miwa, S. Matsuo, H. Misawa, J. Nishii, Femtosecond laser-assisted three-dimensional microfabrication in silica, Opt. Lett. **26**(5), 277–279 (2001).

[7] J. Bonse, S. Höhm, S. V. Kirner, A. Rosenfeld, J. Krüger, Laser-induced periodic surface structures—a scientific evergreen, IEEE J. Selected Top. Quantum Electron. **23**(3), 9000615 (2016).

[8] R. Osellame, G. Cerullo, R. Ramponi, *Femtosecond laser micromachining: photonic and microfluidic devices in transparent materials*, volume 123 (Springer Science & Business Media, 2012).

[9] T. Baldacchini, *Three-dimensional microfabrication using two-photon polymerization* (William Andrew, 2015).

[10] K. Sugioka, Y. Cheng, *Femtosecond laser 3D micromachining for microfluidic and optofluidic applications* (Springer Science & Business Media, 2013).

[11] M. Beresna, M. Gecevičius, P. G. Kazansky, T. Gertus, Radially polarized optical vortex converter created by femtosecond laser nanostructuring of glass, Appl. Phys. Lett. **98**(20), 201101 (2011).

[12] T. Baldacchini, V. Nuñez, C. N. LaFratta, J. S. Grech, V. I. Vullev, R. Zadoyan, Microfabrication of three-dimensional filters for liposome extrusion, Proc. SPIE **9353**, 93530W (2015).

[13] K. Sugioka, Progress in ultrafast laser processing and future prospects, Nanophotonics **6**(2), 393–413 (2017).

[14] G.-L. Tan, M. F. Lemon, R. H. French, Optical properties and London dispersion forces of amorphous silica determined by vacuum ultraviolet spectroscopy and spectroscopic ellipsometry, J. Am. Ceram. Soc. **86**(11), 1885–1892 (2003).

[15] J. R. Lawrence, D. Waugh, *Laser surface engineering: processes and applications* (Elsevier, 2014).

[16] M. Ams, G. D. Marshall, P. Dekker, M. Dubov, V. K. Mezentsev, I. Bennion, M. J. Withford, Investigation of ultrafast laser–photonic material interactions: challenges for directly written glass photonics, IEEE J. Selected Top. Quantum Electron. **14**(5), 1370–1381 (2008).

[17] C. B. Schaffer, A. Brodeur, E. Mazur, Laser-induced breakdown and damage in bulk transparent materials induced by tightly focused femtosecond laser pulses, Meas. Sci. Technol. **12**(11), 1784 (2001).

[18] L. Keldysh, et al., Ionization in the field of a strong electromagnetic wave, Sov. Phys. JETP **20**(5), 1307–1314 (1965).

[19] H. Misawa, S. Juodkazis, *3D laser microfabrication: principles and applications* (John Wiley & Sons, 2006).

[20] R. R. Gattass, E. Mazur, Femtosecond laser micromachining in transparent materials, Nat. Photon. **2**(4), 219–225 (2008).

[21] https://www.schott.com, note = Accessed: 2020-08-20.

[22] N. P. Bansal, R. H. Doremus, *Handbook of glass properties* (Elsevier, 2013).

[23] C. S. Alexander, L. Chhabildas, W. Reinhart, D. Templeton, Changes to the shock response of fused quartz due to glass modification, Int. J. Impact. Eng. **35**(12), 1376–1385 (2008).

[24] Y. Bellouard, A. Said, M. Dugan, P. Bado, Fabrication of high-aspect ratio, micro-fluidic channels and tunnels using femtosecond laser pulses and chemical etching, Opt. Express **12**(10), 2120–2129 (2004).

[25] R. Brueckner, Properties and structure of vitreous silica. I, J. Non-Cryst. Solids **5**(2), 123–175 (1970).

[26] K. Numata, K. Yamamoto, H. Ishimoto, S. Otsuka, K. Kawabe, M. Ando, K. Tsubono, Systematic measurement of the intrinsic losses in various kinds of bulk fused silica, Phys. Lett. A **327**(4), 263–271 (2004).

[27] B. Sloots, Measuring the low OH content in quartz glass, Vib. Spectrosc. **48**(1), 158–161 (2008).

[28] C. Hnatovsky, R. Taylor, P. Rajeev, E. Simova, V. Bhardwaj, D. Rayner, P. Corkum, Pulse duration dependence of femtosecond-laser-fabricated nanogratings in fused silica, Appl. Phys. Lett. **87**(1), 014104 (2005).

[29] E. N. Glezer, E. Mazur, Ultrafast-laser driven micro-explosions in transparent materials, Appl. Phys. Lett. **71**(7), 882–884 (1997).

[30] M. Lancry, B. Poumellec, J. Canning, K. Cook, J.-C. Poulin, F. Brisset, Ultrafast nanoporous silica formation driven by femtosecond laser irradiation, Laser Photon. Rev. **7**(6), 953–962 (2013).

[31] J. Zhang, M. Gecevičius, M. Beresna, P. G. Kazansky, Seemingly unlimited lifetime data storage in nanostructured glass, Phys. Rev. Lett. **112**(3), 033901 (2014).

[32] E. Glezer, M. Milosavljevic, L. Huang, R. Finlay, T.-H. Her, J. P. Callan, E. Mazur, Three-dimensional optical storage inside transparent materials, Opt. Lett. **21**(24), 2023–2025 (1996).

[33] T. Hashimoto, S. Juodkazis, H. Misawa, Void recording in silica, Appl. Phys. A **83**(2), 337–340 (2006).

[34] S. Juodkazis, H. Misawa, T. Hashimoto, E. G. Gamaly, B. Luther-Davies, Laser-induced microexplosion confined in a bulk of silica: Formation of nanovoids, Appl. Phys. Lett. **88**(20), 201909 (2006).

[35] M. Sakakura, Y. Lei, L. Wang, Y.-H. Yu, P. G. Kazansky, Ultralow-loss geometric phase and polarization shaping by ultrafast laser writing in silica glass, Light Sci. Appl. **9**(1), 1–10 (2020).

[36] M. Birnbaum, Semiconductor surface damage produced by ruby lasers, J. Appl. Phys. **36**(11), 3688–3689 (1965).

[37] G. D. Tsibidis, E. Skoulas, E. Stratakis, Ripple formation on nickel irradiated with radially polarized femtosecond beams, Opt. Lett. **40**(22), 5172–5175 (2015).

[38] N. Yasumaru, K. Miyazaki, J. Kiuchi, Femtosecond-laser-induced nanostructure formed on hard thin films of tin and dlc, Appl. Phys. A **76**(6), 983–985 (2003).

[39] M. Mezera, M. van Drongelen, G. Römer, Laser-induced periodic surface structures (LIPSS) on polymers processed with picosecond laser pulses, J. Laser Micro Nanoen. **13**(2), 105–116 (2018).

[40] R. Buschlinger, S. Nolte, U. Peschel, Self-organized pattern formation in laser-induced multiphoton ionization, Phys. Rev. B **89**(18), 184306 (2014).

[41] B. Zhang, X. Liu, J. Qiu, Single femtosecond laser beam induced nanogratings in transparent media-mechanisms and applications, J. Materiomics **5**(1), 1–14 (2019).

[42] R. Taylor, C. Hnatovsky, E. Simova, Applications of femtosecond laser induced self-organized planar nanocracks inside fused silica glass, Laser Photon. Rev. **2**(1-2), 26–46 (2008).

[43] V. Bhardwaj, E. Simova, P. Rajeev, C. Hnatovsky, R. Taylor, D. Rayner, P. Corkum, Optically produced arrays of planar nanostructures inside fused silica, Phys. Rev. Lett. **96**(5), 057404 (2006).

[44] S. Richter, M. Heinrich, S. Döring, A. Tünnermann, S. Nolte, U. Peschel, Nanogratings in fused silica: Formation, control, and applications, J. Laser Appl. **24**(4), 042008 (2012).

[45] C. Hnatovsky, R. Taylor, E. Simova, V. Bhardwaj, D. Rayner, P. Corkum, Polarization-selective etching in femtosecond laser-assisted microfluidic channel fabrication in fused silica, Opt. Lett. **30**(14), 1867–1869 (2005).

[46] R. Taylor, E. Simova, C. Hnatovsky, Creation of chiral structures inside fused silica glass, Opt. Lett. **33**(12), 1312–1314 (2008).

[47] Y. Bellouard, E. Barthel, A. Said, M. Dugan, P. Bado, Scanning thermal microscopy and raman analysis of bulk fused silica exposed to low-energy femtosecond laser pulses, Opt. Express **16**(24), 19520–19534 (2008).

[48] C. A. Ross, D. G. MacLachlan, D. Choudhury, R. R. Thomson, Optimisation of ultrafast laser assisted etching in fused silica, Opt. Express **26**(19), 24343–24356 (2018).

[49] X. Yu, Y. Liao, F. He, B. Zeng, Y. Cheng, Z. Xu, K. Sugioka, K. Midorikawa, Tuning etch selectivity of fused silica irradiated by femtosecond laser pulses by controlling polarization of the writing pulses, J. Appl. Physics **109**(5), 053114 (2011).

[50] M. Hermans, J. Gottmann, F. Riedel, Selective, laser-induced etching of fused silica at high scan-speeds using KOH, J. Laser Micro Nanoen. **9**(2), 126–131 (2014).

[51] J. Qi, Z. Wang, J. Xu, Z. Lin, X. Li, W. Chu, Y. Cheng, Femtosecond laser induced selective etching in fused silica: optimization of the inscription conditions with a high-repetition-rate laser source, Opt. Express **26**(23), 29669–29678 (2018).

[52] S. Richter, M. Heinrich, S. Döring, A. Tünnermann, S. Nolte, Formation of femtosecond laser-induced nanogratings at high repetition rates, Appl. Phys. A **104**(2), 503–507 (2011).

[53] J. Gottmann, M. Hermans, N. Repiev, J. Ortmann, Selective laser-induced etching of 3D precision quartz glass components for microfluidic applications—up-scaling of complexity and speed, Micromachines **8**(4), 110 (2017).

[54] T. Yang, Y. Bellouard, 3D electrostatic actuator fabricated by non-ablative femtosecond laser exposure and chemical etching, MATEC Web Conf. **32**, 02003 (2015).

[55] S. Butkus, M. Rickus, R. Sirutkaitis, D. Paipulas, V. Sirutkaitis, Fabrication of high aspect ratio channels in fused silica using femtosecond pulses and chemical etching at different conditions, J. Laser Micro Nanoen. **14**(1), 19–24 (2019).

[56] J. K. Kang, C. B. Musgrave, The mechanism of HF/H_2O chemical etching of SiO_2, The Journal of chemical physics **116**(1), 275–280 (2002).

[57] P. Liu, W.-J. Liu, H. Jiang, J.-J. Chen, W.-W. Li, H.-Q. Yu, Modification of bio-char derived from fast pyrolysis of biomass and its application in removal of tetracycline from aqueous solution, Bioresour. Technol. **121**, 235–240 (2012).

[58] S. L. Turco, R. Osellame, R. Ramponi, K. C. Vishnubhatla, Hybrid chemical etching of femtosecond irradiated 3D structures in fused silica glass, MATEC Web Conf. **8**, 05009 (2013).

[59] S. Turco, R. Osellame, R. Ramponi, K. Vishnubhatla, Hybrid chemical etching of femtosecond laser irradiated structures for engineered microfluidic devices, J. Micromech. Microeng. **23**(8), 085002 (2013).

[60] S. Richter, C. Miese, S. Döring, F. Zimmermann, M. J. Withford, A. Tünnermann, S. Nolte, Laser induced nanogratings beyond fused silica-periodic nanostructures in borosilicate glasses and ULE™, Opt. Mater. Express **3**(8), 1161–1166 (2013).

[61] D. Wortmann, J. Gottmann, N. Brandt, H. Horn-Solle, Micro-and nanostructures inside sapphire by fs-laser irradiation and selective etching, Opt. Express **16**(3), 1517–1522 (2008).

[62] J. Gottmann, M. Hoerstmann-Jungemann, M. Hermans, D. Beckmann, High speed and high precision fs-laser writing using a scanner with large numerical aperture, J. Laser Micro Nanoen. **4**(3), 192–196 (2009).

[63] T. Gissibl, S. Thiele, A. Herkommer, H. Giessen, Nat. Photonics **10**(8), 554 (2016).

[64] T. Frenzel, M. Kadic, M. Wegener, Science **358**(6366), 1072 (2017).

[65] A. Ovsianikov, S. Schlie, A. Ngezahayo, A. Haverich, B. N. Chichkov, Two-photon polymerization technique for microfabrication of CAD-designed 3D scaffolds from commercially available photosensitive materials, J. Tissue Eng. Regen. Med. **1**(6), 443–449 (2007).

[66] D. Wu, S.-Z. Wu, J. Xu, L.-G. Niu, K. Midorikawa, K. Sugioka, Hybrid femtosecond laser microfabrication to achieve true 3D glass/polymer composite biochips with multiscale features and high performance: the concept of ship-in-a-bottle biochip, Laser Photon. Rev. **8**(3), 458–467 (2014).

[67] X. Zhou, Y. Hou, J. Lin, A review on the processing accuracy of two-photon polymerization, AIP Adv. **5**(3), 030701 (2015).

[68] D. Tan, Y. Li, F. Qi, H. Yang, Q. Gong, X. Dong, X. Duan, Reduction in feature size of two-photon polymerization using SCR500, Appl. Phys. Lett. **90**(7), 071106 (2007).

[69] J. Fischer, M. Wegener, Three-dimensional optical laser lithography beyond the diffraction limit, Laser Photon. Rev. **7**(1), 22–44 (2013).

[70] J. Van Hoorick, H. Ottevaere, H. Thienpont, P. Dubruel, S. Van Vlierberghe, *Polymer and Photonic Materials Towards Biomedical Breakthroughs* (Springer, 2018).

[71] H.-B. Sun, S. Kawata, *Two-photon photopolymerization and 3D lithographic microfabrication* (Springer, 2004).

[72] M. Farsari, M. Vamvakaki, B. N. Chichkov, Multiphoton polymerization of hybrid materials, J. Opt. **12**(12), 124001 (2010).

[73] C. E. Hoyle, J. F. Kinstle, *Radiation curing of polymeric materials*, volume 417 (1990).

[74] M. Malinauskas, M. Farsari, A. Piskarskas, S. Juodkazis, Ultrafast laser nanostructuring of photopolymers: A decade of advances, Phys. Rep. **533**(1), 1–31 (2013).

[75] W. Zhou, S. M. Kuebler, K. L. Braun, T. Yu, J. K. Cammack, C. K. Ober, J. W. Perry, S. R. Marder, An efficient two-photon-generated photoacid applied to positive-tone 3D microfabrication, Science **296**(5570), 1106–1109 (2002).

[76] J.-F. Xing, M.-L. Zheng, X.-M. Duan, Two-photon polymerization microfabrication of hydrogels: an advanced 3D printing technology for tissue engineering and drug delivery, Chem. Soc. Rev. **44**(15), 5031–5039 (2015).

[77] X. Wang, Z. Wei, C. Z. Baysah, M. Zheng, J. Xing, Biomaterial-based microstructures fabricated by two-photon polymerization microfabrication technology, RSC Adv. **9**(59), 34472–34480 (2019).

[78] M. Farsari, B. N. Chichkov, Two-photon fabrication, Nat. Photon. **3**(8), 450–452 (2009).

[79] M. Carlotti, V. Mattoli, Functional materials for two-photon polymerization in microfabrication, Small **15**(40), 1902687 (2019).

[80] C. Schizas, D. Karalekas, Mechanical characteristics of an Ormocomp® biocompatible hybrid photopolymer, J. Mech. Behav. Biomed. Mater. **4**(1), 99–106 (2011).

[81] L. Guerin, M. Bossel, M. Demierre, S. Calmes, P. Renaud, Simple and low cost fabrication of embedded micro-channels by using a new thick-film photoplastic **2**, 1419–1422 (1997).

[82] A. Skarmoutsou, G. Lolas, C. A. Charitidis, M. Chatzinikolaidou, M. Vamvakaki, M. Farsari, Nanomechanical properties of hybrid coatings for bone tissue engineering, Journal of the mechanical behavior of biomedical materials **25**, 48–62 (2013).

[83] F. B. Prinz, C. L. Atwood, R. F. Aubin, J. J. Beaman, R. L. Brown, P. S. Fussell, A. J. Lightman, E. Sachs, L. E. Weiss, M. J. Wozny, *Rapid prototyping in Europe and Japan* (Center for Advanced technology, 1997).

[84] J. Stampfl, R. Liska, A. Ovsianikov, *Multiphoton lithography: Techniques, materials, and applications* (John Wiley & Sons, 2016).

[85] A. Ovsianikov, J. Viertl, B. Chichkov, M. Oubaha, B. MacCraith, I. Sakellari, A. Giakoumaki, D. Gray, M. Vamvakaki, M. Farsari, C. Fotakis, Ultra-low shrinkage hybrid photosensitive material for two-photon polymerization microfabrication, ACS Nano **2**(11), 2257 (2008).

[86] A. Žukauskas, I. Matulaitienė, D. Paipulas, G. Niaura, M. Malinauskas, R. Gadonas, Tuning the refractive index in 3D direct laser writing lithography: towards GRIN microoptics, Laser Photon. Rev. **9**(6), 706–712 (2015).

[87] F. J. Duarte, *Coherence and Ultrashort Pulse Laser Emission* (InTech, 2010).

[88] C. J. Brinker, G. W. Scherer, *Sol-gel science: the physics and chemistry of sol-gel processing* (Academic press, 2013).

[89] A. Ovsianikov, X. Shizhou, M. Farsari, M. Vamvakaki, C. Fotakis, B. N. Chichkov, Shrinkage of microstructures produced by two-photon polymerization of Zr-based hybrid photosensitive materials, Opt. Express **17**(4), 2143–2148 (2009).

[90] C. J. Brinker, Hydrolysis and condensation of silicates: effects on structure, J. Non-Cryst. Solids **100**(1-3), 31–50 (1988).

[91] L. Canham, *Handbook of porous silicon* (Springer, 2018).

[92] S. Maruo, T. Hasegawa, N. Yoshimura, Single-anchor support and supercritical CO_2 drying enable high-precision microfabrication of three-dimensional structures, Opt. Express **17**(23), 20945–20951 (2009).

[93] S. W. Hell, J. Wichmann, Breaking the diffraction resolution limit by stimulated emission: stimulated-emission-depletion fluorescence microscopy, Opt. Lett. **19**(11), 780–782 (1994).

[94] S. Hell, E. H. Stelzer, Properties of a 4Pi confocal fluorescence microscope, J. Opt. Soc. Am. A **9**(12), 2159–2166 (1992).

[95] M. Dyba, S. W. Hell, Focal spots of size $\lambda/23$ open up far-field florescence microscopy at 33 nm axial resolution, Phys. Rev. Lett. **88**(16), 163901 (2002).

[96] H. Blom, H. Brismar, STED microscopy: increased resolution for medical research?, J. Intern. Med. **276**(6), 560–578 (2014).

[97] J. Fischer, M. Wegener, Three-dimensional direct laser writing inspired by stimulated-emission-depletion microscopy, Opt. Mat. Express **1**(4), 614–624 (2011).

[98] R. Wollhofen, J. Katzmann, C. Hrelescu, J. Jacak, T. A. Klar, 120 nm resolution and 55 nm structure size in STED-lithography, Opt. Express **21**(9), 10831–10840 (2013).

[99] L. Li, R. R. Gattass, E. Gershgoren, H. Hwang, J. T. Fourkas, Achieving $\lambda/20$ resolution by one-color initiation and deactivation of polymerization, Science **324**(5929), 910–913 (2009).

[100] J. Fischer, G. von Freymann, M. Wegener, The materials challenge in diffraction-unlimited direct-laser-writing optical lithography, Adv. Mater. **22**(32), 3578–3582 (2010).

[101] T. Baldacchini, *Three-dimensional microfabrication using two-photon polymerization* (second ed., William Andrew, 2019).

[102] S. Varapnickas, M. Malinauskas, Processes of direct laser writing 3D nano-lithography, Preprints (2018).

[103] Y. Li, K. Itoh, W. Watanabe, K. Yamada, D. Kuroda, J. Nishii, Y. Jiang, Three-dimensional hole drilling of silica glass from the rear surface with femtosecond laser pulses, Opt. Lett. **26**(23), 1912–1914 (2001).

[104] Y. Cheng, K. Sugioka, M. Masuda, K. Toyoda, M. Kawachi, K. Shihoyama, K. Midorikawa, 3D microstructuring inside Foturan glass by femtosecond laser, Riken Rev. 101–106 (2003).

[105] K. H. Tantawi, E. Waddel, J. D. Williams, Structural and composition analysis of Apex™ and Foturan™ photodefinable glasses, J. Mater. Sci. **48**(15), 5316–5323 (2013).

[106] K. Sugioka, Y. Cheng, *Ultrafast laser processing: from micro-to nanoscale* (CRC Press, 2013).

[107] K. C. Vishnubhatla, N. Bellini, R. Ramponi, G. Cerullo, R. Osellame, Shape control of microchannels fabricated in fused silica by femtosecond laser irradiation and chemical etching, Opt. Express **17**(10), 8685–8695 (2009).

[108] F. He, J. Lin, Y. Cheng, Fabrication of hollow optical waveguides in fused silica by three-dimensional femtosecond laser micromachining, Appl. Phys. B **105**(2), 379–384 (2011).

[109] C. A. Ross, D. G. MacLachlan, B. J. Smith, R. J. Beck, J. D. Shephard, N. Weston, R. R. Thomson, A miniature fibre-optic raman probe fabricated by ultrafast laser-assisted etching, Micromachines **11**(2), 185 (2020).

[110] C. Weingarten, S. Steenhusen, M. Hermans, E. Willenborg, J. H. Schleifenbaum, Laser polishing and 2PP structuring of inside microfluidic channels in fused silica, Microfluid. Nanofluid. **21**(11), 165 (2017).

[111] J. Drs, T. Kishi, Y. Bellouard, Laser-assisted morphing of complex three dimensional objects, Opt. Express **23**(13), 17355–17366 (2015).

[112] Y. Bellouard, On the bending strength of fused silica flexures fabricated by ultrafast lasers, Opt. Mat. Express **1**(5), 816–831 (2011).

[113] Y. Bellouard, *Microrobotics: methods and applications* (CRC Press, 2009).

[114] C.-E. Athanasiou, Y. Bellouard, A monolithic micro-tensile tester for investigating silicon dioxide polymorph micromechanics, fabricated and operated using a femtosecond laser, Micromachines **6**(9), 1365–1386 (2015).

[115] C.-E. Athanasiou, M.-O. Hongler, Y. Bellouard, Unraveling brittle-fracture statistics from intermittent patterns formed during femtosecond laser exposure, Phys. Rev. Applied **8**(5), 054013 (2017).

[116] B. Lenssen, Y. Bellouard, Optically transparent glass micro-actuator fabricated by femtosecond laser exposure and chemical etching, Appl. Phys. Lett. **101**(10), 103503 (2012).

[117] T. Yang, Y. Bellouard, Monolithic transparent 3D dielectrophoretic micro-actuator fabricated by femtosecond laser, J. Micromech. Microeng. **25**(10), 105009 (2015).

[118] Y. Bellouard, A. A. Said, P. Bado, Integrating optics and micromechanics in a single substrate: a step toward monolithic integration in fused silica., Opt. Express **13**(17), 6635–6644 (2005).

[119] V. Tielen, Y. Bellouard, Three-dimensional glass monolithic micro-flexure fabricated by femtosecond laser exposure and chemical etching, Micromachines **5**(3), 697–710 (2014).

[120] S. I. Nazir, Y. Bellouard, A monolithic gimbal micro-mirror fabricated and remotely tuned with a femtosecond laser, Micromachines **10**(9), 611 (2019).

[121] M. Zanaty, T. Fussinger, A. Rogg, A. Lovera, D. Lambelet, I. Vardi, T. J. Wolfensberger, C. Baur, S. Henein, Programmable multistable mechanisms for safe surgical puncturing, J. Med. Devices **13**(2), 21002 (2019).

[122] L. Jonušauskas, S. Juodkazis, M. Malinauskas, Optical 3D printing: bridging the gaps in the mesoscale, J. Opt. **20**(5), 053001 (2018).

[123] J. Qu, M. Kadic, A. Naber, M. Wegener, Micro-structured two-component 3D metamaterials with negative thermal-expansion coefficient from positive constituents, Sci. Rep. **7**, 40643 (2017).

[124] S. M. Felton, M. T. Tolley, B. Shin, C. D. Onal, E. D. Demaine, D. Rus, R. J. Wood, Self-folding with shape memory composites, Soft Matter **9**(32), 7688–7694 (2013).

[125] M. Pineirua, J. Bico, B. Roman, Capillary origami controlled by an electric field, Soft Matter **6**(18), 4491–4496 (2010).

[126] S. Rekštytė, D. Paipulas, M. Malinauskas, V. Mizeikis, Microactuation and sensing using reversible deformations of laser-written polymeric structures, Nanotechnology **28**(12), 124001 (2017).

[127] Y. Tian, Y.-L. Zhang, H. Xia, L. Guo, J.-F. Ku, Y. He, R. Zhang, B.-Z. Xu, Q.-D. Chen, H.-B. Sun, Solvent response of polymers for micromachine manipulation, Phys. Chem. Chem. Phys. **13**(11), 4835–4838 (2011).

[128] C. N. LaFratta, T. Baldacchini, Two-photon polymerization metrology: Characterization methods of mechanisms and microstructures, Micromachines **8**(4), 101 (2017).

[129] S. Nakanishi, S. Shoji, S. Kawata, H.-B. Sun, Giant elasticity of photopolymer nanowires, Appl. Phys. Lett. **91**(6), 063112 (2007).

[130] S.-J. Zhang, Y. Li, Y.-K. Wang, L.-P. Liu, H.-D. Wang, Y.-F. Xiao, H. Yang, Q. Gong, Controlling Young's modulus of polymerized structures fabricated by direct laser writing, Appl. Phys. A **118**(2), 437–441 (2015).

[131] K. Takada, D. Wu, Q.-D. Chen, S. Shoji, H. Xia, S. Kawata, H.-B. Sun, Size-dependent behaviors of femtosecond laser-prototyped polymer micronanowires, Opt. Lett. **34**(5), 566–568 (2009).

[132] T. Ikegami, M. P. Stocker, K. Monaco, J. T. Fourkas, S. Maruo, Fabrication of three-dimensional metalized movable microstructures by the combination of two-photon microfabrication and electroless plating, Jpn. J. Appl. Phys. **51**(6S), 06FL17 (2012).

[133] H. Xia, J. Wang, Y. Tian, Q.-D. Chen, X.-B. Du, Y.-L. Zhang, Y. He, H.-B. Sun, Ferrofluids for fabrication of remotely controllable micro-nanomachines by two-photon polymerization, Adv. Mater. **22**(29), 3204–3207 (2010).

[134] P. Danilevicius, S. Rekštyte, R. Gadonas, M. Malinauskas, E. Balciunas, R. Jarasiene, D. Baltriukiene, V. Bukelskiene, A. Kraniauskas, R. Sirmenis, Micro-structured polymer scaffolds fabricated by direct laser writing for tissue engineering, J. Biomed. Opt. **17**(8), 081405 (2012).

[135] H.-B. Sun, K. Takada, S. Kawata, Elastic force analysis of functional polymer submicron oscillators, Appl. Phys. Lett. **79**(19), 3173–3175 (2001).

[136] Z. Bayindir, Y. Sun, M. Naughton, C. LaFratta, T. Baldacchini, J. Fourkas, J. Stewart, B. Saleh, M. Teich, Polymer microcantilevers fabricated via multiphoton absorption polymerization, Appl. Phys. Lett. **86**(6), 064105 (2005).

[137] L. Amato, Y. Gu, N. Bellini, S. M. Eaton, G. Cerullo, R. Osellame, Integrated three-dimensional filter separates nanoscale from microscale elements in a microfluidic chip, Lab Chip **12**(6), 1135–1142 (2012).

[138] D. Wu, J. Xu, L.-G. Niu, S.-Z. Wu, K. Midorikawa, K. Sugioka, In-channel integration of designable microoptical devices using flat scaffold-supported femtosecond-laser microfabrication for coupling-free optofluidic cell counting, Light Sci.Appl. **4**(1), e228 (2015).

[139] M. H. Olsen, G. M. Hjortø, M. Hansen, Ö. Met, I. M. Svane, N. B. Larsen, In-chip fabrication of free-form 3D constructs for directed cell migration analysis, Lab Chip **13**(24), 4800–4809 (2013).

[140] J. Xu, H. Kawano, W. Liu, Y. Hanada, P. Lu, A. Miyawaki, K. Midorikawa, K. Sugioka, Controllable alignment of elongated microorganisms in 3D microspace using electrofluidic devices manufactured by hybrid femtosecond laser microfabrication, Microsyst. Nanoeng. **3**(1), 1–9 (2017).

[141] A. Doraiswamy, A. Ovsianikov, S. D. Gittard, N. A. Monteiro-Riviere, R. Crombez, E. Montalvo, W. Shen, B. N. Chichkov, R. J. Narayan, Fabrication of microneedles using two photon polymerization for transdermal delivery of nanomaterials, J. Nanosci. Nanotechnol. **10**(10), 6305–6312 (2010).

[142] J. Fischer, M. Wegener, Three-dimensional direct laser writing inspired by stimulated-emission-depletion microscopy, Opt. Mater. Express **1**(4), 614 (2011).

[143] E. Abbe, The relation of aperture and power in the microscope, J. R. Microsc. Soc. **2**, 300–309 (1882).

[144] T. A. Klar, R. Wollhofen, J. Jacak, Sub-Abbe resolution: from STED microscopy to STED lithography, Phys. Scr. **2014**(T162), 014049 (2014).

[145] E. Mudry, E. L. Moal, P. Ferrand, P. C. Chaumet, A. Sentenac, Isotropic diffraction-limited focusing using a single objective lens, Phys. Rev. Lett. **105**(20), 203903 (2010).

[146] W. Chu, Y. Tan, P. Wang, J. Xu, W. Li, J. Qi, Y. Cheng, Centimeter-height 3D printing with femtosecond laser two-photon polymerization, Adv. Mater. Technol. **3**(5), 1700396 (2018).

[147] S. Hell, E. H. K. Stelzer, Properties of a 4Pi confocal fluorescence microscope, J. Opt. Soc. Am. A **9**(12), 2159 (1992).

[148] S. Hell, E. H. Stelzer, Fundamental improvement of resolution with a 4Pi-confocal fluorescence microscope using two-photon excitation, Opt. Commun. **93**(5-6), 277–282 (1992).

[149] S. W. Hell, S. Lindek, C. Cremer, E. H. Stelzer, Measurement of the 4Pi-confocal point spread function proves 75 nm axial resolution, Appl. Phys. Lett. **64**(11), 1335–1337 (1994).

[150] M. Lang, T. Staudt, J. Engelhardt, S. Hell, 4Pi microscopy with negligible sidelobes, New J. Phys. **10**(4), 043041 (2008).

[151] https://www.micro-shop.zeiss.com/en/us/shop/objectives/420792-9771-000/objective-alpha-plan-apochromat-100x-1.57-oil-hi-dic-corr-m27/, note = Accessed: 2020-05-17.

[152] H. Gugel, J. Bewersdorf, S. Jakobs, J. Engelhardt, R. Storz, S. W. Hell, Cooperative 4Pi excitation and detection yields sevenfold sharper optical sections in live-cell microscopy, Biophys. J. **87**(6), 4146–4152 (2004).

[153] G. Zyla, A. Kovalev, S. Heisterkamp, C. Esen, E. L. Gurevich, S. Gorb, A. Ostendorf, Biomimetic structural coloration with tunable degree of angle-independence generated by two-photon polymerization, Opt. Mater. Express **9**(6), 2630–2639 (2019).

[154] Q.-Q. Liu, Y.-Y. Zhao, M.-L. Zheng, X.-M. Duan, Tunable multilayer submicrostructures fabricated by interference assisted two-photon polymerization, Appl. Phys. Lett. **111**(22), 223102 (2017).

[155] S. Ghosh, G. Ananthasuresh, Single-photon-multi-layer-interference lithography for high-aspect-ratio and three-dimensional SU-8 micro-/nanostructures, Sci. Rep. **6**, 18428 (2016).

[156] B. Mills, D. Kundys, M. Farsari, S. Mailis, R. W. Eason, Single-pulse multiphoton fabrication of high aspect ratio structures with sub-micron features using vortex beams, Appl. Phys. A **108**(3), 651–655 (2012).

[157] M. Born, E. Wolf, *Principles of optics: electromagnetic theory of propagation, interference and diffraction of light* (Pergamon, 1980).

[158] P. Török, P. Varga, Electromagnetic diffraction of light focused through a stratified medium, Appl. Opt. **36**(11), 2305–2312 (1997).

[159] M. J. Nasse, J. C. Woehl, Realistic modeling of the illumination point spread function in confocal scanning optical microscopy, J. Opt. Soc. Am. A **27**(2), 295–302 (2010).

[160] O. Haeberlé, Focusing of light through a stratified medium: a practical approach for computing microscope point spread functions: Part II: confocal and multiphoton microscopy, Opt. Commun. **235**(1-3), 1–10 (2004).

[161] A. Ovsianikov, J. Viertl, B. Chichkov, M. Oubaha, B. MacCraith, I. Sakellari, A. Giakoumaki, D. Gray, M. Vamvakaki, M. Farsari, C. Fotakis, Ultra-low shrinkage hybrid photosensitive material for two-photon polymerization microfabrication, ACS Nano **2**(11), 2257–2262 (2008).

[162] M. Malinauskas, A. Žukauskas, G. Bičkauskaitė, R. Gadonas, S. Juodkazis, Mechanisms of three-dimensional structuring of photo-polymers by tightly focussed femtosecond laser pulses, Opt. Express **18**(10), 10209–10221 (2010).

[163] A. Brahme, *Comprehensive biomedical physics* (Newnes, 2014).

[164] S. Kinoshita, S. Yoshioka, Structural colors in nature: the role of regularity and irregularity in the structure, Chem. Phys. Chem. **6**(8), 1442–1459 (2005).

[165] Z. Gan, Y. Cao, R. A. Evans, M. Gu, Three-dimensional deep subdiffraction optical beam lithography with 9 nm feature size, Nat. Commun. **4**(1), 1–7 (2013).

[166] L. Jonušauskas, S. Rekštytė, M. Malinauskas, Augmentation of direct laser writing fabrication throughput for three-dimensional structures by varying focusing conditions, Opt. Eng. **53**(12), 125102 (2014).

[167] M. Manousidaki, D. G. Papazoglou, M. Farsari, S. Tzortzakis, Long-scale multiphoton polymerization voxel growth investigation using engineered Bessel beams, Opt. Mater. Express **9**(7), 2838–2845 (2019).

[168] M. Manousidaki, D. G. Papazoglou, M. Farsari, S. Tzortzakis, Abruptly autofocusing beams enable advanced multiscale photo-polymerization, Optica **3**(5), 525–530 (2016).

[169] L. Kelemen, S. Valkai, P. Ormos, Parallel photopolymerisation with complex light patterns generated by diffractive optical elements, Opt. Express **15**(22), 14488–14497 (2007).

[170] L. Yang, D. Qian, C. Xin, Z. Hu, S. Ji, D. Wu, Y. Hu, J. Li, W. Huang, J. Chu, Two-photon polymerization of microstructures by a non-diffraction multifoci pattern generated from a superposed Bessel beam, Opt. Lett. **42**(4), 743–746 (2017).

[171] M. Manousidaki, D. G. Papazoglou, M. Farsari, S. Tzortzakis, 3D holographic light shaping for advanced multiphoton polymerization, Opt. Lett. **45**(1), 85–88 (2020).

[172] E. Stankevičius, M. Garliauskas, M. Gedvilas, G. Račiukaitis, Bessel-like beam array formation by periodical arrangement of the polymeric round-tip microstructures, Opt. Express **23**(22), 28557–28566 (2015).

[173] L. Jonušauskas, D. Gailevičius, S. Rekštytė, T. Baldacchini, S. Juodkazis, M. Malinauskas, Mesoscale laser 3D printing, Opt. Express **27**(11), 15205–15221 (2019).

[174] D. Wu, Q.-D. Chen, L.-G. Niu, J.-N. Wang, J. Wang, R. Wang, H. Xia, H.-B. Sun, Femtosecond laser rapid prototyping of nanoshells and suspending components towards microfluidic devices, Lab Chip **9**(16), 2391–2394 (2009).

[175] S. Dehaeck, B. Scheid, P. Lambert, Adaptive stitching for meso-scale printing with two-photon lithography, Addit. Manuf. **21**, 589–597 (2018).

[176] F. He, H. Xu, Y. Cheng, J. Ni, H. Xiong, Z. Xu, K. Sugioka, K. Midorikawa, Fabrication of microfluidic channels with a circular cross section using spatiotemporally focused femtosecond laser pulses, Opt. Lett. **35**(7), 1106–1108 (2010).

[177] http://www.holoor.co.il/, accessed: 2020-03-27.

[178] L. Yang, A. El-Tamer, U. Hinze, J. Li, Y. Hu, W. Huang, J. Chu, B. N. Chichkov, Parallel direct laser writing of micro-optical and photonic structures using spatial light modulator, Opt. Laser Eng. **70**, 26–32 (2015).

[179] http://holoeye.com/gaea-4k-phase-only-spatial-light-modulator/, accessed: 2020-03-28.

[180] Q. Geng, D. Wang, P. Chen, S.-C. Chen, Ultrafast multi-focus 3D nanofabrication based on two-photon polymerization, Nat. Commun. **10**(1), 1–7 (2019).

[181] L. Jonušauskas, T. Baravykas, D. Andrijec, T. Gadišauskas, V. Purlys, Stitchless support-free 3D printing of free-form micromechanical structures with feature size on-demand, Sci. Rep. **9**(1), 1–12 (2019).

[182] T. Kondo, S. Matsuo, S. Juodkazis, V. Mizeikis, H. Misawa, Multiphoton fabrication of periodic structures by multibeam interference of femtosecond pulses, Appl. Phys. Lett. **82**(17), 2758–2760 (2003).

[183] C.-Y. Liao, M. Bouriauand, P. L. Baldeck, J.-C. Léon, C. Masclet, T.-T. Chung, Two-dimensional slicing method to speed up the fabrication of micro-objects based on two-photon polymerization, Appl. Phys. Lett. **91**(3), 033108 (2007).

[184] S. H. Park, S. H. Lee, D.-Y. Yang, H. J. Kong, K.-S. Lee, Subregional slicing method to increase three-dimensional nanofabrication efficiency in two-photon polymerization, Appl. Phys. Lett. **87**(15), 154108 (2005).

[185] R. Guo, S. Xiao, X. Zhai, J. Li, A. Xia, W. Huang, Micro lens fabrication by means of femtosecond two photon photopolymerization, Opt. Express **14**(2), 810–816 (2006).

[186] D. Wu, S.-Z. Wu, L.-G. Niu, Q.-D. Chen, R. Wang, J.-F. Song, H.-H. Fang, H.-B. Sun, High numerical aperture microlens arrays of close packing, Appl. Phys. Lett. **97**(3), 031109 (2010).

[187] M. Bhuyan, F. Courvoisier, P. Lacourt, M. Jacquot, R. Salut, L. Furfaro, J. Dudley, High aspect ratio nanochannel machining using single shot femtosecond Bessel beams, Appl. Phys. Lett. **97**(8), 081102 (2010).

[188] X. Yu, M. Zhang, S. Lei, Multiphoton polymerization using femtosecond Bessel beam for layerless three-dimensional printing, J. Micro Nano-Manuf. **6**(1), 010901 (2018).

[189] X.-F. Li, R. Winfield, S. O'Brien, G. Crean, Application of Bessel beams to 2D microfabrication, Appl. Surf. Sci. **255**(10), 5146–5149 (2009).

[190] H. Urey, Spot size, depth-of-focus, and diffraction ring intensity formulas for truncated gaussian beams, Appl. Opt. **43**(3), 620–625 (2004).

[191] P. Danilevičius, S. Rekštytė, E. Balčiūnas, A. Kraniauskas, R. Širmenis, D. Baltriukienė, M. Malinauskas, V. Bukelskienė, R. Gadonas, V. Sirvydis, A. Piskarskas, Direct laser fabrication of polymeric implants for cardiovascular surgery, Mater. Sci **18**(2), 145–149 (2012).

CURRICULUM VITAE

Name: Titas
Surname: Tičkūnas
Date of birth: 1988-02-06
Place of birth: Panevėžys, Lithuania
E-mail: titas.tickunas@gmail.com

Education:

2007	Panevėžys 5th Secondary School *Secondary education*
2007–2011	Vilnius University, Faculty of Physics *Bachelor degree*
2011–2013	Vilnius University, Faculty of Physics *Master degree*
2015–2020	Vilnius University, Faculty of Physics, *Ph.D. studies*

Work experience:

2011–2012	Sales engineer at UAB "Altechna"
2013–present	Researcher at UAB "Femtika"
2017–present	Junior researcher at Vilnius University

Internships

2015 06–2015 07	École Polytechnique Fédérale de Lausanne, Neuchâtel, Switzerland

Additional information

Awards	Outstanding paper award (poster) *Laser Precision Microfabrication* conference Edinburgh, UK, 2018

ACKNOWLEDGEMENT

I would like to express my gratitude to many people with whom I had an opportunity to work with during these recent years.

Firstly, I am sincerely grateful to my former supervisor prof. dr. Roaldas Gadonas, who invited me to this interesting laser microprocessing field, gave me the academic freedom for the research and all of the needed support for my studies.

I would also like to express super huge gratitude to my supervisor dr. Domas Paipulas, and colleague dr. Vytautas Purlys, who both involved me in their projects, conducted my experiments, showed the direction for my research and gave useful insights. Also, I am thankful for encouraging words, keeping me motivated and, of course, pushing me, when it was really needed.

Many thanks to colleagues at Vilnius University, as well as at the company Femtika, which gave me an opportunity to improve myself as a researcher in this scientific world. Especially, I would like to say special thanks to Dr. Sima Rekštytė for the scientific help and sharing her experience and knowledge.

I would like to thank everyone, who helped to improve this Thesis, especially, dr. Vytautas Jukna.

Finally, I am sincerely grateful to my wife Vytautė and my family for the support through these years!

COPIES OF PUBLICATIONS

A1. **T. Tičkūnas**, M. Perrenoud, S. Butkus, R. Gadonas, S. Rekštytė, M. Malinauskas, D. Paipulas, Y. Bellouard, and V. Sirutkaitis, "Combination of additive and subtractive laser 3D microprocessing in hybrid glass/polymer microsystems for chemical sensing applications", Opt. Express. **25**(21), 26280–26288 (2017).

A2. **T. Tičkūnas**, D. Paipulas, and V. Purlys, "4Pi multiphoton polymerization", Appl. Phys. Lett. **116**(3), 031101 (2020).

A3. **T. Tičkūnas**, D. Paipulas, and V. Purlys, "Dynamic voxel size tuning for direct laser writing", Opt. Mat. Express **10**(6), 1432-1439 (2020).

P1

COMBINATION OF ADDITIVE AND SUBTRACTIVE LASER 3D MICROPROCESSING IN HYBRID GLASS/POLYMER MICROSYSTEMS FOR CHEMICAL SENSING APPLICATIONS

T. Tičkūnas, M. Perrenoud, S. Butkus, R. Gadonas, S. Rekštytė,
M. Malinauskas, D. Paipulas, Y. Bellouard, and V. Sirutkaitis

Opt. Express. **25**(21), 26280–26288 (2017)

Research Article Vol. 25, No. 21 | 16 Oct 2017 | OPTICS EXPRESS 26280

Optics EXPRESS

Combination of additive and subtractive laser 3D microprocessing in hybrid glass/polymer microsystems for chemical sensing applications

TITAS TIČKŪNAS,[1] MATTHIEU PERRENOUD,[2] SIMAS BUTKUS,[1] ROALDAS GADONAS,[1] SIMA REKŠTYTĖ,[1] MANGIRDAS MALINAUSKAS,[1] DOMAS PAIPULAS,[1,*] YVES BELLOUARD,[2,3] AND VALDAS SIRUTKAITIS [1]

[1] *Vilnius University, Faculty of Physics, Laser Research Center, Sauletekio Ave. 10, LT-10223 Vilnius, Lithuania*
[2] *Ecole Polytechnique Fédérale de Lausanne (EPFL), Galatea Lab, STI/IMT, Rue de la Maladiére 71b, CH-2002 Neuchatel, Switzerland*
[3] *yves.bellouard@epfl.ch*
[*] *domas.paipulas@ff.vu.lt;*

Abstract: We present a novel hybrid glass-polymer micromechanical sensor by combining two femtosecond laser direct writing processes: laser illumination followed by chemical etching of glass and two-photon polymerization. This incorporation of techniques demonstrates the capability of combining mechanical deformable devices made of silica with an integrated polymer structure for passive chemical sensing application. We demonstrate that such a sensor could be utilized for investigating the elastic properties of polymeric microstructures fabricated via the two-photon polymerization technique. Moreover, we show that polymeric microstructure stiffness increases when immersed in organic liquids.

OCIS codes: (140.3390) Laser materials processing; (140.7090) Ultrafast lasers; (350.3850) Materials processing (160.5470) Polymers; (160.6030) Silica; (230.4000) Microstructure fabrication.

References and links

1. Y. Kondo, J. Qiu, T. Mitsuyu, K. Hirao, and T. Yoko, "Three-dimensional microdrilling of glass by multiphoton process and chemical etching," Jpn. J. Appl. Phys. **38**, L1146 (1999).
2. A. Marcinkevičius, S. Juodkazis, M. Watanabe, M. Miwa, S. Matsuo, H. Misawa, and J. Nishii, "Femtosecond laser-assisted three-dimensional microfabrication in silica," Opt. Lett. **26**, 277–279 (2001).
3. Y. Bellouard, A. Said, M. Dugan, and P. Bado, "Fabrication of high-aspect ratio, micro-fluidic channels and tunnels using femtosecond laser pulses and chemical etching," Opt. Express **12**, 2120–2129 (2004).
4. K. Sugioka, J. Xu, D. Wu, Y. Hanada, Z. Wang, Y. Cheng, and K. Midorikawa, "Femtosecond laser 3D micromachining: a powerful tool for the fabrication of microfluidic, optofluidic, and electrofluidic devices based on glass," Lab Chip **14**, 3447–3458 (2014).
5. S. Maruo, O. Nakamura, and S. Kawata, "Three-dimensional microfabrication with two-photon-absorbed photopolymerization," Opt. Lett. **22**, 132–134 (1997).
6. J. Serbin, A. Egbert, A. Ostendorf, B. Chichkov, R. Houbertz, G. Domann, J. Schulz, C. Cronauer, L. Frohlich, and M. Popall, "Femtosecond laser-induced two-photon polymerization of inorganic–organic hybrid materials for applications in photonics," Opt. Lett. **28**, 301–303 (2003).
7. M. Malinauskas, A. Žukauskas, S. Hasegawa, Y. Hayasaki, V. Mizeikis, R. Buividas, and S. Juodkazis, "Ultrafast laser processing of materials: from science to industry," Light Sci. Appl. **5**, e16133 (2016).
8. S. Kiyama, S. Matsuo, S. Hashimoto, and Y. Morihira, "Examination of etching agent and etching mechanism on femotosecond laser microfabrication of channels inside vitreous silica substrates," J. Phys. Chem. C. **113**, 11560–11566 (2009).
9. D. Tan, Y. Li, F. Qi, H. Yang, Q. Gong, X. Dong, and X. Duan, "Reduction in feature size of two-photon polymerization using SCR500," Appl. Phys. Lett. **90**, 071106 (2007).
10. L. Amato, Y. Gu, N. Bellini, S. Eaton, G. Cerullo, and R. Osellame, "Integrated three-dimensional filter separates nanoscale from microscale elements in a microfluidic chip," Lab Chip **12**, 1135–1142 (2012).
11. D. Wu, S.-Z. Wu, J. Xu, L.-G. Niu, K. Midorikawa, and K. Sugioka, "Hybrid femtosecond laser microfabrication to achieve true 3D glass/polymer composite biochips with multiscale features and high performance: the concept of ship-in-a-bottle biochip," Laser Photon. Rev. **8**, 458–467 (2014).

12. D. Wu, J. Xu, L.-G. Niu, S.-Z. Wu, K. Midorikawa, and K. Sugioka, “In-channel integration of designable microoptical devices using flat scaffold-supported femtosecond-laser microfabrication for coupling-free optofluidic cell counting,” Light Sci. Appl. **4**, e228 (2015).
13. M. Olsen, G. Hjorto, M. Hansen, O. Met, I. Svane, and N. Larsen, “In-chip fabrication of free-form 3D constructs for directed cell migration analysis,” Lab Chip **13**, 4800–4809 (2013).
14. J. Xu, H. Kawano, W. Liu, Y. Hanada, P. Lu, A. Miyawaki, K. Midorikawa, and K. Sugioka, “Controllable alignment of elongated microorganisms in 3D microspace using electrofluidic devices manufactured by hybrid femtosecond laser microfabrication,” Microsyst. Nanoeng. **3**,, 16078 (2017).
15. A. Ovsianikov, X. Shizhou, M. Farsari, M. Vamvakaki, C. Fotakis, and B. N. Chichkov, “Shrinkage of microstructures produced by two-photon polymerization of Zr-based hybrid photosensitive materials,” Opt. Express **17**, 2143–2148 (2009).
16. H. Sun, T. Suwa, K. Takada, R. Zaccaria, M. Kim, K. Lee, and S. Kawata, “Shape precompensation in two-photon laser nanowriting of photonic lattices,” Appl. Phys. Lett. **85**, 3708–3710 (2004).
17. Q. Sun, K. Ueno, and H. Misawa, “In situ investigation of the shrinkage of photopolymerized micro/nanostructures: the effect of the drying process,” Opt. Lett. **37**, 710–712 (2012).
18. K. Takada, D. Wu, Q.-D. Chen, S. Shoji, H. Xia, S. Kawata, and H.-B. Sun, “Size-dependent behaviors of femtosecond laser-prototyped polymer micronanowires,” Opt. Lett. **34**, 566–568 (2009).
19. S. M. Kuebler, A. Narayanan, D. E. Karas, and K. M. Wilburn, “Low-distortion surface functionalization of polymeric microstructures,” Macromol. Chem. Phys. **215**, 1533–1542 (2014).
20. S. Rekštytė, D. Paipulas, M. Malinauskas, and V. Mizeikis, “Microactuation and sensing using reversible deformations of laser-written polymeric structures,” Nanotechnology **28**, 124001 (2017).
21. Y. Li, H. Cui, F. Qi, H. Yang, and Q. Gong, “Uniform suspended nanorods fabricated by bidirectional scanning via two-photon photopolymerization,” Nanotechnology **19**, 375304 (2008).
22. Q. Sun, S. Juodkazis, N. Murazawa, V. Mizeikis, and H. Misawa, “Freestanding and movable photonic microstructures fabricated by photopolymerization with femtosecond laser pulses,” J. Micromech. Microeng. **20**, 035004 (2010).
23. T. Ikegami, M. P. Stocker, K. Monaco, J. T. Fourkas, and S. Maruo, “Fabrication of three-dimensional metalized movable microstructures by the combination of two-photon microfabrication and electroless plating,” Jpn. J. Appl. Phys. **51**, 6S (2012).
24. H. Xia, J. Wang, Y. Tian, Q.-D. Chen, X.-B. Du, Y.-L. Zhang, Y. He, and H.-B. Sun, “Ferrofluids for fabrication of remotely controllable micro-nanomachines by two-photon polymerization,” Adv. Mater. **22**, 3204–3207 (2010).
25. P. Danilevičius, S. Rekštytė, R. Gadonas, M. Malinauskas, E. Balčiūnas, R. Jarašienė, D. Baltriukienė, V. Bukelskienė, A. Kraniauskas, and R. Širmenis, “Micro-structured polymer scaffolds fabricated by direct laser writing for tissue engineering,” J. Biomed. Opt. **17**, 081405 (2012).
26. H.-B. Sun, K. Takada, and S. Kawata, “Elastic force analysis of functional polymer submicron oscillators,” Appl. Phys. Lett. **79**, 3173–3175 (2001).
27. S. Nakanishi, S. Shoji, S. Kawata, and H.-B. Sun, “Giant elasticity of photopolymer nanowires,” Appl. Phys Lett. **91**, 063112 (2007).
28. Z. Bayindir, Y. Sun, M. J. Naughton, C. N. LaFratta, T. Baldacchini, J. T. Fourkas, J. Stewart, B. E. A. Saleh, and M. C. Teich, “Polymer microcantilevers fabricated via multiphoton absorption polymerization,” Appl. Phys Lett. **86**, 064105 (2005).
29. T. Baldacchini, V. Nuñez, C. N. LaFratta, J. S. Grech, V. I. Vullev, and R. Zadoyan, “Microfabrication of three-dimensional filters for liposome extrusion,” Proc. SPIE **9353**, 93530W (2015).
30. C. N. LaFratta and T. Baldacchini, “Two-photon polymerization metrology: Characterization methods of mechanisms and microstructures,” Micromachines **8**, 101 (2017).
31. A. Žukauskas, I. Matulaitienė, D. Paipulas, G. Niaura, M. Malinauskas, and R. Gadonas, “Tuning the refractive index in 3D direct laser writing lithography: towards GRIN microoptics,” Laser Photon. Rev. **9**, 706–712 (2015).
32. Y. Bellouard, A.A. Said, and P. Bado, “Integrating optics and micro-mechanics in a single substrate: a step toward monolithic integration in fused silica,” Opt. Express **13**, 6635–6644 (2005).
33. Y. Bellouard, “On the bending strength of fused silica flexures fabricated by ultrafast lasers [Invited],” Opt. Mater. Express **1**, 816–831 (2011).
34. A. Ovsianikov, J. Viertl, B. Chichkov, M. Oubaha, B. MacCraith, I. Sakellari, A. Giakoumaki, D. Gray, M. Vamvakaki, M. Farsari, and C. Fotakis, “Ultra-low shrinkage hybrid photosensitive material for two-photon polymerization microfabrication,” ACS Nano **2**, 2257–2262 (2008).
35. A. Skarmoutsou, G. Lolas, C. A. Charitidis, M. Chatzinikolaidou, M. Vamvakaki, and M. Farsari, “Nanomechanical properties of hybrid coatings for bone tissue engineering,” J Mech. Behav. Biomed. **25**, 48–62 (2013).
36. W. Xiong, Y. Liu, L. Jiang, Y. Zhou, D. Li, L. Jiang, J.-F. Silvain, and Y. Lu, “Laser-directed assembly of aligned carbon nanotubes in three dimensions for multifunctional device fabrication,” Adv. Mat. **28**, 2002–2009 (2016).
37. S. Rekštytė, T. Jonavičius, D. Gailevičius, M. Malinauskas, V. Mizeikis, E. Gamaly, and S. Juodkazis, “Nanoscale precision of 3D polymerization via polarization control,” Adv. Opt. Mater. **4**, 1209–1214 (2016).

1. Introduction

Femtosecond laser pulses have enabled high precision fabrication of 3D structures in glass by subtractive laser-assisted etching (LAE) [1–4] as well as additive fabrication of polymers via two-photon polymerization (2PP) [5–7]. Due to their high-peak intensities, tightly focused femtosecond laser beams can trigger non-linear two-photon or multi-photon absorption phenomena. This unique characteristic leads to a modification of transparent material only within the focal point of laser beam. By spatially moving the laser focus, well-defined 3D patterns can be written. In the LAE technique glass is structurally modified so that laser affected zones are etched significantly faster than unaffected ones. This is observed in both HF [2] and KOH [8]. This technique allows for processing mm-cubes volumes or more with yet, micron resolution. Glass material provides robustness, transparency and biocompatibility to the structures [4].

Contrary to LAE, 2PP is an additive technique, which is based on the structuring of a photosensitive polymer, when polymerization reactions occurs at the focus point of the laser beam [5]. 2PP technique provides stretchable, but at the same time soft, complex-shape polymeric structures with a feature size resolution as small as few tens of nanometers [9]. Recently, novel device concepts were unraveled as 2PP technique was employed for additively incorporating functional 3D polymeric components in glass micro-voids/-channels [10].

Although, LAE and 2PP techniques exhibit different advantages and drawbacks, the combined use of subtractive and additive techniques open new possibilities for the fabrication of microstructures whose manufacturing was difficult or inaccessible using only one of the two techniques individually. New applications and functionalities could be achieved with such hybrid fabrication method for creating microfluidic devices for cell sorting, counting, liquid mixing and filtering applications [10–14].

An important feature of 2PP-made structures is that, during the development and drying processes, there is always a change in material state. On one hand, the polymerized material becomes denser and consequently geometrical structure dimensions turn out inevitably smaller than expected. This irreversible volume reduction is an effect of dissolution of the non-polymerized internal nanometer size pores of the structure [15–17]. On the other hand, polymeric structures can also swell after rinsing in solvents after (or during) developing process [18–20]. Strongly wetting solvents tend to penetrate the nanometric pores washed out by the developer so that polymeric structure expands. Although these phenomena have been investigated in a number of articles, most of the studies have been done only qualitatively and within a range of one to several tens of micrometers [17, 21, 22]. Furthermore, shrinkage and swelling phenomena have a potential to be applied in chemical sensing applications [20].

2PP-formed microstructures are also used in applications in the fields of microelectromechanics (MEMS) [23, 24] and bioengineering [25], where knowledge of the mechanical and elastic properties of a structure is essential. Several studies have investigated the elastic behavior of microstructures made with the 2PP technique: Sun *et al.* used optical tweezers to deflect polymeric micro-springs [26, 27], while others applied distance-force probing with a commercial atomic force microscope [28] or MEMS based force sensing probes [29] (a recent review on this topic can be found in reference [30]). These studies indicate that laser fabricated microstructures have lower stiffness if compared to the bulk polymer, due to inhomogeneous (voxel-to-voxel) polymerization [28], while in some cases giant elasticity (extreme low stiffness/shear module values) was reported [27]. Permeation of organic liquids in the polymer or scaling effects were considered as plausible causes for such unexpected behavior [27]. The wide range of factors that can contribute to microstructure elasticity makes this topic particularly challenging to investigate, but the emerging attractive applications that rely on elastic properties require detailed investigation.

In this article, to further improve hybrid manufacturing technology we present a coupled device concept consisting of LAE fabrication of a cantilever out of fused silica substrate with

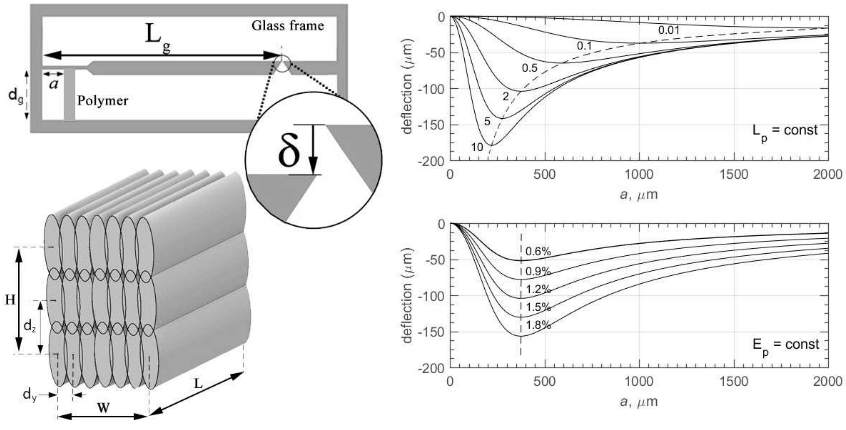

Fig. 1. *(top-left)* Sketch of the glass cantilever with integrated polymeric beam that may induce cantilever deflection due to the shrinkage/swelling effects. *(bottom-left)* A schematic construction of a polymer beam fabricated by LAE and 2PP methods. *(right)* Modeled cantilever tip deflection values versus distance along the cantilever where the polymer is integrated. Top graphs are modeled with a constant polymer shrinkage value (in this case 1.2% from original design value (d_g)) and a different Young's modulus (in GPa), while the bottom graph depicts a situation where the Young's modulus is constant (2 GPa) and shrinkage value is varied. Dashed curves depict maximum deflection trends in both graphs.

the direct integration of a polymeric beam via the 2PP technique. Through this combination of techniques, we demonstrate a novel hybrid glass-polymer micromechanical sensor used to investigate the elastic properties of polymeric microstructures. The well-defined geometry of the fused silica cantilever acts as an amplification system and tester for the quantitative investigation of the polymeric beam properties. In this context, we present the polymeric beam length change due to the shrinkage/swelling phenomena, as well as the Young's modulus estimation results of the SZ2080 polymer in different ambient surroundings, giving new insights into the behavior of the polymeric microstructures.

2. Cantilever design and theoretical model

The glass cantilever with the integrated polymeric beam is depicted in Fig. 1. The polymeric structure links the fixed glass base to the cantilever. Upon shrinkage or swelling, the beam shrinks or expands causing the cantilever to bend upwards or downwards. In a first approximation, this system can be analyzed as a cantilever beam with a point load. As the elastic properties of fused silica are well known, and considering the fact that silica is inert in most chemicals, the cantilever deflection allows for evaluating the reaction force applied on the polymer and in turn, for estimating its elastic properties.

Based on the assumption formulated above, the magnitude of the cantilever tip deflection (δ) is expressed as follows:

$$\delta = \frac{E_p S_p (L_p - d_g)(3L_g - a)a^2}{2(E_p S_p a^3 + 3E_g I_g L_p)}; \tag{1}$$

where E_g is the fused silica Young's modulus (72 GPa), L_g – the total cantilever length (10 mm), d_g – the distance between the cantilever and the glass base (342 µm), a – the distance between

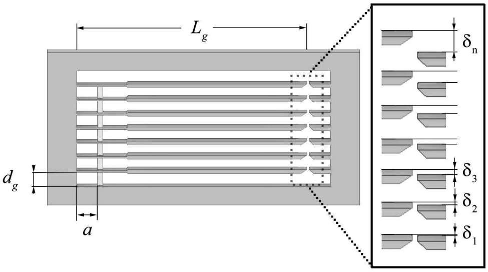

$$\begin{bmatrix} k+f & f & f & f & \dots & f \\ -k & k+f & f & f & \dots & f \\ 0 & -k & k+f & f & \dots & f \\ 0 & 0 & -k & k+f & \dots & f \\ \vdots & \vdots & \vdots & \vdots & \ddots & \vdots \\ 0 & 0 & 0 & \dots & -k & k+f \end{bmatrix} \begin{bmatrix} \delta_1 \\ \delta_2 \\ \delta_3 \\ \delta_4 \\ \vdots \\ \delta_n \end{bmatrix} = \frac{(3L_g - a)(L_p - d_g)k}{2a}$$

$$f = \frac{3E_g I}{a^3} \qquad k = \frac{E_p S_p}{L_p}$$

Fig. 2. A sketch of a coupled cantilever system consisting of several cantilevers interlinked with the polymer beam (each polymer segment is identical). A linear system equation that can be used to compute deflection of each cantilever is also included.

the fixed cantilever end and the polymer, I_g is the silica's second moment of inertia, (which for a rectangular cross-section is $I_g = \frac{t_g w_g^3}{12}$, with w_g – the cantilever width (35 μm), and t_g – its thickness (480 μm)). The polymer cross-section is denoted by S_p (50 μm × 50 μm).

Two parameters remain unknown: E_p – the Young's modulus of the polymer, and L_p – the final length of the polymer after swelling or shrinkage in the absence of a reaction force. These parameters can be estimated using a set of cantilevers in which the polymer beams are attached at different positions, a (see Fig.1). Shifting the polymer beam attachment point scales the reaction force and allows for probing the polymer elasticity under fixed conditions and polymer beam length. Figure 1 (right) shows typical plots of cantilever deflection with different polymer elasticity. One can see that the shrinkage/swelling of the polymer (change in L_p value) influences only the overall magnitude of deflection, while a change in E_p shifts the maximum deflection position along the cantilever beam. Therefore, it is possible to unambiguously fit the data to both unknown parameters using Eq. (1). As we will see later, both parameters are environmentally dependent and can be utilized for chemical sensing applications.

The modulus of elasticity is a material property, while the stiffness (k) describes elasticity of a structure made from the material in question. In our case the polymeric structure is a rectangular beam made by direct laser writing (DLW) with a dense patterning algorithm. Although, the structure is made by combining discrete patterns, we assume it is dense enough, so that it is reasonable to consider it as an plain and homogeneous beam of Young modulus E_p. If necessary E_p could be interchanged with k in Eq. (1) using Young's modulus expression as $E_p = \frac{kL_p}{S_p}$.

A slightly different cantilever sensor can be designed by linking several identical cantilevers into one combined system as shown in Fig. 2. Here, each cantilever's reaction force applies to all polymeric segments that are below the cantilever, therefore in each segment different force scaling is achieved allowing for probing the polymer elasticity. To compute each cantilever deflection, one needs to solve the linear system equation depicted in Fig. 2. As in Eq. (1), there are two unknown parameters: E_p and L_p. The benefit of such a system lies in its simpler polymeric beam integration procedure, as the polymeric beam can be recorded in one single step (simultaneously through all cantilevers), automatically making all segments identical in term of geometry and exposure parameters, an increase in repeatability can be expected. The main drawback is the reduced lack of accuracy, because polymeric segments close to the glass base experiences a higher glass stiffness resulting in greater reaction forces that considerably reduces the cantilever deflections, making it hard to measure (optimizing the sensor design by making each cantilever of different thickness can overcome this problem). This design was created as a substitute for the simple cantilever model if sufficient polymeric integration repeatability could not be achieved in the former case. It turned out that repeatability was not a problem; therefore we used the coupled cantilever design as an alternative method to estimate polymeric elastic properties.

3. Experimental details

The glass processing and polymer integration experiments were conducted using a DLW method employing a single Yb:KGW femtosecond laser system (Pharos, Light Conversion). The sample was translated using dual XY linear stages (ANT130-XY, Aerotech Inc.), while the laser focus spot was changed using a vertical Z stage (ANT160L-Z, Aerotech Inc.).

The monolithic glass cantilevers were produced from a single piece of 500 μm-thick fused silica substrate by combining femtosecond laser radiation and subsequent chemical etching. Glass modifications were induced with laser beam having circular polarization at 1030 nm laser wavelength, using 270 mW laser power (rep. rate 610 kHz), while focusing with 0.4 NA objective. Laser pulse duration was increased to 600 fs in order to achieve better etching selectivity. The multiple laser-modified tracks along the predefined cantilever perimeter were recorded at 15 mm/s velocity in layer-by-layer fashion with 4.5 μm spacing.

After laser exposure, the fused silica substrate was immersed in a low-concentration 5% (v/v) hydrofluoric acid (HF) solution for 6 hours. Cantilevers were later rinsed in distilled water and afterwards dried. Using this method several cantilevers were made close to each other in one monolithic glass block.

Afterwards, the fabricated cantilever structure was put on a standard microscope cover glass and fully covered with photosensitive polymer using the drop-casting method. For this experiment we used a hybrid inorganic/organic photosensitive polymer SZ2080, which was additionally photo-sensitized with 1% wt of 2-benzyl-2-(dimethylamino)-4’-morpholinobutyrophenone photoinitiator. SZ2080 polymer immersed in glass cantilevers was firstly prebaked for 1.5 h on a hot-plate with a temperature ramp of 40°C – 90°C.

The 2PP experiments were carried out using a frequency-doubled wavelength (515 nm) at 200 fs-width pulses operated at a 610 kHz repetition rate. The specimen was loaded on the same XY linear stage system, but using a tighter focusing objective (0.8 NA). A polymeric rectangular-shape beam was integrated in the glass structure (top surface of the polymer was 10 μm below the glass surface level). The total size of the polymeric beam was (HxWxL=50x50x342) μm^3, while two different pattern densities were used: one (I) with parameters $dy = 0.25$ μm and $dz = 1.5$ μm while the other (II) with $dy = 0.5$ μm and $dz = 4.5$ μm (see Fig. 1). In both cases the voxels overlap in all three dimensions, forming a continuously polymerized structure. However in the first case the total exposure dose is higher allowing for a higher degree of conversion of monomers, which impacts polymer swelling properties [20, 31]. In both hatching cases, an average power of 0.8 mW was used and the writing velocity was 3 mm/s. To scale the cantilever reaction force, polymeric microbeams were integrated at different positions from the cantilever base and, in each configuration, three equal polymer-cantilever systems were fabricated in order to test the experiment’s repeatability. After 2PP processing, the samples were immersed in a developer bath (4-methyl-2-pentanone (PEN)) for 20 – 30 min to wash out unexposed material.

The glass cantilever based on previous work on glass flexures [32, 33] has low stiffness in one plane while remaining stiff for out-of-the-plane movement. By immersing such a composite micromechanical system in various liquids or allowing the sample to dry (a critical point dryer K850 (Quorum Technologies) was used for drying specimens), a polymer swelling/shrinkage phenomenon occurs, causing the cantilever beam to deform through bending. The composite micromechanical cantilever system was immersed in different liquids (PEN, ethanol and water), which resulted in different cantilever deflection angles, demonstrating the sensing mechanism.

4. Results and discussion

The fabricated cantilever with integrated polymer beam is shown in Fig. 3. The polymeric beam fabricated in high pattern density condition (I), as discussed in the previous paragraph, undergoes shrinkage right after development as can be seen from the cantilever deflection data depicted in Fig. 4. Initially, the deflection is measured when the sensor is still in the developer (PEN), which later is interchanged with ethanol. Afterwards, the liquids are evaporated and the deflection is measured in air. The evaporation has to be carried out in a critical point drying condition, in order to prevent capillary forces from acting on the glass cantilever, resulting in polymer breakage or detachment of the polymeric beam from the glass substrate. In all cases the data were fitted using the least square method applied to the Eq. (1). As can be seen, there is a good fit of the experimental data with the theoretical model. The fitting parameters (E_p, L_p) are as follows: immersed in PEN: (0.188 ± 0.005 GPa; 339.5 ± 0.1 μm); ethanol: (0.158 ± 0.007 GPa; 339.6 ± 0.1 μm) and air: (0.138 ± 0.008 GPa; 340.1 ± 0.1 μm). Fitting errors are within the 95% confidence interval (dashed curves in figures). Note that the possible cantilever geometry estimation errors are not present in the fitted data (all cantilevers are identical), and are not important if comparative analysis between three different environments is carried out. If one includes geometrical measurement errors (i.e. assuming 5% precision in measuring all cantilever dimensions), the absolute values for Young's modulus and shrinkage/swelling can be estimated with ~25% precision (evaluated by Monte Carlo simulation) by this method.

The results show that the average polymer shrinkage is about 0.6 %. This value is expected as SZ2080 is considered as an ultra-low shrinkage photosensitive polymer [15, 34]. However there is an evident increase in the Young's modulus when the polymeric beam is immersed in the organic liquid. The cantilever reaction force builds up due to the increased polymer stiffness and not to the polymer shrinkage.

A similar tendency is present in samples made with the lower density (II) scheme. In these cases, the samples swell as high affinity (strongly wetting) solvents such as PEN or ethanol penetrate the internal nanoscale pores causing the polymer to expand. In contrast, water or other low affinity solvents empty the pores causing the polymers to shrink [20].

The cantilever deflection curves are shown in Fig. 5(a), and fitted values are as follow: PEN (0.467 ± 0.018 GPa; 345.8 ± 0.1 μm) and ethanol (0.493 ± 0.015 GPa; 345.1 ± 0.1 μm). Samples were also tested in water, but the cantilever did not show any deflection, suggesting that shrinkage/swelling is too low to induce sufficient forces (for the same reason sample drying was not attempted in this case). Remarkably, these results indicate an increase of up to 3 times in the Young's modulus if compared to the higher density patterning scheme. Internal presence of organic liquid molecules in the polymer network considerably increases its stiffness and makes

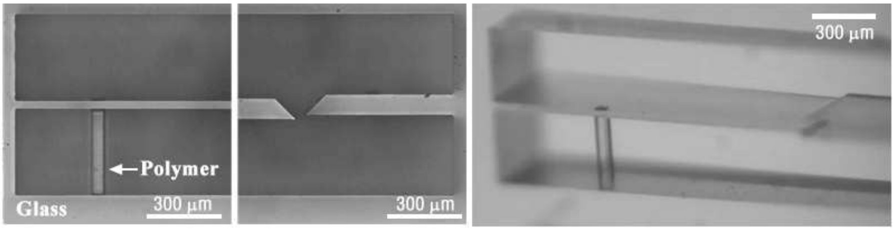

Fig. 3. Fused silica cantilever with SZ2080 polymeric beam fabricated by the hybrid femtosecond laser processing technique. The optical microscope images indicate the deflection of the cantilever after polymer shrunk in air. The picture on the right shows a stereoscopic microscope image of a hybrid sensor.

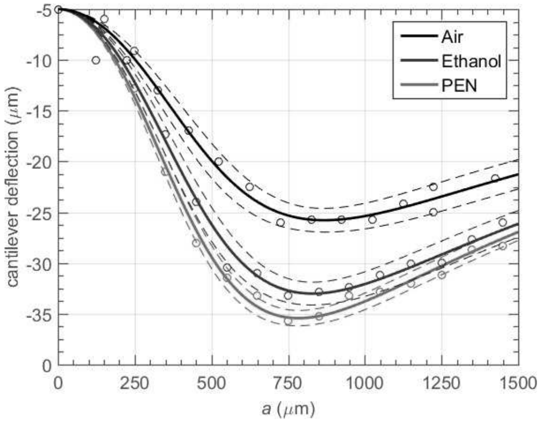

Fig. 4. Cantilever deflection induced by polymer shrinkage in various organic liquids and air.

cantilever actuation stronger. Additionally, the swelling behavior is reversible and repeatable. Figure 5(b) depicts the cantilever deflection change when the sample is periodically immersed in different liquids. Even after 10 cycles of ethanol–PEN changes, the deflection magnitude remained the same. This also applies to water–organic solvent cycles, when deflection changes are maximized. This fact makes such hybrid micromechanical systems attractive for chemical sensing applications.

Similar values for polymer elastic properties were acquired with the coupled cantilever system, as shown in Fig.6. The least square fit of the model gives slightly lower Young's modulus values than in the previous case, but taking into account absolute 25 % precision the values match in both experiments.

Our study shows that the Young's modulus in 2PP fabricated structures differ by an order of magnitude from typical values for bulk SZ2080 polymer hardened by continuous UV radiation [35]. A similar trend was observed in other laser-polymerized photosensitive resins such as SR369 [29] and SR499/368 [28]. On the contrary, Sun *et al.* reported much lower stiffness values when a sample is immersed in organic liquid [26,27]. Solvent permeation into the polymer was speculated

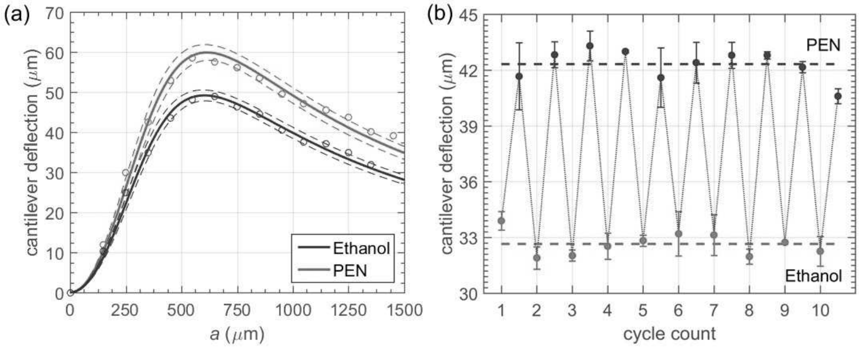

Fig. 5. (*a*) Cantilever deflection induced by polymer swelling in organic liquids. (*b*) Cantilever deflection dependence on the solvent change cycle number.

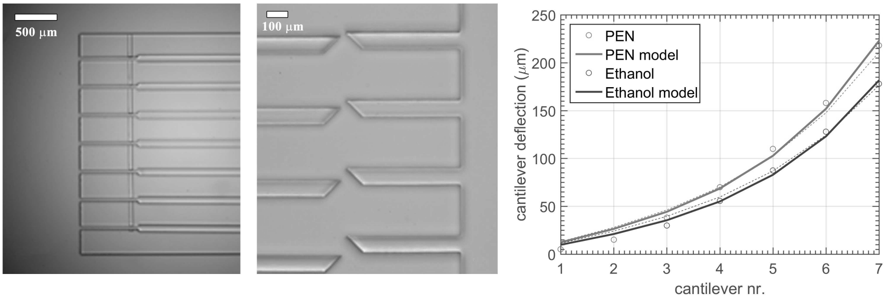

Fig. 6. The manufactured cantilever system, consisting of seven interlinked cantilevers. Microscope images are shown on the *left* and *center* (cantilevers are immersed in PEN). (*right*) Deflection of the coupled system in different solvents: solid curves show the least square fit of the data computed from the coupled cantilever model (Fig. 2), fit parameters: PEN (0.40 GPa, 346.4 µm) and ethanol (0.389 GPa, 345.6 µm); dashed curves show the model fit with parameters evaluated from the single cantilever experiment (Fig. 5(a)).

as one of the possible causes for a drop in the polymer elasticity. In our research, we show that organic solvent increases the polymer stiffness, especially in those cases where the degrees of conversion were lower. These contradicting results can be attributed to different polymer type and/or scaling effects.

5. Conclusions

In summary, we have demonstrated a novel hybrid glass-polymer micromechanical sensor that can be utilized for investigating the elastic properties of polymeric microstructures fabricated by the 2PP technique. The results indicate that the 2PP made microstructures of hybrid organic-material can vary in mechanical properties depending on the surrounding solvent. In most cases there is an evident increase in Young's modulus while the structure is submerged in organic liquids. Some further studies could be conducted to reveal the influence of the direct laser writing scanning trajectory [36], exposure conditions – including dose, voxel overlap, and considering polarization for final 3D microstructures mechanical properties [37]. The change in Young's modulus can be utilized for chemical sensing applications as shown with our glass cantilever setup.

Funding

Swiss-Lithuanian Institution Cooperation Programme "Research and Development" (Grant No. CH-3-ŠMM-02/05).

Acknowledgment

The Galatea Lab at EPFL acknowledges the sponsoring of Richemont International.

P2

4PI MULTIPHOTON POLYMERIZATION

T. Tičkūnas, D. Paipulas, and V. Purlys

Appl. Phys. Lett. **116**(3), 031101 (2020)

Applied Physics Letters ARTICLE scitation.org/journal/apl

4Pi multiphoton polymerization

Cite as: Appl. Phys. Lett. **116**, 031101 (2020); doi: 10.1063/1.5128786
Submitted: 22 September 2019 · Accepted: 4 January 2020 ·
Published Online: 21 January 2020

T. Tičkūnas,[1,2,a)] D. Paipulas,[1] and V. Purlys[1,2]

AFFILIATIONS

[1]Laser Research Center, Vilnius University, Vilnius 10223, Lithuania
[2]Femtika Ltd., Vilnius 10224, Lithuania

[a)]**Electronic mail:** titas.tickunas@ff.vu.lt

ABSTRACT

We present a 4Pi multiphoton polymerization technique—a technique that, similar to microscopy, enables a significant improvement of the axial resolution of the fabricated features. We describe this technique in detail and present a numerical simulation analysis of the light intensity distribution in the focal plane as well as experimental results. Using the 1030 nm wavelength, we were able to achieve 150 nm height features, which is about three times shorter than that using the traditional excitation technique, resulting in nearly spherical voxels. Furthermore, we show that depending on the focusing conditions, it is also possible to fabricate periodic interference patterns along the illumination direction, which can be utilized for photonics applications.

Multiphoton polymerization (MPP) is a powerful tool allowing the fabrication of arbitrarily shaped three-dimensional microstructures with feature sizes beyond diffraction limited resolution.[1,2] This technique has been applied to a broad range of applications, such as micro-optics,[3] biomedicine,[4] and microelectromechanics.[5] Typically, this technology allows us to achieve the lateral feature resolution of hundreds of nanometers; however, the axial dimension is at least ∼3 times larger than the transversal dimension even when using high numerical aperture (NA) state-of-the-art microscope objectives.[5,6] This voxel anisotropy might be a limiting factor for some applications, e.g., for fabrication of woodpile photonic crystals, where not only the transversal but also the axial feature size is important. Therefore, a focal spot with a 1:1 aspect ratio could significantly enhance the final resolution and functionality of the fabricated structures. In general, to fundamentally overcome this aspect ratio problem, the more advanced focusing techniques need to be implemented, such as stimulated emission depletion (STED),[6,7] spatial light modulator (SLM),[8] or spatiotemporal beam shaping techniques.[9]

In microscopy, which shares the same focusing principles as MPP, a 4Pi focusing technique can be used for improving the resolution in the axial direction. The 4Pi excitation principles were first pioneered by Hell *et al.*[10–12] The idea behind 4Pi microscopy is to provide uniform excitation over the complete solid angle of 4π steradians, hence the name. Under such conditions, the excitation region is completely spherical. A single high-NA objective traditionally used for microscopy typically covers only an aperture angle of up to 136°[10,13] (1.25π), which in turn results in an elongated, ellipsoid shaped focal region. This limitation can be overcome by using two opposing high NA objectives to focus counterpropagating laser beams in such a way that the foci spatially coincide and the pulses temporally overlap. By using this optical configuration, the effective solid angle could be increased twofold, which becomes much closer to the ideal 4π excitation.

In such a way, the constructive interference at the common focus takes place, leading to the improvement of the axial resolution by several times. In practice, the entire 4π solid angle is not covered; therefore, the central peak is also followed by the so-called sidelobes above and below the focal spot for high NA objectives. The lower the NA, the more pronounced this effect becomes, leading to a periodic intensity pattern along the optical axis. The additional optical techniques could be used to suppress the sidelobes, such as a non-linear excitation.[11,14] Similarly, the integration of 4Pi illumination into the traditional MPP setup could be used to sharpen the spatial light distribution in the focal region and hence reduce the axial feature sizes for 3D microstructures made by MPP technology.

In this paper, we present our results on implementing the 4Pi-MPP technique. We demonstrate that by changing the focusing conditions, it is possible to either create a highly periodic pattern along the writing axis or enhance the axial resolution significantly and achieve almost spherical diffraction limited voxel shape. Both properties are difficult to achieve using the traditional MPP technique; thus, these results might find a practical application where high resolution is required.

To calculate the point spread function (PSF) under the tight focusing conditions with a single high NA objective, the polarization of the light plays an important role and needs to be considered. For this purpose, we used vectorial Debye theory. We followed the theory described in Refs. 15 and 16, which also takes into account the contribution of spherical aberrations due to several interfaces between the objective lens and the focal point. In general for a single objective illumination, the solution for the electric field vector E at the focus point P could be expressed as[16]

$$\begin{aligned} E = (E_x, E_y, E_z) = (-iK(I_0 + I_2 \cos 2\phi), \\ -iKI_2 \sin 2\phi, -2KI_1 \cos\phi), \end{aligned} \tag{1}$$

where ϕ denotes the angle between the polarization direction of the incident field and the observation direction, K, is a constant. The integrals I_0, I_1, I_2 are defined by[15]

$$\begin{aligned} I_0 = \int_0^{\alpha} A(\theta_1) \sin\theta_1 J_0(k_1 r \sin\theta_1)(T_s + T_p \cos\theta_3) \\ \times \exp[ik_0\psi] \exp(ik_3 z \cos\theta_3) \mathrm{d}\theta_1, \end{aligned} \tag{2}$$

$$\begin{aligned} I_1 = \int_0^{\alpha} A(\theta_1) \sin\theta_1 J_1(k_1 r \sin\theta_1) T_p \sin\theta_3 \\ \times \exp[ik_0\psi] \exp(ik_3 z \cos\theta_3) \mathrm{d}\theta_1, \end{aligned} \tag{3}$$

$$\begin{aligned} I_2 = \int_0^{\alpha} A(\theta_1) \sin\theta_1 J_2(k_1 r \sin\theta_1)(T_s - T_p \cos\theta_3) \\ \times \exp[ik_0\psi] \exp(ik_3 z \cos\theta_3) \mathrm{d}\theta_1, \end{aligned} \tag{4}$$

where α is the aperture angle ($NA = n_1 \sin\alpha$), r is the radial distance, and the wave vector in the different media is given as $k_3 = k_0 n_3 = 2\pi n_3/\lambda_0$, with λ_0 being the wavelength in vacuum and n the refraction index of the medium. J_0, J_1, J_2 are the Bessel functions of the first kind, and ψ stands for the aberration function. $A(\theta_1)$—describes the apodization function, which satisfies the sine condition. The terms T_s and T_p are transmission coefficients through stratified media for s- and p-polarized light, respectively. The angles $\theta_1, \theta_2, \theta_3$ are linked by Snell's law as shown in Fig. 1(a).

For the 4Pi excitation case, the illumination intensity distribution h_{4Pi} in the focal region can be expressed as[11]

$$h_{4Pi} = |E_1 + E_2|^2, \tag{5}$$

where E_1 and E_2 are the electric fields generated by the illumination from the first and second objectives, respectively. During the simulations, we assumed that focusing depth and coverslips thickness were identical for both objectives, and the light is linearly polarized with the electric field vector lying in the YZ plane.

The results of the theoretical analysis of the light intensity distribution at the focal region under different illumination conditions are shown in Figs. 1(b)–1(d). Compared to Fig. 1(b), where a PSF of a single 0.8 NA objective is shown, the simulation of two objectives [Fig. 1(c)] shows a similar ellipsoid-shaped distribution, but additionally having an interference pattern. The period between the layers is approximately equal to $\lambda/2n$ and slightly depends on the numerical aperture. For $\mathrm{NA} = 0.8$ and $n = 1.504$, the period of the interference pattern resulted in ~360 nm for the 1030 nm laser wavelength. The number of generated sidelobes in the PSF could be lowered by increasing the NA of the objectives, but even by using 4Pi excitation with 1.4 NA objectives, the results show a pair of relatively high intensity sidelobes [Fig. 1(d)]. However, it is possible to tune the laser intensity in such a way that the polymerization threshold is exceeded only at the central peak, while the intensity of the sidelobes remains below the threshold. As demonstrated further, such conditions lead to the nearly spherical voxel shape. It is worth noting that some background cross-linking might appear at the sidelobe regions even if they are below the polymerization threshold. If the same sidelobe regions are exposed multiple times, the background cross-linking might accumulate and prevent the development of these regions. In such cases, the scanning trajectories and exposure parameters have to be selected more carefully. On the other hand, the generation of the sidelobes could be a benefit—the highly periodic interference pattern is difficult to produce using the conventional technique as the feature sizes of individual planes are far below the excitation wavelength.

To experimentally verify the theoretical predictions, we implemented the 4Pi excitation to our traditional MPP setup. The experimental setup is schematically shown in Fig. 2(a). A femtosecond Yb:KGW laser system (Pharos, Light Conversion) was employed, having a laser wavelength of 1030 nm, a pulse duration of ~200 fs, and a pulse repetition rate of 200 kHz. The laser beam was split into two equal-intensity beams by a beam splitter. Both of the beams were steered by dielectric mirrors and focused into the sample by the pairs of two identical objectives (20× 0.8 NA or subsequent experiments

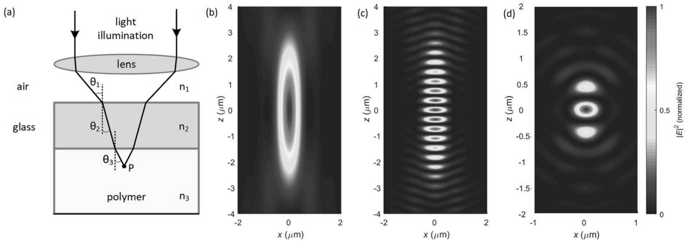

FIG. 1. (a) Schematic illustration of laser beam propagation through stratified media. Calculated PSF in the XZ plane for (b) single 0.8 NA objective with $\lambda = 1030$ nm laser wavelength; (c) an interfered PSF of 4Pi excitation with a pair of 0.8 NA and (d) 1.4 NA objectives.

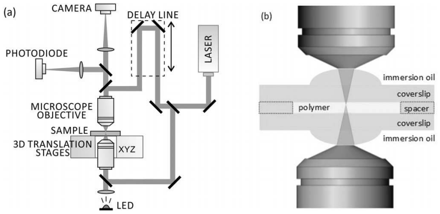

FIG. 2. (a) Schematic drawing of the 4Pi-MPP experimental setup used with oil-immersion high NA objectives and (b) more detailed view of the sample with the photopolymer enclosed between two glass coverslips.

with 63× 1.4 NA). For aligning the foci spatially, the fluorescent light was collected from the sample and directed through the tube lens into the CCD camera. A dichroic mirror before the camera was used to filter the laser beam from the fluorescence signal. By observing the camera view of the fluorescence, the beam path of the upper arm was adjusted accordingly. Afterwards, the pulses from both optical arms were overlapped temporally by precisely moving a pair of mirrors in a delay line. A proper spatial and temporal alignment gave a rise of almost twofold stronger fluorescence signal, detected by the silicon photodiode.

Sample positioning was achieved by piezo XYZ motion stages. During the structure fabrication, the samples were translated at a 50 μm/s velocity. All the experiments were performed with a negative tone resin SZ2080[17] with 0.5% of 4,4′-bis(diethylamino)benzophenone photoinitiator. This polymer has a refractive index of around 1.5 at 632.8 nm.[18]

The polymer was drop-cast on a standard glass coverslip with a thickness of 170 μm. Then, samples were prebaked on a hot-plate with temperature short ramps 40 °C, 70 °C, and kept at 90 °C for 1 h. A U-shaped 100-μm-thick glass spacer was put on the coverslip to ensure a constant polymer thickness. Finally, this structure was enclosed with a second 170-μm-thick glass coverslip on top. The laser irradiation samples were immersed into a 4-methyl-2-pentanone developer bath for 1 h to wash out the laser unexposed material. Later, the samples were submerged into pure ethanol and developed with a critical point dryer. For inspection with a scanning electron microscope (SEM), the samples were coated with a 5–10 nm thick gold layer via sputter-coating.

In the first 4Pi-MPP experiments, a series of individual pillars ($5 \times 5 \times 25\,\mu\text{m}^3$) were fabricated using 0.8 NA objectives by a raster scanning. Figure 3(a) shows an illustration of structure fabrication. The resulting 4Pi-MPP voxels consisted of periodic planes oriented along the optical axis due to the interference of counterpropagating beams. Each of the pillars was fabricated by overlapping transversely the voxels with a period of 0.5 μm, while vertical separation between the adjacent layers was 4.5 μm. Even after the development process, the structures with sub-micrometer thickness planes remained as shown in Fig. 3(b). The periodicity between the polymerized planes was ∼340 nm and was in close agreement with the value predicted by the modeling. Afterwards, the structure was partly milled by focused ion beam (FIB) to reveal the core of the micro-pillar structure as depicted in Figs. 3(c) and 3(d). The cross section showed a non-uniform structure. The exterior section consisted of the interference pattern of alternating air/polymer planes, which was observed in a thin superficial layer around the micro-pillar structure. Toward the core, the air-gap layers turn to lower density zones of the polymer. The center section was polymerized at a higher degree of conversion in cross-linking, but still the interference pattern of different density polymer zones is clearly visible. Most likely, the solvent could not effectively penetrate and wash out the lower degree of conversion polymer zones. From the practical point of view, it would be preferable to have even alternating planes with a higher refractive index change between the adjacent layers (e.g., air/polymer). However, the material and solvent need to be optimized if wider multilayered structures are required.

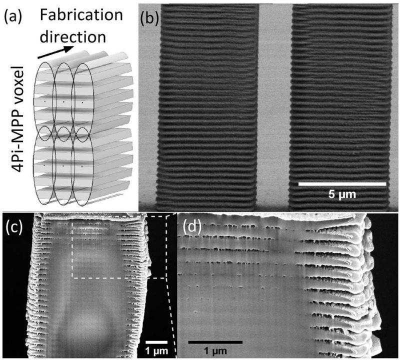

FIG. 3. (a) Principle sketch of the micro-pillar structure fabrication using 4Pi-MPP excitation and (b) side-view SEM image of the fabricated structure by using 4Pi-MPP excitation. An interference pattern was obtained with a period of around 340 nm. (c) and (d) Cross section of the FIB-milled micro-pillar structure revealing the interior morphology.

In addition, we observed a feature that the gaps between interference planes of narrow microstructures could be fully washed out. This might be applied to the narrow structures suspended between additional supports, which allow us to maintain the order of the interlayers and avoid collapse between each of the polymerized planes. Accordingly, we have manufactured a structure as depicted in Fig. 4(a) as an example demonstration of structural coloration.[19] The overall size of structure was $150 \times 75\,\mu\text{m}^2$, composed of 4 μm width and 75 μm length periodic rectangular supports that were spaced at an 8 μm distance. A series of narrow parallel suspended polymerized lines were fabricated by a single laser scan between the supporting blocks using the 4Pi-MPP method. The support structures were fabricated with a single objective only. The applied concept would result in a stack of thin suspended polymeric planes with well-defined air cavities in between. Multiple alternations of periodic sub-micrometer features provide a Bragg reflection, which causes the coloration effect.

After the development, the structure was analyzed under the optical microscope in reflection mode. A coloration was seen in the

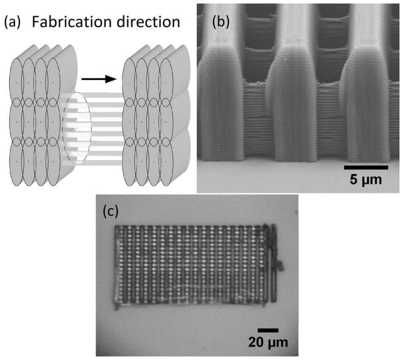

FIG. 4. (a) A sketch of the structure fabrication scheme, (b) a 60°-tilted-view SEM image of the grating structure, and (c) structural colors visible by an optical microscope in reflection mode, resulting from the periodic features in the fabricated lines.

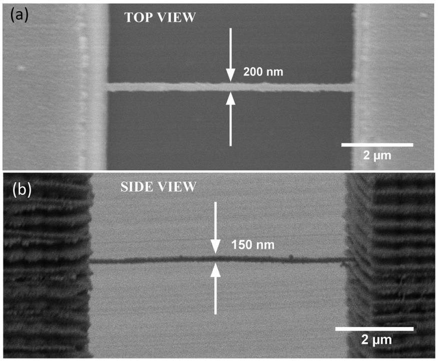

FIG. 5. (a) Top- and (b) side-view of SEM images of 3D suspended fiber between supporting pillars.

blue/green light spectrum range, as demonstrated in Fig. 4(c). SEM inspection of the structure has shown the multiple polymeric layers along the optical axis and each was approximately 180 nm, while air-gap was around 160 nm thick. Such alternating multi-layers can produce a reflection at 860 nm in the near-infrared range, while the second order diffraction would result in the blue spectrum range. The observed broad spectrum coloration came due to the slightly uneven distance among alternating layers caused by the development process. Since the periodicity of the planes is directly proportional to the wavelength, the 4Pi-MPP experiments using shorter wavelengths would reduce the distance between the polymerized planes. For instance, in our case, a frequency doubled wavelength (515 nm) would reduce it by twofold. In such a case, we expect the reflectance in the visible spectral range to be even stronger as it would be caused by the first Bragg diffraction order.

The subsequent experiments were carried out with 1.4 NA objectives in order to improve the feature size in the axial dimension and reduce the voxel aspect ratio using 4Pi excitation. The feature size tests were done by fabricating another series of pillars and a set of suspended lines between them, which were anchored to the glass substrate. Each of the lines was written with an incrementally decreasing laser power, ending far below the polymerization threshold.

At higher excitation powers, the suspended lines consisted of several sidelobes along the optical axis, while at $40\,\mu$W power, we have achieved the condition, when the polymerization threshold was exceeded only at the central peak. SEM images revealed that the axial size of the voxels was 150 nm, while the lateral feature size was 200 nm [Figs. 5(a) and 5(b)]. In this way, the voxel was almost spherical, and the aspect ratio was decreased to 1:0.75. It is worth noting that we considered only the suspended lines, which had survived the developing process and were still hanging between the supporting pillars. Some torn lines showed even better results, and the axial feature size was down even to 110 nm. In comparison, focusing with a single objective resulted in 200 nm lateral and 450 nm axial feature sizes of the suspended lines.

The generation of the interference pattern in the structures fabricated by MPP was already reported in a number of articles, named interference assisted MPP.[19–22] In this technique, the incident laser beam interacts with the reflected one from the interface of material of different refractive indices, e.g., glass/silicon. In general, such light interaction is similar to in 4Pi excitation; however, such multi-layer structures could be generated only near the boundary of the polymer and other material with a relatively high difference in the refractive index.

Similar to 4Pi, STED inspired MPP (STED-MPP) also allows the enhancement of resolution.[23,24] It was shown that the axial feature sizes could be decreased down to $\lambda/20$.[23] However, in contrast to 4Pi-MPP, it supports a very limited amount of suitable photoinitiators and requires special spatial beam profiles.[6] Both STED-MPP and 4Pi-MPP require a precise alignment of two lasers beams, which is not a trivial task in both cases. Moreover, in principle, these two techniques can be combined together, resulting in a STED with 4Pi excitation (as demonstrated in advanced microscopy setups[25]).

Compared to the traditional MPP, the 4Pi arrangement is a more complex technique, requiring a very precise adjustment of both beams in space and time. In principle, foci matching can also be slightly deteriorated by the already exposed regions, especially if the refractive index change after the exposition is high or the exposed regions are long (i.e., having large differences in the optical path); however, under our experimental conditions, we did not observe any strong influence of this effect. In order to solve these issues and broaden the applicability of the 4Pi-MPP technique, the alignment procedure can be automated by using piezo or similar positioners and a feedback loop from the fluorescence signal.

In conclusion, we present the results of the 4Pi multiphoton polymerization technique. We demonstrate that by changing the focusing conditions, it is possible to create highly periodic patterns along the writing axis or enhance the axial resolution significantly and achieve almost spherical diffraction limited voxels. In our case, the period of the periodic pattern was 340 nm for a 1030 nm writing laser wavelength and the axial feature size was enhanced by approximately three times down to 150 nm. Both properties are difficult to achieve using the traditional multiphoton polymerization technique and are useful for various applications where ultra-high resolution is required.

Authors are grateful to Dr. Sima Rekštytė for the help in modeling PSF distributions. V.P. acknowledges the financial support from "FOKRILAS" (Project No. S-MIP-17-109) from the Research Council of Lithuania.

REFERENCES

[1] S. Maruo, O. Nakamura, and S. Kawata, Opt. Lett. **22**, 132 (1997).
[2] M. Malinauskas, M. Farsari, A. Piskarskas, and S. Juodkazis, Phys. Rep. **533**, 1 (2013).
[3] T. Gissibl, S. Thiele, A. Herkommer, and H. Giessen, Nat. Photonics **10**, 554 (2016).
[4] M. T. Raimondi, S. M. Eaton, M. M. Nava, M. Laganà, G. Cerullo, and R. Osellame, J. Appl. Biomater. Funct. Mater. **10**, 56 (2012).
[5] T. Baldacchini, *Three-Dimensional Microfabrication Using Two-Photon Polymerization* (Elsevier, Amsterdam, The Netherlands, 2015).
[6] J. Fischer and M. Wegener, Opt. Mater. Express **1**, 614 (2011).
[7] T. A. Klar, R. Wollhofen, and J. Jacak, Phys. Scr. **2014**, 014049.
[8] E. Mudry, E. L. Moal, P. Ferrand, P. C. Chaumet, and A. Sentenac, Phys. Rev. Lett. **105**, 203903 (2010).
[9] W. Chu, Y. Tan, P. Wang, J. Xu, W. Li, J. Qi, and Y. Cheng, Adv. Mater. Technol. **3**, 1700396 (2018).
[10] S. Hell and E. H. K. Stelzer, J. Opt. Soc. Am. A **9**, 2159 (1992).
[11] S. Hell and E. H. K. Stelzer, Opt. Commun. **93**, 277 (1992).
[12] S. W. Hell, S. Lindek, C. Cremer, and E. H. K. Stelzer, Appl. Phys. Lett. **64**, 1335 (1994).
[13] M. Lang, T. Staudt, J. Engelhardt, and S. Hell, New J. Phys. **10**, 043041 (2008).
[14] H. Gugel, J. Bewersdorf, S. Jakobs, J. Engelhardt, R. Storz, and S. W. Hell, Biophys. J. **87**, 4146 (2004).
[15] M. J. Nasse and J. C. Woehl, J. Opt. Soc. Am. A **27**, 295 (2010).
[16] P. Török and P. Varga, Appl. Opt. **36**, 2305 (1997).
[17] A. Ovsianikov, J. Viertl, B. Chichkov, M. Oubaha, B. MacCraith, I. Sakellari, A. Giakoumaki, D. Gray, M. Vamvakaki, M. Farsari, and C. Fotakis, ACS Nano **2**, 2257 (2008).
[18] A. Žukauskas, I. Matulaitienė, D. Paipulas, G. Niaura, M. Malinauskas, and R. Gadonas, Laser Photonics Rev. **9**, 706 (2015).
[19] G. Zyla, A. Kovalev, S. Heisterkamp, C. Esen, E. L. Gurevich, S. Gorb, and A. Ostendorf, Opt. Mater. Express **9**, 2630 (2019).
[20] Q.-Q. Liu, Y.-Y. Zhao, M.-L. Zheng, and X.-M. Duan, Appl. Phys. Lett. **111**, 223102 (2017).
[21] S. Ghosh and G. Ananthasuresh, Sci. Rep. **6**, 18428 (2016).
[22] B. Mills, D. Kundys, M. Farsari, S. Mailis, and R. W. Eason, Appl. Phys. A **108**, 651 (2012).
[23] L. Li, R. R. Gattass, E. Gershgoren, H. Hwang, and J. T. Fourkas, Science **324**, 910 (2009).
[24] Z. Gan, Y. Cao, R. A. Evans, and M. Gu, Nat. Commun. **4**, 2061 (2013).
[25] M. Dyba and S. W. Hell, Phys. Rev. Lett. **88**, 163901 (2002).

P3

DYNAMIC VOXEL SIZE TUNING FOR DIRECT LASER WRITING

T. Tičkūnas, D. Paipulas, and V. Purlys

Opt. Mat. Express **10**(6), 1432-1439 (2020)

Research Article Vol. 10, No. 6 / 1 June 2020 / Optical Materials Express 1432

Optical Materials EXPRESS

Dynamic voxel size tuning for direct laser writing

TITAS TIČKŪNAS,[1,2,*] DOMAS PAIPULAS,[1] AND VYTAUTAS PURLYS[1,2]

[1] *Laser Research Center, Vilnius University, Vilnius, 10223, Lithuania*
[2] *Femtika Ltd., Vilnius, 10224, Lithuania*
[*] *titas.tickunas@ff.vu.lt*

Abstract: We present a straightforward method to dynamically tune the voxel size in the multiphoton polymerization technique by changing the incident laser beam diameter with a motorized beam expander. In such a manner, the beam underfilling of the objective aperture leads to an effective numerical aperture drop. Therefore, the voxel could be expanded in the lateral and the axial directions without changing the objective. Here, we present the theoretical simulation analysis of the light intensity distribution for different underfilling conditions, as well as the measured experimental results of the voxel feature sizes for high numerical aperture objective. The presented approach extends technology capabilities and could significantly increase the fabrication speed while maintaining the possibility for obtaining the highest resolution features.

1. Introduction

Multiphoton polymerization (MPP) is a powerful tool allowing the fabrication of complex shape 3D microstructures with the feature sizes beyond sub-diffraction limited resolution [1]. Due to a tightly focused femtosecond laser beam in the volume of transparent photopolymer, the cross-linking reactions happen only at a tiny focal spot, which is known as a volumetric pixel - voxel. By spatially moving the laser focus in a layer-by-layer fashion, well-defined complex shape 3D structures could be fabricated. Subsequently, in the negative-tone photopolymer case, the laser unexposed areas are simply washed-out with a developer leaving only solidified structures. This technique could be widely applied in a vast range of the applications, for instance, fabrication of the micro-optics [2], metamaterial elements [3], scaffolds for tissue engineering [4], microfluidic devices [5], etc.

However, apart from the resolution beyond the diffraction limit and versatility of technology capabilities, the major drawback of MPP technology is its relatively low throughput using high numerical aperture objectives. In additive manufacturing, the common principle is to hatch 3D object into multiple separate lines on each of the plane and stack up into layers. The voxel spacing parameters have to be selected more carefully that each individual voxel overlaps onto the previous one. Usually, larger voxels are selected for bulky less precision required structures, while critical tiny features need to be done with smaller voxels. Under tight focusing conditions, the typical layer-by-layer processing method of the mm-size structure fabrication with high resolution features would require an unreasonable and impractical laser processing time. Nonetheless, there are multiple ways to increase the writing speed and shorten the process. For instance, the processing speed could be improved by using alternation of different numerical aperture objectives [6], shaped laser beams (e.g. Bessel [7] or ring-Airy [8]), multiple laser beam focus by diffractive optical elements [9] or spatial light modulator [9,10], advanced holographic light shaping [11], interference-lithography [12], voxel control by spatiotemporal focusing [13], scanning with synchronized linear stages and galvo-scanner mirrors [14]. Throughput could also be improved by different scanning approaches, as fabrication of the superficial layer (shell) of the structure and subsequent ultraviolet exposure [15], or applying adaptive stitching algorithms [16].

In this work, we present our results on implementing the dynamic voxel control for a traditional MPP system by using a motorized beam expander. In contrast with feature size change by incrementally increasing the laser exposure, this method hugely extends the dynamic range of fabrication window for a single high numerical aperture (NA) objective. We demonstrate that by changing the focusing conditions, the resolution of feature size could be easily tuned and realized for continuous single fabrication of 3D structures. Furthermore, this potential technique gives the ability to optimize the fabrication process and have on-demand feature size control without sacrificing precision.

2. Laser experimental setup

The experiments were performed with a commercial laser system (Laser Nanofactory, Femtika Ltd.) with an Yb-based femtosecond laser (Carbide, Light Conversion Ltd.), which was operated at a frequency-doubled wavelength of 515 nm, ~250 fs pulse duration and at a 1 MHz repetition rate. The principal experimental setup is displayed in Fig. 1. The initial beam waist diameter was 1.1 mm ($1/e^2$). The laser beam was directed to the entrance aperture of an integrated motorized telescope. Then, the expanded beam was delivered to the high NA microscope objective, which focused the light into the volume of photosensitive resin. The fabrication process was realized by moving XYZ linear motion stages, and the average laser power was varied by an acousto-optical modulator (AOM). The fabrication speed was kept 100 µm/s for all the structures.

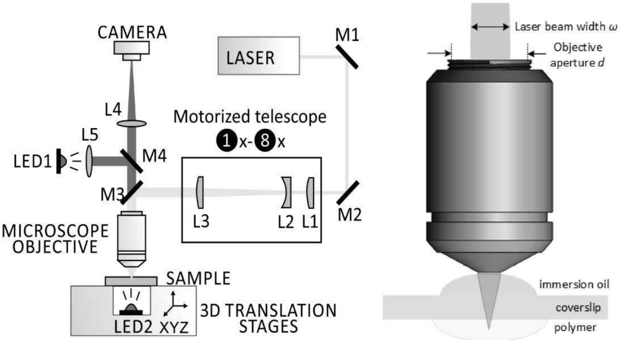

Fig. 1. Schematics of direct laser writing optical setup with a motorized telescope (1-8x expansion ratio) and high NA objective. M1-M4 – reflective mirrors; L1-L5 – lenses.

To change the beam diameter, we used a motorized beam expander (MEX18, Optogama Ltd.), which had a possibility to enlarge the beam between 1- to 8-fold. It consisted of 3 lenses, the last element was fixed, while the first two lenses were driven by two independent motors along the optical axis. The used motorized telescope had high pointing stability of <0.2 mrad and a response time of <50 ms from sent command to the stage/motor motion. The position of the lenses are achievable within 0.2 s and then are corrected and stabilized. Practically, any operation took less 1 s, including the movement and stabilization process over the entire dynamic beam expansion range. Moreover, the motorized beam expander had the ability to regulate/compensate laser beam divergence. In principle, by changing the position of the lenses, the divergence angle could be adjusted. Therefore, the same setup could work as a dynamic laser focus along the optical z axis, which could be applied for 3D micro-processing.

For the experiments, we used a hybrid inorganic/organic photosensitive polymer SZ2080 [17], which was additionally photo-sensitized with 1%wt of Irgacure 369 photoinitiator. The negative tone SZ2080 liquid polymer was drop-casted on a standard glass coverslip and then prebaked on a hot-plate with short temperature ramps at 40°C, 70°C, and kept at 90°C for 1 h. During the prebake procedure, the solvent was evaporated and the polymer turned into a soft gel. Afterwards, the sample was used for the laser fabrication step. The laser irradiated samples were immersed into a 4-methyl-2-pentanone developer bath for 30 min to wash out the laser non-scanned, not polymerized areas. Later, the samples were submerged into isopropanol and dried in ambient air. For inspection with a scanning electron microscope (SEM), the samples were coated with a thin gold layer *via* sputter-coating.

3. Results and discussion

Typically, the laser beam is expanded to completely fill the input objective aperture in order to obtain ultimate feature size resolution. In this case, the voxel size is mainly defined by NA of the objective. Certainly, it could be enlarged and tuned by the applied laser power, i.e., laser exposure dose. If the laser beam is not covering the front aperture of the objective completely, then this effect would lead to a numerical aperture drop and, hence, to a larger voxel size. We have done numerical calculations in order to calculate the point spread function (PSF) dependence on laser beam size to the entrance of the objective aperture. The amount of laser light covering the input aperture of the objective we define as a filling factor $T = \omega/a$, i.e., simply the ratio of the Gaussian beam waist radius (ω) (at the $1/e^2$) to the objective's aperture radius (a) [18,19]. As reported in [19], the focused Gaussian beam is unclipped for the values $T < 0.5$. The moderate filling ratio increases the achievable resolution. However, it also provides a hybrid focused beam spot size, as the Gaussian beam starts to be truncated and transforms into an Airy pattern as $T \longrightarrow \infty$. Moreover, a further increase of filling factor ($T > 1$) provides just a minor change in focused beam spot size, while the total power loss increases together with intensities of the diffraction rings of the Airy pattern [19,20].

Contrary, if the filling ratio T is below 1, then underfilling of the objective input aperture leads to a drop of effective numerical aperture ($\mathrm{NA_{eff}}$), which could be recalculated using $\mathrm{NA_{eff}}=n \sin\theta_{\max}$, where n - refractive index of the propagation medium, $\theta_{\max}$ - highest marginal ray angle. By simply changing the incident beam waist, the voxel could be enlarged in the lateral and the axial directions. If the $\mathrm{NA_{eff}}$ of the objective is lower, the voxel aspect ratio increases and becomes even more elongated in respect to the optical axis. Under low-NA focusing condition, the beam propagation could be treated using standard scalar theory [20].

For the scalar model, the focused beam spot dimensions could be calculated through the following equations: laser beam radius at the new waist position (after the lens) (at $1/e^2$):

$$\omega_0 = \sqrt{\frac{\lambda z_0}{\pi}} = \frac{\lambda f}{\pi\omega}; \tag{1}$$

depth of focus of laser beam spot size at FWHM:

$$2z_0 = 2\frac{n\pi\omega_0^2}{\lambda} = 2\frac{n\lambda}{\pi}\left(\frac{f}{\omega}\right)^2, \tag{2}$$

where λ - laser wavelength, f - effective focal length of the objective, ω - laser beam waist radius (before the lens), z - the position along the optical axis, z_0 - Rayleigh length, n - refractive index at the focus.

On the other hand, higher NA objectives are typically employed for MPP process to ensure high feature resolution. In that case, the marginal ray angle $\theta_{\max}$ is much larger, therefore a paraxial approximation could not be used anymore. To calculate the PSF under the tight focusing conditions with a high NA objective, spherical aberrations and the polarization effects have to be considered. For this purpose, the PSF needs to be calculated using vectorial Debye theory [20,21].

The theoretical simulation of the light intensity distribution for different objective underfilling conditions were done using vectorial and scalar models. The equations used for the vectorial Debye model can be found elsewhere [18,22]. This model takes into account the polarization state (circular in our case), the contribution of spherical aberrations due to several interfaces (see Fig. 2 (a)) between the objective lens and the focal point. Figures 2 (b)-(g) show the variation of the PSF of intensity distribution calculations for different T (from 0.2 to over 1) filling factors for 0.95 NA objective with 515 nm laser wavelength. For instance, the filling factor T of 0.5 would mean that the diameter of the Gaussian laser beam is twice smaller than the objective's entrance diameter. It is worth noting that the underfilling of the aperture mostly affects the axial voxel resolution, while the lateral is enlarged at much lower scale. As can be clearly seen by incrementally changing the filling factor, the feature axial size could be tuned from sub-micron to tens of microns regime within the same high NA objective.

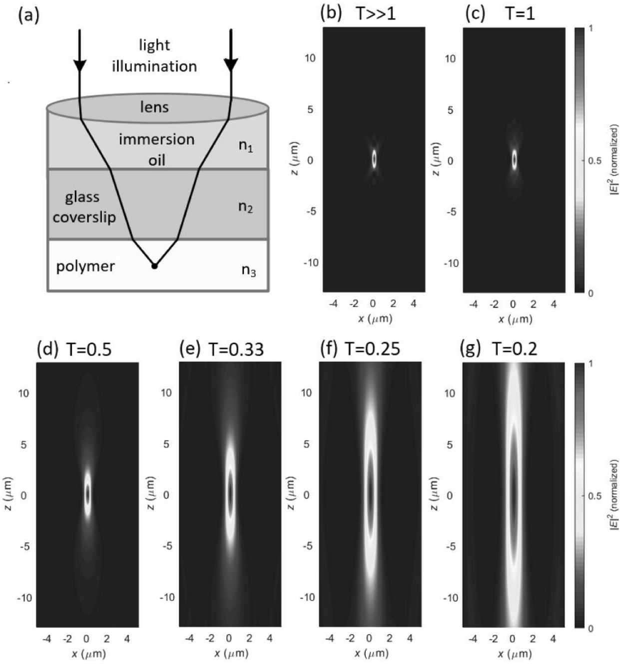

Fig. 2. (a) Schematic illustration of laser beam propagation through stratified media. Calculated PSF by vectorial theory for 0.95 NA objective with λ=515 nm laser wavelength with different filling factors T for the input aperture of the objective. Parameters: (b) $T \gg 1$, (c) $T = 1$, (d) $T = 0.5$, (e) $T = 0.33$, (f) $T = 0.25$, (g) $T = 0.2$.

To quantitatively investigate the voxel dimensions change dependence on the input filling factor, we chose to fabricate suspended fibers between supporting pillars [22]. A series of narrow parallel fibers were done with incrementally increasing the laser power for each of the following fiber and covering the whole dynamic range from polymerization to damage threshold. In this work, we used tight focusing conditions with a 1.4 NA oil-immersion objective, which is very common for the MPP application. The fabricated structures were investigated under the SEM to measure the lateral and axial feature size dimensions, as shown in Fig. 3.

Figure 4 depicts a graphical representation of experimental data, as well as theoretical simulations are plotted as a function of filling factor T. Modelling and experiment were done

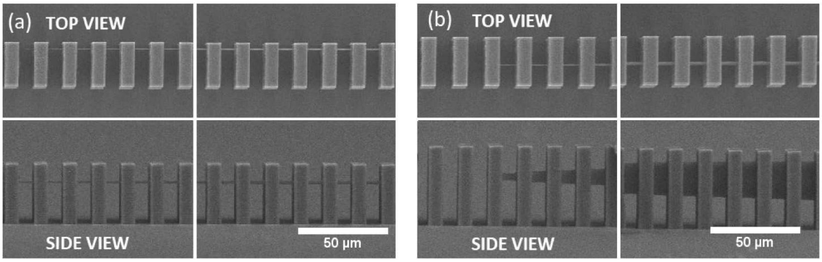

Fig. 3. Top- and side-views of SEM images of suspended fibers between supporting pillars for NA_{eff} of (a) 1.4 and (b) 0.32. The set of individual lines shows voxel growth dynamics with an increasing laser power for (a) 1.4 NA_{eff}, near the (*left*) polymerization (0.09-0.14 mW) and close to (*right*) damage threshold (0.16-0.21 mW). While for (b) 0.32 NA_{eff}, in the ranges of (*left*) 0.17-0.25 mW and (*right*) 0.43-0.53 mW, respectively.

with 1.4 NA objective and λ=515 nm wavelength. As can be seen for underfilling conditions for this objective, there is a good agreement between vectorial and scalar models as the beam diameter is small, up to ~0.7 of T. When exceeding this value, the paraxial approximation cannot be applied anymore, then only the vectorial model is valid. The numerical calculations fit quite well with experimental data, which represent the polymerization threshold for each set of experiment with different filling factor T. In a complete filling case (T = 1), the theoretical modeling predicts better feature resolution than it was achieved during the experiment. It is worth noting that feature size could be experimentally improved by narrowing the distance between the supporting pillar, as well as applying additional post-processing techniques, as critical point dryer for development process.

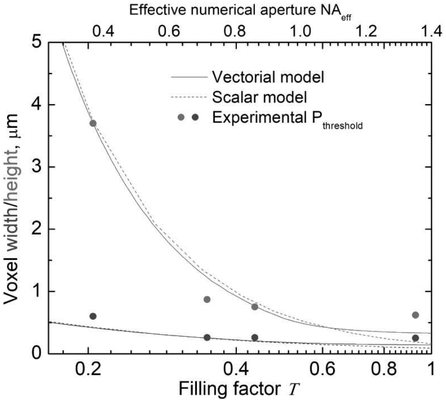

Fig. 4. Comparison of modeled PSF size by using scalar and vectorial theories for 1.4 NA objective. Bullet points represent experimental measurements of polymerization threshold under different filling factor conditions.

A variation of dynamic range, from polymerization to damage threshold, with different light filling conditions is depicted in Fig. 5. The measurements were done through SEM analysis, each of suspended fiber was measured at the middle of the line. The depicted graph is indicative, showing the trend of the feature size growth. Our motorized telescope allowed to change the laser beam expansion from 8x to 1x magnification, which enabled to have the NA_{eff} of 1.4 with a complete filling of the aperture while the least expanded beam dropped the NA_{eff} to 0.32, respectively. The experiments showed that the 1.4 NA_{eff} allowed to produce fine voxels, but had a short fabrication window of features from 0.25 to 0.5 μm in lateral and from 0.62 to 1.27 μm in axial dimensions. In contrast, 0.32 NA_{eff} suffered from limited resolution, but exhibited large dynamic range from 0.6 to ~2 μm transversely and from 3.7 to 22 μm longitudinally. A dynamic variation of NA_{eff} would give the ability to overlap those high and low NA objective regimes, and largely extend the dynamic range within the same single objective.

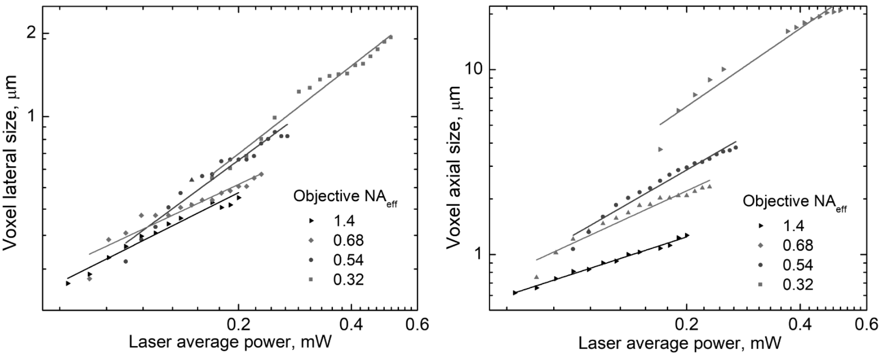

Fig. 5. Measured (a) lateral and (b) axial voxel dimensions fabricated with a single objective by varying its NA_{eff} and laser exposure dose over the entire fabrication window.

In order to demonstrate the potential capability of the dynamics of the voxel size in one structure, we fabricated a woodpile structure, which fully reveals the single voxel size contrast by changing the incident beam on-demand. The grating structure consisted of two different optimized pattern sets (see Fig. 6). The upper and lower sections of the structure were done with first pattern with horizontal periods d_{xy}=5 μm and vertical spacing d_z=6 μm, NA_{eff}=0.54, laser average power P=0.4 mW, while the middle part with second pattern of d_{xy}=2.5 μm and d_z=1.5 μm, NA_{eff}=1.23, P=0.12 mW. With the fixed scanning speed of 100 μm/s the structure was printed in 8 min.

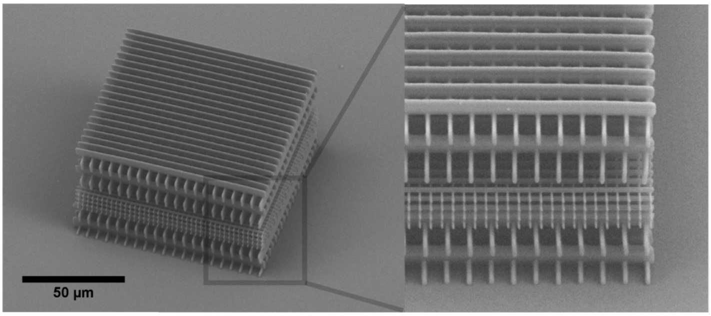

Fig. 6. SEM image of the woodpile structure having two different voxel segments: upper and lower parts were done with NA_{eff}=0.54, while the middle section with NA_{eff}=1.23. Whole structure was fabricated using the same microscope objective as well as constant translation velocity.

In microscopy, the principles of the resolving power (or resolution) dependence on the lens aperture was already known by E. Abbe more than a century ago, however, this straightforward method has never been applied for the additive manufacturing. For the MPP technique, a high NA objective is not always considered as the first choice for all applications. For instance, scaffolds in bio-medicine, the lower NA objectives are even more desired for bigger structures, which provide larger voxels and faster structuring [23]. However, the large-size structures with small features require tight focusing conditions, which could prolong the fabrication process to an unreasonable time. In this case, compared to the traditional MPP scheme, the dynamic voxel control gives an extra degree of freedom in the MPP fabrication process for the same objective. A large NA_{eff} tuning range has been achieved from 1.4 to 0.32 NA. It should be noted that we were limited by the least magnification of the telescope. A further reduction of the beam size would result in even lower achievable NA_{eff}. However, from an engineering point of view, this method requires a precise alignment of the optical system, otherwise variation of beam diameter may introduce laser focus shift in the field of the objective. In addition, the focal spot size could be easily scaled by this technique, however, the physical focal length and field of view remain unaffected. As the high NA objectives have a short working distance, the overall height of the achievable structures could be a limiting factor for some of the applications. Nonetheless, this beam expansion/reduction approach could easily be integrated into MPP systems and applied for large-size (mm) prototype structures with tiny features with hundred of nanometers of feature resolution. It could be used as an alternative to currently used approaches or solve the need to change objectives for up-scaling the voxel size with different objectives.

4. Conclusion

In this paper we present the possibility to employ dynamic voxel control by changing the incident beam diameter to the input of the objective with a motorized beam expander. An expanded beam with almost complete filling of the input aperture for 1.4 NA objective allowed to obtain the voxel feature size of 0.25 µm in the lateral and 0.62 µm in the axial direction, while unexpanded beam ($T = 0.2$) allowed to enlarge the voxel up to ~2 µm transversely and 22 µm longitudinally, respectively. This ability provides a huge extension of the fabrication window for high NA objective. We have modeled the PSF by vectorial and scalar models, which had a quite good agreement with our experimental results. It should be noted that a straightforward scalar model well describes the PSF variation up to 0.7 of the filling factor for 1.4 NA objective, then the vectorial theory should be used. Finally, we successfully demonstrated the realization of dynamically tunable voxel size. The presented approach extends the technology capabilities and could significantly increase the fabrication speed while maintaining the possibility to obtain high resolution features at the same time.

Funding

Lithuanian Business Support Agency (J05-LVPA-K-03-0006).

Acknowledgments

Authors thank to Dr. Sima Rekštytė for the help in modeling PSF distributions.

Disclosures

The authors declare no conflicts of interest.

References

1. M. Malinauskas, M. Farsari, A. Piskarskas, and S. Juodkazis, "Ultrafast laser nanostructuring of photopolymers: A decade of advances," Phys. Rep. **533**(1), 1–31 (2013).

2. T. Gissibl, S. Thiele, A. Herkommer, and H. Giessen, “Two-photon direct laser writing of ultracompact multi-lens objectives,” Nat. Photon. **10**(8), 554–560 (2016).
3. T. Frenzel, M. Kadic, and M. Wegener, “Three-dimensional mechanical metamaterials with a twist,” Science **358**(6366), 1072–1074 (2017).
4. A. Ovsianikov, S. Schlie, A. Ngezahayo, A. Haverich, and B. N. Chichkov, “Two-photon polymerization technique for microfabrication of CAD-designed 3D scaffolds from commercially available photosensitive materials,” J. Tissue Eng. Regener. Med. **1**(6), 443–449 (2007).
5. D. Wu, S.-Z. Wu, J. Xu, L.-G. Niu, K. Midorikawa, and K. Sugioka, “Hybrid femtosecond laser microfabrication to achieve true 3D glass/polymer composite biochips with multiscale features and high performance: the concept of ship-in-a-bottle biochip,” Laser Photon. Rev. **8**(3), 458–467 (2014).
6. L. Jonušauskas, S. Rekštytė, and M. Malinauskas, “Augmentation of direct laser writing fabrication throughput for three-dimensional structures by varying focusing conditions,” Opt. Eng. **53**(12), 125102 (2014).
7. M. Manousidaki, D. G. Papazoglou, M. Farsari, and S. Tzortzakis, “Long-scale multiphoton polymerization voxel growth investigation using engineered bessel beams,” Opt. Mater. Express **9**(7), 2838–2845 (2019).
8. M. Manousidaki, D. G. Papazoglou, M. Farsari, and S. Tzortzakis, “Abruptly autofocusing beams enable advanced multiscale photo-polymerization,” Optica **3**(5), 525–530 (2016).
9. L. Kelemen, S. Valkai, and P. Ormos, “Parallel photopolymerisation with complex light patterns generated by diffractive optical elements,” Opt. Express **15**(22), 14488–14497 (2007).
10. L. Yang, D. Qian, C. Xin, Z. Hu, S. Ji, D. Wu, Y. Hu, J. Li, W. Huang, and J. Chu, “Two-photon polymerization of microstructures by a non-diffraction multifoci pattern generated from a superposed bessel beam,” Opt. Lett. **42**(4), 743–746 (2017).
11. M. Manousidaki, D. G. Papazoglou, M. Farsari, and S. Tzortzakis, “3D holographic light shaping for advanced multiphoton polymerization,” Opt. Lett. **45**(1), 85–88 (2020).
12. E. Stankevičius, M. Garliauskas, M. Gedvilas, and G. Račiukaitis, “Bessel-like beam array formation by periodical arrangement of the polymeric round-tip microstructures,” Opt. Express **23**(22), 28557–28566 (2015).
13. W. Chu, Y. Tan, P. Wang, J. Xu, W. Li, J. Qi, and Y. Cheng, “Centimeter-height 3D printing with femtosecond laser two-photon polymerization,” Adv. Mater. Technol. **3**(5), 1700396 (2018).
14. L. Jonušauskas, D. Gailevičius, S. Rekštytė, T. Baldacchini, S. Juodkazis, and M. Malinauskas, “Mesoscale laser 3D printing,” Opt. Express **27**(11), 15205–15221 (2019).
15. D. Wu, Q.-D. Chen, L.-G. Niu, J.-N. Wang, J. Wang, R. Wang, H. Xia, and H.-B. Sun, “Femtosecond laser rapid prototyping of nanoshells and suspending components towards microfluidic devices,” Lab Chip **9**(16), 2391–2394 (2009).
16. S. Dehaeck, B. Scheid, and P. Lambert, “Adaptive stitching for meso-scale printing with two-photon lithography,” Addit. Manuf. **21**, 589–597 (2018).
17. A. Ovsianikov, J. Viertl, B. Chichkov, M. Oubaha, B. MacCraith, I. Sakellari, A. Giakoumaki, D. Gray, M. Vamvakaki, M. Farsari, and C. Fotakis, “Ultra-low shrinkage hybrid photosensitive material for two-photon polymerization microfabrication,” ACS Nano **2**(11), 2257–2262 (2008).
18. M. J. Nasse and J. C. Woehl, “Realistic modeling of the illumination point spread function in confocal scanning optical microscopy,” J. Opt. Soc. Am. A **27**(2), 295–302 (2010).
19. H. Urey, “Spot size, depth-of-focus, and diffraction ring intensity formulas for truncated gaussian beams,” Appl. Opt. **43**(3), 620–625 (2004).
20. T. Baldacchini, *Three-dimensional Microfabrication using Two-photon Polymerization* (William Andrew, 2015).
21. M. Born and E. Wolf, *Principles Of Optics: Electromagnetic Theory of Propagation, Interference and Diffraction Of Light* (Pergamon, 1980).
22. T. Tičkūnas, D. Paipulas, and V. Purlys, “4Pi multiphoton polymerization,” Appl. Phys. Lett. **116**(3), 031101 (2020).
23. P. Danilevičius, S. Rekštytė, E. Balčiūnas, A. Kraniauskas, R. Širmenis, D. Baltriukienė, M. Malinauskas, V. Bukelskienė, R. Gadonas, V. Sirvydis, and A. Piskarskas, “Direct laser fabrication of polymeric implants for cardiovascular surgery,” Mater. Sci. **18**(2), 145–149 (2012).

Vilnius University Press
9 Saulėtekio Ave., Building III, LT-10222 Vilnius
Email: info@leidykla.vu.lt, www.leidykla.vu.lt
Print run copies 20